

Università degli Studi di Catania

Dipartimento di Ingegneria  
Elettrica, Elettronica ed Informatica

International Ph.D. in Energy  
XXVII Cycle

Graphene Heterostructures  
with  
Wide-Bandgap Semiconductors

Gabriele Fisichella

Coordinator: Prof. Ing. L. Marletta

UniCT Supervisor: Prof. Ing. A. Raciti

IMM-CNR Supervisor: Dott. F. Giannazzo

*2011/2014*

# Abstract

Graphene (Gr) is a two-dimensional material constituted by an atomically thin carbon membrane, characterized by a unique combination of excellent electrical, optical, thermal and mechanical properties. Its main limitation for microelectronic applications is related to the lack of a bandgap, leading to a poor  $I_{on}/I_{off}$  ratio when it is considered as channel material for MOSFET devices. Novel device concepts based on Gr heterostructures with semiconductors are currently under consideration, in order to overcome these limitations. These devices are based on the vertical current transport through Gr interfaces with semiconductors or thin insulators. Their working principle exploits some unique properties of Gr, such as the atomic thickness and the field effect modulation of its workfunction. Some demonstrations of these devices, recently reported in the literature, have been based on the integration of Gr with Si technology.

This thesis work has been focused on the fabrication and the electrical characterization of high quality heterostructures of Gr with wide-bandgap semiconductors (WBS), such as Silicon Carbide (4H-SiC), Gallium Nitride (GaN) and related alloys ( $Al_xGa_{1-x}N$ ), which present superior properties for high power and high frequency electronic applications.

At first, the fabrication methods have been discussed, i.e.

- (i) the controlled graphitization of the surface by high temperature thermal annealing, for 4H-SiC;
- (ii) a highly reproducible transfer method to move Gr, grown by CVD on copper foils, to the surface of AlGaN/GaN heterostructures.

A detailed structural, morphological and spectroscopic characterization of these Gr/WBS heterostructures has been carried out by the joint application of several analytical techniques, such as AFM; TEM, micro-Raman spectroscopy.

Secondly, the current transport mechanisms through these heterostructures have been investigated in details by properly fabricated test devices and by nanoscale resolution electrical characterization techniques (CAFM, SCM). A correlation between the nanoscale structural, morphological and electrical properties of the interfaces with the devices average electrical behavior has been achieved.

Basing on these results, some potential devices applications (such as the Gr/SiC Schottky diode with a gate modulated barrier and the hot electron transistor constituted by a Gr/AlGaN/GaN heterostructures with a Gr-base) have been discussed and their advantages with respect to the Si counterparts have been estimated.

## Acknowledgments

These research activities have been carried out within the International Ph.D. course in Energy (University of Catania) and supported by the National Project PON Ambition Power (PON01\_00700).

The course was organized in two main phases:

- (i) the academic training, which was carried out at the Department of Electric, Electronic and Computer Engineering (DIEEI), University of Catania
- (ii) the research activity, entirely carried out in the laboratories of the Institute of Microelectronic and Microsystems (IMM-CNR), Catania

In that regard, I want to thank Prof. Ing. Luigi Marletta, coordinator of Ph.D. course and Prof. Ing. Luigi Fortuna, academic training project manager. Furthermore, I would like to thank Dr. Corrado Spinella, former Director of CNR-IMM, Catania and Dr. Guglielmo Fortunato, present acting Director, for the access to the facilities of the Institute.

I would like to thank all the people who have supported and assisted me in this work.

I would like to express my gratitude at first to my Supervisor at CNR-IMM, Dr. Filippo Giannazzo, who has provided me, with great patient and care, all the essential basis on which I could build the activities described in this work.

I would like to express my thanks to my Supervisor at the University of Catania, Prof. Ing. Angelo Raciti, for his presence and his willingness.

Thanks to all the people of the team at CNR-IMM of which I was part: Dr. Fabrizio Roccaforte, who oversaw with determination the activity in its entirety, to Salvo DiFranco, who helped me with his experience to solve major practical problems in the manipulation of materials, to Dr. Raffaella Lo Nigro, who introduced me in this research field and to all the other members of the team, Dr. Patrick Fiorenza, Dr. Giuseppe Greco, Dr. Marilena Vivona, Aurora Piazza and Emanuela Schiliro, for the scientific and the moral support given to me on several occasions.

My thanks go also to other members of the CNR-IMM, Dr. Corrado Spinella, Dr. Giuseppe Nicotra and Corrado Bongiorno for the useful TEM analysis, Dr.

Antonino LaMagna and Dr. Ioannis Deretzis for their contribution with simulations and Dr. Nicolò Piluso for Raman measurements.

Thanks to the people from ST Microelectronics, Catania, for the essential support regarding materials and electrical measurements apparatus necessities for the continuation of this activity and in particular to Dr. Sebastiano Ravesi and his team, Dr. Stella Loverso and Dr. Silvestra DiMarco, to Dr. Noemi Spartà to Dr. Cristina Tringali, to Dr. Corrado Accardi, to Dr. Ferdinando Iucolano and to Dr. Mario Saggio and his team.

Thanks to Prof. Guido G. Condorelli, and to Dr. Cristina Tudisco from the department of Chemistry of the University of Catania, for the collaboration with XPS measurements and to Prof. Simone Agnello and his team from the department of Physics of the University of Palermo, for Raman measurements.

Thanks to Ing. Mattia Frasca for the administrative support during the Ph.D. activity.

I would like to thank all the international partners, and in particular Prof. Heiko B. Weber and the members of his team, Prof. Michael Krieger, Dr. Stefan Hertel and Dr. Andreas Albert from the Chair for Applied Physics, Friedrich-Alexander University – Erlangen-Nuremberg (Germany), and Prof. Rosita Yakimova from the IFM, Linkoping University (Sweden), for their essential contributions within the framework of Gr on SiC.

# Contents

<b>Introduction</b>	<b>1</b>
<b>Chapter 1: Graphene, physical properties and production methods</b>	<b>7</b>
1.1 <i>Physical properties</i>	7
1.2 <i>Graphene preparation methods</i>	21
1.2.1 Exfoliation of Graphite	21
1.2.3 Chemical Vapor Deposition of graphene on catalytic metals	22
1.2.4 Epitaxial graphene by controlled graphitization of Silicon Carbide	25
1.2.5 Graphene transfer	35
<b>Chapter 2: Graphene heterostructures with semiconductors</b>	<b>43</b>
2.1 <i>Physics of the Gr/semiconductor junction</i>	45
2.2 <i>Devices based on the Gr/semiconductor junction</i>	50
2.3 <i>Hot electron transistors with a graphene base</i>	53
2.4 <i>Graphene field effect tunnelling transistors</i>	56
<b>Chapter 3: Fabrication of graphene heterostructures with wide-bandgap semiconductors</b>	<b>59</b>
3.1 <i>Transfer of CVD grown graphene by electrolytic delamination and thermo-compression printing</i>	61
3.1.1 Description of the transfer procedure	61
3.1.2 Study of the electrolytic delamination kinetic	74
3.1.3 Graphene transferred on AlGaN/GaN substrates	82
3.2 <i>Epitaxial Graphene on SiC (0001): role of the miscut angle</i>	85

3.2.1 Fabrication of Schottky contacts on on-axis and off-axis SiC (0001) by hydrogen intercalation at epitaxial Gr/SiC interface	95
<b>Chapter 4: Electrical characterization of graphene heterostructures with wide-bandgap semiconductors</b>	<b>97</b>
4.1 <i>Gr/AlGaN/GaN heterostructures</i>	97
4.1.1 Lateral current transport in Gr in contact to AlGaN	97
4.1.2 Vertical current transport in Gr/AlGaN/GaN heterostructures	99
4.1.3 From Schottky to ohmic graphene contacts to AlGaN/GaN heterostructures: role of the AlGaN layer microstructure	116
4.2 <i>Lateral and vertical electrical characterization of epitaxial graphene on SiC</i>	121
4.2.1 Lateral current transport	121
4.2.2 Vertical current transport through EG/SiC interface	130
4.3 <i>Perspective vertical devices based on Gr/WBS heterostructures</i>	135
4.3.1 Barristor based on the QFEG/SiC Schottky barrier	135
4.3.2 Graphene base HET based on the Gr/AlGaN/GaN heterostructure	139
<b>Summary</b>	<b>145</b>
<b>Bibliography</b>	<b>151</b>

# List of Figures

- Figure 1.1: allotropes of carbon represented starting from a Gr sheet (a): (b) graphite, (c) carbon nanotubes and (d) fullerene. 7
- Figure 1.2: (a) Crystal structure of monolayer Gr with A and B atoms shown as empty and full circles. The shaded rhombus is the conventional unit cell while  $a_1$  and  $a_2$  are primitive lattice vectors. (b) Reciprocal lattice of Gr where the first Brillouin Zone is indicated with the high symmetry point  $\Gamma$  as the centre,  $K$  and  $K'$  as the two non-equivalent corners and  $M$ ,  $M'$ , and  $M''$  as the three non-equivalent centers of the edge while  $b_1$  and  $b_2$  are reciprocal lattice vectors. 9
- Figure 1.3: (a) Energy dispersion relation of the  $\sigma$  (red) and the  $\pi$  (blue) bands of the momentum  $|\mathbf{k}|$  along the directions defined by the high symmetry points  $\Gamma$ ,  $M$  and  $K$ . (b) Dispersion relation of Gr for the whole set of points of the first Brillouin Zone. 10
- Figure 1.4: carrier density as a function of  $E_F - E_D$  at a temperature  $T = 300$  K and (above) the variation of the  $E_F$  in the Dirac cones. 12
- Figure 1.5: calculated intrinsic electron mean free path (a), mobility (b) and conductivity (c) versus the carrier density  $n$  at three different temperatures ( $T = 10, 100$  and  $300$  K) for a Gr sample with size  $W = 1 \mu\text{m} \times 1 \mu\text{m}$ . 15
- Figure 1.6: UV-vis spectra for a different number of Gr layers, from the single layer to a four layer stack [52]. The transmitted light decreases almost proportionally with the number of layer. 16
- Figure 1.7: Phonon dispersion of Gr along high symmetry lines in the hexagonal Brillouin zone. Three Acoustic ( $A$ ) and three Optical ( $O$ ) phonon modes are reported. At low  $q$ , the wave vector  $q$  is linear for Longitudinal ( $LA$ ) an in-plane Transverse ( $TA$ ) Acoustic phonons and quadratic for out-of-plane flexural ( $ZA$ ) Acoustic Phonon [64]. 18

Figure 1.8: Phase diagrams for the binary system (a) Ni-C and (b) Cu-C: the maximum solid solubility of C is strongly different in Ni and Cu, with $\sim 0.6\%$ at $T_M = 1455^\circ\text{C}$ and $\sim 0.0076\%$ at $T_M = 1085^\circ\text{C}$ for Ni and Cu respectively. (c) and (d) illustrate the different growing mechanisms of Gr on (c) Ni where the segregation of C from bulk is the main phenomena and on (d) Cu where the surface epitaxial growth dominates.	23
Figure 1.9: SEM image of Gr domains grown on Cu before merging. Insert in the top shows a magnification of the same domains [92].	25
Figure 1.10: 3D illustration of the hexagonal polytype SiC which exposes two faces with different terminations: the Si-terminated face (0001) on top (magenta) and the C-terminated face (000-1) on the bottom (blue).	26
Figure 1.11: Schematic illustration of Gr growth: (a) sublimation of Si atoms and reorganization of remaining C atoms in a Gr islands; (b) merging of the islands in a Gr layer and starting formation of a second Gr layer under the first layer; (c) repetition of the same mechanism for a third Gr layer.	27
Figure 1.12: AFM morphologies and low energies electron diffraction images (left and right of each group respectively) in the cases of (a) Gr grown in UHV at $1280^\circ\text{C}$ and (b) in Ar at 900 mbar [19].	28
Figure 1.13: LEED patterns for Gr grown on (a) the S-terminated face and on (b) the C-terminated face. Dispersion of the $\pi$ -bands measured with ARPES perpendicular to the $\Gamma K$ -direction of the Gr Brillouin zone for (c) a Gr single layer and (d) a double layer on the S-terminated face and for (e) multilayer Gr on the C-terminated face.	30
Figure 1.14: temperature dependence of the Gr mobility for the case of the n-type doped Gr in the presence of the underlying buffer layer. The mobility drop from 20 K to 300 K is more than 50% [107].	32
Figure 1.15: Dispersion of the $\pi$ -bands measured with ARPES perpendicular to the $\Gamma K$ -direction of the Gr Brillouin zone and correspondent schematic illustration before and after the hydrogen treatment for an as grown buffer layer (a,b) and an as grown buffer layer plus a second Gr layer (c,d) [22].	33
Figure 1.16: temperature dependence of the Gr mobility for the case of the p-type doped Gr after the hydrogen treatment. The mobility drop from 20 K to 300 K is less than 10% [107].	34



- Figure 1.17: Schematic illustration of Gr transferred from a TRT to a target substrate by roll-to-roll or by hot pressing [121]. 38
- Figure 2.1: (a) Gr and n-type semiconductor in separated systems, (b) connected in an ideal Schottky barrier without surface states and (c) considering the effect of the interfacial states. (d) Analogues representation of Gr with the p-type semiconductor in separated systems, (e) connected in an ideal Schottky barrier without surface states and (f) considering the effect of the interfacial states. 46
- Figure 2.2: qualitative atom disposal sketch (above) and schematic representation (below) of the band diagrams for the epitaxial (a) and the quasi-free-standing (b) Gr interface with 6H-SiC (0001). Large blue and small red circles represent silicon and carbon atoms of the SiC lattice respectively, grey circles represent carbon reorganized over SiC and magenta circles represent the hydrogen that passivates SiC surface. The polarization vector inside and outside of the SiC is indicated at the bottom of the figure. Circled charges represent the pseudo-charge induced by polarization.  $D$  sketches the electrostatic potential between the SiC surface and the Gr layer [152]. 49
- Figure 2.3: (a) A schematic diagram to show the concept of a Gr *Barristor*. (b-c) Schematic representation of the band diagrams of the n-type device with an applied gate bias on the top of Gr. Applying negative voltage on the gate induces holes in Gr, increasing its work function and increasing the SBH (c) while positive gate voltage decreases the SBH (d) [9]. 52
- Figure 2.4: (a) A schematic diagram to show the collector-up GB-HET structure and the common-base configuration. Gr is used as the base region for an HET structure. The purple arrows indicate the transport direction of the hot electrons. (b-c) schematic representation of the band diagrams of the device, where red arrow represent hot electrons tunnel from the silicon emitter to the Gr base through the  $\text{SiO}_2$  tunnelling barrier. Depending on the  $V_{BE}$  hot electrons possesses different kinetic energy, which allows or not allows traveling over the filtering barrier. (d) The output  $I$ - $V$  characteristics at various  $V_{BE}$  bias [11]. 54

- Figure 2.5: (a) Schematic structure of Gr field-effect tunnelling transistor. (b-c) Graphic representation of the band structure for the operational principle when a  $V_g$  is applied measuring a zero bias  $V_b$  when no tunnelling current is reached (c) and for a finite  $V_b$ . (d). Tunnelling characteristics through ~6 hBN layers measured for different  $V_g$  from 5 V to -45 V [12]. 57
- Figure 3.1: (a) Optical image and (b) Raman Spectroscopy of the as-grown Gr on Cu. 61
- Figure 3.2: (a) AFM morphologies of as-grown Gr on Cu. A line scan perpendicular to a wrinkle of Gr on Cu is depicted and the corresponding height profile is reported in (b). 62
- Figure 3.3: (a) hot embossing NIL equipment by Karl-Suss. and (b) detail of the thermo-compressive chamber inside, consisted of thermally and mechanically controllable elements i.e. a chuck (below) and an arm (above) . 63
- Figure 3.4: (a-c) Schematic illustration of the copper planarization obtained pleasuring the wrinkled copper foil (in orange) on the chuck x-y plane (a), pressing it respect to the z axes, by the arm (b) and realizing the arm pressure (c) as described by the pressure ramp in (d). (e-g) Schematic illustration of the copper attachment on a rigid substrate, obtained fishing the copper foil by the arm vacuum aspiration and aligning it above a silicon substrate (in violet) on which a double face TRT is attached (in yellow). The attachment is obtained repeating the pressure ramp in (d). 64
- Figure 3.5: (a -d) Schematic illustration of the TRT/PMMA/Gr/Cu stack preparation performed by the spin coating of Cu with PMMA (represented in blue) (a), the bake of PMMA and the contemporary release of the double face TRT (in yellow) at 150°C (b) followed by the single face TRT attachment (in magenta) on the PMMA surface, pressing the tape respect to the z axes, by the arm (c). Finally the arm releases the pressure and fishes by vacuum aspiration the final TRT/PMMA/Gr/Cu stack (d). Graphic description of the bake ramp (in magenta) followed by a pressure ramp (in black) respect to the time axis (e). 66

- Figure 3.6: Schematic representation of the electrolytic cell defined by a Gold foil (in yellow) working as the anode and the TRT/PMMA/Gr/Cu foil (in magenta, blue and orange respectively) working as the cathode, in a KOH solution. 67
- Figure 3.7: (a) AFM morphology of Gr after its separation from the metal foil (b), i.e., when it is still attached to the PMMA/TRT stack.. A line scan perpendicular to a wrinkle of Gr on PMMA is depicted in (a) and the corresponding height profile is reported in (c). A small crack in the Gr membrane is also indicated in (a) with a circle. 69
- Figure 3.8: (a-d) Schematic illustration of thermo-compressive transfer-printing process to transfer the PMMA/Gr stack (in blue) from the TRT (in magenta) (a) to the target substrate (in grey) (d), pressing it respect to the Z axes and heating by the chuck and the arm (b). Chemical elimination of PMMA to obtain a free Gr (in black) on the target substrate (d). 70
- Figure 3.9: (a-d) AFM morphologies of Gr transferred on SiO<sub>2</sub> substrates and (e-g) corresponding thermo-compressive ramps exploited for the transferring; (a) Gr transferred by hand, (b) Gr transferred with the high pressure and fast ramp (e), (c) Gr transferred with the optimal pressure and a fast ramp (f), Gr transferred with the final slow thermo-compressive ramp (g). 71
- Figure 3.10: (a) Set of Raman spectra collected on different positions of the Gr transferred on a SiO<sub>2</sub> substrate, (b) plot of 2D shift and of  $I_{2D}/I_G$  for the set of the collected positions and (c) optical image of the sampled positions. 74
- Figure 3.11: AFM morphology of Gr membranes transferred on SiO<sub>2</sub>/Si substrates after electrolytic delamination with three different KOH concentrations: 0.05 M (a), 0.15 M (b), 0.60M (c). Histograms of wrinkles height (d), (e), (f), and distances (j), (k), (l) for the three samples. 76

- Figure 3.12: (a) Schematic representation (front view) of H<sub>2</sub> bubbles nucleation and growth at Cu perimeter: Gr wrinkle at the Cu foil perimeter (i); bubble nucleation and growth, with the deformation of the wrinkle cavity (ii); detachment of Gr from Cu (iii); coalescence of two expanding neighboring cavities (iv). (b) Schematic representation (side view) of the cavity at its maximum expansion and representation of the forces involved in the Gr delamination. (c) Measured time  $t_d$  for Gr delamination from 1 cm<sup>2</sup> Cu foil as a function of the electrolyte concentration ( $C_{KOH}$ ) and fit with the discussed microscopic model. In the inset, the dependence of H<sub>2</sub> supersaturation in the solution is reported versus CKOH and fitted with the expression  $S = aC_{KOH}^b$ . 80
- Figure 3.13: Representative tAFM analyses of the bare AlGa<sub>N</sub> surface of samples A (a) and B (b). Cross-sectional TEM images of the same samples are shown in (c) and (d). 82
- Figure 3.14: Two typical tAFM images of Gr transferred to the AlGa<sub>N</sub> surface of the samples A (a) and B (b). Representative Raman spectra of Gr on AlGa<sub>N</sub> and SiO<sub>2</sub> (c). 83
- Figure 3.15: (a) schematic representation of the miscut angle  $\theta$  formed by the SiC ingot growth axis [0001] and the vector orthogonal to the plane of cutting of the wafer. (b) 3D projection of the SiC ingot grown in the [0001] direction intersected by the plane of cutting (blue plane) with a miscut angle  $\theta$ . 85
- Figure 3.16: Atomic force microscopy image of the surface morphology (a) and line profile (b) on a virgin 4H-SiC(0001) substrate cut at an angle of 8° with respect to the basal plane along the [1120] direction. 87
- Figure 3.17: tAFM Surface morphology for the samples annealed at 1600 (a) and 1700°C (b). 87
- Figure 3.18: (a) 3D projection of the surface morphology of the sample annealed at 1700°C to highlight the topography of wrinkles. The blue line in (a) corresponds to the line-profile scan in (b) taken in the direction parallel to the steps to estimate the heights of a wrinkle. 89
- Figure 3.19: Typical Raman spectra measured on virgin 4H-SiC (0001) and after epitaxial Gr growth at 1600°C and 1700°C. 89

## VIII

- Figure 3.20: HRTEM of the step profile for an EG sample grown at 1700°C on 8° off axis 4H-SiC (0001) cross-sectioned perpendicularly to the [1-100] (b) Statistical distribution of the angle measured for different steps. HRTEM measures used to evaluate the number of Gr layers on the (0001) face grown at 1600 C (c) and 1700°C (d). 91
- Figure 3.21: Optical image on the O<sub>2</sub> etched stripes in the graphitized 4H-SiC sample by annealing at 1700°C (a). AFM height profile taken on a stripe of pristine SiC (b) and on a stripe of the sample annealed at 1700°C (c), respectively. 92
- Figure 3.22: HAADF atomic resolution STEM image of the cross sectioned profile along the [1120] direction of the (0001) surface (a) and the (11-2n) surface (b). EELS spectra and the simultaneously acquired HAADF STEM image of a faceted step in the annealed 4H-SiC sample cross-sectioned along the [1120] direction (c). Schematic cross section of the structural configuration of the 1<sup>st</sup> C layer on the faceted surface, as deduced from STEM and EELS analyses (d). 94
- Figure 3.23: schematic illustration of (a) an n<sup>+</sup>-doped 4H-SiC 3,5° off-axis with a n<sup>-</sup>-doped epitaxial layer and (b) a nominally on-axis semi-insulating SiC where a nitrogen ion implantation was employed to obtain a surface n<sup>-</sup>-well region and a buried n<sup>+</sup>-layer. (c) and (d) schematically illustrate the QFEG grown by thermal decomposition at 1680°C under Ar flux near atmospheric pressure followed by hydrogen intercalation at 850°C in a H<sub>2</sub> flux, for the off-axis (c) and the on-axis (d) samples. 95
- Figure 3.24: Schematic representation of Au-capped (a) and uncapped (b) QFBLG contacts on on-axis SiC (0001) with a n<sup>-</sup>-well region and a buried n<sup>+</sup>-layer obtained by nitrogen ion implantation. Schematics of Au-capped (a) and uncapped (b) QFBLG contacts on a 3.5° off-axis SiC (0001) epilayer. 96

- Figure 4.1: (a) Schematic representation of a TLM test structure fabricated on the Gr membrane residing on AlGa<sub>N</sub>. (b)  $I$ - $V$  characteristics measured between pairs of contacts at different distances and (c) extracted resistance plotted vs. the pads distance. Analogous (d) schematic representation, (e)  $I$ - $V$  characteristics and (f) resistance plotted vs. the pads distance for Gr residing on SiO<sub>2</sub>. From the linear fit of  $R$  versus  $d$ , the Gr sheet resistance was evaluated. 98
- Figure 4.2: Sheet resistance ( $R_{sh}$ ) plotted vs. versus  $V_g$  from -40 V to 40 V, for Gr residing on SiO<sub>2</sub>. 99
- Figure 4.3: Two different series of  $I$ - $V$  curves collected using an Au coated AFM tip displaced on a square array of 25 positions on AlGa<sub>N</sub>/Ga<sub>N</sub> (a) and Gr/AlGa<sub>N</sub>/Ga<sub>N</sub> (b). Schematic representations of the experimental setup for local  $I$ - $V$  measurements by CAFM, in the inserts of (a) and (b). Fitting of two representative forward bias  $\ln(I)$ - $V$  curves acquired on AlGa<sub>N</sub> (c) and Gr/AlGa<sub>N</sub> (d). Conduction band diagrams of AlGa<sub>N</sub>/Ga<sub>N</sub> (e) and Gr/AlGa<sub>N</sub>/Ga<sub>N</sub> heterostructures (f) with the equivalent circuit of a Schottky AlGa<sub>N</sub>/Ga<sub>N</sub> diode represented as two diodes back-to-back in series. 101
- Figure 4.4: Histograms of the  $\Phi_{B1}$ ,  $\Phi_{B2}(0)$  (a), and  $n_{s0}$  (b) obtained on an array of 25 tip positions (spaced 1  $\mu\text{m}$  from each other) on the AlGa<sub>N</sub>/Ga<sub>N</sub> and Gr/AlGa<sub>N</sub>/Ga<sub>N</sub> heterostructures. 106
- Figure 4.5: Behavior of  $\Phi_{B1}$ , and  $\Phi_{B2}(0)$  versus the deflection set point (DSP), for the AlGa<sub>N</sub>/Ga<sub>N</sub> and Gr/AlGa<sub>N</sub>/Ga<sub>N</sub> heterostructures. 107
- Figure 4.6: Behavior of  $\Phi_{B1}$ ,  $\Phi_{B2}(0)$  (a) and  $n_{s0}$  (b) versus the metal workfunction for the AlGa<sub>N</sub>/Ga<sub>N</sub> and Gr/AlGa<sub>N</sub>/Ga<sub>N</sub> heterostructures. 108
- Figure 4.7: Calculated conduction band diagram for the Gr/AlGa<sub>N</sub>/Ga<sub>N</sub> heterostructure at zero bias. 109
- Figure 4.8: AFM morphology (a) and phase (b) images of a region including bare AlGa<sub>N</sub> and AlGa<sub>N</sub> coated by few layers of Gr (1, 4, 5, 6 and 7 layers in a step-like fashion). (c) Height profile measured along the indicated line in (a). (d) Height values measured with respect to the AlGa<sub>N</sub> baseline level as a function of the layer number  $N$ . By linear fitting of the data, the interlayer separation ( $h = 0.34 \pm 0.01$  nm) and the intercept with the height axis ( $t_0 = 0.07 \pm 0.04$  nm) were extracted. 110

Figure 4.9: Histogram of $n_{gr0}$ at the different positions in the Gr/AlGaIn/GaN heterostructure.	111
Figure 4.10: (a) Two representative $C$ - $V_{tip}$ curves measured on the AlGaIn/GaN and on the Gr/AlGaIn/GaN heterostructures using an Au coated tip. In the insert, there is a schematic representation of the SCM experimental setup. (b) Electron density $n_s$ of AlGaIn/GaN 2DEG as a function of $V_{tip}$ , obtained by integration of the representative $C$ - $V_{tip}$ curves in (a). (c) Electron density $n_{gr}$ in Gr, as a function of $V_{tip}$ . The relation between $n_s$ and $n_{gr}$ is shown in the insert.	113
Figure 4.11: Measured capacitance of the Gr/AlGaIn/GaN heterostructure ( $C_{tot}$ ) compared with the quantum capacitance of the AlGaIn/GaN 2DEG ( $C_{Q,ord}$ ) and the Gr quantum capacitance ( $C_{Q,gr}$ )	114
Figure 4.12: The energy band structures of the Gr/AlGaIn/GaN heterostructure at equilibrium ( $V_{tip} = 0$ ) (a), under reverse ( $V_{tip} < 0$ ) (b) or forward polarization ( $V_{tip} > 0$ ) (c).	115
Figure 4.13: $I$ - $V$ characteristics collected on the bare AlGaIn surface of samples A (a) and B (b) and on the Gr-coated regions of samples A (c) and B (d). The fitting of representative forward bias $I$ - $V$ curves (with $I$ on logarithmic scale) using the thermoionic emission model has been reported in the insets of (a), (b) and (c).	117
Figure 4.14: Histograms of the SBH values obtained from the $I$ - $V$ characteristics at different tip positions on bare AlGaIn (samples A and B) and Gr-coated AlGaIn (sample A).	118
Figure 4.15: (a) AFM Morphology and (b) correspondent current map collected for the a highly defective AlGaIn surface of sample B.	119
Figure 4.16: Schematic band-diagrams for Au contacts (a) on planar AlGaIn and Au/Gr contacts (b) on planar AlGaIn (solid lines) and on a V-defect (dashed lines), where the AlGaIn thickness is locally reduced.	120
Figure 4.17: Schematic representations of TLM test patterns oriented in the direction (a) parallel ([1-100]) and (b) orthogonal [11-20] to the substrate steps. (c) Optical image of the TLM devices. Measured resistance $R$ vs. the pad distance (d) in the two directions. The calculated sheet resistances from the fit of experimental data are also reported.	121

- Figure 4.18: Cross-section schematics of a top-gated EG field effect transistor with channel length  $LG = 10 \mu\text{m}$  and channel width  $W = 100 \mu\text{m}$  (a). Channel conductance vs. top-gate bias and carrier density for FETs with the channel length along the [11-20] direction, i.e. orthogonal to the SiC steps, and the [1-100] direction, i.e. parallel to the SiC Steps (b). Calculated mobility  $\mu$  in the electron branch for FETs with the channel length along [11-20] and [1-100] directions (c). 123
- Figure 4.19: Surface morphology (a) and the corresponding current map (b) measured by CAFM on the as-grown EG/4H-SiC(0001) sample. Line-profiles of the height (c) and of the current (d) along the indicated directions in the maps. 124
- Figure 4.20: 3D projection of the surface morphology measured in a region nearby a 200 nm-thick Ni/Au contact onto EG(a). High resolution morphology (b) and resistance map (c) obtained by CAFM in the  $100 \text{ nm} \times 100 \text{ nm}$  region indicated in (a) by the circle. Line-scan taken in the direction perpendicular to the steps (d), indicated by the horizontal arrow in (c). Line-scans taken in the direction parallel to the steps along (11-2n) and (0001) faces (e), as indicated by the vertical black and red arrows in (c). 125
- Figure 4.21: Histograms of the  $R_{EG}$  values, obtained on 20 different terraces and facets within the EG sample. 126
- Figure 4.22: Histogram of the local mean free path distribution in EG grown on  $8^\circ$  off axis 4H-SiC (0001) by annealing at 1600 C. 129
- Figure 4.23: Representative  $I$ - $V$  characteristics measured on Au capped QFBLG contacts to SiC with  $10 \mu\text{m}$  (a) and  $1 \mu\text{m}$  diameter (b). AFM morphologies of the contacts are shown in the inserts. 131
- Figure 4.24: Dependence of the measured SBH on the contacts diameter for QFBLG contacts fabricated on SiC substrates with large (a) and small terraces (b). 132
- Figure 4.25: CAFM morphology (a,c) and current map (b,d) on uncapped QFBLG-SiC contacts to on on-axis SiC (upper images) and  $3.5^\circ$  off-axis SiC (lower images). 133



- Figure 4.26: (a) Dependence of the ideality factor on the contacts diameter for QFBLG contacts fabricated on SiC substrates with small terraces. (b) plot of the ideality factor vs. the correspondent SBH. The red line is the linear fit which indicates that when  $n$  tends to the unity the SBH approximate the value  $\sim 1.6$  eV. 134
- Figure 4.27: (a) schematic cross section of a QFEG/SiC vertical Barristor and (b) expected behavior of  $\Phi_B$  vs.  $V_g$ . 135
- Figure 4.28: (a) forward bias  $I_{ds} - V_{ds}$  characteristics for different values of  $V_g$  and (b)  $I_{ds} - V_g$  transcharacteristics for different  $V_{sd}$  voltages calculated for a *barristor* based on the QFEG/SiC Schottky barrier. 137
- Figure 4.29: (a) schematic cross section of a Gr/Si vertical Barristor, considering an ideal Gs/Si interface obtainable by hydrogen passivation of the Si surface. (b) Expected behavior of  $\Phi_B$  vs.  $V_g$  for this device. 137
- Figure 4.30: (a) forward bias  $I_{ds} - V_{ds}$  characteristics for different values of  $V_g$  and (b)  $I_{ds} - V_g$  transcharacteristics for different  $V_{sd}$  voltages calculated for a *Barristor* based on the Gr/Si Schottky barrier. 138
- Figure 4.31: Schematic representations of the cross-section (a) and of the top-view (b) of a Metal/ $\text{Al}_2\text{O}_3$ /Gr/AlGaN/GaN HET where the AlGaN layer works as the emitter-base barrier, the 2DEG at AlGaN/GaN interface as the emitter and Gr as the base. 140
- Figure 4.32: energy band diagram of the Metal/ $\text{Al}_2\text{O}_3$ /Gr/AlGaN/GaN HET: for  $V_{eb} = 0$  and  $V_{bc} = 0$  (a), for  $V_{eb} > 0$  and  $V_{bc} = 0$  and finally for  $V_{eb} > 0$  and  $V_{bc} > \Phi_{bc0} - \Phi_{eb0}$ , when an  $I_c$  is observed for Fowler-Nordheim tunneling across an affective barrier  $\Phi \approx \Phi_{bc0} - V_{eb}$  (c). 140
- Figure 4.33: estimated plot of the  $I_b$  injected in the base as a function of  $V_{eb}$  (a). The calculated  $I_c$  plotted as a function of  $V_{eb}$  for various values of  $V_{bc}$  (b) and vice versa as a function of  $V_{bc}$  for various values of  $V_{eb}$  (c). A strong dependence of the  $I_c$  from the  $V_{bc}$  bias is clearly visible. 142
- Figure 4.34: comparison between the emitter current ( $I_e$ ), the current injected in the base ( $I_b$ ) and the collector current ( $I_c$ ) plotted vs. the  $V_{be}$  for a fixed value of  $V_{bc}$ . 143

## List of Tables

Table 1.1: Main physical properties of Gr and possible applications.	20
Table 3.1: physical properties of Si, 4H-SiC and GaN [169].	59
Table 3.2: Time ( $t_d$ ) required to obtain the complete delamination of Gr from 1 cm <sup>2</sup> copper foil reported as a function $C_{\text{KOH}}$ .	75

# Acronyms

2DEG	two-Dimensional Electron Gas
4H-SiC	Hexagonal polytype 4H Silicon Carbide
AC-STEM	Aberration Corrected Scanning TEM
AFM	Atomic Force Microscopy
AlGaN/GaN	Aluminum Gallium Nitride/Gallium Nitride
ARPES	Angle-Resolved inverse PhotoEmission Spectroscopy
CAFM	Conductive Atomic Force Microscopy
C-V	Capacitance-Voltage
CVD	Chemical Vapor Deposition
DC	Direct Current
EELS	Electron Energy Loss Spectroscopy
EG	Epitaxial Graphene
FET	Field Effect Transistor
FWHM	Full Width at Half Maximum
GB-HET	Graphene Base Hot Electron Transistor
Gr	Graphene
HAADF	High Angle Annular Dark Field
hBN	hexagonal Boron Nitride
HET	Hot Electron Transistor
HOPG	High Oriented Pyrolytic Graphite
HRTEM	High Resolution TEM
I-V	Current-Voltage
LED	Light Emitting Diode

LEED	Low Energy Electron Diffraction
MOCVD	Metal Organic Chemical Vapor Deposition
MOSFET	Metal-Oxide-Semiconductor Field-Effect Transistor
NIL	Nano-Imprint Lithography
PDMS	PolyDiMethylSiloxane
PECVD	Plasma-Enhanced Chemical Vapor Deposition
PMMA	Poly(Methyl MethAcrylate)
QFBLG	Quasi-Free-standing BiLayer Graphene
QFEG	Quasi-Free-standing Epitaxial Graphene
RMS	Rout Mean Square
SBH	Schottky Barrier Height
SCM	Scanning Capacitance Microscopy
STEM	Scanning Transmission Electron Microscopes
tAFM	tapping mode Atomic Force Microscopy
TEM	Transmission Electron Microscopy
TLM	Transmission Line Model
UHV	Ultra High Vacuum
v. d. W.	van der Waals
WBS	Wide-Bandgap Semiconductor
XPS	X-ray Photoemission Spectroscopy

# Introduction

Graphene [ 1 ] (Gr) is a two-dimensional (2D) sheet of C atoms with  $sp^2$  hybridization. It is currently one of the most investigated topics in condensed matter physics, with an exponential growth in the number of scientific papers (but also patent applications) published yearly on this subject. In only ten years from the first pioneering experiments by Geim and Novoselov [2], the research on Gr evolved into several branches, addressing different potential applications of this material, including electronics, optoelectronics, spintronics, nanomechanics, magnetism, chemistry, nanomedicine and so on. Furthermore, this research field covers nowadays an entire class of (2D) materials, including chemical derivatives of Gr (such as the graphene oxide, graphane, fluorographene,...), boron nitride, transition metal dichalcogenides ( $MoS_2$ ,  $WS_2$ ,  $MoSe_2$ ,  $WSe_2$ ,...), topological insulators, silicene, germanene, phosphorene, [3]...

The strong interest of the scientific community on Gr is mainly due to the unique combination of excellent electrical [ 4 ], optical [ 5 , 6 ], thermal [ 7 ] and mechanical [8] properties in this atomically thin material, which paved the way to several applications in different fields.

In particular, the excellent carrier mobility ( $> 10^5 \text{ cm}^2\text{V}^{-1}\text{s}^{-1}$  under “ideal” conditions and  $10^4 - 10^5 \text{ cm}^2\text{V}^{-1}\text{s}^{-1}$  in “ordinary” conditions), the carrier density modulation by field effect [9,10,11,12], the excellent thermal conductivity, the optical transparency ( $\sim 97.3\%$  for a monolayer of Gr) and the mechanical flexibility, make Gr a material of choice for some applications in electronics, such as RF devices, optoelectronics, photovoltaics, flexible electronics.

The main limitation of Gr for electronic applications is represented by the “zero-bandgap”, which results in a low ratio between the on- and off-state currents when Gr is used as a channel material in a conventional Metal-Oxide-Semiconductor Field-Effect Transistor (MOSFET) architecture. Several studies have been performed in the last years with the aim to open a bandgap in the Gr band structure, either by quantum confinement effects in Gr nanoribbons lithographically defined from 2D Gr, or by proper chemical modification (hydrogenation, fluorination,..) of Gr. In most of the cases, the observation of a bandgap was accompanied to a strong degradation of Gr mobility, i.e. to losing one of the main advantages of Gr.

Currently, two main trends emerged for Gr used in electronics:

- (i) Replacing Gr with other semiconducting 2D materials (such as MoS<sub>2</sub>) in the channel of MOSFETs devices, and using Gr for interconnects or as a source/drain or gate contact;
- (ii) Employing Gr as active material in new device architectures (i.e. different from MOSFET), where some of its peculiar physical properties (atomic thickness, field effect modulation of workfunction, low density of states...) can be profitably used. These alternative device concepts (more extensively discussed in the following) are mainly based on *heterostructures* of Gr with semiconductors or insulating materials.

Due to the unavailability of high quality semiconducting 2D materials on large area, the first approach is currently pursued only on explorative basis.

On the other hand, the second solution can take benefit of the huge progresses in the synthesis of high quality Gr on large area during the last 10 years, in particular by Chemical Vapor Deposition (CVD) on catalytic metals or by controlled graphitization of the silicon carbide (SiC) surface. Obviously, the fabrication of heterostructures of Gr with semiconductors or insulators requires significant efforts aimed at the integration of these materials.

It is well known how Gr electronic properties (carrier density, mobility) are strongly affected by the interaction with the underlying substrate. To date, many of the efforts have been directed to minimize the effect of such interactions in order to preserve as much as possible the outstanding “in plane” transport properties of Gr, to be used as a high mobility conductor in “lateral” devices.

On the other hand, a deeper understanding of the current transport phenomena through Gr/semiconductor or Gr/insulator interfaces are highly required to adequately describe the working principle of the above mentioned “vertical” devices, based on Gr heterostructures.

This thesis work is focused on the fabrication of high quality heterostructures of Gr with Wide-Bandgap Semiconductors (WBS), such as Silicon Carbide (SiC) [13], Gallium Nitride (GaN) and related alloys (Al<sub>x</sub>Ga<sub>1-x</sub>N) [14,15,16], and on the investigation of current transport at these interfaces. SiC and GaN are, to date, the most technologically relevant and strategic materials for high power, high frequency and energy efficient electronics. In particular, SiC plays a major role in the fabrication of Schottky diodes and MOSFETs, for high power applications (already commercially available in the range of 600 - 1200 V), whereas GaN-based devices are especially interesting for optoelectronics (LEDs) and for medium

power and high frequency applications, taking advantage of the high mobility two dimensional electron gas (2DEG), which is spontaneously formed at the interface between AlGaN and GaN in  $\text{Al}_x\text{Ga}_{1-x}\text{N}/\text{GaN}$  heterostructures [14,17].

Hence, the motivation of this work is to exploit Gr in junction with these WBSs, taking advantage from their peculiar electronic properties, such as the high critical electric field and the presence of a 2DEG at  $\text{Al}_x\text{Ga}_{1-x}\text{N}/\text{GaN}$  interface. This can result in the demonstration of novel electronic device concepts or in the introduction of new functionalities in existing SiC and GaN devices.

SiC is particularly interesting for the fabrication of heterostructures with Gr, since Gr can be directly grown on its surface by controlled graphitization during high temperature thermal treatments. SiC polytype, crystalline orientation and wafer miscut angle strongly influence Gr growth. In particular, using the (0001) face of the hexagonal polytypes (4H or 6H), monolayer or few layers of Gr epitaxially oriented with respect to the substrate are obtained, with highly homogeneous coverage also on wafer scale [18,19,20]. Due to these peculiar qualities, Gr on SiC has been widely investigated in the last years. Gr provides a high-mobility 2DEG suitable for low power RF devices fabrication on SiC surface [21]. Furthermore, it is very interesting also as a contact to SiC, since excellent quality ohmic or Schottky contacts can be obtained by properly tailoring the atomic structure of Gr/SiC interface [22,23]. However, much remains to understand about the impact of SiC peculiar morphology both on the lateral current transport in the Gr sheet and on the vertical current transport through the Gr/SiC interface [24].

Gr integration with GaN has been recently considered, both for optoelectronic applications (i.e., as a transparent conductor in GaN LEDs [25]), and as a heat dissipation element for thermal management in power High Electron Mobility Transistors (HEMTs) [26]. Probably, a limiting factor in this case is the difficulty to grow Gr directly on the GaN surface. Therefore, in order to have a Gr single sheet over a sufficiently large area, suitable for electronic applications, a transfer procedure must be adopted to move the Gr membrane from the growth substrate (typically copper) to GaN. This is a critical step for the final quality of the heterostructure.

In my Ph.D. activities, the following experimental issues have been addressed:

- (i) The fabrication and the high-resolution structural and morphological characterization of high quality Gr heterostructures with 4H-SiC (0001) and  $\text{Al}_x\text{Ga}_{1-x}\text{N}/\text{GaN}$ ;

- (ii) The electrical characterization of transport properties through these Gr/semiconductor interfaces, employing advanced nanoscale-resolved characterization techniques (conductive atomic force microscopy and scanning capacitance spectroscopy), in order to correlate the local structural and electrical properties.

This thesis is organized in *four* chapters, as follows:

In *Chapter 1*, an overview of the Gr general physical properties and of the state-of-the-art Gr production methods is provided. Particular attention will be paid to the two main large-area growth methods, i.e. the CVD growth on catalytic metals and the controlled graphitization of SiC. The current transfer methods to move Gr from the metal foil to an arbitrary target substrate will be discussed in details, since it represents a critical step for the final quality of Gr.

In *Chapter 2*, an overview of the literature results on Gr heterostructures with semiconductors and/or insulators is reported. In particular, the basic physics of Gr/semiconductor contacts will be introduced. Furthermore, an introduction will be provided on the device concepts based on Gr heterostructures reported to date in the literature, i.e. (i) the Gr/Si Schottky diode with a gate modulated barrier (*Barristor*), (ii) the Hot Electron Transistor (HET) with a Gr base, and (iii) the field effect modulated tunnel devices.

In *Chapter 3* is illustrated the experimental activity on the fabrication of Gr heterostructures with  $\text{Al}_x\text{Ga}_{1-x}\text{N}/\text{GaN}$  and with 4H-SiC. A highly reproducible transfer method has been developed to move Gr grown by CVD on copper foils to the final substrate. This approach was based on some innovative solutions, such as the electrolytic delamination process to separate Gr from the copper foil [27] and a thermo-compressive transfer printing of the delaminated Gr on the target substrate. These solutions can have significant potential impact in the industrialization of Gr transfer procedure. Differently than the typical transfer approach (where Gr is separated from Cu by chemical etching of this metal), this method preserves Cu, making it available for an unlimited number of CVD growth cycles. This would reduce both the production costs and the environmental impact, in the perspective of a process scale-up. Furthermore, it potentially eliminates Cu contaminations on Gr, which can hinder its integration in semiconductor fabs. The use of thermo-compression printing (based on the hot embossing nanoimprint lithography technology) allows a highly reproducible stamping of delaminated Gr on the desired substrate position.



This transfer method was demonstrated to be valid to transfer Gr on several substrates (including Si, SiO<sub>2</sub>, SiC, GaN,...).

In particular, it has been employed to fabricate Gr heterostructures with AlGa<sub>x</sub>N/GaN, obtaining a uniform Gr coverage on AlGa<sub>x</sub>N layers with different morphologies, i.e. on flat and defects rich ones.

Gr heterostructures with SiC were obtained by the controlled graphitization of the surface during high temperature (1600 – 1700°C) thermal treatments. The effect of the annealing temperature and of the wafer miscut angle on the number of Gr layers was accurately investigated using different characterization techniques (including Atomic Force Microscopy, Transmission Electron Microscopy, micro-Raman spectroscopy). The atomic scale structural properties of Gr interface with SiC surface were investigated by atomic resolution scanning transmission electron microscopy, revealing peculiar difference between local structure on (0001) terraces and (11-2n) facets of SiC. [28,29].

In *Chapter 4*, a detailed electrical characterization of the fabricated Gr heterostructures with 4H-SiC and Al<sub>x</sub>Ga<sub>1-x</sub>N/GaN will be reported. Firstly, the lateral current transport in Gr residing on these two substrates was investigated on properly fabricated test devices, extracting characteristic Gr electrical properties such as the sheet resistance, carrier density and mobility. Therefore, the vertical current transport through the Gr/semiconductor interfaces was extensively investigated. In particular, advanced nanoscale electrical measurements (Conductive Atomic Force Microscopy and Scanning Capacitance Microscopy) were employed to this aim to get an insight on the lateral uniformity of the contact. In the case of Gr onto AlGa<sub>x</sub>N/GaN heterostructures, the vertical current transport mechanisms, and in particular the role of the AlGa<sub>x</sub>N surface states and the impact of the AlGa<sub>x</sub>N layer microstructure were properly investigated observing the possibility to have a low Schottky Barrier Height (SBH) [30] or even to convert the rectifying contact in an ohmic contact. [31].

In the case of Gr on 4H-SiC (0001), a peculiar anisotropy of the lateral current transport in Gr was observed and related to the peculiar morphology of SiC substrate, which exhibits parallel steps originating from the wafer miscut angle [28,29].

The vertical current transport through the Gr/SiC heterostructure allowed to elucidate the impact of the interface atomic structure on the Gr electronic properties [32]. It is worth noticing that an ohmic behavior is typically observed for the as grown epitaxial Gr on SiC (0001) even in the case of lowly doped SiC.

Conversely, a rectifying (Schottky) contact (with a barrier height of 0.9 – 1 eV measured by Current-Voltage ( $I$ - $V$ ) analyses and ~1.5 eV measured by Capacitance-Voltage ( $C$ - $V$ ) analyses, respectively) was obtained after passivation of the interface between Epitaxial Graphene (EG) and SiC by a post-growth hydrogen intercalation. The ohmic behavior in the as-grown epitaxial Gr depends on the presence of an interfacial C layer (the buffer layer) partially covalently bonded with the Si face of SiC. The charged Si dangling bonds at the interface cause a high n-type doping of the overlying Gr and a low SBH (~0.3 eV), resulting in an ohmic contact. This is converted into a Schottky contact by the hydrogen intercalation, which causes a decoupling of the aforementioned buffer layer from the Si face (i.e. its conversion into a Quasi-Free-standing Epitaxial Gr layer) and the saturation of the interfacial Si dangling bonds [22,23]. Nanoscale resolution  $I$ - $V$  characterizations by Conductive Atomic Force Microscopy (CAFM) clarified some peculiar electrical properties of the hydrogen intercalated Gr/SiC heterostructure, such as locally reduced SBH at Gr interface with (11-2n) facets, which can explain the discrepancy between the macroscopically evaluated Schottky barriers by  $I$ - $V$  and  $C$ - $V$  analyses.

Basing on this understanding of the current transport mechanisms at Gr/SiC and Gr/AlGaIn/GaN heterostructures, some of the possible devices applications will be discussed. In particular, the performance of a *Barristor* based on Gr Schottky contacts to SiC will be evaluated and compared with those of a similar device structure based on Gr contacts to silicon. Significant advantages in terms of lower current dissipation in the off-state and of superior breakdown voltage are expected in the case of epitaxial Gr Schottky contacts to SiC.

The potential applications of Gr/AlGaIn/GaN heterostructures will be discussed, as well, like a HET where the 2DEG at AlGaIn/GaN interface works as the emitter, Gr works as a base and the AlGaIn barrier layer works as emitter-base barrier. The advantages of this device structure will be discussed with respect to Gr-base HET devices with Si emitter and SiO<sub>2</sub> emitter-base barrier.

# Chapter 1: Graphene, physical properties and production methods

## 1.1 Physical properties

Gr is a crystalline allotrope of carbon, consisting of a two-dimensional (2D) layer of atoms packed in a honeycomb lattice (see Figure 1.1 (a)). It represents the basic structure for other allotropes of carbon of all other dimensionalities: the 3D graphite, formed by a sequence of stacked Gr layers (Figure 1.1 (b)), the 1D nanotubes, described as rolled Gr [33] (Figure 1.1 (c)), the 0D fullerene, described as wrapped Gr [34,35] (Figure 1.1 (d)).

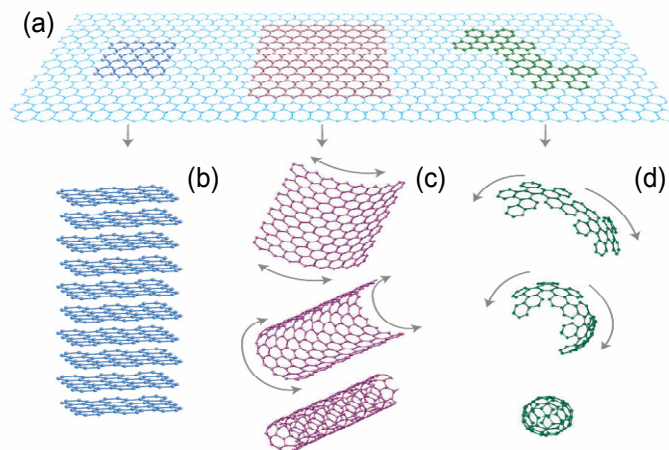


**Figure 1.1:** allotropes of carbon represented starting from a Gr sheet (a): (b) graphite, (c) carbon nanotubes and (d) fullerene.

From a molecular point of view, Gr can be also suitably described as an indefinitely extended polycyclic aromatic molecule. Each C atom in the hexagonal Gr lattice forms  $\sigma$ -bonds with three adjacent C atoms by the overlapping of  $sp^2$  hybridized molecular orbitals in a trigonal planar geometry on the xy-plane and mutual  $120^\circ$  angles. In this configuration, for each C atom a single not hybridized  $2p_z$  orbital (oriented perpendicularly to the x-y plane) containing a free electron is

preserved. The energy distribution of molecular orbitals in an aromatic system can be calculated by the Linear Combination of Atomic Orbitals (LCAO) method. Within this approach, the linear combination of a number  $N$  of  $2p_z$  orbitals generates an equal number of molecular orbitals:  $N/2$  are totally filled  $\pi$ -bonding orbitals at lower energies and  $N/2$  are totally empty  $\pi^*$  anti bonding orbitals at higher energies. The electrons in these  $\pi$  and  $\pi^*$  orbitals are completely delocalized over the aromatic system. As a consequence, the C-C distance of 0.142 nm for each pair of nearest-neighbor C atoms is roughly the average length of a single (0.154 nm) and a double bond (0.134 nm), which is a scenario that is analogous to that of benzene described by Pauling since 1931 [36].

Looking at Gr as an indefinitely extended 2D crystal, the problem of energy band structure calculation can be addressed solving the Schrodinger equation for the electrons in the Gr hexagonal lattice in the tight-binding approximation [37]. The Gr structure, which is not a Bravais lattice because of the non-equivalence of neighboring sites, can be divided in two sub-lattices A and B, as indicated in Figure 1.2 (a) by full and empty circles respectively, in order to satisfy the equivalence conditions to define Bravais lattices. Consequentially grouping two neighboring carbon atoms (one for each sub-lattice) in a single basis, a triangular Bravais lattice is rigorously defined.

The basis lattice vectors  $a_1$  and  $a_2$  (see Figure 1.2 (a)) can be defined as:

$$a_1 = \frac{a}{2}(3, \sqrt{3}), \quad a_2 = \frac{a}{2}(3, -\sqrt{3}) \quad (1.1)$$

where  $a$  is the C-C distance which is exactly 0.142 nm in the case of Gr.

Considering the Gr reciprocal lattice in the momentum space, the corresponding basis vectors  $b_1$  and  $b_2$  are:

$$b_1 = \frac{2\pi}{3a}(1, \sqrt{3}), \quad b_2 = \frac{2\pi}{3a}(1, -\sqrt{3}) \quad (1.2)$$

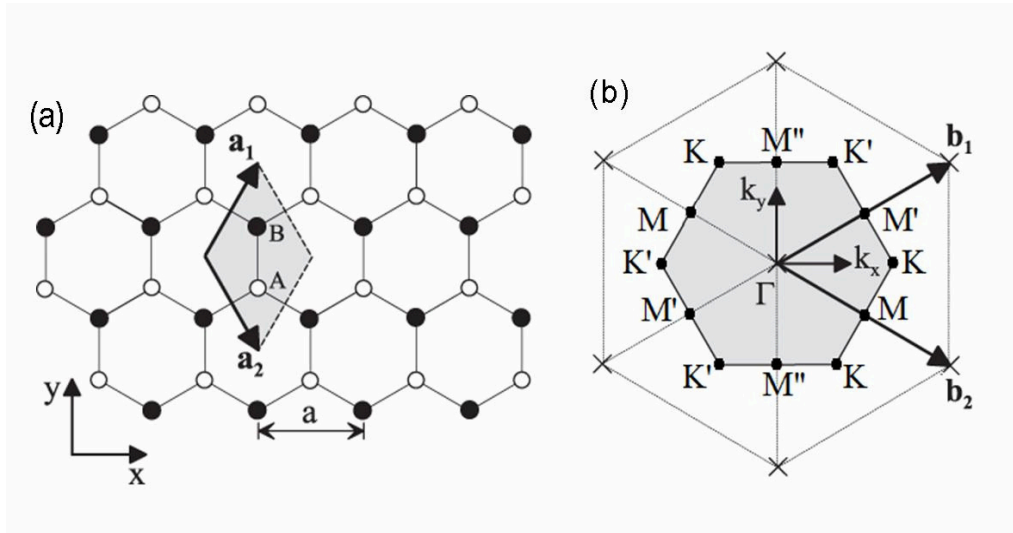


**Figure 1.2:** (a) Crystal structure of monolayer Gr with A and B atoms shown as empty and full circles. The shaded rhombus is the conventional unit cell while  $a_1$  and  $a_2$  are primitive lattice vectors. (b) Reciprocal lattice of Gr where the first Brillouin Zone is indicated with the high symmetry point  $\Gamma$  as the centre,  $K$  and  $K'$  as the two non-equivalent corners and  $M$ ,  $M'$ , and  $M''$  as the three non-equivalent centers of the edge while  $b_1$  and  $b_2$  are reciprocal lattice vectors.

In Figure 1.2 (b) the first Brillouin Zone of the Gr reciprocal lattice is indicated with the high symmetry point  $\Gamma$  as the centre,  $K$  and  $K'$  as the two non-equivalent corners and  $M$ ,  $M'$ , and  $M''$  as the three non-equivalent centers of the edge.

The  $K$  and  $K'$  high symmetry points are especially interesting because of the very peculiar shape of the conduction and the valence bands close to these point, as it will be discussed in the following.

The energy bands obtained from the solution of the Schrödinger equation in the tight-binding approximation can be expressed as:

$$E_{\pm}(k) = \pm t \sqrt{3 + f(k)} \quad (1.3)$$

Where  $f(k)$  is a function of the momentum  $k$  and  $t$  is the hopping energy ( $t \approx 2.8$  eV estimated by *ab initio* calculations [38]), defined as the energy required for an electron to hop from a C atom to the three nearest-neighbors atoms. The positive or the negative signs in Equation (1.3) refer to the upper antibonding band ( $\pi^*$ ) and the lower bonding band ( $\pi$ ) respectively.

In Figure 1.3 (a) the calculated valence and the conduction band energies are plotted as a function of the momentum  $|k|$  along the directions defined by the high symmetry points (e.g.  $\Gamma$ ,  $M$  and  $K$ ) of the first Brillouin Zone. The energy difference between the conduction and valence band is maximum in correspondence with the Brillouin zone centre  $\Gamma$ , whereas it is null (zero band gap) in the  $K$  and  $K'$  corners of the Brillouin zone, where the valence band maximum and conduction band minimum merge in the singularity points  $D$  and  $D'$ , called Dirac points (see Figure 1.3 (b)).

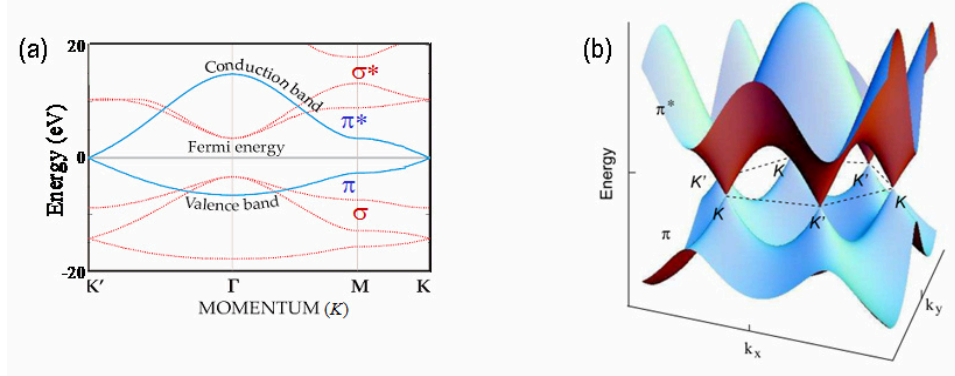


**Figure 1.3:** (a) Energy dispersion relation of the  $\sigma$  (red) and the  $\pi$  (blue) bands of the momentum  $|k|$  along the directions defined by the high symmetry points  $\Gamma$ ,  $M$  and  $K$ . (b) Dispersion relation of Gr for the whole set of points of the first Brillouin Zone.

Considering that for neutral Gr the chemical potential (i.e. the Fermi energy  $E_F$ ) is coincident with the Dirac points ( $D$  and  $D'$  for  $K$  and  $K'$  respectively), it is relevant to calculate the dispersion relations close to  $K$  (or  $K'$ ).

For this purpose, the wavevector  $k$  can be expressed as  $k = K + k'$ , where  $K$  is the wavevector of the  $K$  point (with the origin in the Brillouin zone center) and  $k'$  is a wavevector with the origin in the  $K$  point. Close to the  $K$  point, i.e. for  $|k'| \ll |K|$ , Equation (1.3) can be expanded using the Taylor series and approximated as [37]:

$$E_{\pm}(k') \approx \pm \hbar v_F k' \quad (1.4)$$

Where  $v_F$  is the Fermi velocity, defined as  $v_F = 3ta/2\hbar$ , with a value  $v_F \approx 10^6$  m/s. It is worth noting that this linear dispersion relation for electrons in Gr is different from the usual parabolic relation:

$$E(k) = \frac{\hbar^2 k^2}{2m} \quad (1.5)$$

For electrons in semiconductors, where the electron velocity is:

$$v = k / m = \sqrt{2E / m} \quad (1.6)$$

The above linear dispersion resembles that of massless particles (such as photons) or that of ultra-relativistic particles, with the exception of the Fermi velocity value which is  $v_F \approx c/300$  lower than the speed of light  $c = 3 \times 10^8$  m/s.

The linear dispersion relation in Gr has been experimentally verified in different ways. The most direct approach is using angle resolved photoemission spectroscopy, which is able to simultaneously probe the energy and wavevector of photoemitted electrons with energy below the Fermi level.

Many of the peculiar electronic properties of Gr, such as the density of electronic states linearly depending on the energy and the ambipolar current transport, are a direct consequence of the linear dispersion relation.

The density of electronic states ( $\rho$ ) in Gr can be calculated starting from the dispersion relation [37,39]. Clearly, close to the Dirac point ( $E = 0$ ) it is a linear function of the energy  $E$ :

$$\rho(E) = \frac{g_s g_v}{2\pi\hbar^2 v_F^2} |E| \quad (1.7)$$

Where  $g_s = 2$  and  $g_v = 2$  are the spin and valley degeneracy, respectively. This dependence of the density of states on the energy for Gr has strong implications both on the electronic and optical properties of Gr. As an example, it means that, changing the Fermi energy from the Dirac point to  $E_F$  by the application of an external electric field, only a limited number of states are available to be occupied by electrons at that fixed value of  $E_F$ . This makes Gr very different from common metals, for which the density of electronic states at the Fermi level is so high to accommodate all the electrons induced by the electric field. Because of that, while a thin metal film is able to screen completely an electric field to penetrate through it, a Gr membrane causes only a partial screening.

For a fixed value of the Fermi energy, the carrier density in Gr can be expressed as:

$$n = \int_0^{\infty} \rho(E) f(E) dE \quad (1.8)$$

Where  $\rho(E)$  is the density of states and

$$f(E) = \frac{1}{1 + \exp\left(\frac{E - E_F}{kT}\right)} \quad (1.9)$$

Is the Fermi distribution. A plot of the carrier density as a function of  $E_F - E_D$  at a temperature  $T = 300$  K is reported in Figure 1.4. The majority carriers are electrons when  $E_F - E_D > 0$  (Fermi level in the conduction band) and holes when  $E_F - E_D < 0$  (Fermi level in the valence band). Noteworthy, even at the neutrality point ( $E_F = E_D$ ), where the density of states is zero, a finite value of the carrier density

$$n_i = p_i = \frac{\pi}{6} \left( \frac{k_B T}{\hbar v_F} \right)^2 \approx 6,5 \times 10^{10} \text{ cm}^{-2} \quad (1.10)$$

is found, due to thermal agitation effects.

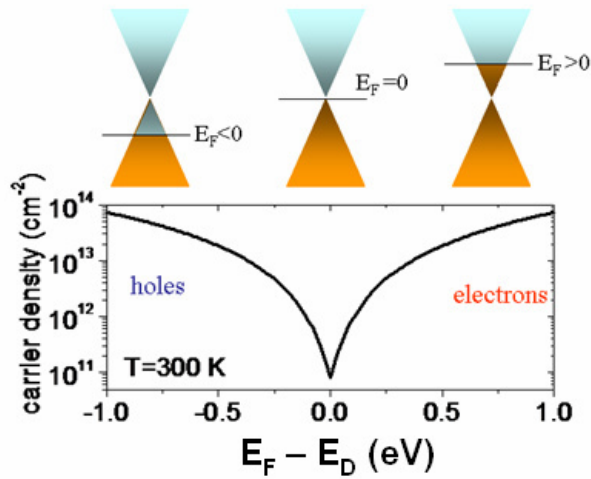


**Figure 1.4:** carrier density as a function of  $E_F - E_D$  at a temperature  $T = 300$  K and (above) the variation of the  $E_F$  in the Dirac cones.

On the basis of these properties it is relevant a direct comparison between Gr and a conventional 2DEG, that can be found in the channel region of MOSFETs (in the inversion regime) or at the heterointerface of semiconductor heterostructures (such as AlGaAs/GaAs, AlGaN/GaN,...).



Gr actually deserves the definition of 2DEG in the strictest sense of the word because of the real confinement of the electron gas within its atomically thick dimensionality. A conventional 2DEG is instead confined in a thin bulk region, with a thickness in the order of 1 – 10 nm depending on the material and the electron confinement mechanism. Electrons confined in a thin sheet can be defined as a 2DEG when the thickness  $t$  of this region is smaller than the Fermi wavelength  $\lambda_F$ .

Considering that the expression of the Fermi wavelength is

$$\lambda_F = 2\pi / k_F = 2\sqrt{\pi} / \sqrt{n} \quad (1.11)$$

$t < \lambda_F$  for Gr is always satisfied even if unphysically large  $n = 10^{14} \text{ cm}^{-2}$  is considered.

The 2D electron nature of Gr was immediately clarified since the first experiments on this material [2,40] by the observation of the quantum Hall effect, which is the straightest demonstration to reveal 2D electron phenomenon. However, an unconventional quantization of Hall conductivity as a function of the carrier density was found for a single layer of Gr with respect to that previously observed in other 2DEGs. This is a consequence of the linear, Dirac-like, spectrum of quasiparticle excitations of Gr and by “pseudospin” degeneracy associated to the presence of two carbon sublattices [41].

The main effective differences between Gr and a traditional 2DEG are related to the transport properties. The linear dispersion relation for Gr close to the Dirac points remains valid for electron energies  $|E| < 1 \text{ eV}$ . These energy range is large enough with respect to the thermal excitation energy ( $k_B T$ ) to allow the observation of many electronic properties deriving from this peculiar band-structure even at temperatures as high as 300 K (i.e. room temperature) [42].

In general, the experimental quantity that is measured during current transport measurements is the conductivity  $\sigma$ , which is related to the carrier mobility  $\mu$  and to the electron density  $n$  as

$$\sigma = qn\mu \quad (1.12)$$

Being  $q$  is the electron charge.

Under ideal experimental conditions, such as for free-standing [4] or boron nitride encapsulated Gr [ 43 , 44 , 45 ], giant carrier mobility was observed, i.e.  $\mu > 10^6 \text{ cm}^2\text{V}^{-1}\text{s}^{-1}$  at low temperatures and  $\mu \approx 10^5 \text{ cm}^2\text{V}^{-1}\text{s}^{-1}$  at room temperature.

The relation between the mobility and the electron mean free path  $l$  can be obtained by a semi-classical approach based on the Boltzmann transport theory and the relaxation time approximation [46,47], as

$$\mu = \frac{qv_F\tau}{\hbar\sqrt{\pi m}} = \frac{ql}{\hbar\sqrt{\pi m}} \quad (1.13)$$

where  $\tau$  is the relaxation time for a fixed value of Fermi energy.

From this relation it is clear that the limiting factors for the electron mobility of Gr are directly related to the scattering mechanisms, which limit the electron mean free path.

Under nearly ideal conditions which allows Gr to be considered as a defect-free planar sheet without any contamination or environmental influence, the solely limiting factor for the electron mean free path is the scattering of longitudinal acoustical phonons ( $l_{AD,Phon}$ ), inversely proportional to the electron density and to the temperature  $T$  as

$$l_{AD,Phon} \approx \frac{\hbar^2 \rho_{gr} v_s^2 v_F^2}{\sqrt{\pi D_A^2 k_B T}} n^{-1/2} \quad (1.14)$$

where  $\rho_{gr} \approx 7.6 \times 10^{-7} \text{ kg m}^{-2}$  [48] is the Gr mass density,  $D_A \approx 18 \text{ eV}$  [48] is the acoustic deformation potential,  $v_s \approx 2.1 \times 10^4 \text{ m s}^{-1}$  is the acoustic phonons group velocity and  $k_B$  is the Boltzmann constant.

Under proper experimental conditions, it is possible to approach the theoretical phonon-scattering limit, even at room temperature. As illustrated in Figure 1.5, the expected electron mean free path (Figure 1.5 (a)), mobility (Figure 1.5 (b)) and conductivity (Figure 1.5 (c)) plotted vs. the carrier density are calculated at different temperatures for a micrometric Gr sample. A  $l_{AD,Phon}$  higher than the device size (typically in the order of  $1 \mu\text{m}$  or below) is actually obtainable at low-temperatures, allowing the observation of ballistic current transport without any energy dissipation [45].

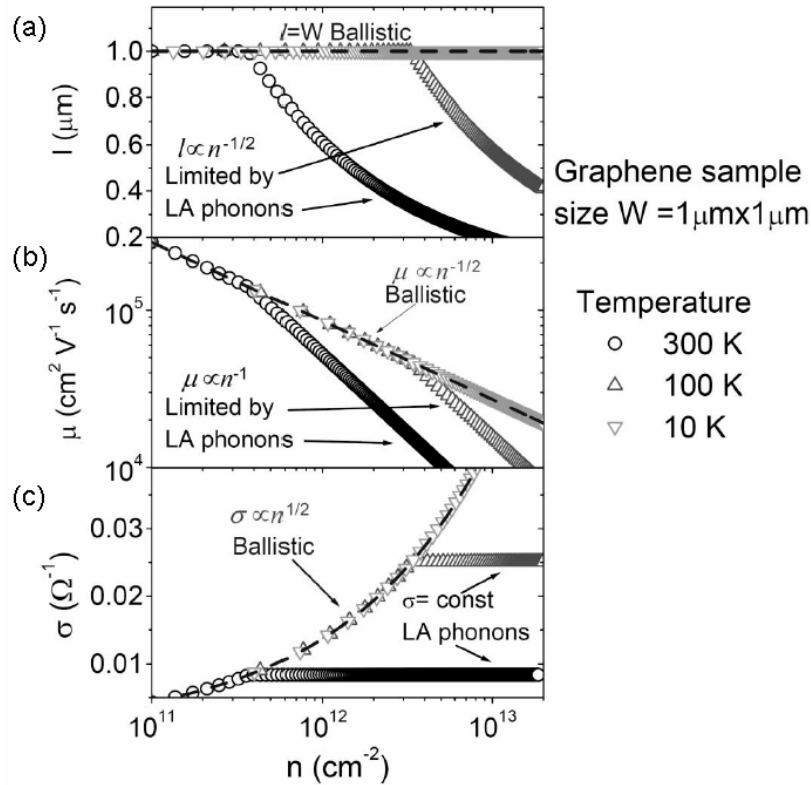


**Figure 1.5:** calculated intrinsic electron mean free path (a), mobility (b) and conductivity (c) versus the carrier density  $n$  at three different temperatures ( $T = 10, 100$  and  $300$  K) for a Gr sample with size  $W = 1 \mu\text{m} \times 1 \mu\text{m}$ .

Under practical experimental conditions, e.g. at room temperature and under ambient environment, the mobility as well as the electron mean free path of Gr can be significantly reduced due to several effects. Gr is very sensitive to the interaction with the substrate and with the external environment. Furthermore, mobility can be strongly dependent on the Gr synthesis method (polycrystallinity, defects and deformations, chemical modifications) and on the subsequent manipulation processes (e.g. the Gr transfer procedure) and/or on any additional processes for devices fabrication, which can introduce structural and morphological damages or chemical residues. Typical mobility values of Gr devices reported in the literature can range from  $\sim 10^2 \text{ cm}^2 \text{V}^{-1} \text{s}^{-1}$  to  $\sim 10^4 \text{ cm}^2 \text{V}^{-1} \text{s}^{-1}$  at room temperature and under ambient environment.

The most common “extrinsic” scattering mechanisms, which reduce the electron mean free path in Gr are: (i) the scattering by charged impurities [49], which can be localized on top of Gr or at the interface between Gr and the substrate; (ii) the resonant scattering [50] due to Gr lattice defects (e.g. vacancies) or to various organic groups covalently bonded in place of C-C double bonds [51].

The peculiar electronic structure of Gr is reflected not only in the electrical properties but also on the optical ones, in particular in the absorption and transmission of light. Noteworthy, the optical absorption of a monolayer is quite constant ( $\sim 2.3\%$ ) over the entire spectrum of visible wavelengths, covering also part of the UV and the IR band, as illustrated in Figure 1.6. Furthermore, the absorbance of a few-layers of Gr stack increases proportionally to the number of layers (for  $N$  up to 4) [52,5].

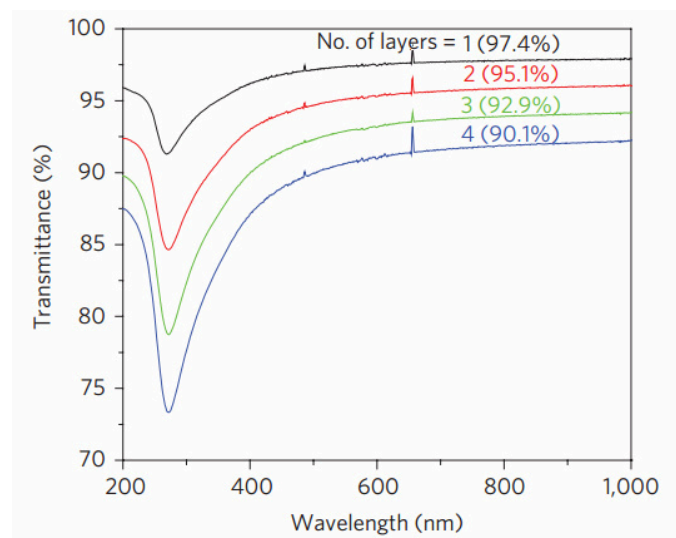


**Figure 1.6:** UV–vis spectra for a different number of Gr layers, from the single layer to a four layer stack [52]. The transmitted light decreases almost proportionally with the number of layer.

As a consequence of the linear dispersion relation of Gr around the Dirac point, the optical conductance  $G$  (related to the optical inter-band transitions) results to be independent on frequency in a broad range of photon energies and corresponds to the universal optical conductance  $G_0$  [53]:

$$G(\omega) = G_0 \equiv \frac{\pi e^2}{2h} \approx 6.08 \times 10^{-5} \Omega^{-1} \quad (1.15)$$

This constant behavior of  $G$  with the photon frequency implies that other observable quantities such as the optical transmittance  $T$ , the absorbance  $A$  and the reflectance  $R$  are frequency independent as well.

For a freestanding Gr monolayer  $T$ ,  $R$  and  $A$  can be expressed applying the Fresnel equations in the thin-film limit, in the form:

$$T \equiv (1 + 2\pi G/c)^{-2} = (1 + 0.5\pi\alpha)^{-2} = 1 - \pi\alpha = 97.7\% \quad (1.16)$$

$$R \equiv 0.25\pi^2 \alpha^2 T < 0.1\% \quad (1.17)$$

$$A = 1 - T = 2.3\% \quad (1.18)$$

Where:

$$\alpha = 2\pi e^2 / hc \approx 1/137 \quad (1.19)$$

is the fine structure constant.

The remarkable optical absorption of Gr was the key property that allowed the easy identification of single layers of this material in the first pioneering works of by Geim and coworkers. In fact, transferring Gr over a Si substrate capped with SiO<sub>2</sub> of appropriate thickness (~100 nm or ~300 nm), it is possible to achieve a significant optical contrast between regions coated and uncoated with Gr [54,55].

Despite its high absorbance (in relation to its atomic thickness), in absolute terms Gr can be considered as an excellent transparent conductor. It is currently investigated as a replacement of ITO for applications in optoelectronics (light emitting diodes [25,56]) and photovoltaic (new generation solar cells [57]). Due to its high flexibility, it is the ideal candidate for flexible and organic light emitting devices [58].

In addition to the electronic band-structure, also the phononic dispersion relation has very important implications on some physical properties of Gr such as the thermal conductivity and the specific heat.

Gr exhibits an in-plane thermal conductivity among the highest of known material, ranging from 2000 to 5000 W m<sup>-1</sup>K<sup>-1</sup> [7,59,60,61] for suspended single layer membranes, at room temperature, in contrast with the thermal conductivity along

the  $c$ -axis which is three order of magnitude lower (as estimated in the case of pyrolytic graphite [62]). However, as in the case of electrical conductivity, many factors can strongly degrade these out of the ordinary values. The specific heat for a single layer of Gr, which has not been measured directly to date, can be discussed by analogy with graphite. It is mainly related to the lattice vibrations (phonons) at all practical temperatures. At room temperature the specific heat of graphite is  $\sim 30\%$  higher than that of diamond due to the higher density of states at low phonon frequencies [63].

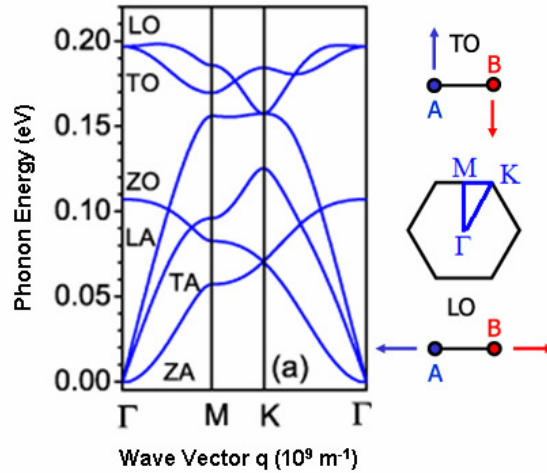


**Figure 1.7:** Phonon dispersion of Gr along high symmetry lines in the hexagonal Brillouin zone. Three Acoustic ( $A$ ) and three Optical ( $O$ ) phonon modes are reported. At low  $q$ , the wave vector  $q$  is linear for Longitudinal ( $LA$ ) and in-plane Transverse ( $TA$ ) Acoustic phonons and quadratic for out-of-plane flexural ( $ZA$ ) Acoustic Phonon [64].

Considering again the unit cell of the Gr lattice, formed by two carbon atoms, three Acoustic ( $A$ ) and three Optical ( $O$ ) phonon modes can be calculated. It is particularly relevant to consider that the dispersion relation between the phonon energy and the wave vector  $q$  is linear for low  $|q|$  values, i.e. near to the centre of the Brillouin zone, for Longitudinal ( $LA$ ) and in-plane Transverse ( $TA$ ) Acoustic phonons, while the out-of-plane flexural ( $ZA$ ) Acoustic phonons follows a quadratic dispersion (see Figure 1.7). The group velocities for  $TA$  and  $LA$  in the case of Gr ( $13.6 \text{ km s}^{-1}$  and  $21.3 \text{ km s}^{-1}$  respectively) are from 4 to 6 times higher

than those in other materials such as silicon or germanium and it can be attributed to the strength of the  $sp^2$  bonds and to the small mass of carbon atoms.

The thermal conductivity  $\kappa$  is linearly related to the specific heat  $C$ , to the group velocity  $v$  and to the phonon mean free path  $\lambda$ . In the diffusive regime (i.e. for a Gr size  $L \gg \lambda$ ), where  $\kappa$  can be expressed as:

$$\kappa = \sum C v \lambda \quad (1.20)$$

It is clear that the extraordinary high values of  $\kappa$  measured for a suspended Gr membrane are the result of the high specific heat, the high group velocities and the long phonon mean free path (600 nm for suspended Gr). On the other hand, structural disorder or fabrication residues can easily degrade the thermal conductivity of Gr [65]. Analogously to the current transport properties described above, also the in-plane thermal conductivity is seriously conditioned when the carbon membrane is sustained by a substrate. This effect is given by the extreme sensitivity of the phonon propagation to the target surface perturbations. In the case of Gr sustained on  $SiO_2$  a decrease of the thermal conductivity of one order of magnitude occurs as a result of the coupling and scattering of Gr phonons with the substrate vibrational modes [66].

Also from the mechanical viewpoint, Gr reveals outstanding properties, such as a high flexibility alongside one of the highest in-plane tensile modulus, which are related again to the peculiar 2D hexagonal structure of  $sp^2$  hybridized carbon atoms. These mechanical properties are the basis for many potential applications of Gr. A systematic experimental analysis of elastic and strength properties [8] were conducted on  $\mu m$  size suspended circular membranes of Gr stressed by Atomic Force Microscope (AFM) tips. By these results it was possible to calculate a Young's modulus of  $\sim 1$  TPa under the experimental conditions such that the energy from in-plane strain was the most relevant contribution [67]. The other remarkable result concerns the breaking force which shows a relatively narrow distribution between values and a good agreement with the *ab initio* calculations [68,69], suggesting that the one observed is the intrinsic strength rather than a brittle fracture where a more dispersed situation is expected depending on size, number and distribution of defects under the AFM tip. The intrinsic strength is the theoretical an ideal highest limit achievable by a defect-free crystal [70] (at 0 K) and it is more and more desirable with the progress of nanotechnology. This

property rightfully places pristine and monocrystalline Gr among the family of nano-size ultra-strength materials in development for this purpose.

As a way of conclusion the most relevant properties of Gr together with the relative potential applications is reported in Table 1.1.

	<b>Physical Properties</b>	<b>Potential Applications</b>
Electronic	Giant intrinsic mobility ( $\sim 2 \times 10^5 \text{ cm}^2\text{V}^{-1}\text{s}^{-1}$ ) [71] Large intrinsic electron mean free path ( $\sim 1 \mu\text{m}$ ) [71]	High-frequency (GHz-THz) devices
Thermal	Very high thermal conductivity ( $\sim 2000\text{-}5000 \text{ W m}^{-1}\text{K}^{-1}$ ) [7,59,60,61]	Heat dissipation
Mechanical	Very high Young's modulus $\sim 0.5 - 1 \text{ TPa}$ [8,72,73]	MEMS, NEMS
Optical	High transparency ( $\sim 97.7 \%$ ) from visible to near-infrared wavelengths [6]	Transparent conductive electrodes

**Table 1.1:** Main physical properties of Gr and possible applications.



## 1.2 Graphene preparation methods

### 1.2.1 Exfoliation of Graphite

Gr was first experimentally isolated in 2004 by Andre Geim and Konstantin Novoselov [55] who simply exfoliated the material from bulk graphite by scotch tape to transfer it on the surface of a Si wafer capped with silicon dioxide. Monolayer flakes were identified exploiting the optical contrast due to the interference of light reflected at Gr/SiO<sub>2</sub> and SiO<sub>2</sub>/Si interfaces, which is maximized for properly chosen SiO<sub>2</sub> thicknesses [55]. The series of ground-breaking experiments elucidating the unique properties of this 2D material led the two researchers to be awarded in 2010 with the Nobel price in Physics, as the demonstration of the vibrant interest of the scientific community in this research field. The used production technique, generally known as mechanical exfoliation, still provides the best quality Gr crystallites and is currently used for several research purposes. However, due to the limited lateral size of obtained Gr flakes (not exceeding 100 μm in the best of conditions)[1], this approach is not suitable for all those activities that require larger membranes on extended area, i.e. for purposes that are aimed at industrial scalability.

Several other strategies have been proposed to increase the yield and the efficiency of the exfoliation approach [74]. A successful exfoliation is able to overcome the van der Waals (v. d. W.) interactions between Gr layers in bulk graphite.

Alternatively it is possible to enhance the exfoliation yield by oxidative and chemical-intercalating reactions which limit the v. d. W. interactions as well as the hydrophobic character of the carbon membrane in order to enhance its dispersibility in a wide range of solvents. The weakness in this case is connected to the reverse reaction to reduce Gr oxide, for example with hydrazine hydrate, which gives back a partially damaged and not totally reduced Gr [75].

In both cases, one of the most important approaches to exfoliate the stacked material is the application in solution of mechanical forces via stirring, shaking, or ultrasonication. Moreover the exfoliation can be assisted by solvents with a surface tension of around 40 mJ m<sup>-2</sup> such as the organic solvent NMP [76], by surfactant in hydrophilic solutions such as sodium dodecyl benzene sulfonate in water [77] or by ionic liquids such as in bis(trifluoro-methane-sulfonyl)imide [78].

Thermal exfoliation techniques are also capable of achieving near-complete exfoliation into single-layer materials with high efficiency. Rapid high temperature

heating through graphite oxide [79] as well as low temperature exfoliation of graphite under vacuum [80], have yielded some of the highest surface areas of all exfoliation methods.

Several other kinds of exfoliation methods have been proposed during the years it is the case of the electrolytic exfoliation, which leads to the formation of functionalized or blandly oxidized Gr, or the thermal quenching which exploits high temperatures and fast cooling down steps, or finally the superficial fluid exfoliation in organic solvent and in presence of surfactants.

However, all the exfoliation approaches are suitable for applications requiring macroscopic quantities of Gr, as an example for bulk applications, but are unsuitable for applications in microelectronic fields.

To date, the real alternatives to produce large area Gr appropriate for electronic applications are the Chemical Vapor Deposition of Gr on catalytic metals and the controlled graphitization of Silicon Carbide (SiC) surface.

Both strategies are able to give high quality, controllable thickness and wafer scale Gr membranes, suitable for several applications which require the incorporation of this material with integrated devices.

### ***1.2.3 Chemical Vapor Deposition of graphene on catalytic metals***

The formation of thin films of graphite on the surface of transition metals, such as Ni [81,82,83] was reported already in 1961. It was supposed that the graphitization was the consequence of the carbon incorporation inside the metal bulk after the exposure to a carbon source at high temperature followed by the segregation of the carbonaceous material during the cooling down step. In addition to Ni, several other transition metals, such as Ru, Ir, Co, Re, Pd, have been considered during the years as catalysts to obtain graphitic materials.

Recently, and following the explosion of the research interest on the Gr topic, the study of these phenomena has regained a great deal of attention in order to achieve the formation of few or single layers of Gr [84].

To date, the most effective and controllable strategy to grow few or even single layers of Gr on polycrystalline transition metal substrates such as Ni, Pd, Ru, Ir, Cu, Pt, Re or Co, is the CVD. The catalytic metal is exposed to an organic gas flow, such as methane, that decompose to carbon radicals to form, through different mechanisms and depending on the substrate, few layers or even a single layer of Gr. Currently the most used substrates for Gr CVD growth are Ni and Cu. This is due to the fact that these metals can be chemically etched in a straightforward way,

according to the typical procedure to transfer Gr from the metal to the target substrate (see Section 1.2.5). Gr films, grown on these two metallic catalysts, exhibit very different morphologies, i.e. few layers of Gr with inhomogeneous thickness in the case of Ni and a single layer of Gr on most of the surface area in the case of Cu. These different properties are the result of the very different maximum solubility of carbon atoms in Ni ( $\sim 0.6\%$  at the melting temperature ( $T_M$ )  $1455^\circ\text{C}$ , as illustrated in Figure 1.8 (a)) and Cu metals ( $\sim 0.0076\%$  at the melting temperature  $1085^\circ\text{C}$ , as illustrated in Figure 1.8 (b)).

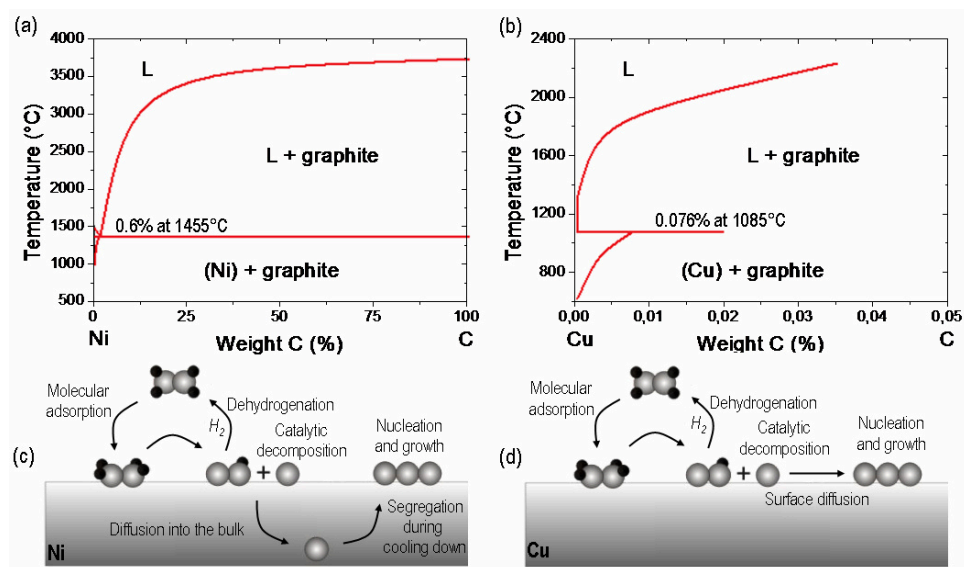


**Figure 1.8:** Phase diagrams for the binary system (a) Ni-C and (b) Cu-C: the maximum solid solubility of C is strongly different in Ni and Cu, with  $\sim 0.6\%$  at  $T_M = 1455^\circ\text{C}$  and  $\sim 0.0076\%$  at  $T_M = 1085^\circ\text{C}$  for Ni and Cu respectively. (c) and (d) illustrate the different growing mechanisms of Gr on (c) Ni where the segregation of C from bulk is the main phenomena and on (d) Cu where the surface epitaxial growth dominates.

When a polycrystalline Ni substrate is exposed at high temperature ( $\sim 900 - 1000^\circ\text{C}$ ) to the hydrocarbon gas (Hydrogen/Methane), the latter decomposes in carbon radicals, which dissolves into the metal bulk. During the cooling down step, due to the reduced C solubility in the metal with decreasing the temperature, carbon atoms segregate on Ni surface forming graphitic layers (see Figure 1.8 (c)). Clearly, this phenomenon is strongly affected by the cooling rate.

Furthermore, a higher number of Gr layers is typically formed in areas where segregation is enhanced, such as Ni grain boundaries. The Gr layers exhibit an epitaxial growth on the Ni(111) face with  $< 1\%$  lattice mismatch [85].

Due to the possibility of obtaining a single layer of Gr on more than 95 % of the area, the interest for Cu as catalytic metal has exceeded that for Ni. Cu is typically annealed in hydrogen gas at 1000°C, then exposed to a Hydrogen/Methane flow [91] (see Figure 1.8 (d)). Due to the extremely low solubility of carbon atoms in the Cu bulk, Gr growth is a surface phenomenon, resulting from (i) the hydrocarbon decomposition on the Cu surface, (ii) the nucleation of Gr domains, (iii) the domains growth and (iv) their coalescence to form a continuous Gr membrane. The formation of the first Gr layer on Cu hinders the diffusion to the Cu surface, resulting in a self limiting growth mechanism. Due to this peculiar growth mechanism on Cu surface, the cooling rate is a less critical parameter for Gr quality than in the case of Ni. The CVD grown Gr film on Cu is a polycrystalline membrane formed by the merging of growing Gr domains with different orientations [86, 87,88], as illustrated in Figure 1.9 where the growing process is stopped before the domains merging. The grains boundaries separating the domains represent one of the main factors that degrade the electrical and mechanical properties of this material [89,90]. Moreover, the as-grown Gr shows characteristics corrugations generically called “wrinkles” [91]. Their formation originates from the difference between the negative thermal expansion coefficient of Gr ( $\alpha_{Gr} = -6 \times 10^{-6} \text{ K}^{-1}$  at 27°C) and the Cu positive one ( $\alpha_{Cu} = 24 \times 10^{-6} \text{ K}^{-1}$ ). This difference results in a relevant shrinkage of Cu respect to the overlying Gr during the cooling down step of the CVD growth and in the consequent “wrinkle-like” folding of the weakly bound carbon membrane. Several effort are currently in progress to obtain Gr films with very large domains (up to mm size) by proper pre-treatment of the Cu surface, in order to reduce density of nucleation sites [92]. Nevertheless, the polycrystalline nature of Gr remains typical of the growth on this substrate. Other catalytic substrates have been taken into account in order to improve the quality of the Gr grown by CVD. An interesting example is Pt [93], which shows lower activation energies to decompose hydrocarbons, enabling the growth at ambient pressure and at relatively low temperature (750°C) of Gr films formed by  $\sim 100 \mu\text{m}$  smooth hexagonal grains with lower wrinkling than that observed on Cu and Ni. Obviously the use of Pt as a catalyst for Gr growth implies the need to adopt alternative methods to detach Gr from its surface than the simple

chemical etching of the substrate (typically adopted for Ni and Cu), since Pt is very resistant to etchants. This is a crucial point in the transfer procedure of CVD Gr to the target substrate, that will be discussed in section 1.2.5.

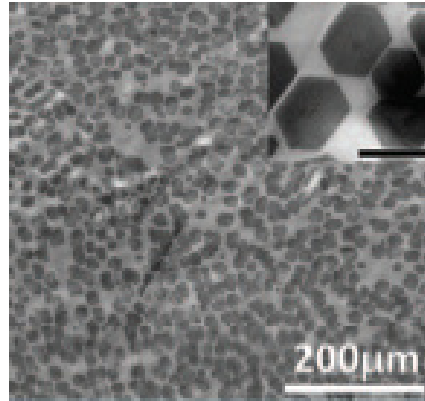


**Figure 1.9:** SEM image of Gr domains grown on Cu before merging. Insert in the top shows a magnification of the same domains [92].

A recently reported breakthrough in the field of CVD has been the growth of a single crystal Gr membrane on the hydrogen-terminated surface of Germanium (110) thin films on a Si(110) wafer [94]. In this case, it has been shown that all the Gr domains nucleating on Ge surface are perfectly aligned along the [-110] direction of the substrate, in such a way that they grow and merge without the formation of grain boundaries. Moreover, due to the very poor adhesion of Gr on the hydrogen terminated Ge surface, a facile and mechanical dry detachment of the Gr has been shown to transfer it on another substrate. Wrinkles are not observed probably because of the combined effect of a low difference in thermal expansion coefficient between Gr and Ge and the weak interaction of Gr with the Ge surface.

#### ***1.2.4 Epitaxial graphene by controlled graphitization of Silicon Carbide***

Silicon Carbide (SiC) is a WBS with several excellent physical properties (wide-bandgap, high breakdown field, high saturation velocity), that currently make it the material of choice for high power electronics. Different polytypes of SiC can be found in nature, but the most used ones for applications are the hexagonal polytypes (6H- and 4H-SiC). Due to their high technological interest,

the growth of 6H- and 4H-SiC has been strongly improved in the last 2 decades, so that high crystalline quality wafers with diameters up to 100 mm and well controlled doping are currently available.

Si and C atoms are covalently bonded in SiC. The hexagonal polytypes consists in a stacking of planes formed by Si-C dimers with peculiar sequence, giving rise to the 4H- or 6H-SiC. As a consequence, SiC wafers always expose two faces with different terminations, i.e. the Si-terminated face (0001) and the C-terminated face (000-1), which are oriented orthogonally to the growth axis (c-axis) of the hexagonal lattice (growth axis) as also illustrated in Figure 1.10.

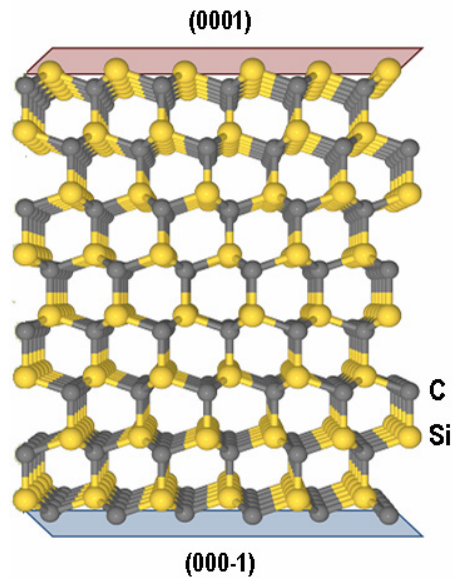


**Figure 1.10:** 3D illustration of the hexagonal polytype SiC which exposes two faces with different terminations: the Si-terminated face (0001) on top (magenta) and the C-terminated face (000-1) on the bottom (blue).

When SiC is subjected to high temperature thermal processes, a preferential sublimation of silicon from the surface occurs, leaving an excess of carbon, which reorganizes as graphene-like islands that grow until merging each other forming an extended Gr film. (see Figure 1.1 (a) and (b)). The mechanism can repeat between the formed Gr and the SiC surface until Si atoms are free to sublime (see Figure 1.11 (b) and (c)).

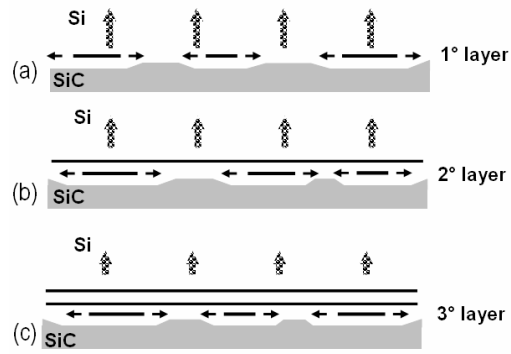


**Figure 1.11:** Schematic illustration of Gr growth: (a) sublimation of Si atoms and reorganization of remaining C atoms in a Gr islands; (b) merging of the islands in a Gr layer and starting formation of a second Gr layer under the first layer; (c) repetition of the same mechanism for a third Gr layer.

This phenomenon was known from a long time within the scientific community working on SiC [95,96] and was mainly considered as an unwanted consequence of thermal processes.

However, almost in the same period when the first experiments on Gr exfoliated from graphite were carried at Manchester (UK), the group led by W. de Heer at Georgetech (US) [97] started to work on the controlled graphitization of SiC to achieve the formation of single or few layers of Gr. Also in the case of these thin Gr films grown on SiC, quantum oscillations in both magneto-conductance and Hall resistance were observed, which indicate a 2DEG behavior. Furthermore, the control of the 2DEG carrier density via electrostatic gating was also demonstrated. Some other properties were subsequently investigated like quantum confinement of electrons [18], the band structure by angle-resolved photoemission spectroscopy (ARPES) [98,99] and the Schottky barrier between graphite and n-type and p-type SiC [100].

In the first period of these activities, the graphitization of SiC was mainly carried out in Ultra-High Vacuum (UHV) in a range of temperatures typically around 1200-1400°C. This growth technique was exploited to obtain Gr layers on both the (0001) Si-terminated face [99, 101], and the opposite (000-1) C-terminated one [102,18]. However, it was immediately clear that the Gr stack grown on the Si-terminated face was much thinner and easily controllable in terms of layers number than on C-terminated face. Moreover, Gr grown on both sides by the UHV

method was affected by a limited homogeneity and by a low general quality on large area.

Higher homogeneity and larger Gr domains with uniform thickness was obtained by performing the thermal treatments in inert gas (Ar) atmosphere at higher pressure (up to the atmospheric one) and at higher temperatures (above 1600°C) [19,20]. In Figure 1.12 are reported representative images of the surface morphology (measured by atomic force microscopy) of the Gr thickness uniformity (measured by low energy electron diffraction) in the cases of Gr grown in UHV at 1280°C and in Ar at 900 mbar [19]. A high Ar partial pressure in the growth chamber causes a strong reduction of the Si sublimation rate from SiC substrate compared to the corresponding one in UHV at the same temperature. This allows increasing the process temperature, with beneficial effects both on the SiC surface morphology, which exhibits large and ordered terraces (as better discussed in the following), and on the uniformity of the Gr film. The latter effect is a consequence of the significantly higher mobility of excess C atoms on the Si surface at higher temperature.

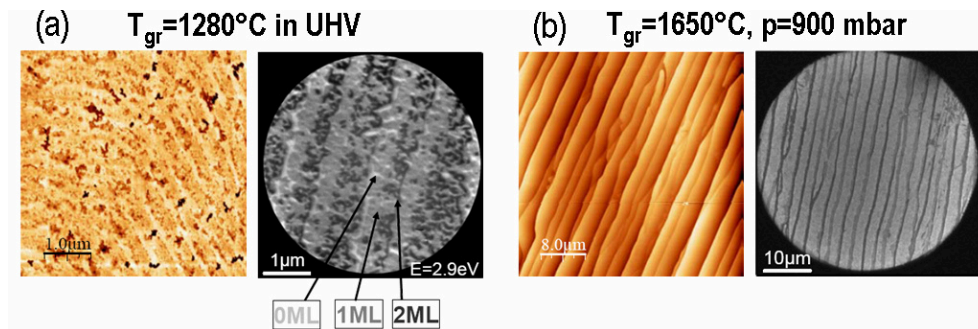


**Figure 1.12:** AFM morphologies and low energies electron diffraction images (left and right of each group respectively) in the cases of (a) Gr grown in UHV at 1280°C and (b) in Ar at 900 mbar [19].

The possibility of growing uniform Gr layers on large area opened the way to the application of refined spectroscopic techniques (typically requiring  $\text{mm}^2$  sample areas), such as X-ray Photoemission Spectroscopy (XPS) and Angle-Resolved Inverse Photoemission Spectroscopy (ARPES), which are able to provide detailed information both on the chemical bonds and on the electronic structure of epitaxial Gr [103].



In addition to the pressure and temperature, Gr growth on SiC strongly depends also on the SiC orientation. As already mentioned, the formation of Gr layers is observed both on the (000-1) C-terminated and on the (0001) Si-terminated faces of 6H or 4H--SiC. However, the structural and electronic properties of these layers are very different. Single or few layers of Gr can be obtained on the Si-terminated face, with a very good control on the thickness. These layers also exhibit a very precise epitaxial alignment with respect to the substrate and are stacked each other with the Bernal stacking (i.e. the same stacking of Gr sheets within graphite). On the other hand, under similar experimental conditions, multilayers of Gr are obtained on the C face, with a poor control on the lateral uniformity. Furthermore, a rotational (turbostratic) misorientation between the different layers is observed [104]. These different structural features are evident from Low Energy Electron Diffraction (LEED) patterns, reported in Figure 1.13 Gr layers on the Si-terminated and C-terminated face of SiC. They are also reflected in the electronic structure, probed by ARPES measurements. Representative ARPES spectra for single layer and bilayer Gr on the Si face are reported in Figure 1.13 (c) and (d) respectively, clearly indicating a modification of the band structure with increasing the number of layers, consistently with the Bernal stacking. In the case of Gr multilayers on the C face, the ARPES spectra consist of several Dirac cones shifted along the wavevector axis (Figure 1.13 (e)), indicating that the different Gr layers are electronically decoupled each other, i.e. they behave as isolated Gr layers. This also explains the result similarity between magneto-transport [18] and infrared magneto-transmission [105] measurement performed on Gr grown on C-terminated face and similar measurements on single Gr sheets.

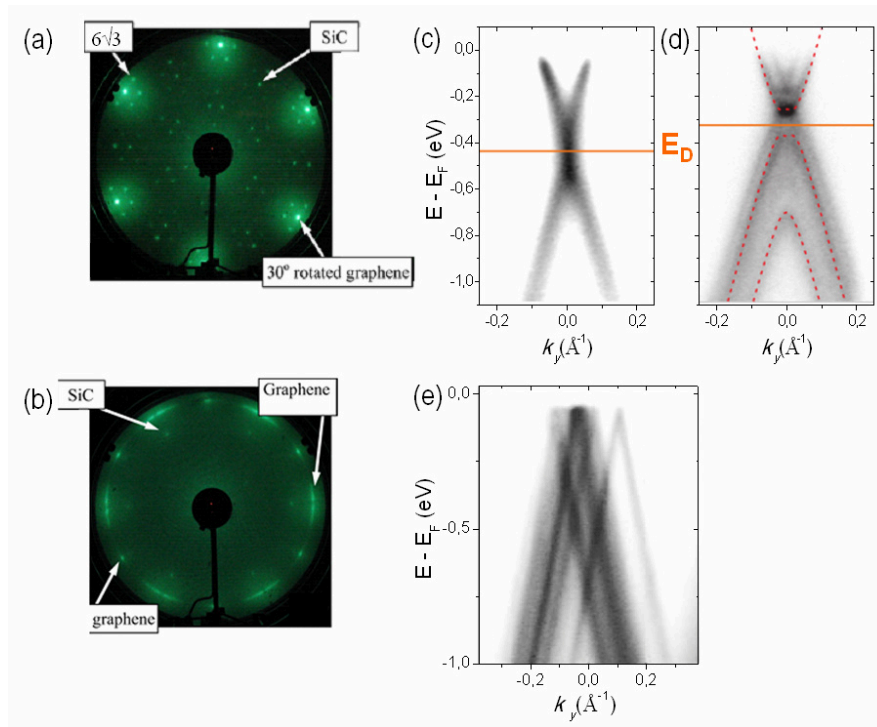


**Figure 1.13:** LEED patterns for Gr grown on (a) the S-terminated face and on (b) the C-terminated face. Dispersion of the  $\pi$ -bands measured with ARPES perpendicular to the  $\Gamma K$ -direction of the Gr Brillouin zone for (c) a Gr single layer and (d) a double layer on the S-terminated face and for (e) multilayer Gr on the C-terminated face.

Clearly, the different structural and electronic properties between Gr on the Si and C faces are the consequence of different growth mechanisms. The higher C sublimation rate from the C-terminated face than from the Si terminated one can qualitatively account for this difference. However, the atomistic details of the interface between SiC and Gr must be considered to provide a complete description of this scenario.

To date, a good understanding of the Gr growth mechanism on the Si-terminated face has been reached. In this case, the growth is mediated by the formation of a  $(6\sqrt{3} \times 6\sqrt{3})R30^\circ$  reconstructed C interface layer (commonly called “buffer layer”) which represents the precursor of Gr formation [24]. It consists of a layer of carbon atoms with hexagonal lattice, which are partially  $sp^3$  hybridized due to covalent bonds with Si atoms of the substrate. The first Gr layer is obtained after the formation of a new interfacial buffer layer and the conversion of the old one into a

fully  $sp^2$  hybridized sheet. Hence, the formation of new Gr layers proceeds through a gradual consumption of the SiC substrate, with 3 layers of SiC consumed to form a Gr layer. This mechanism implies a Si outdiffusion through the previously formed Gr sheets and can account for the self-limiting growth at fixed temperature. Furthermore, the role played by the buffer layer as a template for Gr growth fully explains the stacking order (Bernal stacking) between Gr layers on the Si face [106].

A clear understanding of Gr growth on the C face of SiC has not been reached. Differently than for Si-terminated face, an interfacial buffer layer has not been observed for the C terminated one and this can account for the rotational disorder between stacked Gr layers. Recently, the presence of ~1 nm thick interfacial amorphous layer of SiC has been observed by atomic resolution transmission electron microscopy (with low energy, 60 keV, electron beam) for Gr grown at high temperatures and atmospheric pressure on the C-terminated SiC face. Interestingly this layer exhibits a not uniform composition along its thickness, with the Si content decreasing and the C content increasing toward the interface with Gr. This amorphous layer can work as a precursor for Gr formation on the C terminated SiC face.

From the point of view of applications in electronics, Gr grown on the Si face is certainly the best option, due to the possibility to control precisely the number of layers. The presence of the buffer layer has significant influence on Gr electronic properties. A high n-type doping ( $\sim 10^{13} \text{ cm}^{-2}$ ) is observed in Gr residing on the buffer layer. It is induced by the high density of positively charged Si dangling bonds at the interface between the (0001) face and the buffer layer, which are due to the lattice mismatch between the (0001) surface and the buffer layer itself [107]. The high n-type doping of Gr is also partially responsible of the relatively low mobility values [19,108], with respect to those typically reported ( $\sim 10^4 \text{ cm}^2 \text{ V}^{-1} \text{ s}^{-1}$ ) for Gr exfoliated from High Oriented Pyrolytic Graphite (HOPG) to substrates such as  $\text{SiO}_2$  or SiC itself [109,110,111]. The typical behavior of Gr mobility with the temperature is reported in Figure 1.14.

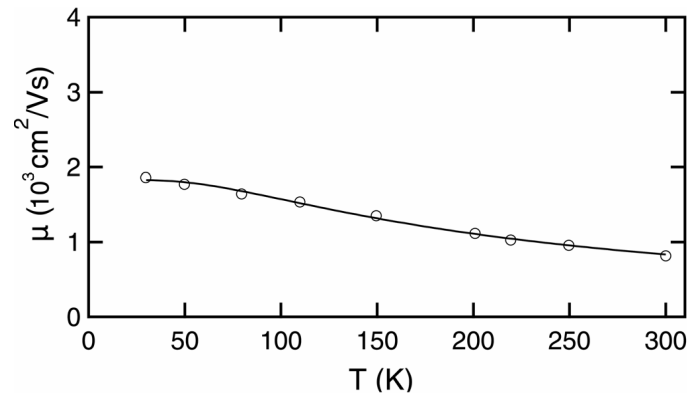


**Figure 1.14:** temperature dependence of the Gr mobility for the case of the n-type doped Gr in the presence of the underlying buffer layer. The mobility drop from 20 K to 300 K is more than 50% [107].

It has been also shown that, if this n-type doping is compensated using a tetrafluoro-tetracyanoquinodimethane overlayer (p-type dopant for Gr), the mobility is restored to values similar to those observed for Gr exfoliated from HOPG to SiO<sub>2</sub> substrates and close to charge neutrality ( $\sim 29000 \text{ cm}^2 \text{ V}^{-1} \text{ s}^{-1}$  at  $T = 25 \text{ K}$  [108]), but with a strong temperature dependence.

One of the most interesting properties of the Gr/SiC (0001) system is the possibility of tailoring the electronic properties by intercalation of proper atomic species at the interface. The most commonly used intercalating species is hydrogen. During annealing at temperatures between 600°C and 1000°C in molecular hydrogen at atmospheric pressures, hydrogen intercalation occurs, which decouples the buffer layer from the SiC (0001) surface [22]. This intercalation causes the breaking of the covalent bonds between the sp<sup>3</sup>-hybridized C atoms of the buffer layer and the Si atom of the SiC (0001) surface with the consequent conversion of the buffer layer into a Quasi-Free-standing Epitaxial Graphene (QFEG) layer. The formation of an H-terminated SiC (0001) surface is indicated by XPS spectra of the Si 2p core level, while LEED patterns displayed a strong suppression of the buffer layer superstructure spots. ARPES (Figure 1.15) measurements of the valence band structure around the K point of the Gr first Brillouin zone showed not only the appearance of the  $\pi$ -bands of an additional Gr layer, attributable to the conversion of the buffer layer, but also the inversion of the previously indicated high n-type doping in a slight p-type doping. In particular, in the case of the sole buffer layer, no evidence of the dispersion of the  $\pi$ -band is observed (Figure 1.15(a)) until the

hydrogen intercalation converts the carbon film in a quasi-free-standing and slightly p-type doped Gr layer (Figure 1.15 (b)). When a single layer of Gr over the buffer layer is considered, the dispersion of the  $\pi$ -band indicates a single and n-type doped Gr film (Figure 1.15 (c)) and two coherently stacked and slightly p-type doped Gr films (Figure 1.15 (d)) before and after the hydrogen treatment respectively.

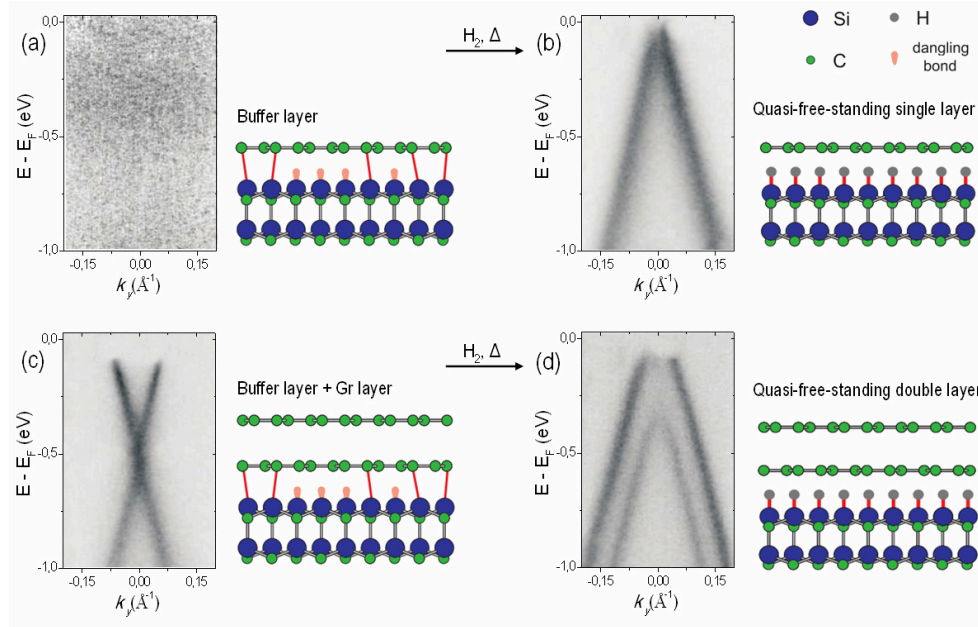


**Figure 1.15:** Dispersion of the  $\pi$ -bands measured with ARPES perpendicular to the  $\Gamma K$ -direction of the Gr Brillouin zone and correspondent schematic illustration before and after the hydrogen treatment for an as grown buffer layer (a,b) and an as grown buffer layer plus a second Gr layer (c,d) [22].

A further evidence of the quasi-free-standing nature of Gr after the hydrogen intercalation is given by the weaker temperature dependence of the mobility as shown in Figure 1.16 where the variation of  $\mu$  from 20 K to 300 K is less than 10% while before the intercalation (see Figure 1.14) the mobility drop was more than 50% in the same temperature range. Considering that for both cases the carrier concentration is basically constant in the whole temperature range, the temperature dependence is totally correlated to the Gr interaction strength with the substrate.

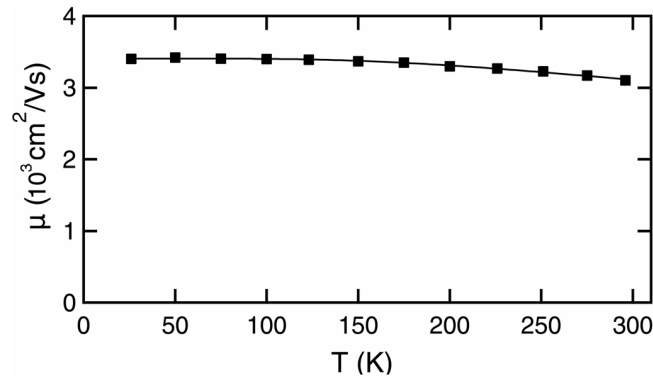


**Figure 1.16:** temperature dependence of the Gr mobility for the case of the p-type doped Gr after the hydrogen treatment. The mobility drop from 20 K to 300 K is less than 10% [107].

The presence or the absence of the buffer layer has important implications under the electrical point of view as it will be illustrated in the next chapter [22].

However, before analyzing this aspect, the peculiar nature of the SiC (0001) surface has to be discussed. Hexagonal SiC wafers grown in the [0001] direction are typically cut with a miscut angle  $\theta$  with respect to the growth axis (typically along the [11-20] direction). The wafer is considered on-axis for  $\theta < 0.1^\circ$  and off-axis for larger angles. This miscut angle is at the origin of the stepped surface morphology of SiC (clearly visible in Figure 1.12) which consists in a succession of (0001) terraces separated by facets with (11-2n) orientation. The larger is the miscut angle the higher is the fraction of SiC surface area covered by facets.

Differently than (0001) terraces, facets have non-polar or partially non-polar character.

Recent studies on non-polar SiC surfaces, such as the (1-100) and the (11-20), revealed the absence of the buffer layer at the interface between Gr and SiC [112].

This suggest that also on facets some differences in the interface structure could occur. This aspect be investigated in details in chapters 3 and 4 where the lack of a buffer layer in the facets regions will be demonstrated and its on the local structural and electrical properties on EG will be discussed.

To conclude, the main advantages of this growing technique over the CVD deposition on catalytic metals are:

the possibility to grow high quality and laterally homogeneous Gr directly on a semiconductor (or semi-insulating) substrate;

the epitaxial alignment between Gr and SiC (in the case of the Si face), with a good control on the number of layers (when few layers of Gr are grown).

the possibility to effectively tailoring the electronic transport properties of Gr and of the Gr/SiC contact by intercalation of proper atomic species at the interface (as extensively discussed in Chapter ).

On the other hand, transfer of Gr grown on SiC to other substrates is not straightforward, as discussed in section 1.2.5, making this process limited to all the applications which require Gr directly in contact on SiC.

### ***1.2.5 Graphene transfer***

For most of the applications, Gr grown by CVD on metals must be separated from the growth substrate and transferred to a suitable insulating or semiconducting substrate. To date, a certain number of strategies have been proposed in order to handle this atomically thick membrane until the target substrate [113], preserving its structural integrity on large area and minimizing the degradation of its electrical properties. As a matter of fact, the approach used to transfer the Gr membrane can have a strong impact on its final quality.

The most used approach to separate Gr from the growth substrate exploits the chemical etching of the metal layer. Ni and Cu are commonly etched away by chemical solutions such as  $\text{FeCl}_3$  [114],  $\text{Fe}(\text{NO}_3)_3$  [115],  $(\text{NH}_4)_2\text{S}_2\text{O}_8$  [52]. Although, in principle, Gr can be fished using the target substrate directly from the etching solution after the complete dissolution of the metal [114], this procedure exposes the Gr membranes to a high probability of rippling and breaking and cannot be applied for large area samples. To minimize these problems, a support film is typically attached to the Gr membrane, before metal etching. It works as carrier layer for Gr and helps to preserve the material integrity and planarity as well as to improve the handling.

One of the first polymers adopted as carrier layer was the PolyDiMethylSiloxane (PDMS) [114], which is one of the most used materials for soft lithography. It has a low adhesion force (W. d. V. interaction) with the Gr surface and acts as a mechanical support during the metal etching. Gr release from the PDMS stamp to the target substrate is easily obtained, provided its surface has a better adhesion with Gr than PDMS. This approach offers several possibilities to transfer a patterned Gr, by direct patterning on the growing substrate [114] or by a specifically molded PDMS stamp which sustains Gr, after the chemical etching, exclusively on the protruded PDMS pattern [116]. The limit of this approach is

directly related to the need of stronger adhesion between Gr and the final surface than between Gr and the PDMS that could be not satisfied with certain hard, flat and hydrophilic surfaces [116], and could result in a breaking of the membrane.

The other widely used polymeric carrier layer is the Poly(Methyl-MethAcrylate) (PMMA), which is typically deposited on the top of Gr by spin-coating. After metal etching, the PMMA/Gr film is placed on the desired target substrate and the PMMA layer is removed using proper solvents (acetone, as an example) [117]. The kind of interaction of PMMA with Gr is partially covalent, introducing a stronger bonding with Gr, if compared with the case PDMS. The carrier layer, in this case, does not compete with the target substrate for the Gr release, but it is simply washed away, without any limitation in the choice of the target material. Nevertheless, this approach is affected by several weaknesses: due to the rigidity of the baked PMMA layer, Gr is frozen with the wrinkled topography formed during the cooling down step of the CVD growth and coherently transferred on the final substrate. This rigid topography causes a bad accommodation on the target surface so that Gr risks of being rippled and cracked during the PMMA dissolution.

Several attempts have been made to overcome this limitation such as the deposition of a second PMMA layer directly over the transferred PMMA/Gr layer to dissolve the first polymer film and rearrange the entire stack [115] or the introduction of a heat treatment step to increase the adhesion between the PMMA/Gr stack and the substrate [118] driven by a partial softening of the polymer. PMMA has another major weakness: the partial covalent character of the bonding with the Gr membrane results in an incomplete elimination of the polymers residues, with a consequent partial degradation on the Gr electrical performances. The Gr cleanness and the related properties can be improved by appropriately choosing chemical baths to dissolve PMMA [119] or alternatively exploiting thermal annealing in H<sub>2</sub> gas and at the appropriate temperature [120][119].

Another carrier layer for Gr is the Thermal Release Tape (TRT), consisting of a semi-rigid plastic film covered by a glue layer that degrades at a specific temperature releasing the supported material. This kind of carrier layer is suitable to implement scalable transfer methods such as the roll-to-roll [52] and the hot pressing [121]. As schematically illustrated in Figure 1.17, the roll-to-roll method [52] potentially allows a continuous transfer of large area Gr membranes grown on Cu foils, exploiting a sequence of compressive rollers, which perform the following operations: (i) the attachment of the TRT support to Gr, (ii) the copper etching and (iii) the dry transfer-printing on the target substrate. Alternatively, in



the hot pressing method the TRT/Gr stack is pressed onto the target substrate where Gr is released (see Figure 1.17). This equipment consists of two hot metal plates pressing each other with precisely controlled temperature and pressure. Except for the final dimensions, in this case limited by the compressive system size, the hot pressing approach has the advantage of avoiding any shear stress on the Gr membrane. This can be instead introduced by the roll-to-roll approach, particularly in the case of transferring to rigid substrates, leading to a higher level of cracks and holes.

Even if the chemical etching of the metal substrate is still the most typically used approach to separate the polymer/Gr stack, it presents several drawbacks.

It can be applied only to Gr grown on catalytic metals that can be easily etched, and limits the use of catalysts, such as Pt, which is instead extremely difficult to be dissolved in a chemical bath.

The harsh etching step can damage Gr and introduce chemical groups or metal impurities with a doping effect [122,123].

In the perspective of an industrial scale up of Gr production, metal waste by etching would strongly raise the cost of the process, with a relevant environmental impact.

Finally, metal contaminations are strictly prohibited in some sections of semiconductor fabs, and these would hinder the integration of Gr with semiconductor technology.

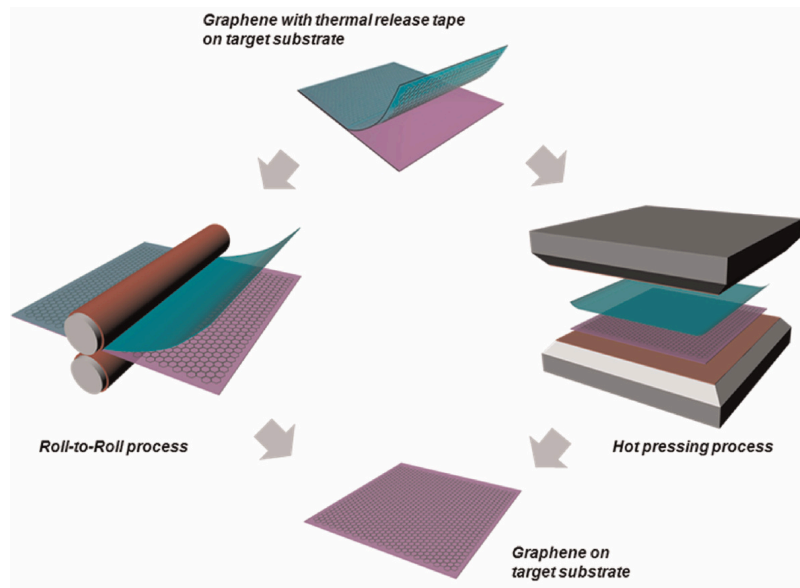


**Figure 1.17:** Schematic illustration of Gr transferred from a TRT to a target substrate by roll-to-roll or by hot pressing [121].

For these reasons, novel Gr separation methods avoiding the metal etching step are under consideration.

A direct exfoliation of Gr from the catalytic metal was demonstrated using azide based molecules [124] or epoxy glue [125] to create covalent bonds on the surface of Gr and peel off the carbon membrane from the metal foil. This approach has the merit to avoid the chemical etching of metal. However, there is no proposed solution to remove effectively the layer of glue, confining this approach to applications that are not effected by the remaining material.

Soak-and-peel delamination in hot deionized water [126] and electrolytic delamination through hydrogen bubbling at the interface between Gr and metal [127] are probably the most interesting approaches which could completely substitute the chemical etching.

Soak-and-peel delamination in hot deionized water is the most recent proposal for a chemical free separation of Gr from metal. The method exploits a deionized water solution at 90°C for 2 hours to obtain a separation form the metal foil of Gr, which is previously coated by a PMMA layer and sustained by a TRT. The separation is driven by the water penetration at the Gr-Cu interface without any chemical degradation of the metal foil, which results completely reusable. Apparently, the Gr

final quality on the transferred substrate, if directly compared with the same CVD growth Gr transferred following the traditional approach, reveals a comparable or even better result. However, that technique is extremely time consuming and, although promising, still not mature and well discussed in literature.

The other and probably most promising technique to separate Gr from metal is the electrolytic delamination. In this case, the catalytic metal foil is exploited as the cathode for water electrolysis. The hydrogen bubbles formed at the interface between Gr and the metal foil generate a gentle mechanical action to win the weak v. d. W. interactions between the two layers. As it will be discussed in Chapter 3, this delamination proceeds from the outer perimeter gradually to the centre of the foil. The first configuration for an electrolytic delamination of Gr [127] was proposed with an extremely low rate and in combination with a partial oxidation of the metal foil. The electrolytic cell was constituted by the Gr/Cu foil, covered by a PMMA carrier layer, as the cathode and a carbon anode in an aqueous solution of  $K_2S_2O_8$  as electrolyte in an extremely low concentration ( $\sim 0.05$  mM). Applying a voltage of  $-5$  V and due to the extremely low concentration of the electrolyte, a Gr foil with a dimension around  $25\text{ cm}^2$  was delaminated in about 50 minutes. Copper oxidation simultaneously occurs by the oxidative action of the persulfate, which is reduced to sulfate. The local alkalization drives the copper oxide precipitation, which passivates the copper foil avoiding further chemical etching. Subsequently, the same mechanism was proposed in alkali hydroxide solutions with higher concentration, to delaminate Gr grown on Pt [93] and again on Cu [128]. In both cases, the delamination exploits substantially the previously described cell design with a relevantly higher electrolyte concentration that, for similar applied potentials, generates a stronger bubbling and a faster delamination (times in the order of tens of seconds). Moreover, no chemical reaction of the metal foil with the electrolyte solution was observed, proving that the delamination process can be totally controlled by the mechanical action of the bubbling. It is worth noticing that the possibility to delaminate Gr from Pt demonstrates another important achievement of this technique, which allows separating Gr from Pt, and potentially from other chemical inert metals, which is instead not possible with the traditional chemical etching. It means that not only the reusability of the metal foil could drastically reduce the Gr fabrication costs but also allows to evaluate several different catalytic growth substrates previously merely avoided for issues related to their problematic separation from Gr. Furthermore, the delamination speed, which allows obtaining centimeters square areas of Gr in few decades of seconds,

represents a not trivial gain in terms of practical operations and in the prospective of an industrial scale up. However, the delamination speed, which can be easily controlled by the electrolyte concentration [127] or by the applied potential [127], cannot be indefinitely increased without incurring in a growing degradation of the Gr quality and, as described in Chapter 3, a certain understanding of the basic delamination mechanisms is needed to operate with a high level of control.

As the most recent Soak-and-peel delamination, also this approach can be defined as a chemical free process considering that it involves negligible amounts of reacted material. However, granting to the Soak-and-peel delamination the benefit of time in consideration of its recent discovering, at the state of art the electrolytic delamination seems the best solution to totally replace the chemical etching approach, not only for the previously described benefits but also because an electrolytic cell design offers a plenty of room to act in control parameters such as the electrolytic kinetics, the supplied potential shape in function of time or the geometry of several elements (the electrodes, the reciprocal distance, the depth in solution) which are all potentially implantable parameters to increase the quality of the final delaminated Gr or to tune the appropriate conditions in relation with the peculiar properties of different catalytic growth substrates.

To separate Gr from SiC the only practicable way is a direct exfoliation, due to the high resistance of SiC to conventional chemical etching [129] and the high costs of the substrate. Gr was exfoliated from SiC and transferred to a target substrate using a double layer of metal and polymer: Au [130] and, with better results, Pd [131], as the layer directly in contact with Gr, obtained by Electron Beam Evaporation, and Polyimide (PI) layer deposited for spin coating over the metal. The PI/Metal/Gr stack was gently lifted from the SiC surface and transferred on the target substrate. Finally, the polymeric and the metallic carrier layer were properly eliminated to restore the sole Gr. However, the final membrane exhibited a certain density of holes and a high defect peak ( $D \sim 1380 \text{ cm}^{-1}$ ) in Raman spectroscopy. The mobility measured by fabrication of back gated Field Effect Transistor (FET) showed an ambipolar characteristic with a hole mobility of  $\sim 100 \text{ cm}^2 \text{ V}^{-1} \text{ s}^{-1}$ , an order of magnitude lower than what observed in free standing Gr [71]. Gr was also exfoliated directly by a TRT [132] but the final morphology showed holes in the order of  $10 \mu\text{m}$  of size and the electrical properties were again significantly decreased with an average mobility of  $201 \text{ cm}^2 \text{ V}^{-1} \text{ s}^{-1}$ . Moreover, the high efficiency of the TRT in lifting off Gr brings to a multilayered material on the target substrate. Recently Gr has been successfully delaminated from SiC

exploiting Gr a self exfoliation mechanism driven by the tensile strength of a Ni film deposited on the SiC surface [133]. Ni possesses a stronger binding energy per atom with Gr than compared to SiC and an internal stress which is able to balance the Gr-SiC binding energy if a critical Ni thickness is reached. In this conditions Ni bends for internal stress and Gr remains attached on it promoting the self-exfoliation from SiC. The final Gr membrane was revealed by Raman mapping to be a single layer membrane with a low defect peak over 99% of the area. Despite these recent results, which open a potential pathway to reevaluate this Gr growth technique as a ubiquitous method, the segregation on SiC remains an approach confined to all the applications that involve the carbon membrane directly in contact with SiC.

*This*

*Page*

*Intentionally*

*Left*

*Blank*

## Chapter 2: Graphene heterostructures with semiconductors

As discussed in the Chapter 1, Gr band structure is characterized by the absence of a bandgap. This results in a low ratio between the on- and the off-state currents ( $I_{on}/I_{off} < 10$ ) when Gr is used as channel material in a conventional lateral FET configuration. Such low  $I_{on}/I_{off}$  ratio seriously limits the range of possible applications of Gr in electronics, in particular for switching devices and logic applications [134].

To overcome these limitations, several approaches to open a bandgap in the Gr band structure have been proposed in the last years. They include the lateral confinement of the 2DEG in Gr nanoribbons [134], the hydrogenation or fluorination of the  $sp^2$  Gr lattice to obtain the  $sp^3$  hybridized derivatives of Gr named *graphane* and *fluorographene*, respectively [135,136], the application of a transversal electric field to a bilayer of Gr [137], or the introduction of an uniaxial strain in the Gr lattice [138]. However, in some of these cases the opening of a bandgap is accompanied by a partial degradation of Gr electronic transport properties. As an example, in Gr nanoribbons produced by lithographic processes from a Gr sheet, the disorder at the edges strongly reduces the carrier mobility.

Currently, two main trends have emerged for future applications of Gr and, more generally, 2D materials in electronics.

The first one is to replace Gr with other 2D materials holding semiconducting properties for the channel region of lateral FETs. Among these new 2D materials, Transition Metal Dichalcogenides (TMD), such as  $MoS_2$ ,  $WS_2$ ,  $MoSe_2$ ,  $WSe_2$  are attracting particular interest, due to some interesting electronic and optical properties, such as a large bandgap. Bulk or few layers of  $MoS_2$  present an indirect bandgap of  $\sim 1.2$  eV, whereas a direct bandgap of  $\sim 1.8$  eV is found for monolayers.  $MoS_2$  typically exhibits lower mobility values (from  $\sim 1$  to  $\sim 200$   $cm^2V^{-1}s^{-1}$ ) with respect to 2D Gr sheets, but comparable or even higher than those reported for Gr nanoribbons (with a bandgap  $< 100$  meV). In some cases, Gr has been proposed as source/drain or gate contact of FETs with a  $MoS_2$  channel or for the interconnection between these FETs [139].

The alternative route to use Gr for switching applications is to consider novel device architectures (different than the lateral FET), where high  $I_{on}/I_{off}$  ratios can be obtained exploiting some peculiar properties of Gr, such as the atomic thickness, the linear density of states with energy, the partial screening of electric fields. Such devices mainly consist of heterostructures of Gr with semiconductors or insulators. Their working principle relies on the field effect modulation of the vertical current transport at Gr interfaces with these materials.

In the last years, several types of Gr-based vertical devices have been considered, which can be grouped into three categories:

devices based on the Gr/semiconductor Schottky junction [9], where the current flowing through this junction is modulated by changing the Gr workfunction (and hence the Gr/semiconductor Schottky barrier) by an electric field applied to a gate electrode;

HETs [10,11], where Gr (working as the base contact) is sandwiched between two insulating layers (the emitter-base and base-collector barriers) and the hot electron current from the emitter to the collector contacts is modulated by the emitter-base bias. In this case, Gr atomic thickness guarantees an extremely low transit time through the base and, hence, high switching speed;

devices based on the current tunnelling between two Gr layers separated by an atomically thin barrier layer, such as boron nitride thin films [12,140]. In this case, the tunnelling probability is modulated by changing the Fermi level alignment between the two Gr layers with an external electric field applied to a gate electrode. In this Ph.D. thesis work Gr heterostructures with WBSs (SiC, GaN and  $Al_xGa_{1-x}N$ ) have been investigated. As it will be discussed in Chapter 4, these heterostructures can be used to implement devices such as Schottky junction or hot electron transistors. The combination of the above-discussed Gr electronic properties with some of the peculiar properties of WBSs would allow in principle to achieve superior performances with respect to those of the prototypes reported to date in the literature.

In this chapter, a general introduction to the physics of the Gr/semiconductor junction is provided. Furthermore, a brief overview of the literature results related to the above-mentioned Gr heterostructures devices will be given.



## 2.1 Physics of the Gr/semiconductor junction

A Gr layer isolated from any substrate is ideally intrinsic, i.e. its Fermi level is coincident with the Dirac point, where the Density Of electronic States (DOS) is vanishing [42], but a not negligible carrier density is still present at temperatures  $T > 0$  due to thermal excitation effects [141,142,143].

However, when Gr is placed in contact with a substrate, charge transfer can occur, which cause a shift of the Fermi level from the Dirac point. Additional charge transfers can be due to several doping sources, such as the charged impurities present on Gr or trapped at Gr/substrate interface. Due to the low DOS close of the Dirac point, the Gr displays an extraordinary sensitivity to the environment. As an example, it can be calculated that a transfer of just  $0.01 e^-$  per unit cell would rise up raise the Fermi level of 0.47 eV [144].

This premise is fundamental to understand what may imply the formation of a Gr/semiconductor junction respect to a traditional metal/semiconductor junction.

When a metal and a semiconductor are put in contact a Schottky barrier is typically formed at the interface, as an effect of the alignment of the Fermi levels under thermal equilibrium conditions and of the consequent charge transfer at the interface [145]. However, this charge transfer can barely vary the Fermi level of the metal because of its high DOS at the Fermi energy, so that the Fermi level changes only in the semiconductor.

A different scenario is shown by Gr: due to the low DOS around the Dirac point, the formation of the junction and the consequent charge transfer at the thermal equilibrium will change the Fermi level on both the semiconductor and Gr, breaking the symmetry of electron and hole concentrations in the Dirac cones of Gr. Therefore, if Gr is in contact with an n-type semiconductor, the electron transfer from the bulk semiconductor to Gr will rise up the Fermi level into Gr with a consequent reduction of the barrier height.

Analogously the holes transfer from a p-type semiconductor to Gr will also result in a reduction of the barrier height by the downshift of the Fermi level into the Dirac cones [146].

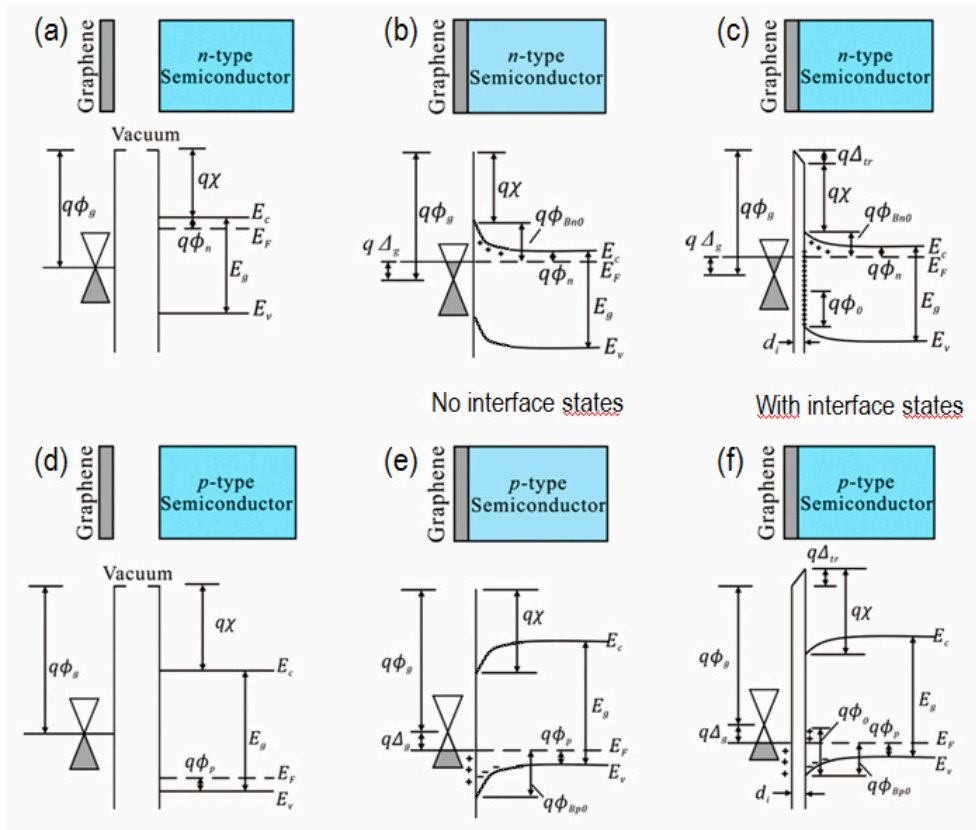


**Figure 2.1:** (a) Gr and n-type semiconductor in separated systems, (b) connected in an ideal Schottky barrier without surface states and (c) considering the effect of the interfacial states. (d) Analogues representation of Gr with the p-type semiconductor in separated systems, (e) connected in an ideal Schottky barrier without surface states and (f) considering the effect of the interfacial states.

Let us consider for simplicity and in the first approximation, an ideal Schottky barrier without surface states at the semiconductor surface. When a Gr membrane is in contact with an n-type (or a p-type) semiconductor, an electron (hole) transfer to Gr is observed with a rise of the Fermi level in Gr and a lowering in the semiconductor (and vice versa for p-type semiconductors) [146, 147]. Figure 2.1 (a,b) and Figure 2.1 (d,e) illustrate the band diagrams of Gr and the semiconductor before and after the junction formation in the cases of an n-type and the p-type doped semiconductor, respectively. The charge transfer between Gr and the semiconductor substrate induces the shift of the Fermi level in Gr.

In this first approximation, the charge  $Q_G$  transferred into the Gr is equal to the space charge  $Q_s$  in the depletion layer of the semiconductor, which is, in turn, correlated with the barrier height  $\Phi_{Bn0}$ . Clearly,  $Q_G$  is related to the Fermi level shift in Gr ( $\Delta_g$ ). From the band-diagrams in Figure 2.1 (b) and Figure 2.1 (e), it is possible to extract the following equations relating  $\Delta_g$  with the Gr barrier heights  $\Phi_{Bn0}$  and  $\Phi_{Bp0}$ :

$$\Phi_g - \Delta_g = \chi + \Phi_{Bn0} \quad (2.1)$$

and

$$\Phi_g + \Delta_g = E_g/q + \chi - \Phi_{Bp0} \quad (2.2)$$

Where  $\Phi_g$  is the metal work function of the neutral Gr while  $\chi$  and  $E_g$  are the electron affinity and the band gap of the semiconductor respectively.

However, it is clear that the described situation is an ideal case. In reality, other effects, such as that of the interface states have to be considered. These states can introduce additional charge transfer to Gr and their contribution could result as relevant as the contribution by the other terms in Equations (2.1) and (2.2).

To consider the interface states contribution, the balance between the charges  $Q_G$  in Gr and those in the depletion region of the semiconductor  $Q_s$  and at the interface,  $Q_i$  can be expressed as:

$$Q_G = - (Q_s + Q_i). \quad (2.3)$$

Furthermore, a common way to account for the effect of semiconductor surface states is to assume the presence of an ultrathin insulating (vacuum) interface layer (with thickness  $d$ ), which is able to sustain a potential difference  $\Delta_{tr}$  between Gr and the semiconductor surface, as illustrated in Figure 2.1 (c) and (f) for the n-type and the p-type semiconductors respectively. This potential difference can be calculated by applying the Gauss' law. From the energy band diagrams in Figure 2.1 (c) and (f) it is possible to extract the equations connecting  $\Delta_g$  and the barrier heights  $\Phi_{Bn0}$  and  $\Phi_{Bp0}$ .

$$\Phi_g - \Delta_g = \Delta_{tr} + \chi + \Phi_{Bn0} \quad (2.4)$$

And

$$\Phi_g + \Delta_g + \Delta_{tr} = E_g/q + \chi - \Phi_{Bp0} \quad (2.5)$$

for n-type and p-type semiconductors respectively.

A relevant case of Gr/semiconductor junction is represented by the epitaxial Gr on the Si-terminated face of hexagonal polytype SiC [18,19,20]. The contact behavior between Gr and SiC (0001) was early investigated [100,148] to understand its potential advantages compared to a traditional metal contact. An as-deposited metal usually shows a Schottky contact behavior with SiC [149] while to obtain ohmic behavior a heavily n-type or p-type doping on SiC followed by high temperature annealing of the metal-semiconductor junction is needed [150,151].

The analysis of the Gr-semiconductor junction was performed on Gr grown both on n-type and p-type doped SiC (0001) and SBH values  $\Phi_{Bn} = 0.3 \pm 0.1$  eV and  $\Phi_{Bp} = 2.7 \pm 0.1$  eV were extracted in the two cases, respectively. Clearly, the rather small barrier height on n-type SiC (0001) implies a nearly ohmic behavior. The origin of this low SBH is strictly related to the source of the high electron doping of EG grown on SiC (0001), i.e. the presence of the  $(6\sqrt{3} \times 6\sqrt{3})R30^\circ$  reconstructed C interface layer, as already discussed in the previous chapter [106]. To demonstrate the role of the buffer layer a comparison between the SBH of EG grown on 4H-SiC (0001) and of Gr transferred on virgin SiC from HOPG was also reported, showing a lower SBH for EG (~0.3 eV) than for Gr transferred to SiC (~0.9 eV) [111]. The Fermi level pinning in the case of EG on SiC (0001) is ascribed to the presence of positively charged states, associated to the Si dangling bonds of the (0001) face located below the buffer layer, as schematically illustrated in Figure 2.2 (a).

The influence of the buffer layer on the doping was definitively demonstrated by Riedl et al. [22], which converted the buffer layer in QFEG by hydrogen intercalation as described in the previous chapter. Silicon dangling bonds were passivated because of the hydrogen intercalation, thus eliminating the source of the Gr n-type doping, as illustrated in Figure 2.2 (b). Interestingly, the QFEG on (0001) was not neutral, but a residual p-type doping ( $5 \times 10^{12} \text{ cm}^{-2}$ ) was observed. This was explained by Ristein et al. [152] as an effect of piezoelectric nature of hexagonal SiC, which exhibits a spontaneous polarization  $P_0$  in the [0001] direction, inducing a positive charge on Gr surface.

The displacement field in a piezoelectric material with an applied electric field can be expressed as the sum of two components, i.e. the displacement due to the electric field  $E$  and of that due to the spontaneous polarization  $P_0$ :

$$\vec{D} = \epsilon_0 \epsilon_r \vec{E} + \vec{P}_0 \quad (2.6)$$

The charge density (per unit area)  $\sigma$  induced on the QFEG can be obtained from the Gauss' law for the displacement field:

$$\nabla \vec{D} = \sigma \quad (2.7)$$

From Equations (2.6) and (2.7) results:

$$\epsilon_0 \epsilon_r \nabla \vec{E} = \sigma - \nabla \vec{P}_0 \quad (2.8)$$

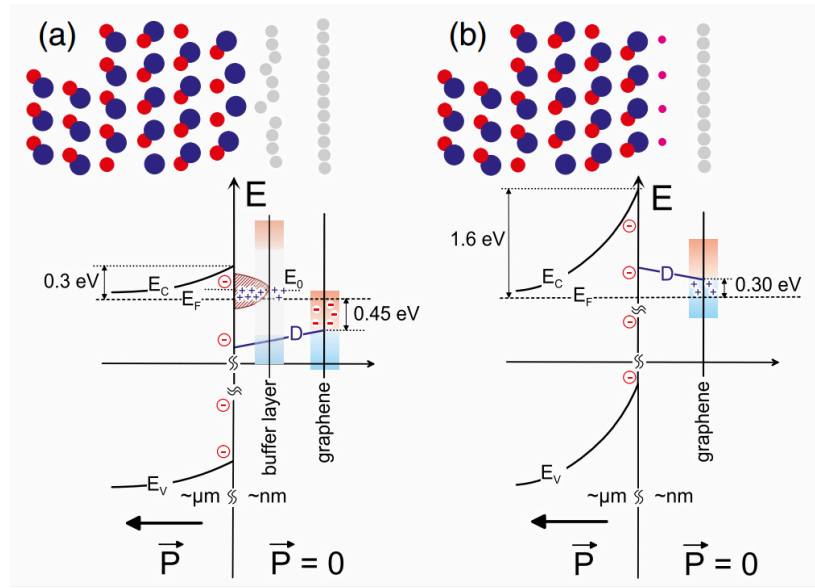


**Figure 2.2:** qualitative atom disposal sketch (above) and schematic representation (below) of the band diagrams for the epitaxial (a) and the quasi-free-standing (b) Gr interface with 6H-SiC (0001). Large blue and small red circles represent silicon and carbon atoms of the SiC lattice respectively, grey circles represent carbon reorganized over SiC and magenta circles represent the hydrogen that passivates SiC surface. The polarization vector inside and outside of the SiC is indicated at the bottom of the figure. Circled charges represent the pseudo-charge induced by polarization.  $D$  sketches the electrostatic potential between the SiC surface and the Gr layer [152].

It means that the gradient of the spontaneous polarization produces a sheet of negative charge on the SiC (0001) surface, which in turns induces a p-type doping on the Gr layer on top. Such substrate polarization induced p-type doping is overcompensated by the interface states n-type doping in the case of as grown epitaxial Gr. In the case of QFEG (with a hydrogen-passivated interface), the piezoelectric polarization from the substrate becomes the main doping source of Gr, as illustrated in Figure 2.2 (b).

Hydrogen intercalation results also in a significant change of the vertical current transport through the Gr/SiC interface, with the observation of a rectifying (i.e. Schottky like) contact [23]. Interestingly, a discrepancy between the QFEG/SiC SBH values  $\Phi_B$  extracted by different characterization methods has been observed, with the SBH values obtained by  $I$ - $V$  measurements ( $\Phi_B \approx 0.9 - 1$  eV) significantly lower than those obtained from  $C$ - $V$  analyses and by XPS ( $\Phi_B \sim 1.5$  eV) [23]. Similar discrepancies are not uncommon in the case of Schottky contacts between a metal and a semiconductor. They are typically an indication of a laterally inhomogeneous contact, consisting of nanometric size regions with low SBH embedded in the macroscopic contact area with higher SBH [153]. These nanoscale inhomogeneities can be related to several factors, such as defects in the semiconductor near surface regions, disuniformities in the metal layer. They act as preferential conduction paths through the Schottky interface and can account for the reduced effective SBH value measured using forward bias  $I$ - $V$  characterization, whereas they are expected not to affect the SBH evaluated from reverse bias  $C$ - $V$  analysis.

The origin of the inhomogeneous Schottky barrier in the case of the atomically perfect interface between QFEG and SiC will be the object of the nanoscale electrical characterization on this system reported in Chapter 4.

## 2.2 Devices based on the Gr/semiconductor junction

To date, several devices based on the above discussed Gr/semiconductor junction have been considered, such as Schottky diodes [154], solar cells [155, 156], photodetectors [157] and transistors with a field effect modulated Gr/semiconductor Schottky barrier [9]. In particular, the latter device concept was introduced by Yang et al. [9] in 2010 and was named *Barristor*.

As illustrated in Figure 2.3 (a), it is a three terminal device, which consists of a vertical Gr/Si Schottky diode (with Gr and Si connected to the source and drain

terminals, respectively), in which the junction region is covered by a gate dielectric and controlled by a top gate contact. A key requirement for the fabrication of a nearly ideal Gr/Si Schottky barrier is a proper passivation of the Si surface, e.g. by hydrogen treatments. This results in a suppression of the interface states at the junction between the naturally inert Gr and the H-saturated silicon surface. Due to the low DOS above discussed, Gr work function can be electrostatically modulated by tuning the Fermi energy via gate bias. In particular, the authors have shown a field effect modulation of the SBH (as schematically illustrated in Figure 2.3 (b-c)), both in the case of Gr junctions with p-type and n-type doped Si, demonstrating  $I_{on}/I_{off}$  ratio up to  $\sim 10^5$ . Furthermore, they demonstrated that the shift of the Fermi level  $\Delta E_F = \hbar v_F (\pi n)^{1/2}$  calculated from the carrier density  $n$  measured by Hall effect, corresponds to the variation in the SBH  $\Delta \Phi_B$  (see Figure 2.3 (d)) for a wide range of gate voltages, suggesting a control on the  $\Phi_B$  fully related to the Gr work function modulation in the absence of Fermi-level pinning [158]. As a result the Schottky barrier between Gr and Si can be approximated to the ideal Schottky-Mott limit, by the difference between the Gr work function ( $W_G = E_{vac} - E_F$ , with  $E_{vac}$  the vacuum level) and the Si electron affinity ( $\chi_{Si} = E_{vac} - E_c$ , with  $E_c$  the conduction band minimum of Si) [159].

Obviously, not only silicon but also several other semiconductors have been taken into account to fabricate heterostructures with Gr.

As an example, Gr/semiconductor junctions were also obtained transferring Gr on binary III-V direct bandgap semiconductors such as on Gallium Arsenide [160,161] and on Gallium Nitride [146,147] revealing in both cases a rectifying behavior comparable to what observed on other substrates in similar conditions [161]. n-type doped GaAs was, for example, considered for potential applications in Schottky junction solar cells with Gr [162]. In the case of GaN, Gr has been mainly considered as transparent conductive electrode for light emitting diodes in replacement to the commonly used ITO [163,164,25].

SiC is a strategic material for high power and high frequency applications. The possibility to tailor the properties of Gr contacts grown on it the (0001) face by intercalation of proper atomic species [18,19,20] opens the way to the development of new device concepts fully exploiting the potentialities of both Gr and SiC. Among these, the possibility to exploit the properties of the QFEG/SiC Schottky junction to fabricate a *Barristor* on SiC will be discussed in Chapter 4.

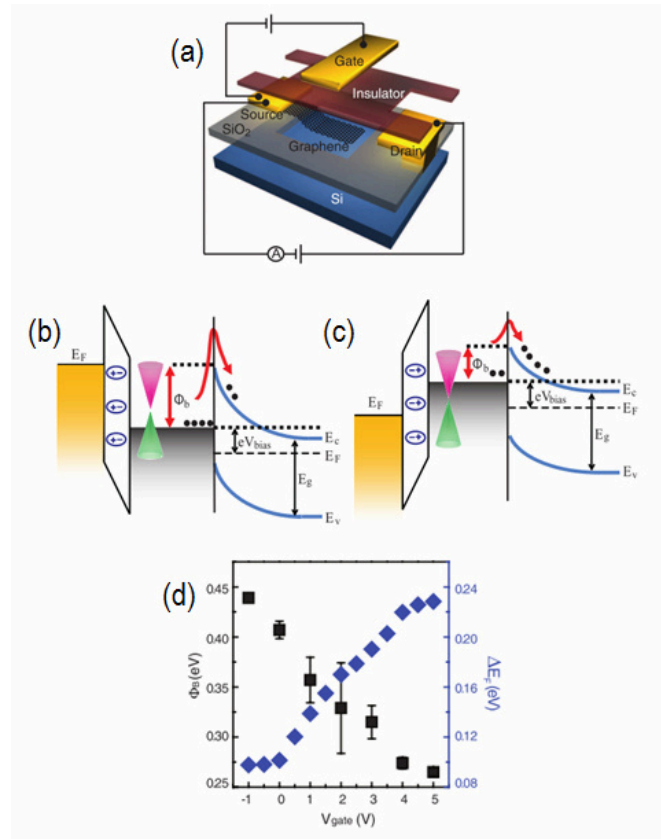


**Figure 2.3:** (a) A schematic diagram to show the concept of a Gr *Barristor*. (b-c) Schematic representation of the band diagrams of the n-type device with an applied gate bias on the top of Gr. Applying negative voltage on the gate induces holes in Gr, increasing its work function and increasing the SBH (c) while positive gate voltage decreases the SBH (d) [9].



### 2.3 Hot electron transistors with a graphene base

The hot electron transistor is a three terminal device, where an ultrathin metallic base (B) is separated by the emitter (E) and the collector (C) by two insulating layers (emitter-base and base-collector insulators). Electrons injected from the emitter to the base by Fowler-Nordheim tunnelling, transit to the base and are finally collected at the collector electrode. Although this device concept was introduced already in the 1980's, its practical implementation has been hampered by the unavailability of high quality ultrathin metal layers working as base terminal. Gr has some distinct advantages over a common metal base in terms of device performances. In fact, the potential DC and RF performance are strongly limited when a metallic base is used by two mechanisms: carrier scattering, which is lowered by thinning the metal, and the in-plane voltage drop which instead increase the base resistance and the self-bias crowding when the material is thinner [165]. In this sense Gr is the ideal base due to its atomic thickness together with a high in plane conductivity.

The prototype of a Graphene Base Hot Electron Transistor (GB-HET) was proposed by Vaziri et al. [10] immediately followed by Zeng et al. [11]. They presented a HET with a base contact made of Gr instead of metal, over a few nm thick silicon dioxide insulator as tunnelling barrier (or base-emitter barrier), an n-type doped silicon substrate as emitter and an overlying  $\text{Al}_2\text{O}_3$  or  $\text{HfO}_2$  as filter barrier (or base-collector barrier) for the collector (see Figure 2.4 (a)). In this kind of device a current flow is achieved applying an appropriate voltage between the base and the emitter ( $V_{BE}$ ) to induce hot electrons tunnelling across the lowered barrier, from the conduction band of the n-type doped silicon to the Gr base through the Fowler–Nordheim mechanism (Figure 2.4 (b,c)). Depending on the  $V_{BE}$  hot electrons possesses different kinetic energy. When  $V_{BE}$  is small, the kinetic energy of most hot electrons is insufficient to overcome the filtering barrier between base and collector while a sufficiently high kinetic energy allows hot electrons to traverse the filtering layer, as illustrated by the red arrow in Figure 2.1 (b) and Figure 2.1 (c) respectively. Considering common-base output characteristic it has been demonstrated that the collector current ( $I_C$ ) is mainly controlled by emitter-base voltage  $V_{BE}$  and is not sensitive to the collector-base voltage. The weak dependence of the filtering barrier height on  $V_{CB}$  explains the  $I_C$  saturation observed in Figure 2.4 (d). At the state of art a reasonable  $I_{on}/I_{off}$  ratio of two orders of magnitude was achieved observing also  $I_{on}/I_{off}$  ratio over  $10^5$  under

specific conditions that however induce also a dramatic decrease of gain (which indicates the fraction of the injected electrons that actually reach the collector) [11].

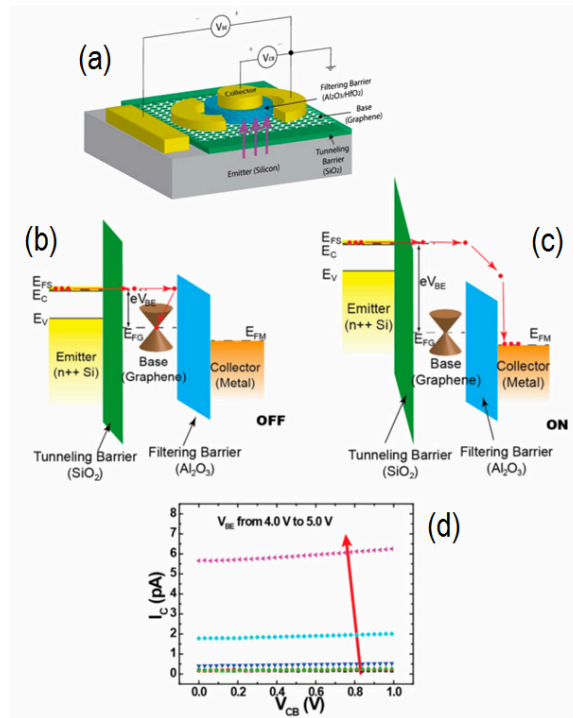


**Figure 2.4:** (a) A schematic diagram to show the collector-up GB-HET structure and the common-base configuration. Gr is used as the base region for an HET structure. The purple arrows indicate the transport direction of the hot electrons. (b-c) schematic representation of the band diagrams of the device, where red arrow represent hot electrons tunnel from the silicon emitter to the Gr base through the SiO<sub>2</sub> tunnelling barrier. Depending on the  $V_{BE}$  hot electrons possesses different kinetic energy, which allows or not allows traveling over the filtering barrier. (d) The output  $I$ - $V$  characteristics at various  $V_{BE}$  bias [11].

It is worth noticing that, under suitable conditions, the vertical current transport through the base-emitter barrier layer is potentially achievable not only by tunnelling but also by a thermionic emission mechanism expanding the possible scenarios for this kind of device concept.

Moreover, a similar kind of configuration can be designed considering Gr in combination with an “ordinary” 2DEG, such as the one formed at the heterointerface of a conventional III-V semiconductor, such as AlGaAs/GaAs or

AlGa<sub>N</sub>/Ga<sub>N</sub> heterostructures. In this way Gr could act as base, the 2DEG at the heterointerface as emitter the AlGaAs or the AlGa<sub>N</sub> layer as the base-emitter barrier layer (which could be crossed by a tunnelling or a thermionic emission mechanism).

To date heterostructures hosting a high mobility 2DEG combined with Gr already deserve attention, since their combination with a Gr sheet can represent the basis of a new class of Dirac-Schrodinger hybrid electron systems, as recently discussed in the literature in the case of Gr/AlGaAs/GaAs heterostructures [166].

Such hybrid systems with Al<sub>x</sub>Ga<sub>1-x</sub>N/GaN heterostructures [14] also deserve special interest, due to some peculiar properties and the technological importance of this material [167]. In fact, a conventional III-V semiconductor, such as AlGaAs/GaAs heterostructures, needs an n-type doped barrier layer to provide the charges for the 2DEG formation at the heterojunction. In contrast, for AlGa<sub>N</sub>/Ga<sub>N</sub> the spontaneous polarization of Ga<sub>N</sub> combined with a piezoelectric nature, which introduces an extra-polarization by the strain due to the lattice mismatch, generates a high sheet charge density in the 2DEG even using undoped materials. The absence of doping reduces the coulomb scattering with an enhancement for the electron mobility in 2DEG.

However, to date only few investigations have been reported on the Gr/AlGa<sub>N</sub>/Ga<sub>N</sub> system. Gr has been proposed, as heat-escaping channel due to its excellent heat conductivity for thermal management in high power AlGa<sub>N</sub>/Ga<sub>N</sub> transistors [26] and, more recently, ohmic contact formation between Chromium and AlGa<sub>N</sub>/Ga<sub>N</sub> heterostructure via Gr insertion has been reported [168] supposing a carrier transport trough the AlGa<sub>N</sub> promoted by Al-rich Ga<sub>N</sub>-like preferential pathways across the layer. However, an exhaustive description of the mechanisms of current transport at the Gr/AlGa<sub>N</sub>/Ga<sub>N</sub> interface, and the phenomena related to the interaction of Gr and semiconductor 2DEGs have not been addressed to date.

In the next two chapters, the preparation of Gr/AlGa<sub>N</sub>/Ga<sub>N</sub> heterostructures and a detailed electrical characterization of the vertical current transport from Gr to the AlGa<sub>N</sub>/Ga<sub>N</sub> 2DEG will be discussed in order to explain the basic mechanisms through this starting blinding block for future applications.

## 2.4 Graphene field effect tunnelling transistors

Prototypes of field-effect tunnelling transistors formed by two Gr sheets separated by an atomically thin barrier layer (such as hexagonal Boron Nitride (hBN), molybdenum disulfide or tungsten disulfide) have been recently proposed, as illustrated in Figure 2.5 (a) [12,140]. Under the effect of a gate bias applied to the Si back-gate, (i) both Gr sheets carrier concentration increase from the intrinsic starting condition to a doped situation with a shift of the Fermi level, (ii) the barrier height decrease and (iii) the tunnelling DOS increases as already described, moving away the Fermi level from the Dirac point. Any of these conditions can dominate the current transport through the barrier. A schematic representation of the operational principle is illustrated in Figure 2.5 (b) and Figure 2.5 (c), respectively, for an applied  $V_g$  and at zero bias  $V_b$  (when no tunnelling current is reached) and for a finite  $V_b$ . The tunnelling  $I$ - $V$  characteristics for different  $V_g$  are illustrated in Figure 2.5 (d) for a hBN barrier of  $\sim 6$  atomic layers. These device structures demonstrated an efficient current modulation by electric field with a possible  $I_{on}/I_{off}$  ratio  $> 10^4$ .

However, some practical limitations to date imply a much lower  $I_{on}/I_{off}$  ratio than the expected one. In fact, considering an hBN layer of 6 - 7 nm an unrealistically large  $V_g$  is needed to enter the strongly favorable regime where  $E_F$  becomes comparable with the barrier height between Gr layers allowing a large current flow. Conversely, if a thinner hBN barrier is considered the tunnelling current increases at low gate bias weakening the dependence of  $I$  with  $V_g$  while a thicker layer is prone to electrical breakdown rather than a tunnelling.

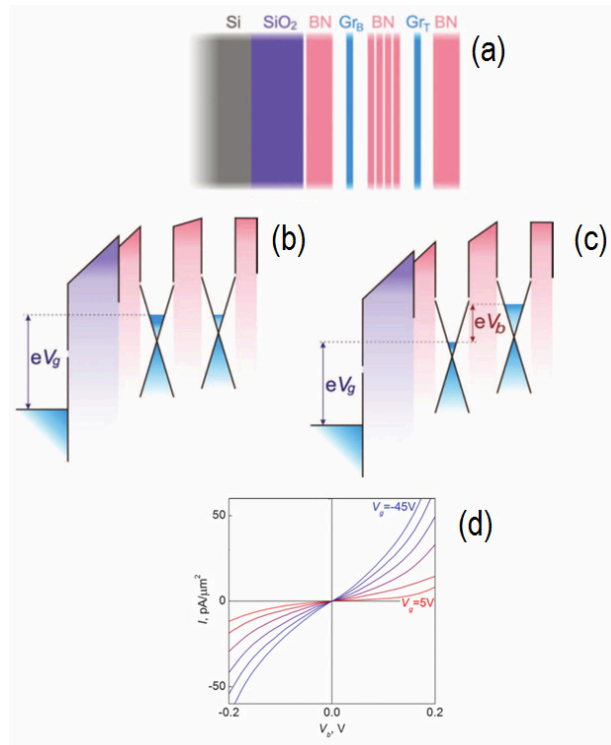


**Figure 2.5:** (a) Schematic structure of Gr field-effect tunnelling transistor. (b-c) Graphic representation of the band structure for the operational principle when a  $V_g$  is applied measuring a zero bias  $V_b$  when no tunnelling current is reached (c) and for a finite  $V_b$ . (d). Tunnelling characteristics through  $\sim 6$  hBN layers measured for different  $V_g$  from 5 V to -45 V [12].

*This*

*Page*

*Intentionally*

*Left*

*Blank*

## Chapter 3: Fabrication of graphene heterostructures with wide-bandgap semiconductors

As previously discussed, one of the main challenges for future applications of Gr is its integration with other advanced materials to fabricate novel devices with improved performances or new functionalities.

In this chapter, we investigated the integration of Gr with WBSs, such as Silicon Carbide (SiC), Gallium Nitride (GaN) and related alloys ( $\text{Al}_x\text{Ga}_{1-x}\text{N}$ ), which currently play a strategic role in the context of high power and high frequency electronics and of highly efficient energy conversion.

The superior performances of such materials compared to silicon are related to some outstanding physical properties, such as the wide-bandgap, the high critical electric field or the saturation velocity, which are particularly relevant in electronics (as reported in Table 3.1).

	Si	SiC (4H)	GaN
Bandgap Energy ( $E_g$ )	1.12 eV	3.26 eV	3.39 eV
Electric breakdown field ( $E_c$ )	0.25 MV/cm	3.0 MV/cm	3.3 MV/cm
Intrinsic electron concentration ( $n_i$ )	$1.5 \times 10^{10} \text{ cm}^{-3}$	$8.2 \times 10^{-9} \text{ cm}^{-3}$	$1.9 \times 10^{-10} \text{ cm}^{-3}$
Thermal conductivity ( $k$ )	1.5 W/cm K	3.3 - 4.5 W/cm K	1.3 W/cm K
Relative permittivity ( $\epsilon_r$ )	11.8	10.1	9.0

**Table 3.1:** physical properties of Si, 4H-SiC and GaN [169].

The wide-bandgap of SiC and GaN determines an electric breakdown field one order of magnitude higher than for Si, which is a property particularly useful within

the high voltage devices. Another consequence of the wide-bandgap is the extremely low intrinsic electron concentration able to grant higher operation temperatures and lower current leakage.

Another relevant property which distinguishes these materials respect to Si is the higher saturation velocity which is a parameter particularly suitable for high current and high frequency applications.

The thermal conductivity is another important parameter for the efficient management of the heat developed by the dissipated power of a device. In this sense, it should be considered that the superior heat dissipation potentiality of SiC and GaN depends, not only by the thermal conductivity value (which is in fact superior only for SiC, as reported in Table 3.1), but also by the higher electric breakdown field, which allows the fabrication of thinner devices compared to Si.

Related to GaN it must be also considered the potentiality to form the already mentioned AlGaN/GaN heterostructures characterized by a 2DEG at the heterointerface between AlGaN and GaN with a high sheet charge density and high carrier mobility (up to  $2000 \text{ cm}^2/\text{V s}$ ).

The preparation methods developed to obtain highly uniform Gr contacts on large sample areas suitable for the fabrication of arrays of microelectronics devices (i.e. from  $\sim 1 \text{ cm}^2$  to wafer scale) are discussed. A highly reproducible, cost-effective, and clean procedure was developed to transfer CVD grown Gr from copper foils to the target substrate. This method was demonstrated to be generally valid, and was adapted to obtain uniform Gr membranes on top of several substrates of interest for micro- and nanoelectronics, as well as for flexible electronics (plastics). In particular, we specifically used this approach to transfer Gr on the surface of AlGaN/GaN heterostructures. Clearly, the structural uniformity of the Gr membrane on top of AlGaN is fundamental to perform a correct evaluation of the current transport properties through the Gr/AlGaN/GaN heterostructure, excluding the influence of damages, imperfections and inhomogeneities of Gr itself.

In the case of Silicon Carbide, Gr contacts were obtained by the controlled graphitization of the Si-terminated (0001) face of the hexagonal polytype (4H-SiC). The structural and morphological properties of both kinds of contacts will be investigated in details by nanoscale resolution microscopy techniques.



### 3.1 Transfer of CVD grown graphene by electrolytic delamination and thermo-compression printing

#### 3.1.1 Description of the transfer procedure

As discussed in the Chapter 1, CVD growth on catalytic metals is, to date, the only viable method to obtain large area Gr membranes [84] that can be transferred to arbitrary substrates. Together with the CVD growth, the optimization of the Gr transfer process is the keystone to obtain a high quality, crack-free and homogeneous Gr membrane [113].

In the following, it is reported a description of the transfer procedure, based on electrolytic delamination and thermo-compression printing, developed during this thesis. The relevant physical parameters involved in each of the two steps are considered and the mechanisms of the delamination of Gr from copper and of its subsequent printing to the target substrate are discussed.

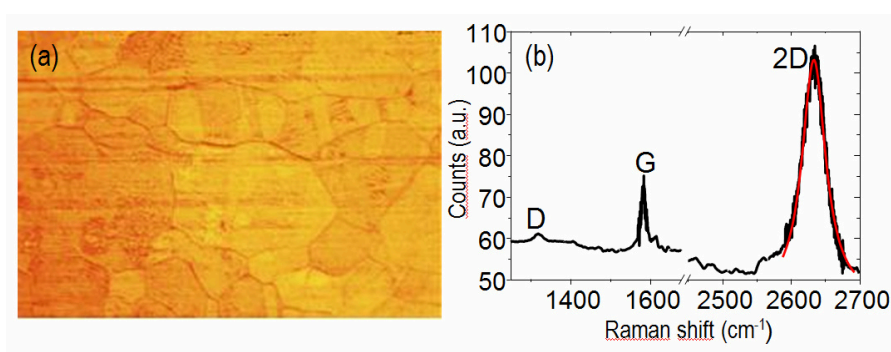


**Figure 3.1:** (a) Optical image and (b) Raman Spectroscopy of the as-grown Gr on Cu.

The starting material was high quality Gr grown by CVD on  $\sim 25 \mu\text{m}$  thick polycrystalline copper foils at a temperature of  $1000^\circ\text{C}$  by using  $\text{CH}_4/\text{H}_2$  as precursors. A typical optical microscopy image and a representative micro-Raman analysis of the as-grown Gr on Cu are reported in Figure 3.1 (a) and (b), respectively. The Raman spectrum reveals the presence of the characteristic peaks of graphitic materials, i.e. the G peak and the 2D peak. The high ratio between the 2D and G peaks intensities, as well as the symmetry of the 2D peak (fitted by a single Lorentzian component with  $\text{FWHM} \approx 38 \text{ cm}^{-1}$ , reported as a red line in Figure 3.1 (b)) demonstrate that a single layer of Gr is observed. Furthermore, the

negligible intensity of the defects related D peak (at  $\sim 1320\text{ cm}^{-1}$ ) indicates a low density of defects in the as-grown material. By Raman spectroscopy mapping over several positions on the copper foil, it was also possible to confirm the homogeneity of single layer Gr coverage on most of the copper surface ( $\sim 95\%$ ), with the exception of a small percentage of double or three layers domains preferentially located at copper grain boundaries.

A morphological image of copper with as grown Gr obtained by tapping mode Atomic Force Microscopy (tAFM) is reported in Figure 3.2 (a). Gr membrane follows the substrate morphology, i.e. the characteristic steps of the copper surface. In addition it is possible to reveal the presence of nanometer high wrinkles which are typical corrugations of the Gr membranes formed during the cooling down step of the CVD growth process and attributed to differences in the thermal expansion coefficients between Gr with respect to copper [170]. The height of wrinkles in the order of  $\sim 1\text{ nm}$  is also reported in the height line profile in Figure 3.2 (b).

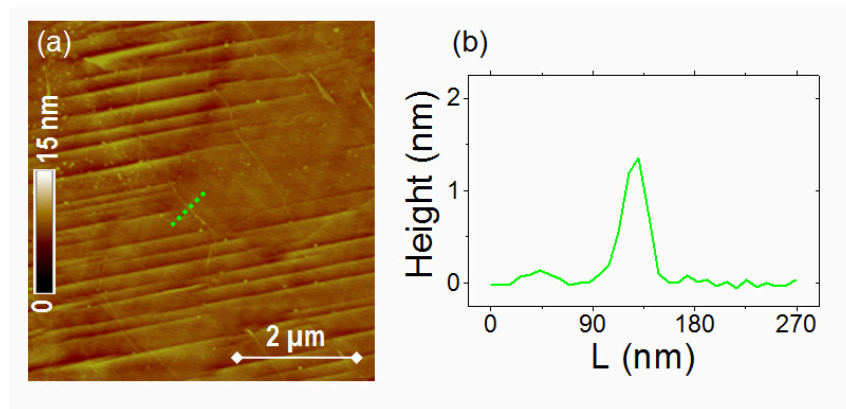


**Figure 3.2:** (a) AFM morphologies of as-grown Gr on Cu. A line scan perpendicular to a wrinkle of Gr on Cu is depicted and the corresponding height profile is reported in (b).

The PMMA was chosen as the polymeric carrier layer for its good adhesion with Gr and for the high mechanical robustness necessary to preserve the integrity of the Gr membrane after its detachment from the metal.

The thermo-compression printing procedure was implemented using the hot embossing NanoImprint Lithography (NIL) equipment by Karl-Suss, inside the CNR-IMM clean room (see Figure 3.3).

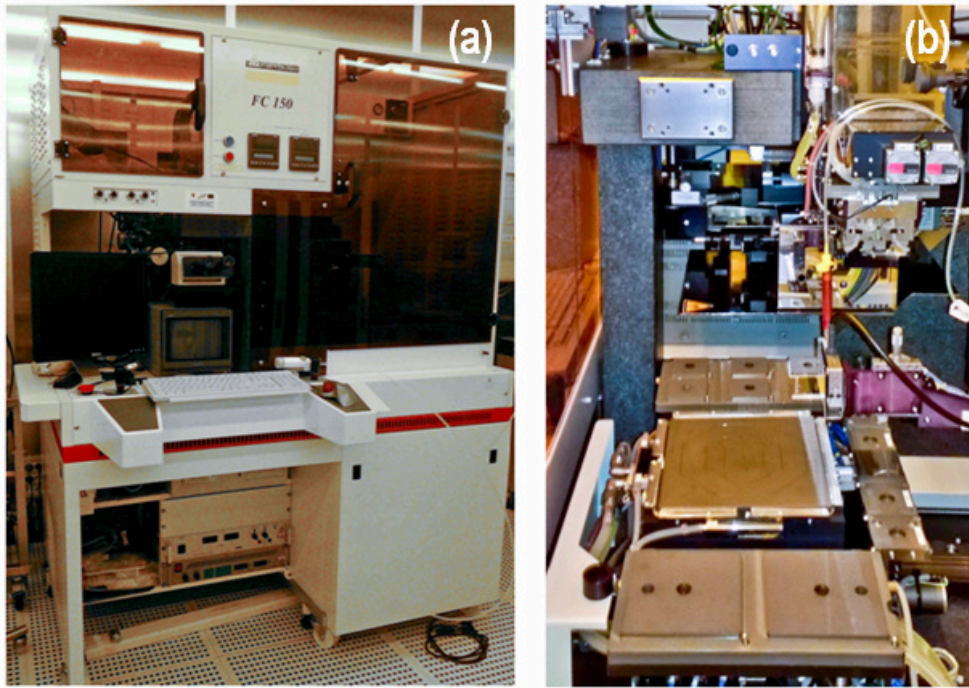


**Figure 3.3:** (a) hot embossing NIL equipment by Karl-Suss. and (b) detail of the thermo-compressive chamber inside, consisted of thermally and mechanically controllable elements i.e. a chuck (below) and an harm (above) .

A NIL equipment basically consists of a chuck and an harm, to which the target substrate and the stamp are fixed, respectively, by vacuum. It allows a very precise optical alignment between the substrate and the stamp, as well as the control of the temperature and pressure ramps applied during the printing of the stamp on the substrate. Clearly, this equipment allows a fully automatic handling of the PMMA/Gr stack and a perfect control on the main parameters involved in the thermo compression printing of this stack on the target substrate. This ultimately ensures a high homogeneity of the transferred Gr and a reproducible quality during several transfer trials.

A crucial requirement for this thermo-compression printing procedure is the planarity of both the stamp and the target substrate in order to impress an equal force over the transferred surface. As a matter of fact, the thin ( $\sim 25 \mu\text{m}$ ) copper foils used in these experiments are inevitably partially folded, since they are typically subjected to manual handling before and after Gr growth. Hence, the

following steps were implemented in the transfer procedure before depositing the PMMA layer.

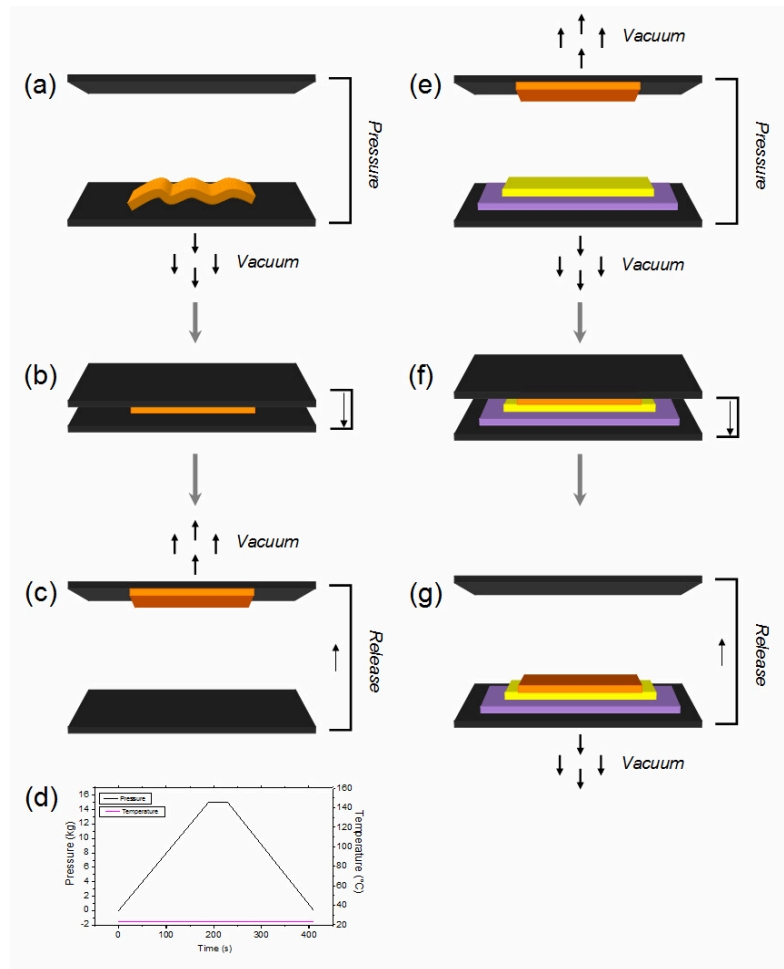


**Figure 3.4:** (a-c) Schematic illustration of the copper planarization obtained pleasuring the wrinkled copper foil (in orange) on the chuck x-y plane (a), pressing it respect to the z axes, by the arm (b) and realizing the arm pressure (c) as described by the pressure ramp in (d). (e-g) Schematic illustration of the copper attachment on a rigid substrate, obtained fishing the copper foil by the arm vacuum aspiration and aligning it above a silicon substrate (in violet) on which a double face TRT is attached (in yellow). The attachment is obtained repeating the pressure ramp in (d).

The copper foil was first planarized using the same NIL equipment. A pressure ramp has been set to press the foil between two perfectly coplanar surfaces: the chuck surface (x-y plane) and a mobile arm (with a controllable force along the z axis) as schematically illustrated in Figure 3.4 (a-c). The pressure ramp has been calibrated to introduce proper rump-up ( $170 \text{ g cm}^{-2} \text{ s}^{-1}$ ), force plateau ( $15 \times 10^3 \text{ g cm}^{-2}$  for 40 s) and rump-down ( $\sim 180 \text{ g cm}^{-2} \text{ s}^{-1}$ ) phases, as illustrated in Figure 3.4 (d), in order to minimize undesired stress or superficial damages due to an excessive or too fast pressure.

The planarized copper foil was attached to a silicon wafer using a double face TRT with a release temperature of  $150^\circ\text{C}$  (purchased by Nitto-Denko). The attachment procedure (fully automatic) is obtained keeping the planarized foil by the arm (sustained by vacuum aspiration), as illustrated in Figure 3.4 (c), aligning it on the silicon substrate placed on the chuck and applying the previously described pressure ramp to print the copper foil on the TRT/silicon stack (Figure 3.4 (e-g)).

After these preliminary steps, a PMMA solution with an average molecular mass of  $950 \text{ kg/mol}$  was spin coated on a planarized  $10 \text{ mm} \times 10 \text{ mm}$  Cu foil at 1000 round/minute and baked at  $150^\circ\text{C}$  to obtain a  $\sim 0.7 \mu\text{m}$  thick film (Figure 3.5 (a)). The polymer is baked at  $150^\circ\text{C}$  directly on the chuck plane (Figure 3.5 (b)) by the temperature ramp reported in Figure 3.5 (e) (magenta). It is worth noticing that the spin coating on a perfectly planar substrate avoids the inhomogeneities and border meniscuses in the polymer film.

The TRT, specifically chosen to release at this temperature, detaches from the back side of the copper foil, i.e. the side not coated by PMMA. Therefore, a single face TRT with a release temperature of  $130^\circ\text{C}$  (appropriately chosen as explained in the following) was attached to the PMMA coated surface. The procedure was similar to the previously described one: the TRT on the arm (Figure 3.5 (b)) was pressed against the PMMA/Gr/Cu stack placed on the chuck (Figure 3.5 (b-d)) using the pressure ramp represented in Figure 3.5 (e), black line. Obviously, this fully automatic procedure makes all the steps highly reproducible, minimizing the inaccuracy and the uncertainty introduced by the operator ability to handle the sample.

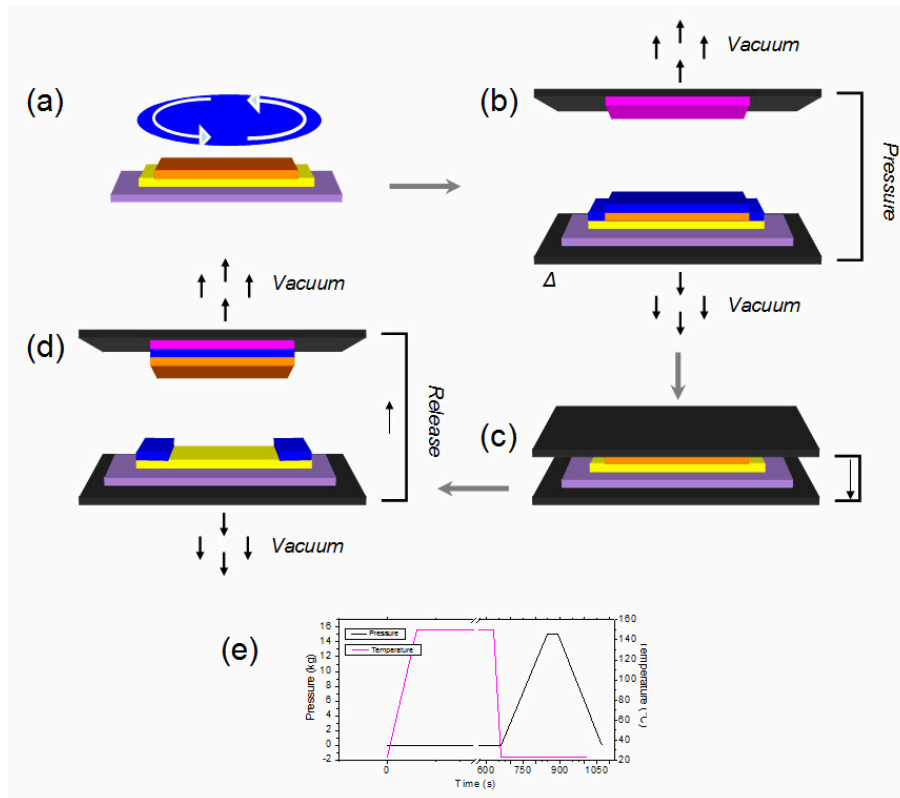


**Figure 3.5:** (a -d) Schematic illustration of the TRT/PMMA/Gr/Cu stack preparation performed by the spin coating of Cu with PMMA (represented in blue) (a), the bake of PMMA and the contemporary release of the double face TRT (in yellow) at 150°C (b) followed by the single face TRT attachment (in magenta) on the PMMA surface, pressing the tape respect to the z axes, by the arm (c). Finally the arm releases the pressure and fishes by vacuum aspiration the final TRT/PMMA/Gr/Cu stack (d). Graphic description of the bake ramp (in magenta) followed by a pressure ramp (in black) respect to the time axis (e).

At the end of this step the sample is ready for the copper detachment.

The TRT/PMMA/Gr stack is separated by the copper foil exploiting an electrolytic delamination procedure [127]. The gentle mechanical delamination by hydrogen bubbles generated at the Gr/metal interface depends on several parameters, including the electrolytic cell geometry, the Gr/metal electrode size, the cell over-voltage, and the electrolyte concentration in the water solution. This offers plenty of room for future optimization of this process, both in terms of Gr

separation speed (a key issue for scalability) and of the final Gr quality (i.e. defectivity).

A description of the microscopic mechanisms of Gr delamination by hydrogen bubbling and a discussion of their relation with the main macroscopic parameters of the electrolytic cell will be provided in the next section.

In this section the complete transfer procedure is described.

The electrolytic cell for the Gr delamination, as schematically illustrated in Figure 3.6, consisted of two vertical, planar, and parallel electrodes at a distance of 10 mm: a gold foil working as the anode (10 mm×10 mm in size) and the TRT/PMMA/Gr/Cu foil working as the cathode. Au was chosen for the anode due to its high corrosion inertness, low electrical resistivity, and electrode-electrolyte activity. Strong alkalis and acids, such as NaOH, KOH, H<sub>2</sub>SO<sub>4</sub>, can be used as electrolytes for water electrolysis reactions. However, considering that Cu can react with many dilute acids in the presence of air, the best choice to completely preserve the Cu foil during the H<sub>2</sub> bubbling process is represented by the use of basis of alkaline metals such as Na or K. In our experiments, water solutions of KOH with different concentrations (from 0.05 M to 0.60 M) were used to establish the role played of this parameter on the delamination rate and on the final Gr quality, as discussed in the next section.

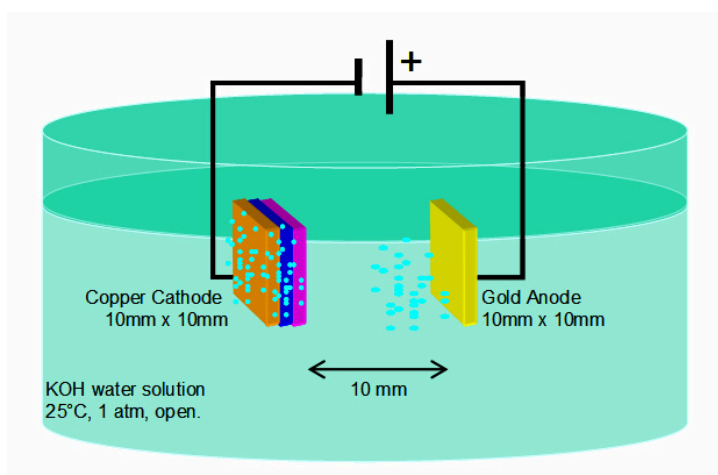
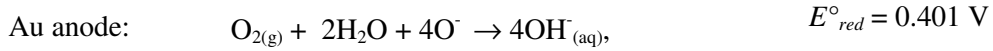
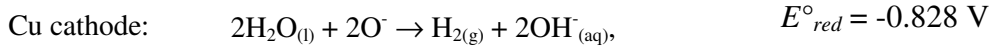
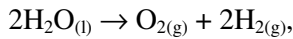


**Figure 3.6:** Schematic representation of the electrolytic cell defined by a Gold foil (in yellow) working as the anode and the TRT/PMMA/Gr/Cu foil (in magenta, blue and orange respectively) working as the cathode, in a KOH solution.

H<sub>2</sub> bubbling at the cathode was obtained applying -5 V bias to this electrode with respect to the grounded anode. This bias value was kept fixed along the entire delamination process up to complete separation of the Gr/PMMA/TRT stack. The standard half-cell potentials ( $E_0$ ) for the two semi-reactions at the Cu cathode and Au anode in a strongly alkaline solution are:



Hence, the complete Red-Ox reaction:



requires a potential  $E^\circ_{red-ox} = -1.229 \text{ V}$  in thermodynamic reversible conditions.

This is the minimum (theoretical) potential required to start H<sub>2</sub> development but additional potential drops must be considered in the cell, such as the electrodes activation over-potentials and the concentration over-potential introduced by the gas evolution at the electrode surfaces, as well as the ohmic series resistance (including the electrolyte resistance) [171]. This justifies the -5 V bias required to start the Red-Ox reaction with an appreciable reaction rate in the whole range of electrolyte concentrations used for this experiment.

The delaminated TRT/PMMA/Gr stack was abundantly washed with deionized water to remove the whole electrolyte crystallized residue. The sample was then dried under nitrogen gas flux.

The Gr surface attached to the PMMA layer was morphologically characterized by AFM in tapping mode, as reported on the representative AFM image of Gr attached to the PMMA after electrolytic delamination using  $C_{\text{KOH}} = 0.60 \text{ M}$  (Figure 3.7 (a)). Consistently with what would be expected, this morphology resembles the complementary to that observed for Gr on copper, i.e., it exhibits steps and wrinkles. The latter can be identified as nanometer deep depressions in the morphology, as shown in the height line profile in Figure 3.7 (b), and required the use of ultra-sharp AFM tips to be measured. In addition to wrinkles, small holes can be observed in this AFM map. Such features, preferentially located at the intersection with wrinkles, can be associated to small cracks of the Gr membrane arising during delamination mechanism, as discussed in the following section.



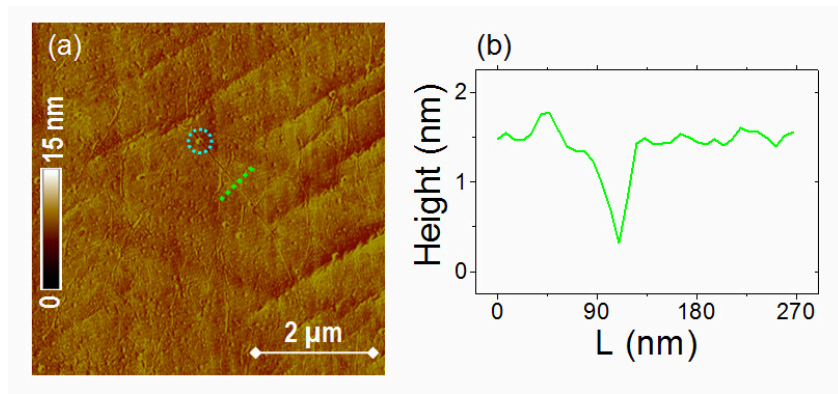


**Figure 3.7:** (a) AFM morphology of Gr after its separation from the metal foil (b), i.e., when it is still attached to the PMMA/TRT stack. A line scan perpendicular to a wrinkle of Gr on PMMA is depicted in (a) and the corresponding height profile is reported in (c). A small crack in the Gr membrane is also indicated in (a) with a circle.

After the delamination from Cu, the TRT/PMMA/Gr stack is ready to be transferred on arbitrary target substrates.

The TRT/PMMA/Gr stack was pressed applying a vertical force onto the substrate, providing at the same time an appropriate heating in order to release the PMMA/Gr stack from the TRT, as illustrated in Figure 3.8 (a-c).

To achieve an optimal quality of the transferred Gr with this thermo-compressive approach, a proper setting of the pressure and temperature ramps applied during the printing need to be found, since the combination of these parameters has an effect on the thermo-mechanical properties of PMMA polymer in contact with Gr.

PMMA is a thermoplastic polymer with a glass transition temperature of  $\sim 105^{\circ}\text{C}$ . Above this temperature the material starts to exhibit a viscous state. [172]. These thermoplastic properties of PMMA are exploited in the thermo-compression printing process of the PMMA/Gr stack on the target substrate. The temperature ramp was chosen in this case to achieve the appropriate viscous behavior of PMMA, in order permit a proper adaptation of the PMMA/Gr stack to the target substrate, independently from the substrate roughness and from the morphology of the Gr attached to the PMMA (Figure 3.7 (a,b)), originating from initial morphology of the Cu foil.

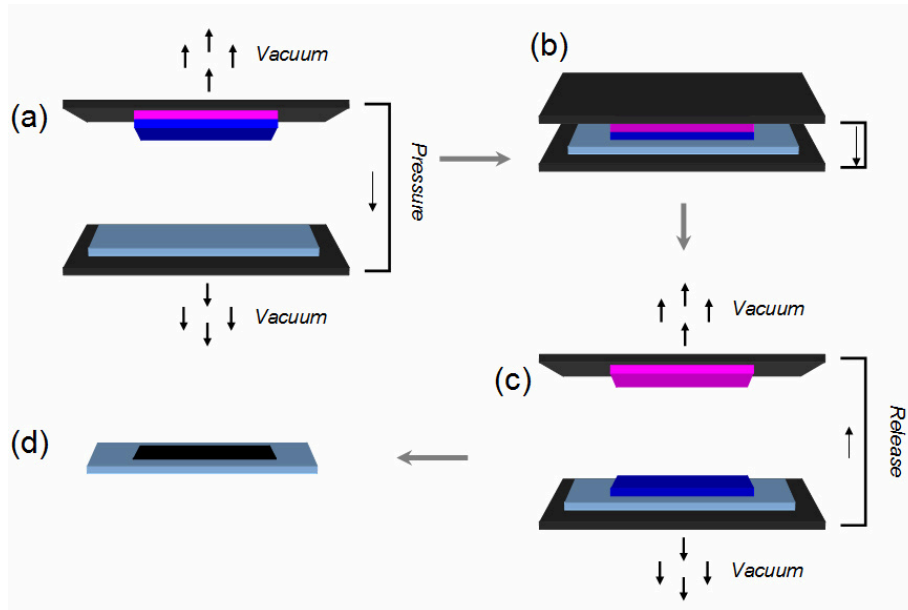


**Figure 3.8:** (a-d) Schematic illustration of thermo-compressive transfer-printing process to transfer the PMMA/Gr stack (in blue) from the TRT (in magenta) (a) to the target substrate (in grey) (d), pressing it respect to the Z axes and heating by the chuck and the arm (b). Chemical elimination of PMMA to obtain a free Gr (in black) on the target substrate (d).

The thermo-compression printing procedure was optimized by Gr transfers on Si wafers capped with 300 nm thick SiO<sub>2</sub>. All the target wafers were cleaned in pure isopropyl alcohol immediately before the transfer process. The advantage of using this substrate is the possibility to have a good optical contrast [54] of the Gr monolayer. This allowed us to make rapid checks by optical microscopy on the macroscopic integrity of Gr transferred on large areas.

The impact of the temperature ( $T$ ) and pressure ( $p$ ) ramps shape on the Gr final quality was investigated. The following parameters of the ramps were considered: the ramp-up and ramp-down, values of the plateau temperature  $T_0$  and pressure  $p_0$  and their duration  $t_{T0}$  and  $t_{p0}$ , the time shift between the two ramps.

An optimal plateau temperature of 130°C, slightly above the  $T_g$  of PMMA, combined to a plateau pressure of  $5 \times 10^3 \text{ g cm}^{-2}$  were finally found. Consequently, the TRT was properly chosen to release at this temperature.

A large matrix of pressure (from  $10^3 \text{ g cm}^{-2}$  to  $30 \times 10^3 \text{ g cm}^{-2}$ ) and temperature (from 100°C to 170°C) values were considered in this set of trials.

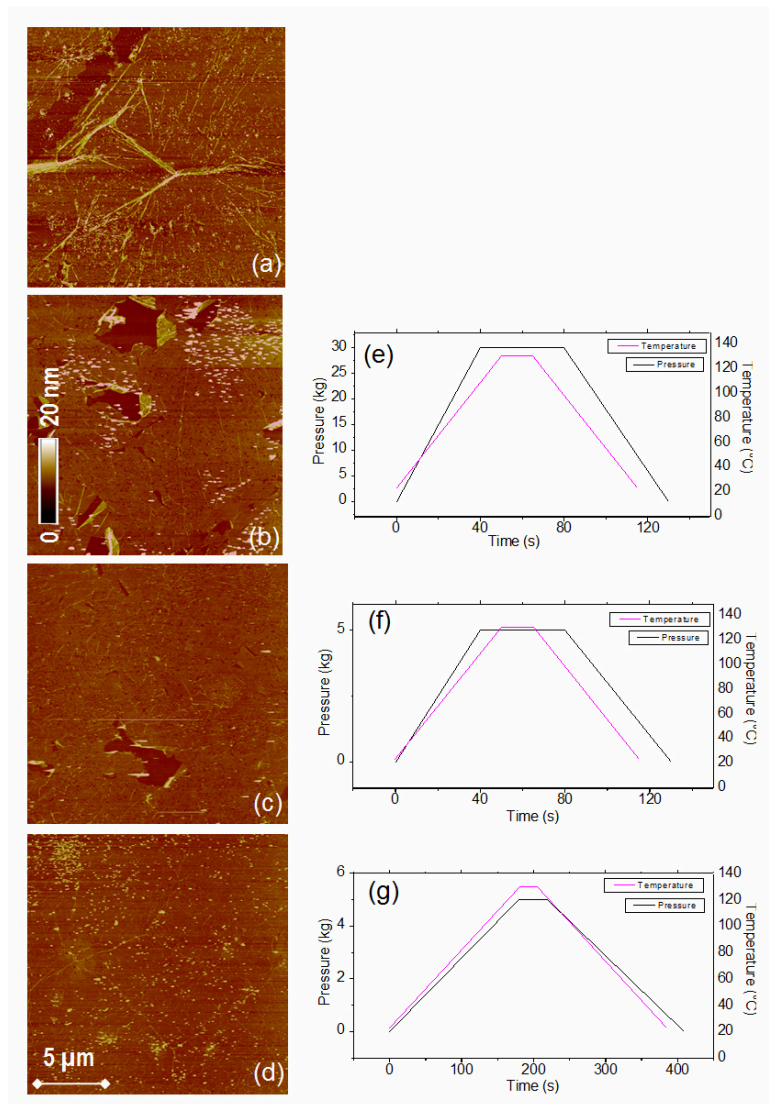


**Figure 3.9:** (a-d) AFM morphologies of Gr transferred on SiO<sub>2</sub> substrates and (e-g) corresponding thermo-compressive ramps exploited for the transferring; (a) Gr transferred by hand, (b) Gr transferred with the high pressure and fast ramp (e), (c) Gr transferred with the optimal pressure and a fast ramp (f), Gr transferred with the final slow thermo-compressive ramp (g).

After the transfer procedure, the PMMA was eliminated with an acetone bath at room temperature and in static conditions, and the transferred Gr was observed by optical microscopy and, subsequently, analyzed by AFM. In most cases the optical

microscopy inspection provided a clear indication on the transferred Gr quality. For low temperatures and pressures the process simply showed no transferred Gr, probably because of an incomplete adhesion of Gr to the target substrate and its consequent elimination together with PMMA during the chemical cleaning with acetone. For the highest pressures and temperatures the transferred Gr showed a macroscopically cracked morphology.

For temperatures around 130°C and for high pressures ( $30 \times 10^3 \text{ g cm}^{-2}$ ) the Gr membrane appeared uniform from a macroscopic optical inspection on the entire  $10 \text{ mm} \times 10 \text{ mm}$  transferred area. However, micrometric and irregular cracks are still observed by higher resolution AFM morphological images. As an example Figure 3.9 (b) shows the typical morphology observed for Gr transferred on  $\text{SiO}_2$  using the temperature and pressure ramps reported in Figure 3.9 (e). Fixing a temperature ramp with a plateau value of 130 °C, different pressure ramps with plateau values starting from  $10^3 \text{ g cm}^{-2}$  were considered. For plateau pressures values  $< 5 \times 10^3 \text{ g cm}^{-2}$ , no Gr was observed after the PMMA elimination.  $5 \times 10^3 \text{ g cm}^{-2}$  was the minimum pressure able to give an effective Gr transfer. With this optimal couple of plateau values ( $T = 130^\circ\text{C}$  and  $p = 5 \times 10^3 \text{ g cm}^{-2}$ ) a high quality Gr morphology with a very low density of micrometric cracks was observed. As an example, Figure 3.9 (c) shows a representative AFM morphology of Gr transferred with the thermo-compressive ramp reported in Figure 3.9 (f).

In addition to the plateau values  $T_0$  and  $p_0$ , also other parameters were demonstrated to have an impact on the Gr final quality, such as the duration  $t_{T_0}$  and  $t_{p_0}$  of the temperature and pressure plateaus, the ramp-up and ramp-down rates and the time delay between the temperature and pressure ramps. In this sense it is important to know that PMMA over the  $T_g$  at which the polymer becomes viscous, the material rheology exhibits viscosity changes with the strain rate. The final stress as well as the relaxation of the elastic component of the PMMA structure can be improved enlarging the period for the thermo-compressive process [173]. In order to obtain a better transferred Gr quality (as reported in Figure 3.9 (d)), longer rump-up, and rump-down were used  $\sim 27 \text{ g cm}^{-2} \text{ s}^{-1}$  and  $\sim 0.6 \text{ C s}^{-1}$  for pressure and temperature variation respectively (quite an order of magnitude lower compared with the initial ramps) as reported in Figure 3.9 (g). It was also useful to introduce a delay between the pressure ramp-down step and the temperature ramp-down step. This adjustment allows a lowering of 10°C of the temperature before the pressure ramp-down step starts. Its importance can be explained considering that

maintaining the applied pressure when the temperature is above the  $T_g$  but lower than the plateau temperature allows a reduced elastic rearrangement of PMMA during the cooling-down step due to the lower viscosity. The transferred Gr is finally optically continuous and free of micrometric and irregular cracks (Figure 3.9 (d)).

The PMMA layer was finally eliminated by a sequence of chemical baths to obtain a polymer-free Gr. As previously reported, the PMMA layer is mostly eliminated in an acetone bath, at room temperature and static conditions, for several minutes. However, a certain density of PMMA residues remain after this cleaning process and quite complex sequence of chemical baths is necessary to further improve the cleanness of Gr surface. Sequences of acetone baths are required at first. In order to remove PMMA without the risk of a peeling effect of PMMA on the underlying Gr, the most of PMMA has to be removed slowly, at room temperature and under static conditions. Subsequently, fresh acetone solutions can be used increasing both the temperature and the mechanical agitation. It has been observed that a sequence of three acetone baths at room temperature,  $\sim 40^\circ\text{C}$  and  $\sim 60^\circ\text{C}$ , with growing mechanical agitation, are enough to reduce the PMMA residues at few sub-micrometric drops per  $\mu\text{m}^2$ . For a further improvement in the cleaning several other chemical baths were evaluated such as, isopropyl alcohol, acetic acid at different dilutions and isopropanolamine solution. Isopropanolamine resulted as the best solution to enhance the cleanness without any evident additive damages on the Gr morphology.

Gr was characterized at different positions on its final substrate by micro-Raman spectroscopy. The set of spectra shown in Figure 3.10 (a) were collected on 5 positions along a straight line with a distance of  $\sim 100 \mu\text{m}$  each other, as reported by the correspondent optical image in Figure 3.10 (c). The low intensity of the D peak means that the density of defects is negligible, similarly to what observed for as grown Gr on copper (Figure 3.1 (b)), indicating that this optimized transfer procedure does not significantly degrade Gr properties. Furthermore, the reproducibility of the Raman spectra measured at different surface positions confirms the high homogeneity of the Gr surface.

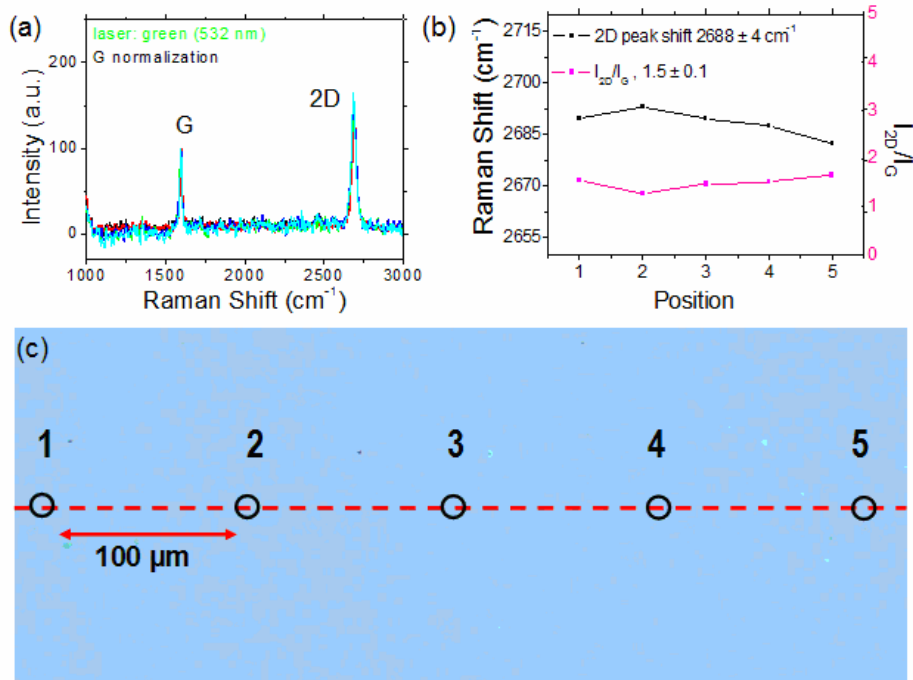


**Figure 3.10:** (a) Set of Raman spectra collected on different positions of the Gr transferred on a  $\text{SiO}_2$  substrate, (b) plot of 2D shift and of  $I_{2D}/I_G$  for the set of the collected positions and (c) optical image of the sampled positions.

### 3.1.2 Study of the electrolytic delamination kinetic

As described in the previous sections, Gr was delaminated from copper exploiting an electrolytic delamination process, which involves the mechanical action of the  $\text{H}_2$  bubbles generated at the interface between Cu and Gr configured as the cathode of water electrolysis. This method offers plenty of room for optimization of the final Gr quality acting on several control parameters. In the following, the role of the concentration of a strong electrolyte (KOH) water solution on the delamination rate and on the Gr final morphology was investigated fixing all the other cell parameters. In particular, cubic cell with 10 mm edges is constituted by two vertical planar and parallel electrodes of  $10 \text{ mm} \times 10 \text{ mm}$ , an Au anode and the TRT/PMMA/Gr/Cu cathode with a distance of 10 mm. The system is maintained at room temperature and in stationary conditions and applying a voltage of -5 V kept constant during the whole delamination [27].

The evolution of the TRT/PMMA/Gr stack delamination from the Cu cathode was accurately monitored for all the different  $C_{KOH}$  concentrations.  $H_2$  bubbling and, consequently, delamination typically starts from the Cu foil perimeter and gradually advances toward the sample centre. The time  $t_d$  required to obtain the complete delamination of  $1\text{ cm}^2$  Gr membrane is reported in Table 3.2 as a function  $C_{KOH}$ , showing a factor of 10 decrease of  $t_d$  (from  $\sim 307\text{ s}$  to  $\sim 26\text{ s}$ ) with increasing  $C_{KOH}$  from  $\sim 0.05\text{ M}$  to  $\sim 0.60\text{ M}$ .

$C_{KOH}$ (M)	0,05	0,15	0,25	0,30	0,60
$t_d$ (s)	$307 \pm 26$	$112 \pm 22$	$50 \pm 12$	$37 \pm 11$	$26 \pm 8$

**Table 3.2:** Time ( $t_d$ ) required to obtain the complete delamination of Gr from  $1\text{ cm}^2$  copper foil reported as a function  $C_{KOH}$ .

The errors represent the standard deviations in the  $t_d$  measured during several delamination experiments on Cu cathodes with the same geometry. The observed inverse dependence of  $t_d$  on the electrolyte concentration is in agreement with the trend reported by other authors [128]. In the following, a quantitative description of this behavior will be provided, using a microscopic model of the heterogeneous nucleation and growth of  $H_2$  bubbles supported by an accurate morphological analysis of Gr transferred to  $SiO_2$ .

A statistical investigation of the size and density of the characteristic morphological features on the Gr surfaces, in particular of wrinkles, was performed on several AFM images at different magnifications for samples obtained using different KOH concentrations. Figure 3.11 (a-c) show three representative surface morphology images of Gr delaminated at  $C_{KOH}$  of 0.05 M, 0.30 M, and 0.60 M, respectively, and transferred to  $SiO_2/Si$  substrates. Similar and quite homogeneous distributions of wrinkles over the entire surfaces are observed in all the cases. The presence of small cracks with 20 - 50 nm size is observed for the highest electrolyte concentration, i.e., for the highest delamination rate, suggesting that the formation of these defects can be related to the bubbling process. Interestingly, these cracks are preferentially located at the intersection of wrinkles, consistently with the model of Gr delamination discussed in the following. It is worth noting that the density of these cracks is low, and it does not significantly affect the average electrical properties (mobility and sheet resistance) of the Gr membranes. The histograms of wrinkle heights obtained from AFM analyses are reported in Figure 3.11 (d-f) for  $C_{KOH}$  of 0.05 M, 0.30 M, and 0.60 M respectively. A shift of

these distributions to larger height values can be noticed as the electrolyte concentration increases. In particular, the average heights shift from  $\sim 1.35$  nm for  $C_{KOH} = 0.05$  M, to  $\sim 2.11$  nm for  $C_{KOH} = 0.60$  M. The histograms of the distances between neighbor wrinkles are also reported in Figure 3.11 (g-i).

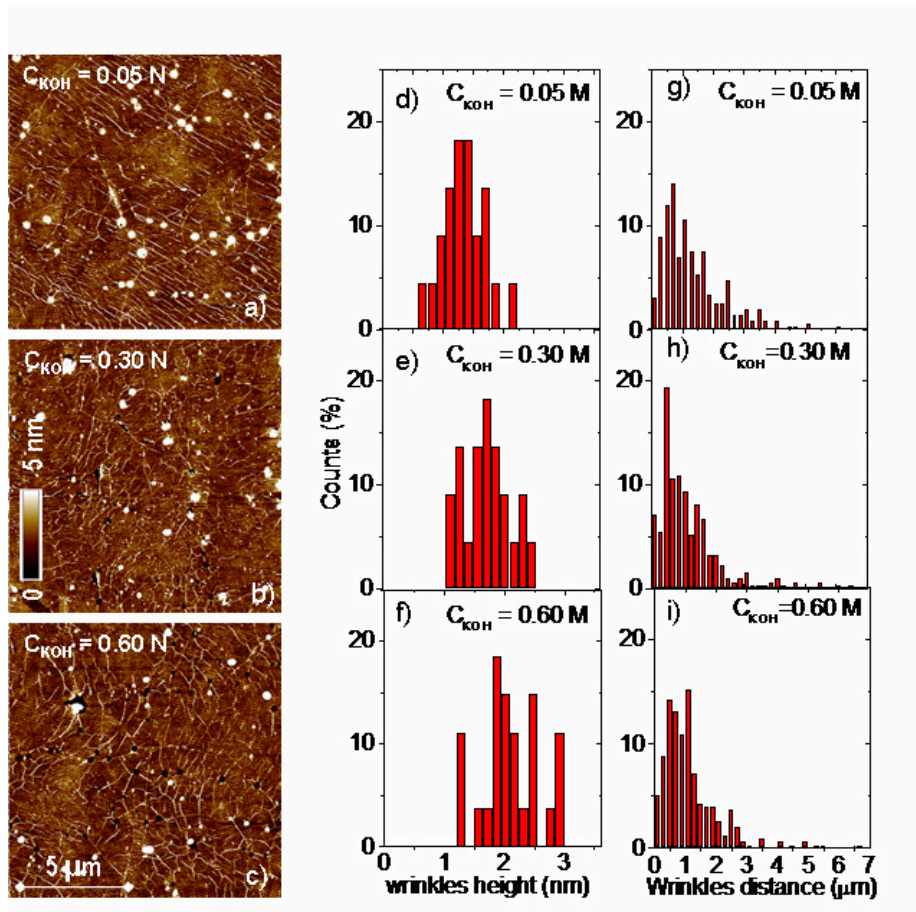


**Figure 3.11:** AFM morphology of Gr membranes transferred on  $\text{SiO}_2/\text{Si}$  substrates after electrolytic delamination with three different KOH concentrations: 0.05 M (a), 0.15 M (b), 0.60M (c). Histograms of wrinkles height (d), (e), (f), and distances (j), (k), (l) for the three samples.

An average wrinkles distance of  $\sim 1.3 \mu\text{m}$  is found for all the samples independently on the electrolyte concentration. Furthermore, the total length of wrinkle lines was measured from AFM images on several samples regions. The



resulting wrinkles length per unit area has approximately same average value ( $\sim 0.49 \mu\text{m}^{-1}$ ) independently on the electrolyte concentration. These latter experimental evidences indicate that the delamination and the following transfer procedure do not produce significant variations in the wrinkles density and spatial distribution with respect to those in the as-grown Gr on Cu. On the other hand, a systematic increase of the average wrinkles height as a function of the electrolyte concentration (i.e. of the  $\text{H}_2$  development rate) has been observed, suggesting that these corrugations of Gr play a role in the mechanisms of electrolytic delamination. To analyze deeply this correlation, the formation mechanisms of  $\text{H}_2$  bubbles during electrolysis have to be considered.  $\text{H}_2$  development at the cathode produces a gas supersaturation ( $S$ ) of the solution in the proximity of the electrode surface, with  $S$  defined as the ratio between the  $\text{H}_2$  gas concentration and its maximum solubility in water at the temperature  $T$ . According to the classical nucleation theory, an energy barrier  $\Delta G_c = 4\pi\gamma r_c^2/3$  is associated to the nucleation of a  $\text{H}_2$  bubble with a critical radius  $r_c = -2\gamma/\Delta G_v$  in a supersaturated gas solution;  $\Delta G_v$  is the free energy change per unit volume associated to the transfer of  $\text{H}_2$  from the solution to the gas phase, and  $\gamma$  is the liquid-gas interfacial free energy of the forming bubble [174]. According to the Gibbs-Thomson relation,  $\Delta G_v$  can be related to the gas supersaturation  $S$  as  $\Delta G_v = k_B T \ln(S)/v$ , being  $k_B$  the Boltzmann constant and  $v$  the volume of a  $\text{H}_2$  molecule. The rate of  $\text{H}_2$  bubbles nucleation can be expressed as an Arrhenius law, i.e.  $J \propto \exp(-\Delta G_c/k_B T) = \exp[-16\pi\gamma^3 v^2/(3k_B^3 T^3 \ln(S)^2)]$ . At a fixed temperature of the solution,  $J$  strongly decreases with  $\gamma$ , whereas it increases more weakly with  $S$ . This makes the homogeneous nucleation of bubbles in the bulk of the liquid an extremely unfavorable process, since it would require very high supersaturation values. Instead, in most of the cases, the heterogeneous nucleation at the electrode surface preferentially occurs. In fact, the liquid-gas interface free-energy  $\gamma$  of a bubble with the shape of a spherical cap nucleating at the liquid-solid interface is lowered by a geometrical factor dependent on the contact angle between the bubble and the solid surface. In particular, micrometer or nanometer size cavities in the electrode surface are preferential nucleation sites for the bubbles due to the ability to trap and stabilize even nanometric bubbles with subcritical radius ( $r \ll r_c$ ) present in the solution [174]. The heterogeneous nucleation at these sites strongly reduces the supersaturation  $S$  required for bubbles formation. Among all the bubbles nucleating at the perimeter of the Cu cathode only those nucleating at Cu/Gr interface can be effective to promote Gr

delamination. Under this point of view, the wrinkles crossing the Cu foil perimeter form nanometer sized cavities where Gr is locally separated from Cu, and certainly act as preferential nucleation sites for bubbles. The different stages of the delamination process are schematically illustrated in Figure 3.12 (a), from panel (i) to panel (iv). Once a bubble has nucleated inside a wrinkle (Figure 3.12 (a), panel (i)), it starts to grow due to the diffusion of  $H_2$  developed in the neighbor electrode regions in contact with the solution. According to the Young-Laplace equation, the gas pressure inside a bubble of radius  $r$  is  $p_g = p_l + 2\gamma/r$ , where  $p_l$  is the external pressure of the liquid ( $p_l \approx 1.01$  atm) and  $\gamma \approx 72.8 \times 10^{-3}$  N/m. Clearly, in the initial stages of nucleation and growth, the internal gas pressure is very high, due to the limited radius of the bubble, corresponding to the wrinkle size.

Since the average wrinkle height estimated for the lowest  $C_{KOH}$  was  $\sim 1.33$  nm, we can argue that in the initial stages of growth  $p_g > 1 \times 10^8$  N/m<sup>2</sup>. A deformation of wrinkles can be therefore expected in this initial phase (as schematically illustrated in Figure 3.12 (a), panel (ii)). AFM analyses indicate that such deformations increase with  $C_{KOH}$ , probably due to a higher  $H_2$  development rate. In some points of the Gr membrane, preferentially located at the junction between two or three wrinkles, this high pressure can cause small cracks. During further bubble growth, a delamination of the TRT/PMMA/Gr stack from copper starts (see Figure 3.12 (a), panel (iii)), and the full delamination from the perimeter is reached when neighbor growing bubbles merge each other (see Figure 3.12 (a), panel (iv)). Bubble growth is due to the diffusion of  $H_2$  molecules from the solution to the gas phase, with the driving force represented by the difference in  $H_2$  concentration between the bubble surface ( $C_s$ ) and the bulk of supersaturated solution (with concentration  $C_b = SC_s$ ).  $C_s$  represents the equilibrium concentration of  $H_2$  in water in contact with the bubble and, assuming that the partial pressure of water is negligible compared with the partial pressure of  $H_2$  inside the bubble, it is related to the internal pressure  $p_g$  of the bubble by the Henry law, i.e.  $p_g = HC_s$ , where  $H = 1281.2$  liters $\times$ atm/moles is the Henry constant for  $H_2$  dissolved in water at  $T = 298$  K. The rate of  $H_2$  molecules diffusion from the supersaturated solution to the bubble surface can be expressed as [174,175]:

$$\frac{dn}{dt} = \frac{AD}{z}(C_b - C_s) = \frac{ADH}{zp_g}(S - 1) \quad (3.1)$$

Where  $A$  is the area of the liquid-gas interface,  $D = 45 \times 10^{-6} \text{ cm}^2/\text{s}$  is the diffusivity of  $\text{H}_2$  in the solution and  $z$  is the thickness of the “boundary layer” that separates the bulk of the supersaturated solution from the bubble surface [174]. The number of gas moles in Equation (3.1) can be related to the bubble volume  $V$  and to the gas pressure  $p_g$  using the ideal gas equation,  $p_g V = nRT$ , where  $R$  is the gas constant. Expressing  $A$  and  $V$  as  $A = f_1 r^2$  and  $V = f_2 r^3$ , with  $f_1$  and  $f_2$  geometrical factors discussed in the following, the rate of growth of the bubble radius  $dr/dt$  can be written as:

$$\frac{dr}{dt} \approx \frac{f_1 D R T}{3 f_2 z H} (S - 1) \quad (3.2)$$

By integrating Equation (3.2) with respect to the time from  $t = 0$  up to  $t_{max}$  (when two neighbour bubbles merge each other), and expressing the boundary layer thickness as  $z = (D t_{max})^{1/2}$ , the following relation between  $t_{max}$ , the maximum bubble radius  $r_{max}$  and  $S$  is obtained:

$$t_{max} = \frac{9 H^2 f_2^2 (r_{max} - r_0)^2}{f_1^2 D R^2 T^2 (S - 1)^2}. \quad (3.3)$$

In Figure 3.12 (b) a schematic side view of the Gr/PMMA/TRT membrane partially detached from Cu is reported. Due to the partially rigid character of the Cu and Gr/PMMA/TRT membranes, the geometry of the bubble has been described subtracting from a spherical cavity with curvature radius  $r_{max}$  two hemispherical caps with basal areas  $A_1$  and  $A_2$  (with slopes  $\alpha$  and  $\beta$ ) corresponding to the gas-solid interfaces with Cu and Gr, respectively. The angles  $\theta$  and  $\eta$  are the contact angles of the liquid-solid-gas interfaces with the Cu and Gr surfaces, respectively. The surface and volume geometrical factors  $f_1$  and  $f_2$  depend on those angles as  $f_1 = 2\pi(\cos \theta + \cos \eta)$  and  $f_2 = \pi(3\cos \theta + 3\cos \eta - \cos^3 \theta + \cos^3 \eta)/3$ . The delamination of Gr from Cu is the result of the balance between the Gr/Cu adhesion force and the vertical component of the force due to the internal pressure  $p_g$ . From the bubble geometry represented in Figure 3.12 (b), the vertical component of the detachment force is  $F_d \approx p_g (A_1 \cos \alpha + A_2 \cos \beta)$ , whereas the adhesion force is  $F_{adh} = E_{adh} \pi r_{max} \cos \theta / \sin \alpha$ , with  $E_{adh} = 4.1 \text{ J/m}^2$  the Gr/Cu bond energy [144].

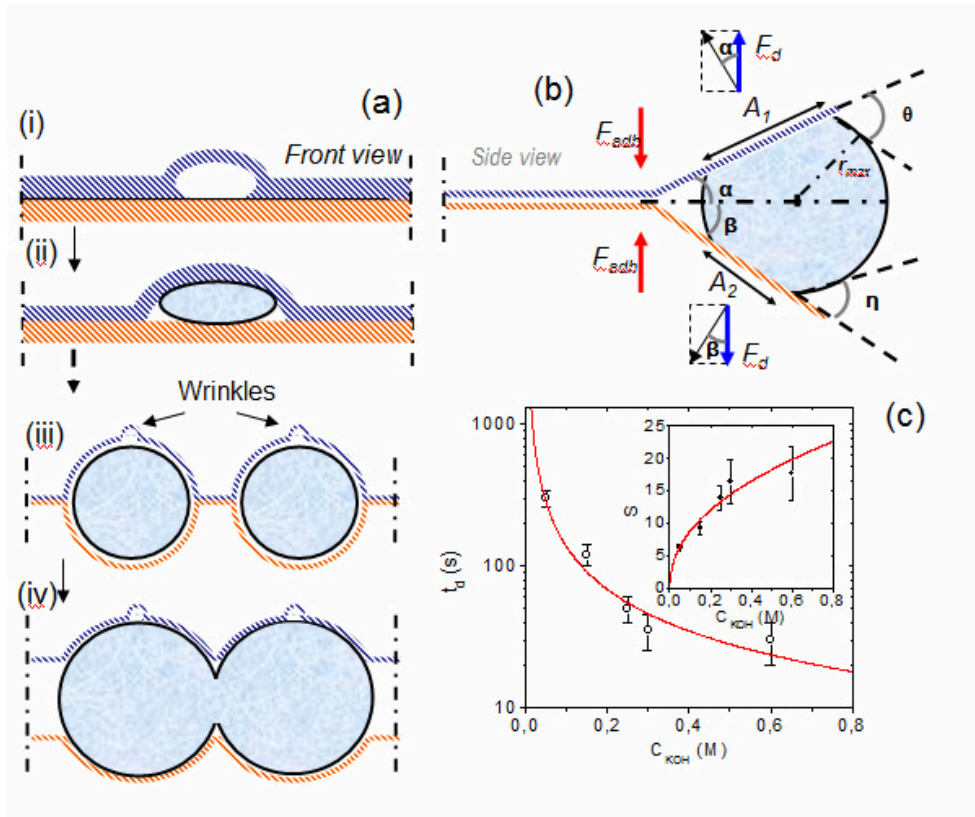


**Figure 3.12:** (a) Schematic representation (front view) of H<sub>2</sub> bubbles nucleation and growth at Cu perimeter: Gr wrinkle at the Cu foil perimeter (i); bubble nucleation and growth, with the deformation of the wrinkle cavity (ii); detachment of Gr from Cu (iii); coalescence of two expanding neighboring cavities (iv). (b) Schematic representation (side view) of the cavity at its maximum expansion and representation of the forces involved in the Gr delamination. (c) Measured time  $t_d$  for Gr delamination from 1 cm<sup>2</sup> Cu foil as a function of the electrolyte concentration ( $C_{KOH}$ ) and fit with the discussed microscopic model. In the inset, the dependence of H<sub>2</sub> supersaturation in the solution is reported versus  $C_{KOH}$  and fitted with the expression  $S = aC_{KOH}^b$ .

Merging of bubbles along the Cu foil perimeter occurs when  $2r_{max} = d_w$ , being  $d_w$  the average wrinkles separation as deduced by AFM analysis. After delamination of a perimeter line of width  $r_{max}$ , the process continues with the detachment of other perimeter lines up to complete detachment of Gr from Cu. The total time  $t_d$  required for complete Gr delamination from a square metal foil with side length  $L$  can be expressed as  $t_d = 2Lt_{max}/d_w$ , i.e.:

$$t_d = \frac{L}{2d_w D} \left[ \frac{3Hf_2(d_w - 2r_0)}{f_1 RT(S-1)} \right]^2 \quad (3.4)$$

In Figure 3.12 (c), the experimental values of the Gr delamination time (open circles) from 1 cm<sup>2</sup> Cu foil are reported on a logarithmic scale as a function of the electrolyte concentration. It can be noticed that in this plot the  $t_d$  values measured for lower KOH concentrations, i.e., from 0.05 M to 0.3 M, approximately follow a straight line, whereas the value at  $C_{KOH} = 0.6$  M deviates from this trend. This means that for high electrolyte concentrations the delamination rate  $v_d \sim 1/t_d$  approaches to a saturation value. As previously discussed, a key parameter for hydrogen bubbles formation is the supersaturation  $S$  of the H<sub>2</sub> gas in water. From Equation (3.4) and using the measured  $t_d$  values, the values of H<sub>2</sub> supersaturation  $S$  produced by the different electrolyte concentrations have been obtained and reported in the inset of Figure 3.12 (c).  $S$  ranges from ~5 for the lowest KOH concentration to ~18 for the highest one. The dependence of  $S$  on  $C_{KOH}$  for the entire range of concentrations has been fitted using the following expression,  $S = aC_{KOH}^b$ , with  $a = (24.9.6 \pm 2.0) M^{-b}$ ,  $b = 0.45 \pm 0.10$  the resulting fitting parameters. According to the first Faraday's law of electrolysis, the H<sub>2</sub> mass developed per unit time at the cathode is proportional to current flowing in the cell. The latter depends on the specific conductivity of the solution, which is proportional to concentration of the ionic species (corresponding to the electrolyte concentration in a water solution of a strong electrolyte) and to their mobility  $\mu$ . The obtained behavior of  $S$  as  $S \sim C_{KOH}^b$ , with  $b \approx 1/2$ , indicates that  $\mu$  decreases with the KOH concentration as  $\mu \sim C_{KOH}^{-1/2}$ .

This means that some mechanisms lowering the ionic mobility take place at increasing electrolyte concentrations, such as the cataphoretic effects occurring under DC bias conditions [176].

Such mechanisms ultimately limit the maximum delamination rate of Gr from Cu by H<sub>2</sub> bubbling. Inserting this functional dependence of  $S$  on  $C_{KOH}$  in Equation (3.4), an expression of the time to delamination *vs.*  $C_{KOH}$  was obtained and has been reported in Figure 3.12 (c) along with the experimental data.

### 3.1.3 Graphene transferred on AlGaN/GaN substrates

Two different kinds of  $\text{Al}_{0.25}\text{Ga}_{0.75}\text{N}/\text{GaN}$  heterostructures, both grown on Si(111) by Metal Organic Chemical Vapor Deposition (MOCVD), were intentionally adopted for the Gr transfer: a substrate with a highly homogeneous AlGaN layer (from now on indicated as sample A) and a sample with a highly defective AlGaN layer (from now on reported as sample B).

The quality of the two AlGaN layers, judged in terms of surface morphology, AlGaN thickness, and defect density, was established by tapping mode AFM and Transmission Electron Microscopy (TEM).

Two representative AFM images of the bare AlGaN surfaces of sample A and sample B are reported in Figure 3.13 (a,b), respectively. Sample A exhibits an uniform and defect-free surface and a low roughness (RMS = 0.85 nm). The corresponding cross section TEM analysis (Figure 3.13 (c)) shows a homogeneous AlGaN layer with a thickness of ~24 nm.

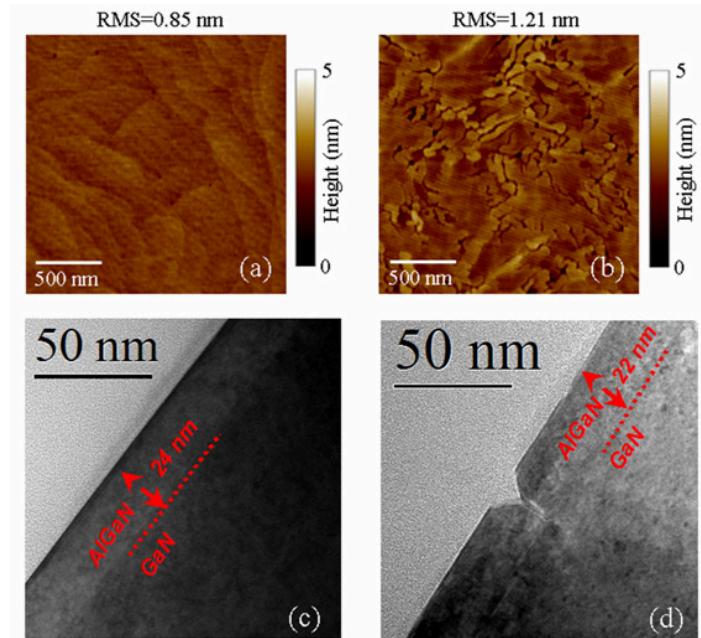


**Figure 3.13:** Representative tAFM analyses of the bare AlGaN surface of samples A (a) and B (b). Cross-sectional TEM images of the same samples are shown in (c) and (d).

Conversely, the AFM morphology of sample B (Figure 3.13 (b)) shows the presence of a high density of characteristic elongated and isotropically oriented depressions in the AlGa<sub>N</sub> surface, which are responsible of the higher measured roughness value (RMS = 1.21 nm). Such morphological features are clearly recognizable also in the corresponding cross sectional TEM in Figure 3.13 (d) as V-shaped defects in the AlGa<sub>N</sub> barrier layer. These defects, often observed in nitrides heterostructures [177, 178, 179, 180, 181, 182, 183, 184], causes a local reduction of the AlGa<sub>N</sub> layer thickness in sample B from ~ 22 nm to ~ 10-12 nm at the bottom of the V-shaped valleys.

Two typical AFM images of Gr transferred to the AlGa<sub>N</sub> surfaces of the sample A and sample B are reported in Figure 3.14 (a) and (b), respectively. In both cases, a very uniform Gr coverage with a low level of cracks can be observed. The higher roughness compared with the corresponding bare AlGa<sub>N</sub> samples (RMS = 1.50 nm for Gr on sample A and RMS = 2.10 nm for Gr on sample B) is due to the wrinkles present in as-grown Gr on Cu.

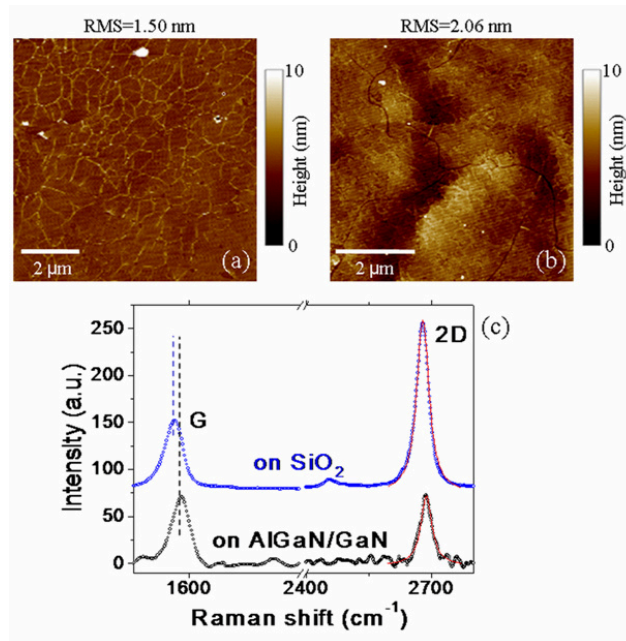


**Figure 3.14:** Two typical tAFM images of Gr transferred to the AlGa<sub>N</sub> surface of the samples A (a) and B (b). Representative Raman spectra of Gr on AlGa<sub>N</sub> and SiO<sub>2</sub> (c).

Micro-Raman spectroscopy was employed to characterize the Gr membranes transferred to the AlGaIn samples. No significant difference was found between the Raman spectra of Gr on samples A and B. A comparison between two representative Gr spectra collected on AlGaIn and SiO<sub>2</sub> is also reported in Figure 3.14 (c). The Raman signal intensities have been normalized to have the same G peak height and the two spectra have been vertically offset for a better readability. The higher background noise of the Gr spectrum on AlGaIn is due to a worse signal to noise ratio than in the case of Gr on SiO<sub>2</sub>. Noteworthy, a significant blue shift of the G peak position (from ~1587 to ~1593 cm<sup>-1</sup>) and a reduction of the ratio between the 2D and G peaks intensities can be observed for Gr on AlGaIn with respect to Gr on SiO<sub>2</sub>. Both these observations are consistent with a higher doping level of Gr residing on AlGaIn [185]. Gr on SiO<sub>2</sub> is known to be typically p-type doped, in the order of ~ 10<sup>12</sup> cm<sup>-2</sup>, under ambient conditions due to the effect of water or residual polymer contamination from the transfer process [186]. The electrical characterization of Gr on AlGaIn (reported in the next *Chapter 3*) shows that it is, instead, highly n-type doped (~1.3×10<sup>13</sup> cm<sup>-2</sup>), and it is in accordance with variation on the AlGaIn Raman spectra listed above.



### 3.2 Epitaxial Graphene on SiC (0001): role of the miscut angle

As discussed in Chapter 1, the growth of Gr by controlled graphitization of hexagonal SiC depends on several parameters, such as the substrate temperature, the gas partial pressure in the furnace, the SiC orientation (Si face or C face) as well as the wafer miscut angle  $\theta$ . This latter is the angle formed by the SiC ingot growth axis [0001] and the vector orthogonal to the plane of cutting of the wafer (see schematic representation in Figure 3. 15). Wafers cut with an angle  $\theta \approx 0^\circ$  (typically  $\theta < 0.1^\circ$ ) are named “nominally on-axis”, whereas those cut with angle  $\theta > 0^\circ$  (typically  $4^\circ$  or  $8^\circ$ ) are named “off-axis”. The two typical directions of cut for SiC wafers are [11-20] and [1-100] directions, with the [11-20] the most commonly employed miscut direction.

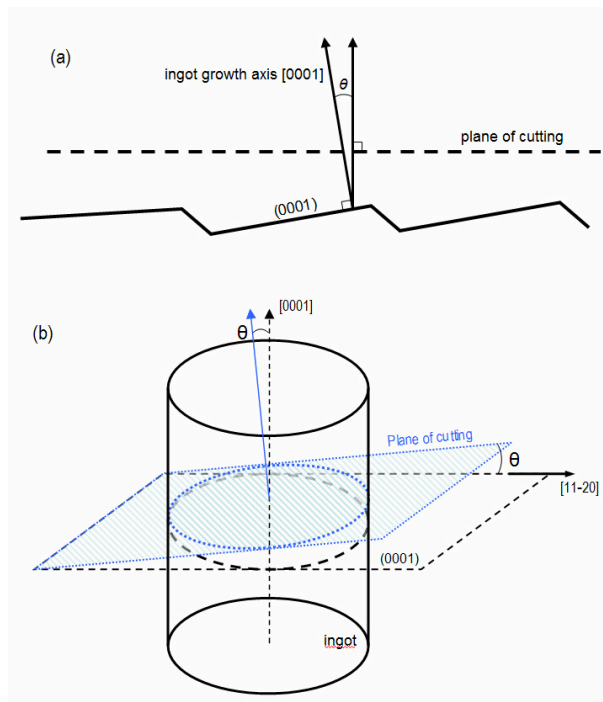


**Figure 3. 15:** (a) schematic representation of the miscut angle  $\theta$  formed by the SiC ingot growth axis [0001] and the vector orthogonal to the plane of cutting of the wafer. (b) 3D projection of the SiC ingot grown in the [0001] direction intersected by the plane of cutting (blue plane) with a miscut angle  $\theta$ .

Due to the miscut, SiC wafers typically exhibit a morphology consisting of parallel atomic steps and terraces. Clearly, the step density increases and the average terrace width decreases with increasing the miscut angle.

Miscut angles of  $\sim 4^\circ$  or  $\sim 8^\circ$  are typically used for the SiC substrates employed for power electronics, since optimal CVD growth of lowly doped SiC epilayers can be performed under these conditions.

The wafer miscut angle plays an important role also in the Gr growth process, since the kinks of SiC terraces are nucleation sites for Gr. As a consequence of this, for fixed annealing conditions, a higher growth rate is observed on off-axis SiC (0001) surfaces than on nominally on-axis ones, due to the reduced spacing between the terrace kinks. Clearly, single layer Gr coverage on a large SiC surface fraction can be easily achieved on on-axis substrates, whereas a few layers or multilayers of Gr are typically obtained on off-axis substrates under similar growth conditions. For this reason, most of the literature studies on Gr growth on SiC have been carried out on on-axis semi-insulating substrates, where the high resistivity of the substrate is necessary to probe current transport within Gr.

However, since the standard platform of current SiC technology for power electronics is mainly based on  $4^\circ$  or  $8^\circ$  off-axis 4H-SiC (0001) wafers with lowly doped epilayers [187], a detailed investigation of the growth of few layers of Gr on both on-axis and off-axis substrates is highly desirable, in the perspective of integrating future Gr electronics with SiC technology.

As an example, a study of Gr growth on  $8^\circ$  off-axis 4H-SiC(0001) is reported in the following.

Gr growth was performed in inert gas (Ar) ambient at atmospheric pressure (900 mbar) on 4H-SiC (0001) wafers with a lowly doped ( $\sim 10^{14} \text{ cm}^{-2}$ )  $\sim 2 \mu\text{m}$  thick epitaxy. The evolution in the number of grown Gr layers as a function of the growth temperature was explored in a temperature range from  $1600^\circ\text{C}$  to  $1700^\circ\text{C}$ . The same 10 minutes heat-treatment time was used for all the samples. A representative AFM morphology of the virgin 4H-SiC (0001) surface is reported in Figure 3.16 (a). It shows parallel terraces oriented in the [00-10] direction. The mean width of the terraces is  $\sim 30 \text{ nm}$  and can be deduced from the line scan in Figure 3.16 (b). The RMS roughness is also estimated from that surface analysis and reports a value of  $\sim 0.2 \text{ nm}$  as a consequence of the nanometric terrace morphology.

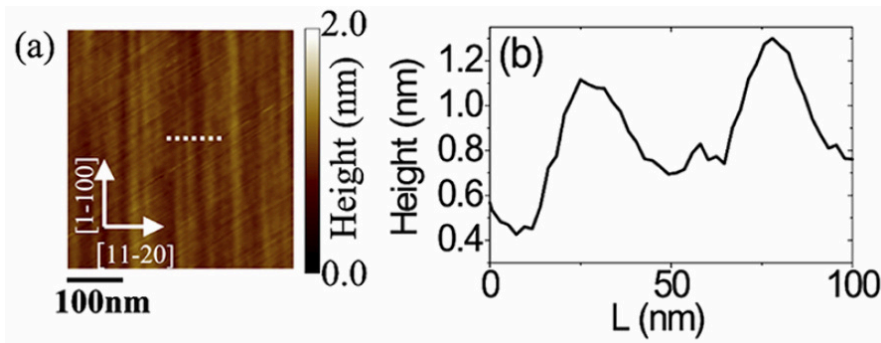


**Figure 3.16:** Atomic force microscopy image of the surface morphology (a) and line profile (b) on a virgin 4H-SiC(0001) substrate cut at an angle of  $8^\circ$  with respect to the basal plane along the [1120] direction.

AFM morphological images for the samples annealed at  $1600^\circ\text{C}$  and at  $1700^\circ\text{C}$  are reported in Figure 3.17 (a) and (b) respectively.

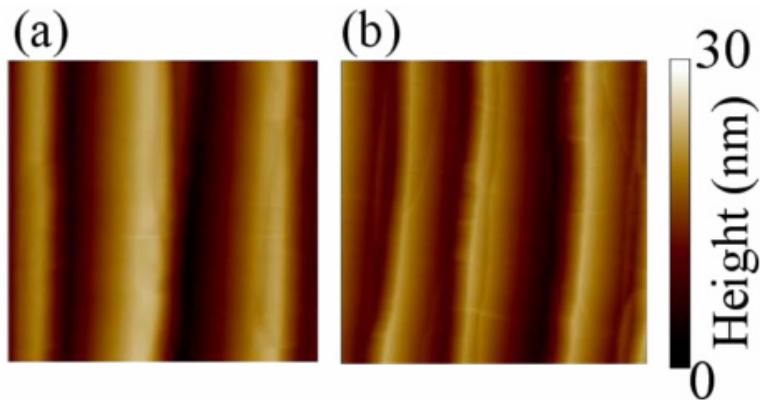


**Figure 3.17:** tAFM Surface morphology for the samples annealed at  $1600^\circ\text{C}$  (a) and  $1700^\circ\text{C}$  (b).

Annealed samples show wide terraces running parallel to the original steps in the virgin sample. An average terrace width of approx 150 to 200 nm has been estimated for both temperatures, a significant increase over the previously observed small terraces for pristine SiC. The estimated RMS roughness for the samples is approx 10 nm, which is significantly higher than on the pristine SiC substrate. Such large terraces on annealed samples are the result of the step-bunching commonly

observed on off-axis SiC substrates after thermal treatments at temperatures  $> 1400^{\circ}\text{C}$ .

Another peculiarity clearly visible on the 3D projection of the AFM morphology reported in Figure 3.18 (a) is the presence of corrugations perpendicular to the steps. The line scan shown in Figure 3.18 (b) and taken in the direction parallel to the steps shows the nanometer high corrugations superimposed to the stepped morphology of EG. These corrugations commonly named “wrinkles”, as already described for Gr grown on catalytic metals, pleats of the Gr membrane that locally lifts from the underlying substrate, the SiC surface in this case. The heights of such corrugations can range from  $\sim 0.8$  to  $\sim 2.2$  nm with an average value of  $\sim 1.1$  nm, as deduced from AFM analyses on several wrinkles. As already discussed for CVD Grown Gr, also on SiC, Gr can show these kinds of corrugations. These peculiar defects has been reported by other authors in the case of few layers of Gr grown on the C face [188] or on the Si face [189] of hexagonal SiC on-axis. In those cases, Gr did not exhibit any preferential orientation with respect to the steps, but formed an isotropic mesh-like network on the surface, where wrinkles were interconnected into nodes (typically three wrinkles merge on a node and the angles subtended by the wrinkles are approx.  $60$  or  $120^{\circ}$  [188]). The formation of that mesh-like network of wrinkles was attributed to the release of the compressive strain, which builds up in few layer Gr during the sample cooling due to mismatch between the thermal expansion coefficients of Gr and the SiC substrate [188,190]. In the present case of few layers Gr grown on the Si face of off-axis 4H-SiC, a preferential orientation of the wrinkles orthogonal to the steps is observed (Figure 3.18 (a)). This peculiar effect suggests that compressive strain in Gr layers is released not only by the formation of parallel wrinkles inside each terrace, but also in an efficient way at step edges. Even if this effect deserves further investigations this observation must be taken in to account considering the potential wrinkles effect on Gr transport properties [170].

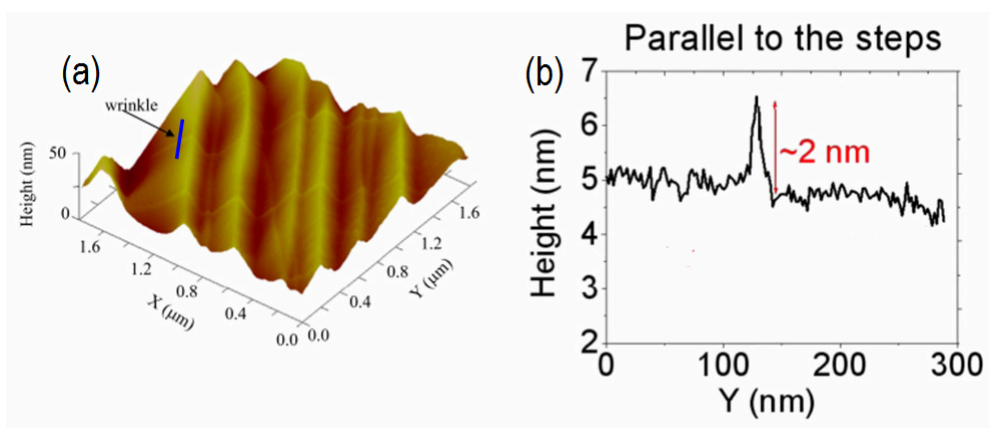


**Figure 3.18:** (a) 3D projection of the surface morphology of the sample annealed at 1700°C to highlight the topography of wrinkles. The blue line in (a) corresponds to the line-profile scan in (b) taken in the direction parallel to the steps to estimate the heights of a wrinkle.

The comparison between micro-Raman spectra on the virgin 4H-SiC (0001) substrate and after EG growth at 1600 and 1700°C, is reported in Figure 3.19. The spectra have been offset vertically for clarity and their intensity has been normalized to the intensity of the most prominent Raman peak of 4H-SiC substrate.

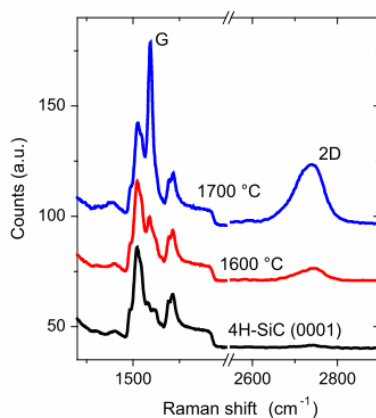


**Figure 3.19:** Typical Raman spectra measured on virgin 4H-SiC (0001) and after epitaxial Gr growth at 1600°C and 1700°C.

The typical G and 2D peaks of graphitic structures are evident on both annealed samples. The asymmetric shape of the 2D peaks is consistent with the formation of

a few layers of Gr with Bernal stacking [191] whereas the increase in the G and 2D peaks' intensities (with respect to the SiC background signal) at increasing annealing temperature indicates an increase in the number of layers. Clearly, Raman spectroscopy allows distinguishing the Gr monolayer (for which the 2D peak is perfectly symmetric) from bilayer and few layers of Gr (which exhibit an asymmetric 2D peak). However, for a number of layers  $> 3$  the 2D peak becomes hardly distinguishable from that of bulk graphite.

High Resolution Transmission Electron Microscopy (HRTEM) on cross-sectioned samples was used to get a direct determination of the number of layers [191]. Due to the mechanisms of image formation in HRTEM, based on electron diffraction, a few layers of Gr over the cross-sectioned SiC surface produce alternating dark and bright interference fringes in the TEM images, with the contrast depending on the defocusing conditions. In Figure 3.20 (a) HRTEM of an EG sample grown at 1700°C is reported, cross-sectioned perpendicularly to the [1-100] direction in order to observe the profile of the steps. The kink region between the (0001) basal plane and the (11-2n) facets of SiC is imaged and the angle ( $\phi \approx 27^\circ$ ) between these planes is indicated. The value of this angle can range from  $27^\circ$  to  $34^\circ$ , as obtained from measurements on several steps (Figure 3.20 (b)). HRTEM was also employed to evaluate the number of Gr layers as a function of the annealing temperature. Figure 3.20 (c,d) reports two representative HRTEM analyses of EG layers grown on the (0001) face of 4H-SiC at 1600°C (Figure 3.20 (c)) and 1700°C (Figure 3.20 (d)), respectively. The interlayer spacing, i.e. the separation of two adjacent bright fringes is  $\sim 3.4 \text{ \AA}$ , whereas the number of C layers was  $3 \pm 1$  and  $8 \pm 1$ , where the error bars come from a statistics on several HRTEM images at different positions on the cross-sectioned samples.

It is worth noticing that these cross-sectional analyses give a direct measure of the number of grown layers, but only on a limited scale. Even if the measure is repeated in various zones of the cross-sectioned sample, statistical information on the lateral variation of the few layers Gr thickness on different sample positions cannot be practically obtained by this method.

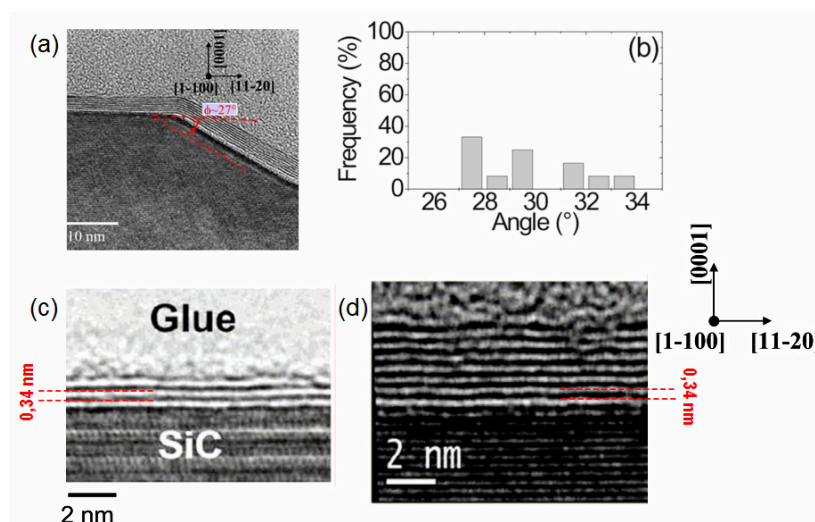


**Figure 3.20:** HRTEM of the step profile for an EG sample grown at 1700°C on 8° off axis 4H-SiC (0001) cross-sectioned perpendicularly to the [1-100] (b) Statistical distribution of the angle measured for different steps. HRTEM measures used to evaluate the number of Gr layers on the (0001) face grown at 1600 C (c) and 1700°C (d).

Another approach to estimate the number of layers at selected surface positions with higher statistics [192] is based on the use of AFM to measure the depth of selectively etched stripes in few layers Gr by O<sub>2</sub> plasma. This plasma treatment is known to remove efficiently carbonaceous species through a chemical reaction leading to the formation of CO<sub>2</sub>. In Figure 3.21 (a), an optical image of the etched stripes in the sample annealed at 1700°C is reported. The accurate estimation was obtained considering also the plasma effect on the SiC substrate, which is slightly etched by the processing. To this aim, a lithographically patterned pristine SiC substrate was simultaneously etched together with the graphitized SiC samples to work as the “tare” of the measure. Figure 3.21 (b) and (c) show the height profiles taken on a stripe on pristine SiC and on the sample annealed at 1700°C, respectively. The pristine SiC depth must be subtracted while evaluating the number of layers on graphitized SiC. Hence, the number of layers can be estimated according to the relation  $n = (D - D_0)/D_{gr}$ , being  $D_{gr}$  the interlayer separation between two stacked Gr layers, ( $D_{gr} \approx 0.35$  nm), which corresponds the interlayer spacing between two stacked Gr planes in HOPG, as typically measured by AFM,

$D$  and  $D_0$  are the height profiles taken on the graphitized material and on pristine SiC respectively.

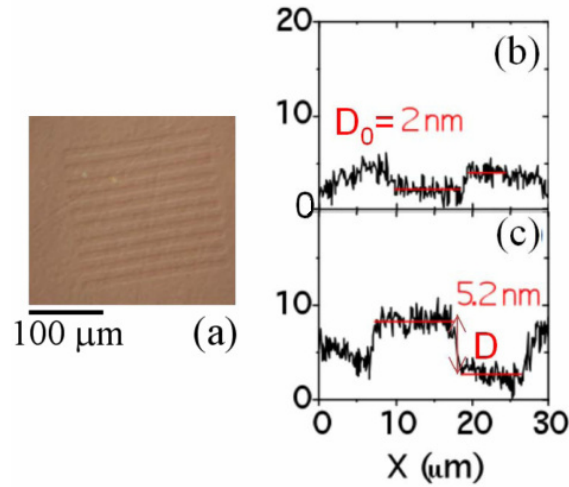


**Figure 3.21:** Optical image on the  $O_2$  etched stripes in the graphitized 4H-SiC sample by annealing at  $1700^\circ\text{C}$  (a). AFM height profile taken on a stripe of pristine SiC (b) and on a stripe of the sample annealed at  $1700^\circ\text{C}$  (c), respectively.

The obtained values are in good agreement with what determined by HRTEM. HRTEM allows direct measurements of the number of layers and the interlayer spacing, but cannot provide information on the detailed atomic structure of the EG/SiC (0001) heterointerface and, in particular, on the presence of the buffer layer, due to the limited resolution. The higher resolution needed for this aim is reached using new generation Aberration Corrected Scanning Transmission Electron Microscopes (AC-STEM) [193], providing direct (atomic scale) images by scanning an electron beam with angstrom (or even sub-angstrom) size and collecting transmitted electrons scattered at large angle. This operation mode is called High Angle Annular Dark Field (HAADF) mode. In particular HAADF-STEM analyses of the EG/SiC interface was performed using a Nion UltraSTEM100 dedicated aberration-corrected microscope operating at 60 keV primary beam energy, i.e. below the knock-on threshold for carbon atoms in Gr ( $\sim 80$  keV) [194]. At this energy, the estimated beam size is  $1.1 \text{ \AA}$ . Furthermore, atomic resolution Electron Energy Loss Spectroscopy (EELS) was jointly performed.



The atomic resolution analyses of the EG/SiC interface both on the (0001) basal plane and (11-2n) facets are reported in Figure 3.22 (a) and (b) respectively. The separations between the topmost SiC surface dimer and the first C layer on (0001) surface was  $2.62 \pm 0.13 \text{ \AA}$ , indicating a very strong bonding of this layer to the substrate, whereas the distance between the first and second carbon layer is  $3.37 \pm 0.13 \text{ \AA}$ , in close agreement with the typically reported interlayer spacing in graphite. By contrast, the distance between the (11-2n) surface and the first C layer above this facet was found to be  $3.46 \pm 0.13 \text{ \AA}$ , whereas the distance between the first and the second C layer was again  $3.37 \pm 0.13 \text{ \AA}$ . This morphological difference was direct (atomic scale) evidence that the first C layer in the stack has a different nature depending on the orientation of the underlying substrate: it can be identified with the buffer-layer on the planar (0001) surface, whereas it appears to delaminate from the (11-2n) surface. The results of this structural analysis were further supported by atomic-scale EELS of the carbon K edge fine structure on individual layers, reported in Figure 3.22 (c). This spectroscopic analysis demonstrated a partial  $sp^3$  hybridization of the first C layer on the basal plane (0001), consistently with its buffer layer nature, while the same layer is fully  $sp^2$  hybridized on the (11-2n) facet, confirming its modification into QFEG. In fact, by the fine structure of the Carbon K edge collected for each layer, it is possible to observe (i) the peak at  $\sim 285 \text{ eV}$  related to the  $1s$  to  $\pi^*$  electronic transitions and indicative of the presence of  $\pi$  bonds (and in particular of  $sp^2$  hybridization for this experimental geometry) and (ii) the peak at  $\sim 295 \text{ eV}$  related to the  $\sigma^*$  and indicative to the presence of  $sp^3$  hybridization. The  $\sim 285 \text{ eV}$  peak intensity drops significantly at the first C layer of the planar (0001) with a simultaneous increase of the intensity at  $\sim 295 \text{ eV}$ , indicative of the solely partial  $sp^2$  hybridization in favor of  $sp^3$  hybridization, as expected from the buffer layer. The same C layer sampled on the (11-2n) facet shows a rise of the  $\sim 285 \text{ eV}$  peak intensity to values similar to those of the overlying Gr layers, as expected from the delaminated membrane which in fact is a free standing Gr.

Figure 3.22 (d) shows a schematic representation of the structural configuration of the 1<sup>st</sup> C layer on the (0001) and (11-2n) surfaces of the faceted SiC, as deduced from the previously discussed STEM and EELS analyses. Interestingly, the delaminated buffer layer exhibits an increased equilibrium distance from the SiC surface, but still follows the SiC morphology. The observed buffer layer delamination can be explained in terms of a lowering of the Gr binding energy with

the substrate moving from the (0001) basal plane to (11-2n) facets, and is expected to occur for facets forming an angle  $\phi \approx 27^\circ$  with the (0001) plane [195].

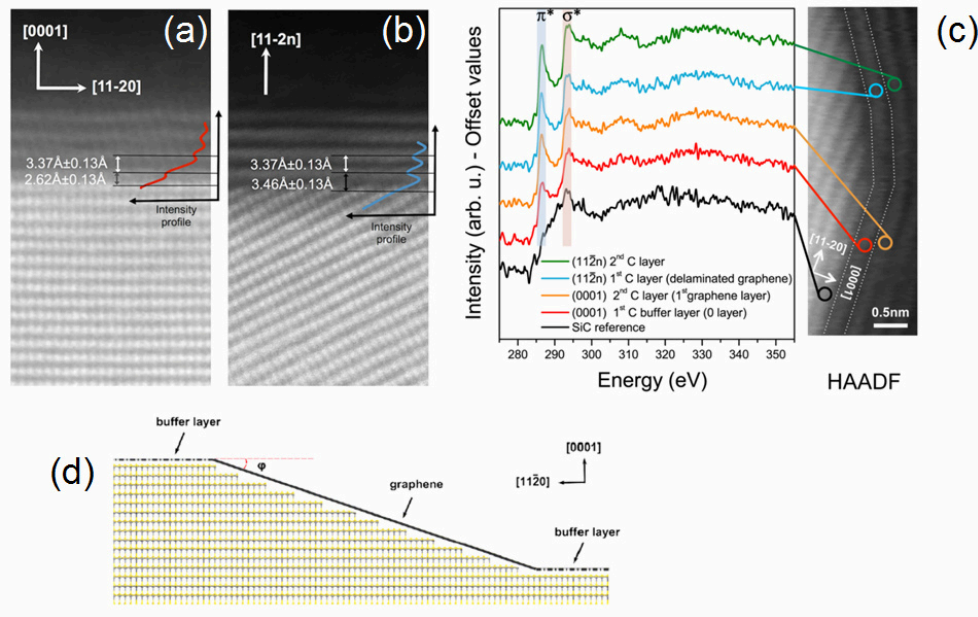


**Figure 3.22:** HAADF atomic resolution STEM image of the cross sectioned profile along the [1120] direction of the (0001) surface (a) and the (11-2n) surface (b). EELS spectra and the simultaneously acquired HAADF STEM image of a faceted step in the annealed 4H-SiC sample cross-sectioned along the [1120] direction (c). Schematic cross section of the structural configuration of the 1<sup>st</sup> C layer on the faceted surface, as deduced from STEM and EELS analyses (d).

### 3.2.1 Fabrication of Schottky contacts on on-axis and off-axis SiC (0001) by hydrogen intercalation at epitaxial Gr/SiC interface

The final aim of this work was to fabricate Schottky contacts on SiC by hydrogen intercalation at epitaxial Gr/SiC interface.

Gr growth was carried out both on-axis and off-axis 4H-SiC (0001) and on 4H-SiC (0001), followed by an hydrogen intercalation process to detach the buffer layer and obtain a QFEG.

For this aim, nominally on-axis semi-insulating SiC substrates and an off-axis  $n^+$ -doped SiC substrate with a  $n^-$ -doped epitaxial layer ( $\sim 1 \times 10^{16} \text{ cm}^{-3}$ , as schematically illustrated in Figure 3.23 (a)) were used. In the case of semi-insulating SiC, multiple energies nitrogen ion implantation with subsequent annealing at  $1700^\circ\text{C}$  for 30 min was employed to obtain a surface  $n^-$ -well region ( $\sim 1 \times 10^{16} \text{ cm}^{-3}$ ) and a buried  $n^+$ -layer ( $1 \times 10^{18} \text{ cm}^{-3}$ ) for contact purposes, as schematically illustrated in Figure 3.23 (b).

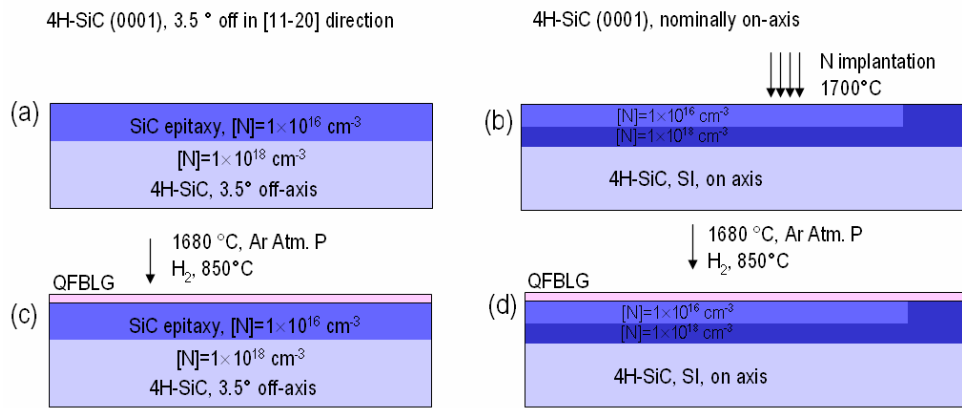


**Figure 3.23:** schematic illustration of (a) an  $n^+$ -doped 4H-SiC 3,5 off-axis with a  $n^-$ -doped epitaxial layer and (b) a nominally on-axis semi-insulating SiC where a nitrogen ion implantation was employed to obtain a surface  $n^-$ -well region and a buried  $n^+$ -layer. (c) and (d) schematically illustrate the QFEG grown by thermal decomposition at  $1680^\circ\text{C}$  under Ar flux near atmospheric pressure followed by hydrogen intercalation at  $850^\circ\text{C}$  in a  $\text{H}_2$  flux, for the off-axis (c) and the on-axis (d) samples.

The Quasi-Free-standing BiLayer Graphene (QFBLG) was therefore grown by thermal decomposition at  $1680^\circ\text{C}$  under Ar flux near atmospheric pressure followed by hydrogen intercalation at  $850^\circ\text{C}$  in a  $\text{H}_2$  flux of 1 slm at atmospheric

pressure (as illustrated in Figure 3.23 (c,d)). Growth on substrates with different miscut angles resulted in the formation of SiC terraces with different widths and, consequently, of different steps/facets densities. The average terrace widths was  $\sim 0.3 - 0.5 \mu\text{m}$  for the  $3.5^\circ$  off-axis substrate and  $\sim 3 - 6 \mu\text{m}$  for the on-axis one, as determined from AFM morphological measurements.

In order to perform the electrical characterization of the vertical current transport, which will be discussed in the next Chapter, a specific array of contact was defined on both substrates.

In particular circular Au contacts with diameters ranging from  $200 \mu\text{m}$  down to  $1 \mu\text{m}$  were fabricated on QFBLG of both the on-axis and the off-axis substrates using electron beam lithography, followed by Au evaporation and lift-off. Gr between contacts was removed by oxygen plasma using the Au contacts as etch mask, thus obtaining Au capped QFBLG contacts of variable sizes. For each kind of substrate some samples were furthermore treated to remove the Au capping, leaving analogously patterned and metal-free Gr contacts on top. In this way four groups of samples were prepared for the electrical characterization discussed in the next Chapter i.e. two groups of Au coated Gr contacts and two groups of metal-free Gr, on on-axis (Figure 3.24 (a,b)) and on off-axis SiC (Figure 3.24 (c,d)) substrates respectively.

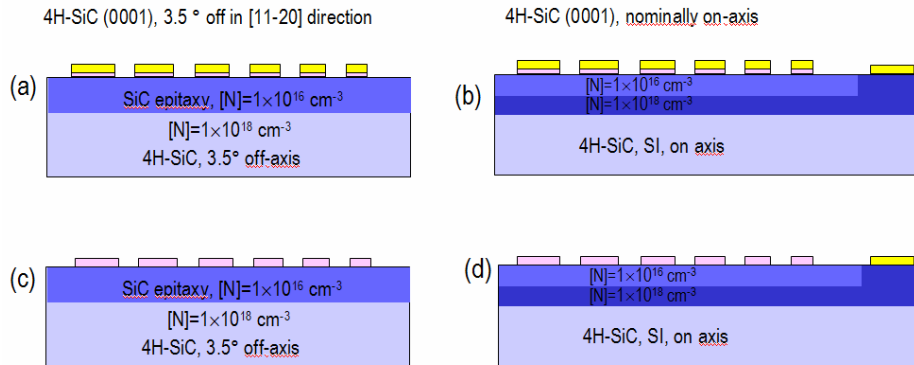


**Figure 3.24:** Schematic representation of Au-capped (a) and uncapped (b) QFBLG contacts on on-axis SiC (0001) with a n<sup>-</sup>-well region and a buried n<sup>+</sup>-layer obtained by nitrogen ion implantation. Schematics of Au-capped (a) and uncapped (b) QFBLG contacts on a  $3.5^\circ$  off-axis SiC (0001) epilayer.

# Chapter 4: Electrical characterization of graphene heterostructures with wide-bandgap semiconductors

As discussed in the previous chapter, Gr contacts were fabricated on top of AlGa<sub>N</sub>/Ga<sub>N</sub> heterostructures (by Gr electrolytic delamination from copper and thermo-compression printing) and on 4H-SiC (by controlled graphitization during high temperature thermal treatments). In this chapter, the lateral current transport in Gr on these two substrates and the vertical current transport through the Gr/semiconductor interface will be investigated using micro and nanoscale characterization techniques. The mechanisms underlying the current transport through the Gr/semiconductor interface will be discussed for both these systems. The implications of these results on the fabrication of new concept devices based on Gr heterostructures with WBSs will be finally discussed.

## 4.1 Gr/AlGa<sub>N</sub>/Ga<sub>N</sub> heterostructures

### 4.1.1 Lateral current transport in Gr in contact to AlGa<sub>N</sub>

The sheet resistance ( $R_{sh}$ ) of Gr after transfer to AlGa<sub>N</sub> was preliminarily investigated to assess its electrical quality and elucidate the impact of the interaction with this specific substrate on the transport properties of Gr. To this aim, the sample A (described in the previous chapter) was chosen as the most appropriate for this kind of measure due to the smooth morphology of the AlGa<sub>N</sub> barrier layer. Transmission Line Model (TLM) test patterns, consisting of a set of metal contacts with identical geometry and different spacing on a Gr stripe (see the schematic representation in Figure 4.1 (a)), were used for this electrical characterization. They were fabricated by lateral isolation of Gr/AlGa<sub>N</sub> rectangular stripes using plasma etching, followed by deposition of a set of Ni/Au metal pads (width  $W = 200 \mu\text{m}$  and length  $L = 100 \mu\text{m}$ ) with different spacing  $d$  (from  $20 \mu\text{m}$  to  $100 \mu\text{m}$ ). To verify anisotropies of the 2D current transport in Gr, different TLM test patterns with various orientations were designed. Furthermore, for reference purposes, TLM devices with the same geometry were fabricated on Gr transferred under identical conditions on a SiO<sub>2</sub>/Si substrate (n<sup>+</sup>-doped Si).

The sheet resistance  $R_s$  of the Gr membrane was determined by  $I$ - $V$  analyses on different pairs of adjacent pads at different distances [186,196].

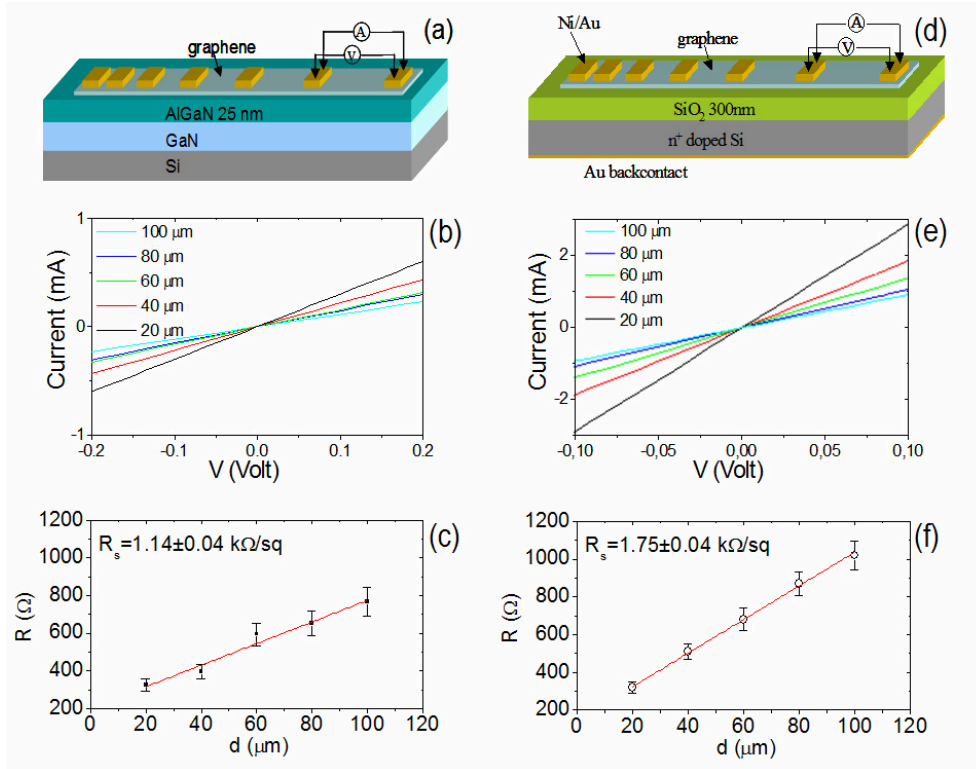


**Figure 4.1:** (a) Schematic representation of a TLM test structure fabricated on the Gr membrane residing on AlGaIn. (b)  $I$ - $V$  characteristics measured between pairs of contacts at different distances and (c) extracted resistance plotted vs. the pads distance. Analogous (d) schematic representation, (e)  $I$ - $V$  characteristics and (f) resistance plotted vs. the pads distance for Gr residing on SiO<sub>2</sub>. From the linear fit of  $R$  versus  $d$ , the Gr sheet resistance was evaluated.

It is worth noticing that the measure was performed in a range of applied voltages lower than the threshold voltage needed, as reported in the next section, to overcome the SBH for a Gr/AlGaIn/GaN vertical current. In this way, a parallel current through the AlGaIn/GaN 2DEG can be excluded and the measured  $R_{sh}$  can be exclusively attributed to Gr.

All these  $I$ - $V$  characteristics exhibit an ohmic behavior, as illustrated in Figure 4.1 (b). The resistance  $R$  between each couple of pads was obtained as the

slope of the  $I$ - $V$  curves and is reported in Figure 4.1 (c) as a function of the pad separation  $d$ . This measured resistance depends on the metal/Gr contact resistance  $R_c$  and on the Gr sheet resistance  $R_{sh}$ , according to the relation:

$$R = 2R_c + \frac{R_{sh}}{W} d \quad (4.1)$$

Hence, the sheet resistance can be determined by the slope in the linear fit of the  $R$  vs.  $d$  plot.

The  $R$  vs.  $d$  plot for Gr onto AlGaIn is reported in Figure 4.1 (c) and a value of  $R_{sh} = 1.14 \pm 0.04$  k $\Omega$ /sq was obtained. The results on TLM analyses of Gr residing on SiO<sub>2</sub> are also reported in Figure 4.1 (d-e), for comparison.

In this case, the Si substrate provides a back-gate that can be used for the electric field modulation of Gr carrier density [186] in order to shift the Fermi level of Gr. It is worth noting that  $R_{sh}$  exhibits a monotonically increasing behavior with the back-gate bias values in the considered bias range, which allows to deduce a p-type doping of the transferred Gr on this substrate (Figure 4.2).

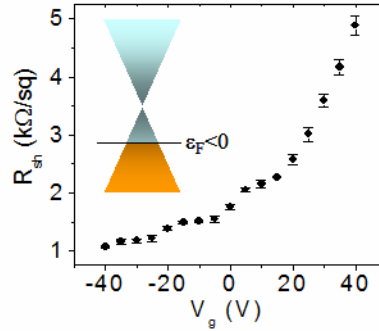


**Figure 4.2:** Sheet resistance ( $R_{sh}$ ) plotted vs. versus  $V_g$  from -40 V to 40 V, for Gr residing on SiO<sub>2</sub>.

A different approach, based on the analysis of the current through Gr/AlGaIn Schottky contacts, will be employed to estimate the doping level in Gr residing on this latter substrate, as discussed in the following.

#### 4.1.2 Vertical current transport in Gr/AlGaIn/GaN heterostructures

Nanoscale resolution electrical analyses were performed on both Gr-coated and bare AlGaIn regions (as reference) of Sample A. Local current measurements were

carried out at room temperature by CAFM. AFM tips with different metal coatings (i.e., Au, Pt, Cu and Ni) obtained by thin film sputtering, was used for this aim [197]. The force between tip and sample was properly set in order to have a stable electrical contact, as it will be described in the following.

CAFM analyses were performed applying a bias between the tip and a large-area contact on bare AlGa<sub>N</sub> during the scan, as schematically illustrated in the inserts of Figure 4.3 (a) and (b). A high sensitivity current amplifier in series collected the current flowing between these two contacts. Clearly, the major contribution to the measured resistance is due to the vertical current path from the tip to the AlGa<sub>N</sub>/Ga<sub>N</sub> 2DEG, whereas the path from this 2DEG to the large-area contact adds a series resistance contribution.

Figure 4.3 (a) and (b) report two different series of  $I$ - $V$  curves collected using an Au coated AFM tip displaced on a square array of 25 positions (spaced 1  $\mu\text{m}$  from each other) on bare AlGa<sub>N</sub> and Gr-coated AlGa<sub>N</sub>, respectively. Both series of curves exhibit a rectifying behavior, with a negligible current at negative biases and rapidly increasing current at forward bias higher than an onset voltage. Interestingly, while a broad  $I$ - $V$  curves distribution has been found in the case of the Au tip/AlGa<sub>N</sub> contact, a very narrow spread between curves at different positions is found for the Au tip/Gr/AlGa<sub>N</sub> contact. Furthermore, in the latter case the current onset occurs at significantly lower bias than for Au tip/AlGa<sub>N</sub>, indicating a reduced SBH. The spread between the local  $I$ - $V$  curves measured on bare AlGa<sub>N</sub> can be associated with surface potential fluctuations, which are typical sources of the laterally inhomogeneous Schottky barrier between metals and Ga<sub>N</sub> or its alloys [198].



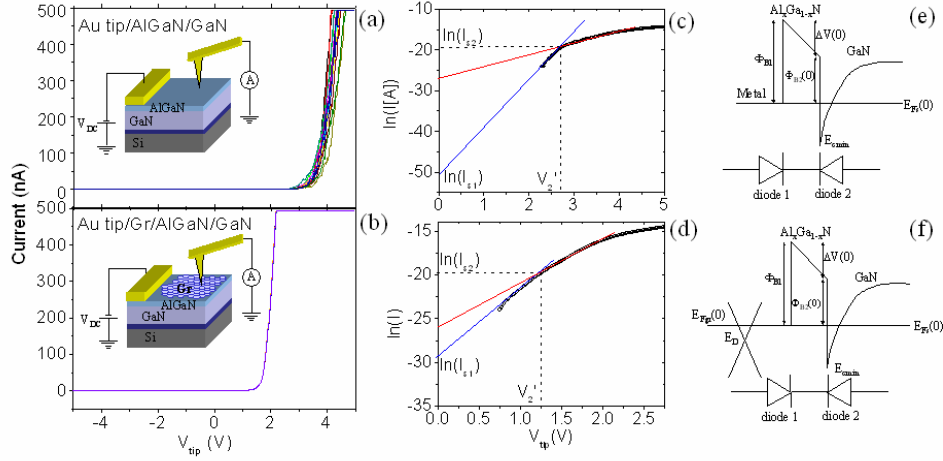


**Figure 4.3:** Two different series of  $I$ – $V$  curves collected using an Au coated AFM tip displaced on a square array of 25 positions on AlGaIn/GaN (a) and Gr/AlGaIn/GaN (b). Schematic representations of the experimental setup for local  $I$ – $V$  measurements by CAFM, in the inserts of (a) and (b). Fitting of two representative forward bias  $\ln(I)$ – $V$  curves acquired on AlGaIn (c) and Gr/AlGaIn (d). Conduction band diagrams of AlGaIn/ GaN (e) and Gr/AlGaIn/GaN heterostructures (f) with the equivalent circuit of a Schottky AlGaIn/GaN diode represented as two diodes back-to-back in series.

Differently than classical metal electrodes, consisting of polycrystalline films composed by grains with different sizes and crystalline orientations, the Gr membrane works as a uniform and atomically thin electrode, which covers the AlGaIn surface in a very conformal way. Most probably, the Gr electrode has an averaging effect on the AlGaIn surface potential fluctuations over the typical length scale of the Gr electron mean free path  $l_{Gr}$ , which is of the order of  $\sim 0.1 \mu\text{m}$  for substrate supported Gr [110]. Clearly,  $l_{Gr}$  is much larger than the electron mean free path of classical metal electrodes. This averaging effect results in the observed superior uniformity of Gr Schottky contacts on the AlGaIn surface.

Current transport from Gr to the AlGaIn/GaN 2DEG occurs through the unintentionally doped AlGaIn barrier layer. For the  $\sim 24 \text{ nm}$  thick and defect-free barrier layer of Sample A, we have found that thermionic emission is the most appropriate model to describe charge transport across this barrier, whereas tunnelling phenomena can be dominant for Gr contacts to a locally thinner AlGaIn layer.

The characteristic parameters of the Schottky contacts, i.e., the barrier height and the ideality factor, were extracted from the forward bias characteristics, by fitting the  $\ln(I)$  vs.  $V$  curves using the thermionic emission theory. A representative  $\ln(I)$ - $V$  curve from the measured array on bare AlGaN is shown in Figure 4.3 (c).

As discussed in ref. [199], the forward bias  $I$ - $V$  curves of Schottky contacts on AlGaN/GaN heterostructures cannot be satisfactorily described by a single metal/AlGaN Schottky diode. Rather, an equivalent circuit of two diodes back-to-back in series should be used [200] as schematically illustrated in Figure 4.3 (e), where the left diode (diode 1) represents the Schottky contact between the metal and the AlGaN barrier layer and the right diode (diode 2) represents the effective Schottky contact between the 2DEG and AlGaN. For forward polarization of the heterostructure, diode 1 and diode 2 are forward and reverse biased, respectively. Hence, according to the thermionic emission model, the  $I$ - $V$  curve of diode 1 can be expressed as:

$$I \approx I_{s1} \exp\left(\frac{qV_1}{n_1 k_B T}\right) \quad (4.2)$$

Where:

$$I_{s1} = SA^* T^2 \exp\left(-\frac{q\Phi_{B1}}{k_B T}\right) \quad (4.3)$$

is the saturation current of diode 1, being  $S$  the tip contact area,  $A^*$  the Richardson constant,  $k_B$  the Boltzmann constant,  $T$  the temperature,  $q$  the electron charge,  $V_1$  the voltage drop across the diode 1,  $n_1$  and  $\Phi_{B1}$  the ideality factor and barrier height respectively. The current voltage characteristics of the reverse biased diode 2 can be expressed as:

$$I \approx SA^* T^2 \exp\left(-\frac{q\Phi_{B2}(V_2)}{k_B T}\right) \quad (4.4)$$

Where  $\Phi_{B2}$  is the 2DEG/AlGaN effective barrier height, which is a function of the voltage drop  $V_2$  across diode 2. Furthermore, the applied bias  $V$  is related to  $V_1$  and  $|V_2|$  as  $V = V_1 + |V_2| + IR$ , where  $R$  is the series resistance of the circuit, whose contribution starts to dominate at high currents.

For low  $V_2$  values,  $\Phi_{B2}(V_2)$  can be expanded by the Taylor series and approximated to the first-order correction, as:

$$\Phi_{B2}(V_2) \approx \Phi_{B2}(0) - \left[ \frac{\partial \Phi_{B2}}{\partial V_2} \right]_{V_2=0} |V_2| \quad (4.5)$$

Where  $\Phi_{B2}(0)$  is the 2DEG/AlGaIn barrier height at zero bias ( $|V_2| = 0$ ). This assumption is justified for low voltages across diode 2, whereas for large  $|V_2|$  values, the series resistance becomes the dominant factor. Using this approximation, the reverse current across diode 2 can be expressed as:

$$I \approx I_{s2} \exp\left(\frac{q|V_2|}{n_2 k_B T}\right) \quad (4.6)$$

With

$$I_{s2} \approx SA * T^2 \exp\left(-\frac{q\Phi_{B2}(0)}{k_B T}\right) \quad (4.7)$$

It is noteworthy that equation (4.6) is formally similar to the expression for forward current across diode 1. Here

$$I \approx SA * T^2 \exp\left(-\frac{q\Phi_{B2}(V_2)}{k_B T}\right) \quad (4.8)$$

represents the effective ideality factor of diode 2, which reflects the degree of barrier height  $\Phi_{B2}$  change due to the change of voltage across it. Hence, the larger is  $n_2$  the smaller is the change of barrier height. According to the above arguments, the current through the heterostructure can be described as due to two diodes in series with the equivalent circuit elements as shown in the insert of Figure 4.3 (e). The parameters  $I_{s1}$ ,  $I_{s2}$ ,  $n_1$  and  $n_2$  of the metal/AlGaIn/GaN heterostructure can be extracted from the plot of  $\ln(I)$  vs.  $V$  in Figure 4.3 (c), using the following procedure. Since  $V \approx V_1$  in the low current regime,  $I_{s1}$  and  $n_1$  can be obtained by linear fitting of the  $\ln(I)$ - $V$  plot at low voltages. The intercept of the fitted straight line gives  $I_{s1}$  and the slope gives the information for  $n_1$ . To obtain  $I_{s2}$  and  $n_2$ , another linear fit is carried out in the higher current regime. This fit is made in the second linear region of the  $\ln(I)$ - $V$  plot at intermediate voltages, whose behavior is determined by the barrier  $\Phi_{B2}$ , as shown in Figure 4.3 (c). This line was

extrapolated to intercept the previous line at the intercept voltage  $V_2'$ , assumed as the onset voltage of the second diode with a saturation current  $I_{s2}$ , as indicated in Figure 4.3 (c). The ideality factor  $n_2$  can be obtained from the slope of this linear fit. It is worth noting that the product  $SA^*$  is not exactly known, since the experimental values of the Richardson constant are typically lower than the ideal one ( $A^* \approx 35.8 \text{ A/K}^2\text{cm}^2$ ) [199] and the tip contact area  $S$  can be subjected to small variations from point to point. The following procedure has been adopted to determine  $\Phi_{B1}$  and  $\Phi_{B2}(0)$  from the fit values of  $\ln(I_{s1})$  and  $\ln(I_{s2})$ , without using  $SA^*$ .

According to the band structure in Figure 4.3 (e), the built-in potential across the AlGa<sub>N</sub> barrier layer at zero bias ( $V_{tip} = 0$ ) is:

$$\Delta V(0) = \Phi_{B1} - \Phi_{B2}(0) = \frac{k_B T}{q} [\ln(I_{s2}) - \ln(I_{s1})] \quad (4.9)$$

Where the last part of the equation derives from the difference of equations (4.3) and (4.7), and  $\ln(I_{s2})$  and  $\ln(I_{s1})$  are directly obtained from the two linear fits.

$\Delta V(0)$  is also related to the difference between the positive surface polarization charge  $+\sigma$  and the density  $n_{s0}$  of the AlGa<sub>N</sub>/Ga<sub>N</sub> 2DEG at zero bias

$$\Delta V(0) = q(\sigma - n_{s0})/C_{\text{AlGa}_N}, \quad (4.10)$$

Where  $C_{\text{AlGa}_N} = \epsilon_0 \epsilon_{\text{AlGa}_N} / d$  is the barrier layer capacitance per unit area, with  $d = 24 \text{ nm}$  the barrier layer thickness and  $\epsilon_{\text{AlGa}_N} = 9.375$  the relative dielectric permittivity for an Al<sub>x</sub>Ga<sub>1-x</sub>N alloy, with an Al concentration of 25% [15]. Using the  $\Delta V(0)$  value obtained from the fit results (equation (4.9)) and the  $\sigma$  value from macroscopic  $C$ - $V$  mercury probe analyses ( $\sigma = 6.93 \times 10^{12} \text{ cm}^{-2}$ ) the value of  $n_{s0}$  can be obtained. The Fermi level position (at zero bias) with respect to the Ga<sub>N</sub> conduction band minimum ( $E_{cmin}$ ), can be expressed as a function of  $n_{s0}$  as: [15]

$$E_{Fs0} - E_{cmin} = \frac{\pi \hbar^2}{q m_{eff}} n_{s0} + \frac{1}{q} \left( \frac{9 \pi \hbar q^2}{8 \epsilon_0 \epsilon_{\text{AlGa}_N} \sqrt{8 m_w^*}} \right)^{\frac{2}{3}} n_{s0}^{\frac{2}{3}} \quad (4.11)$$

Where  $\hbar$  the reduced Planck's constant and  $m_{eff}$  the 2DEG effective mass ( $m_{eff} = 0.22 m_e$ ).

Finally, according to the band structure in Figure 4.3 (e), the diode 2 barrier height  $\Phi_{B2}(0)$  is:

$$\Phi_{B2}(0) = \Delta E_c - (E_{FS0} - E_{cmin}), \quad (4.12)$$

Being  $\Delta E_c = 0.34$  eV the  $\text{Al}_{0.25}\text{Ga}_{0.75}\text{N}/\text{GaN}$  conduction band offset. The diode 1 barrier height  $\Phi_{B1}$  can be obtained using Equation (4.9).

By using the above described procedure, the following local barrier height values  $\Phi_{B1} = 0.96 \pm 0.33$  eV,  $\Phi_{B2}(0) = 0.11 \pm 0.02$  eV,  $n_1 = 3.5 \pm 0.1$ ,  $n_2 = 12.1 \pm 0.3$  were determined by fitting of the representative  $I$ - $V$  curve in Figure 4.3 (c). Furthermore, the local carrier density of the AlGaIn/GaN 2DEG was calculated as  $n_{s0} = (5.2 \pm 0.7) \times 10^{12} \text{ cm}^{-2}$ . Repeating the same procedure for all the local  $I$ - $V$  curves in the array of Figure 4.3 (a), the distributions of barrier height values and 2DEG carrier densities reported in the histograms of Figure 4.4 (a) and (b) are obtained. The average  $\Phi_{B1}$  and  $\Phi_{B2}(0)$  values over the set of curves are  $\Phi_{B1} = 0.95 \pm 0.12$  eV and  $\Phi_{B2}(0) = 0.111 \pm 0.008$  eV, whereas the average  $n_{s0}$  value is  $n_{s0} = (5.17 \pm 0.24) \times 10^{12} \text{ cm}^{-2}$ .

An analogous procedure was followed to extract the characteristic electrical parameters for the Au tip/Gr/AlGaIn/GaN system. By fitting the representative forward bias  $I$ - $V$  curve in Figure 4.3 (b) with the two diodes model in Figure 4.3 (f), the following barrier height and ideality factor values were obtained:  $\Phi_{B1} = 0.41 \pm 0.04$  eV,  $\Phi_{B2}(0) = 0.077 \pm 0.002$  eV,  $n_1 = 5.22 \pm 0.08$ ,  $n_2 = 9.9 \pm 0.2$ . Furthermore a 2DEG density  $n_{s0} = (6.22 \pm 0.08) \times 10^{12}$  at the AlGaIn/GaN interface was evaluated.

The histograms of the  $\Phi_{B1}$ ,  $\Phi_{B2}(0)$  and  $n_{s0}$  obtained by fitting of the entire set of  $I$ - $V$  curves on the Gr/AlGaIn/GaN sample are also reported in Figure 4.4 (a) and (b). Interestingly, a significant reduction of the SBH between the tip and AlGaIn was found in the presence of the Gr interlayer.

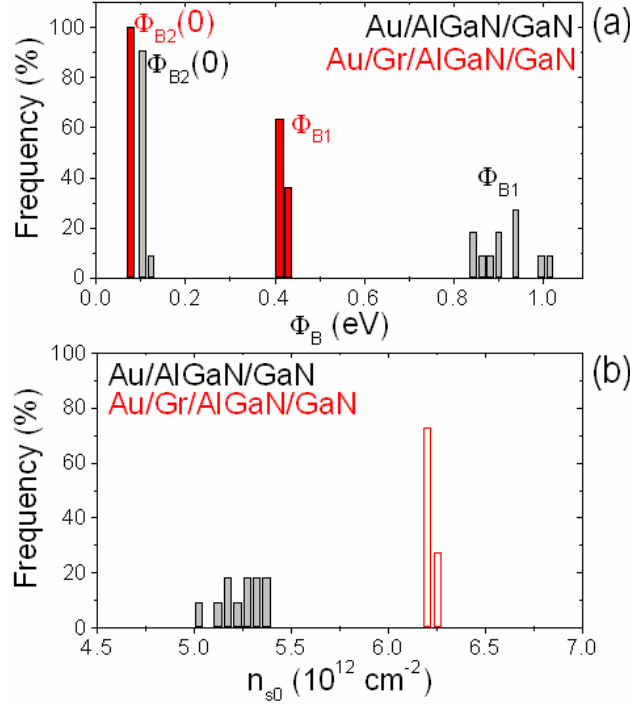


**Figure 4.4:** Histograms of the  $\Phi_{B1}$ ,  $\Phi_{B2}(0)$  (a), and  $n_{s0}$  (b) obtained on an array of 25 tip positions (spaced 1  $\mu\text{m}$  from each other) on the AlGaN/GaN and Gr/AlGaN/GaN heterostructures.

Furthermore, an increase of the local carrier density of the AlGaN/GaN 2DEG was also found. It is noteworthy that the distribution of the barrier height values measured at different tip positions (with 1  $\mu\text{m}$  spacing from each other) is extremely narrow in the presence of Gr, indicating a much higher degree of spatial homogeneity of the Schottky barrier to AlGaN.

In order to confirm the stability of the electrical contact between the AFM tip and the sample surface the local  $I$ - $V$  measures were repeated for different values of the tip-sample force, properly setting the cantilever deflection set point (DSP). As reported in Figure 4.5, it was observed that the  $\Phi_{B1}$  and  $\Phi_{B2}(0)$  on Gr-coated AlGaN give essentially identical values with very similar error bars for DSP values from 0.5 to 2.0 V after which slight deviation and a small increase of the error bar is observed. For bare AlGaN the scenario is almost identical with a higher error bars in agreement to what illustrated before. For all the subsequent measures, a

DSP of 1.0 V was chosen as a reasonable value within the analyzed range and with the lower error bar calculated.

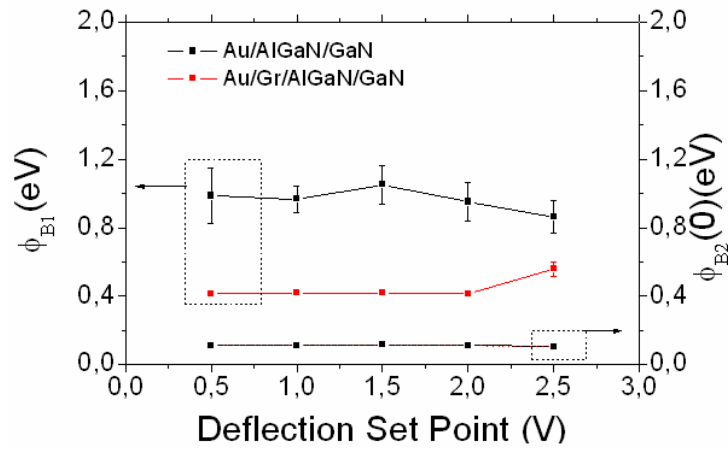


**Figure 4.5:** Behavior of  $\Phi_{B1}$ , and  $\Phi_{B2}(0)$  versus the deflection set point (DSP), for the AlGaIn/GaN and Gr/AlGaIn/GaN heterostructures.

Forward  $I$ - $V$  characterizations were carried out on AlGaIn/GaN and Gr/AlGaIn/GaN heterostructures using AFM tips covered by metals with different workfunctions  $W_M$ . As well as gold ( $W_{Au} = 5.54$  eV), platinum ( $W_{Pt} = 6.13$  eV), nickel ( $W_{Ni} = 5.47$  eV) and copper ( $W_{Cu} = 5.22$  eV) coatings were used [144]. The behavior of  $\Phi_{B1}$  and  $\Phi_{B2}(0)$  and of  $n_{s0}$  vs. the metal workfunction are shown in Figure 4.6 (a) and (b), respectively, with the error bars coming from the standard deviations of measured values at different tip positions.  $\Phi_{B2}(0)$  and  $n_{s0}$  were found to be independent of the tip metal coating both on AlGaIn/GaN and on Gr/AlGaIn/GaN, with smaller values of  $\Phi_{B2}(0)$  in the latter case, which is consistent with the larger values of  $n_{s0}$ . For all tip metal coatings, the  $\Phi_{B1}$  values measured onto bare AlGaIn are much higher than on Gr/AlGaIn. Interestingly, while  $\Phi_{B1}$  significantly increases as a function of  $W_M$  in the case of the tip/AlGaIn contact, it was almost independent of  $W_M$  for the tip/Gr/AlGaIn contacts.

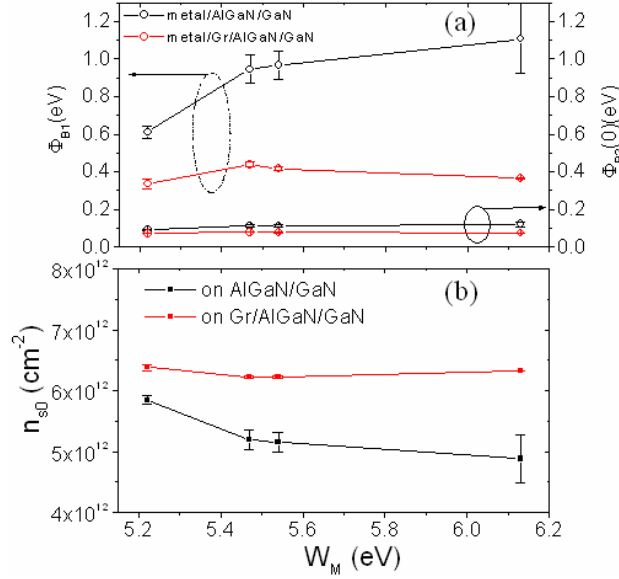


**Figure 4.6:** Behavior of  $\Phi_{B1}$ ,  $\Phi_{B2}(0)$  (a) and  $n_{s0}$  (b) versus the metal workfunction for the AlGaN/GaN and Gr/AlGaN/GaN heterostructures.

According to the Schottky-Mott (SM) model of metal/semiconductor Schottky contacts [201,202] the expected barrier height for an ideal rectifying contact should be given by the difference between the metal workfunction  $W_M$  and the semiconductor electron affinity ( $\chi_{AlGaN} \approx 2.7$  in the case of the  $Al_{0.25}Ga_{0.75}N$  alloy). However, this condition is rarely obtained in reality, since the Schottky barrier formation depends also on the surface states of the semiconductor, which can cause a Fermi level pinning at the interface with the metal (Bardeen model [203]). In the presence of a very high surface states density, a barrier height value independent on the metal workfunction can be found. In most of cases, an intermediate behavior between these two extremes is observed, with  $\Phi_B$  increasing as a function of  $W_M$  following approximately a linear trend but with a slope  $S = d\Phi_B/dW_M < 1$  (interface index). This is what was observed in the case of the tip/AlGaN barrier  $\Phi_{B1}$  in our experiment, with  $S \approx 0.84 \pm 0.26$ .

Due to the different Gr doping levels by charge transfer from various metals [144], different workfunctions of Gr under the tip could be expected using different tip coatings [204]. This would imply a dependence of the tip/Gr/AlGaN barrier height on the metal tip workfunction, assuming that the contact follows the SM rule. Indeed, Gr contacts on several bulk semiconductors, such as Si, 4H-SiC, GaAs and



GaN, have been found to approximately obey the SM rule [161], whereas no specific studies have been carried out for Gr on semiconductor heterostructures (i.e., in the presence of an underlying buried 2DEG). It is noteworthy that the experimentally found  $\Phi_{BI}$  trend independent of  $W_M$  (see Figure 4.6(a)) suggests that the behavior of the Gr/AlGaN contact is dominated by surface states of the AlGaN. In the case of the Gr/AlGaN/GaN heterostructure, these states are located in close proximity to the Gr and are able to efficiently exchange charge with it. The very low Gr/AlGaN Schottky barrier, compared to the value  $W_G - \chi_{AlGaN} \approx 1.8$  eV expected in the case of an ideal Gr contact (with  $W_G \approx 4.5$  eV for intrinsic Gr), indicates a high n-type doping of Gr, which is consistent with the donor like character of AlGaN surface states.

According to the Bardeen model of Schottky barriers with high interface states density [203], the Gr/AlGaN Schottky contact can be described assuming the presence of a very thin insulating layer (vacuum) with thickness  $t$  between Gr and AlGaN (see Figure 4.7), which can be considered completely transparent to electron transport but able to withstand a potential drop  $\Delta$  across it. The presence of an ultra-thin vacuum layer between Gr and AlGaN is reasonable, considering the v. d. W. bonding between the two surfaces. The positively charged AlGaN surface states are located on one side of this insulating layer, while the Gr 2DEG with electron density  $n_{Gr}$  is located on the other side.

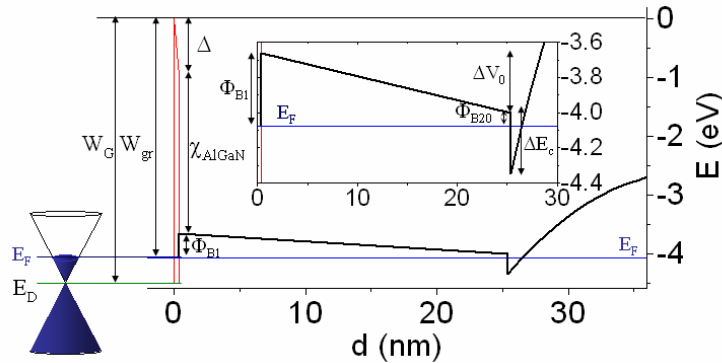


**Figure 4.7:** Calculated conduction band diagram for the Gr/AlGaN/GaN heterostructure at zero bias.

According to Gauss's law, the potential drop  $\Delta$ , indicated in the band diagram in Figure 4.7, must be related to  $n_{gr}$  as:

$$\Delta = qn_{gr}t/\epsilon_0 \quad (4.13)$$

The separation  $t$  between a Gr layer and AlGaN was determined by tAFM, following a procedure demonstrated in previous works to measure the separation between Gr and SiO<sub>2</sub> [205]. To this aim, Gr mechanically exfoliated from HOPG was transferred onto AlGaN.

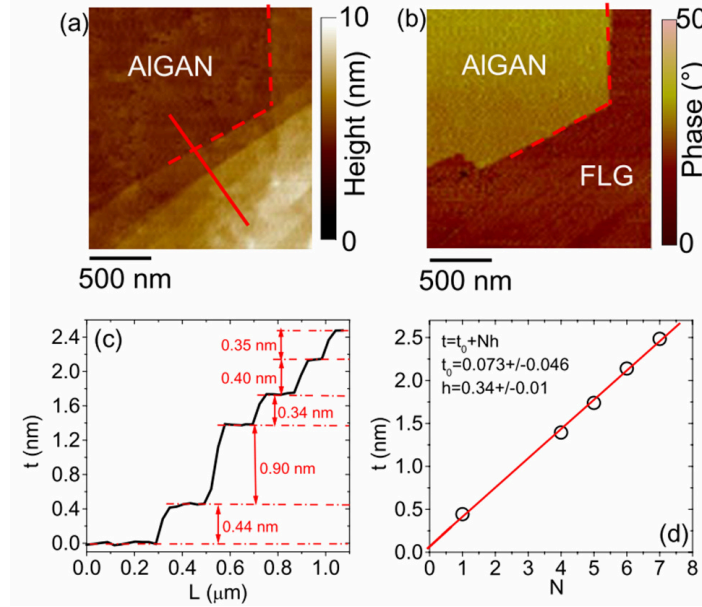


**Figure 4.8:** AFM morphology (a) and phase (b) images of a region including bare AlGaN and AlGaN coated by few layers of Gr (1, 4, 5, 6 and 7 layers in a step-like fashion). (c) Height profile measured along the indicated line in (a). (d) Height values measured with respect to the AlGaN baseline level as a function of the layer number  $N$ . By linear fitting of the data, the interlayer separation ( $h = 0.34 \pm 0.01$  nm) and the intercept with the height axis ( $t_0 = 0.07 \pm 0.04$  nm) were extracted.

Analyses were carried out on few layers of Gr samples including monolayer and  $n$ -layers regions in a step-like fashion. Figure 4.8, reports the morphology (a) and phase (b) images of a region including bare AlGaN and AlGaN coated by the few layer Gr. Figure 4.8 (c) shows the height profile measured along the indicated line in Figure 4.8 (a). The height separation between Gr monolayer and AlGaN and between the stacked layers is also indicated. In Figure 4.8 (d) the height values measured with respect to the AlGaN baseline level were plotted as a function of the

layer number  $N$ . By linear fitting of the data, the interlayer separation ( $h = 0.34 \pm 0.01$  nm) and the intercept with the height axis ( $t_0 = 0.07 \pm 0.04$  nm) were extracted. The separation between a Gr single layer from the AlGaIn was estimated as  $t = h + t_0$ , i.e.  $t \approx 0.41$  nm.

Therefore, the Gr carrier density  $n_{gr0}$  (at zero bias) can be obtained by solving the equation:

$$\Phi_{B1} = W_G - (E_{F_{gr,0}} - E_D) - \Delta - \chi_{AlGaIn} \quad (4.14)$$

Where  $E_{F_{gr,0}} - E_D$  is the distance between the Fermi level in Gr and the Dirac point:

$$E_{F_{gr,0}} - E_D = \frac{\text{sign}(n_{gr,0}) \hbar v_F \sqrt{\pi n_{gr,0}}}{q} \quad (4.15)$$

Where  $v_F$  the Gr 2DEG Fermi velocity. This latter relation derives from the linear dispersion of energy with respect to momentum in Gr. By solving equation (4.14), the carrier density  $n_{gr0}$  was evaluated and a high n-type doping of Gr was found. As an example,  $n_{gr0} = (1.29 \pm 0.16) \times 10^{13} \text{ cm}^{-2}$  was obtained from the analysis of the representative  $I$ - $V$  curve in Figure 4.3 (d) for the Au tip/Gr/AlGaIn/GaN, while the distribution of  $n_{gr0}$  values at different tip positions is reported in the histogram of Figure 4.9.

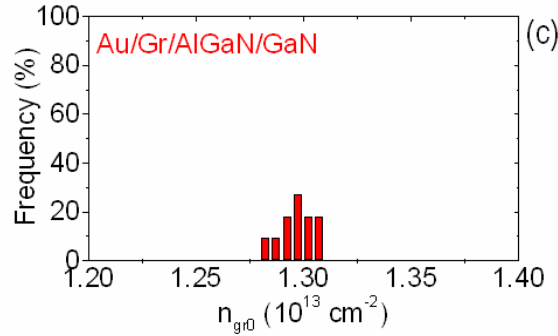


**Figure 4.9:** Histogram of  $n_{gr0}$  at the different positions in the Gr/AlGaIn/GaN heterostructure.

The theoretical Fermi velocity  $v_F \approx 1 \times 10^6$  m/s for ideal, i.e. defect-free, Gr was used in these calculations. We also estimated that a possible local reduction of  $v_F$  due to the presence of defects in the probed Gr area [206] results in a slight increase of  $n_{gr0}$ , which is within the experimental error.

Up to this point, we have extracted the barrier height and the carrier densities of the 2DEG at zero bias by fitting of the forward  $I$ - $V_{tip}$  characteristics and extrapolation to  $V_{tip} = 0$ . In the following, local  $C$ - $V$  measurements under reverse bias made using Scanning Capacitance Microscopy (SCM) are used to determine the dependence of the  $n_s$  and  $n_{gr}$  on the applied bias.

For this aim the SCM were collected adding to the DC bias, a small amplitude-modulating signal at high frequency (100 kHz), applied to the large area contact. A high sensitivity capacitance sensor measured the capacitance variation in response to this signal. Figure 4.10 (a) shows a schematic representation of the SCM experimental setup (see insert) and two representative  $C$ - $V_{tip}$  curves (with  $C$  the capacitance per unit area) measured on the AlGaIn/GaN and on the Gr/AlGaIn/GaN heterostructures using an Au coated tip.

At  $V_{tip} = 0$  capacitance values of  $\sim 0.31 \mu\text{F}/\text{cm}^2$  and  $\sim 0.35 \mu\text{F}/\text{cm}^2$  were measured on AlGaIn/GaN and Gr/AlGaIn/GaN, respectively. The curves exhibit almost constant (for AlGaIn/GaN) or slightly decreasing (for Gr/AlGaIn/GaN) capacitance starting from  $V_{tip} = 0$  up to a certain negative bias and, thereafter, a rapid decrease to very low capacitance values ( $\sim 0.1 \text{ nF}/\text{cm}^2$ ) for bias  $|V_{tip}| > |V_{th}|$ , defined as the threshold voltage.

For  $|V_{tip}| < |V_{th}|$ , i.e. up to AlGaIn/GaN 2DEG depletion, the capacitance of the AlGaIn/GaN system can be described as the series combination of two contributions: (i)  $C_{AlGaIn}$ , i.e., the capacitance of the plane capacitor with the metal tip and the 2DEG as electrodes; (ii)  $C_{Q,ord}$ , the quantum capacitance of the AlGaIn/GaN “ordinary” 2DEG [ 207 ]. The latter term is expressed as  $C_{Q,ord} = m_{eff}q^2/(\pi\hbar^2)$  [208], where  $m_{eff} = 0.22 m_e$  is the electron effective mass in the  $\text{Al}_x\text{Ga}_{1-x}\text{N}/\text{GaN}$  quantum well, and is of the order of  $14.7 \mu\text{F cm}^{-2}$ , i.e., almost 50 times larger than the measured capacitance at  $V_{tip} = 0$ . Hence, it can be concluded that its weight in the series combination is almost negligible, and the first term ( $C_{AlGaIn}$ ) gives rise to the higher capacitance level in the  $C$ - $V_{tip}$  curve for  $|V_{tip}| < |V_{th}|$ . For  $|V_{tip}| > |V_{th}|$  i.e., under full depletion of the 2DEG, the AlGaIn/GaN behaves as a single unintentionally doped semiconductor layer with large thickness, giving rise to a very low capacitance level.

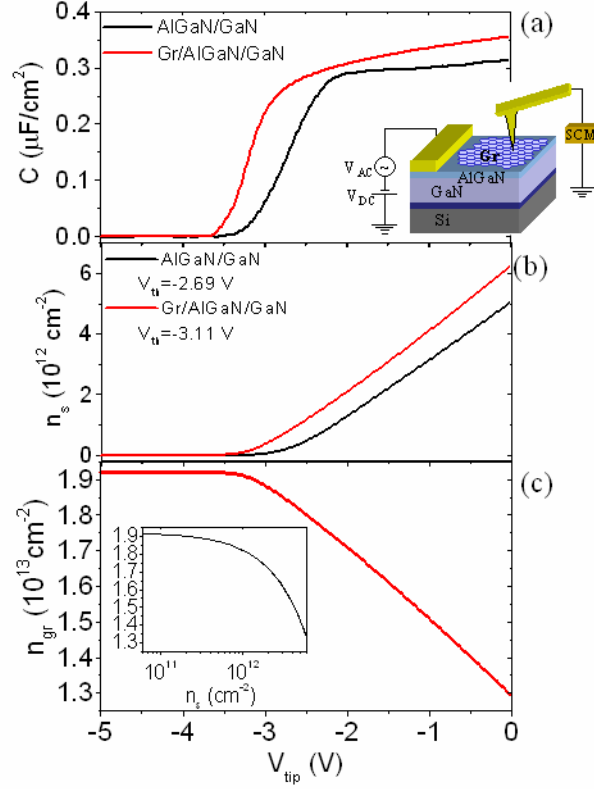


**Figure 4.10:** (a) Two representative  $C$ - $V_{tip}$  curves measured on the AlGaIn/GaN and on the Gr/AlGaIn/GaN heterostructures using an Au coated tip. In the insert, there is a schematic representation of the SCM experimental setup. (b) Electron density  $n_s$  of AlGaIn/GaN 2DEG as a function of  $V_{tip}$ , obtained by integration of the representative  $C$ - $V_{tip}$  curves in (a). (c) Electron density  $n_{gr}$  in Gr, as a function of  $V_{tip}$ . The relation between  $n_s$  and  $n_{gr}$  is shown in the insert.

In the case of the Gr/AlGaIn/GaN heterostructure, an additional capacitance term, i.e., the Gr quantum capacitance  $C_{Q,gr}$  [209,210] should be added to the series combination of the first two terms.  $C_{Q,gr}$  contribution can be expressed as:

$$C_{Q,gr}(n_{gr}) = \frac{2q^2}{\hbar v_F \sqrt{\pi}} \sqrt{n_{gr}} \quad (4.16)$$

and depends on the electron energy and resembles the linear behavior of the density of states  $D$  with  $|E_{Fgr} - E_D|$ .

This quantum capacitance term is also much higher than  $C_{AlGaN}$  and, therefore, can be neglected in the series combination.

$C_{Q,ord}$  and  $C_{Q,gr}$  are reported together with the measured capacitance of the Gr/AlGaN/GaN heterostructure ( $C_{tot}$ ) in Figure 4.11. This comparison shows that both  $C_{Q,ord}$  and  $C_{Q,gr}$  are much larger than  $C_{AlGaN}$ .

From the previous discussion results, both for the AlGaN/GaN and the Gr/AlGaN/GaN heterostructures, the  $C$ - $V_{tip}$  curves are related to the 2DEG density  $n_s$  at the AlGaN/GaN interface [211]. Hence, the  $n_s$  dependence on  $V_{tip}$  can be obtained by integration of these curves [15], i.e.:

$$n_s(V_{tip}) = \int_0^{V_{tip}} C(V) dV \quad (4.17)$$

Figure 4.10 (b) shows the  $n_s$  -  $V_{tip}$  curves obtained by integration of the representative  $C$  -  $V_{tip}$  curves of Figure 4.10 (a). Both curves exhibit a linear decrease of  $n_s$  vs.  $|V_{tip}|$ , until  $n_s \approx 0$ . A simple way to determine the threshold voltages for the two heterostructures is by Fitting the linear region and taking the intercept with the  $n_s = 0$  baseline. A higher  $V_{th}$  value is obtained in the case of the Gr/AlGaN/GaN heterostructure ( $V_{th} = -3.11$  V) than in the case of the AlGaN/GaN heterostructure ( $V_{th} = -2.69$  V), which is consistent with the higher values of  $n_{s0}$ .

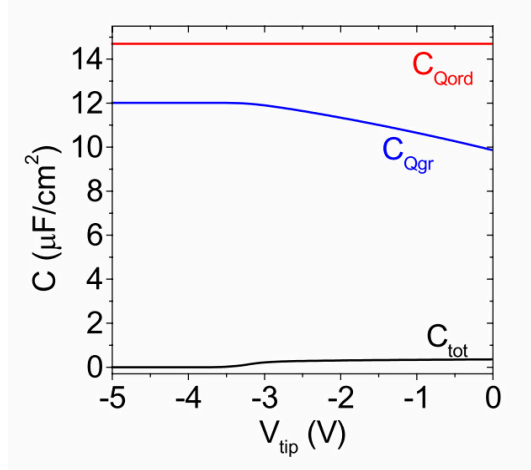


**Figure 4.11:** Measured capacitance of the Gr/AlGaN/GaN heterostructure ( $C_{tot}$ ) compared with the quantum capacitance of the AlGaN/GaN 2DEG ( $C_{Q,ord}$ ) and the Gr quantum capacitance ( $C_{Q,gr}$ )

Clearly, in the case of a biased Gr/AlGaIn/GaN heterostructure, due to the electrostatic coupling between the 2DEGs in close proximity, the changes of  $n_s$  in the AlGaIn/GaN quantum well due to the applied bias induce also variations of the carrier density  $n_{gr}$  in Gr.

As reported in Figure 4.12 the energy band structures of the Gr/AlGaIn/GaN heterostructure at equilibrium ( $V_{tip} = 0$ ) and under reverse ( $V_{tip} < 0$ ) or forward polarization ( $V_{tip} > 0$ ) are schematically depicted in Figure 4.12 (a), (b) and (c), respectively. Here a very thin ( $\sim 0.41$  nm) separation, previously determined as the one between a Gr layer and AlGaIn (Figure 4.8), has been assumed as a vacuum barrier of the Gr layer from the AlGaIn surface, which exhibit a donor-like surface states density  $n_d$ . The carrier density  $n_s(V_{tip})$  of the 2DEG at the AlGaIn/GaN interface can be directly obtained by capacitive measurements, as discussed above. The Gr carrier density under reverse bias can be evaluated by applying the Gauss' law, as schematically illustrated in Figure 4.12 (b).

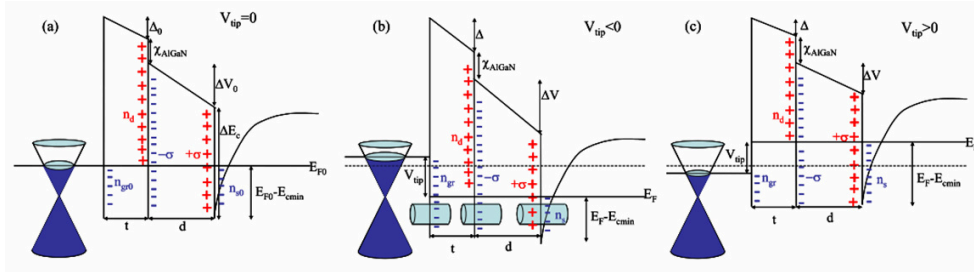


**Figure 4.12:** The energy band structures of the Gr/AlGaIn/GaN heterostructure at equilibrium ( $V_{tip} = 0$ ) (a), under reverse ( $V_{tip} < 0$ ) (b) or forward polarization ( $V_{tip} > 0$ ) (c).

In particular, the Gauss' law applied at the interface between Gr and the vacuum barrier yields:

$$\frac{\epsilon_0 \Delta}{t} = -qn_{gr} \quad (4.18)$$

Applied to the vacuum barrier/AlGaIn interface, it yields:

$$-\frac{\epsilon_0 \Delta}{t} + \frac{\epsilon_0 \epsilon_{AlGaIn} \Delta V}{d} = q(n_d - \sigma) \quad (4.19)$$

Finally, the application to the AlGaIn/GaN gives:

$$-\frac{\epsilon_0 \epsilon_{AlGaN} \Delta V}{d} = q(\sigma - n_s) \quad (4.20)$$

By combining Equations (4.18),(4.19) and (4.20), the following relation between Gr and AlGaN/GaN 2DEGs carrier densities is obtained:

$$n_{gr} = n_d - n_s \quad (4.21)$$

According to Equation (4.21), the surface donors density at  $V_{tip} = 0$  is  $n_{d0} = n_{gr0} + n_{s0}$ , where  $n_{gr0}$  and  $n_{s0}$  are the Gr and AlGaN/GaN 2DEGs carrier densities at  $V_{tip} = 0$ , which have been determined as discussed above. Assuming that  $n_d \approx n_{d0}$ ,  $n_{gr}(V_{tip})$  can be expressed as:

$$n_{gr}(V_{tip}) = n_{gr0} + n_{s0} - n_s(V_{tip}) \quad (4.22)$$

This is illustrated in Figure 4.10 (c), which shows an almost linear increase of  $n_{gr}$  with  $|V_{tip}|$  up to a saturation value  $\sim 1.9 \times 10^{13} \text{ cm}^{-2}$  for  $|V_{tip}| \approx |V_{th}|$ . Clearly, the initial increase of  $n_{gr}$  follows the decrease of  $n_s$ , whereas the constant  $n_{gr}$  for  $|V_{tip}| > |V_{th}|$  is related to the low capacitance value of the AlGaN/GaN system after full 2DEG depletion. The relation between  $n_s$  and  $n_{gr}$  is reported in the insert of Figure 4.10 (c), which demonstrates a  $\sim 100\times$  decrease of  $n_s$  corresponding to a  $1.5\times$  increase of  $n_{gr}$ .

#### **4.1.3 From Schottky to ohmic graphene contacts to AlGaN/GaN heterostructures: role of the AlGaN layer microstructure**

By way of comparison sample B was also electrical characterized following the same procedure illustrated for sample A to collect matrixes of local  $I-V$  characteristics by CAFM using an Au coated tip as a nanometer size metal contact both on the bare and Gr-coated AlGaN surface.

Figure 4.13 summarizes the  $I-V$  characteristics (with the fitting of representative forward bias of  $\ln(I)-V$  curves reported in the inserts of each graphitic) of both sample A (a,b) and sample B (c,d) on bare and on Gr-coated AlGaN.

As expected, the  $I-V$  characteristics measured at the different positions on bare AlGaN of sample B exhibit a rectifying behavior, already observed for sample A and typically found for not alloyed metal contacts to AlGaN.

According to the thermionic emission model for an equivalent circuit of two diodes back-to-back in series described above to calculate  $\Phi_{B1}$  and  $\Phi_{B2}(0)$  for sample A, also for bare AlGaN of sample B  $\Phi_{B1}$  and  $\Phi_{B2}(0)$  where extracted.



The average  $\Phi_{B1}$  and  $\Phi_{B2}(0)$  values over the set of curves for sample B are  $\Phi_{B1} = 0.63 \pm 0.17$  eV and  $\Phi_{B2}(0) = 0.09 \pm 0.01$  eV. It is possible to compare these results with the values obtained in the case of bare AlGaN for sample A ( $\Phi_{B1} = 0.95 \pm 0.12$  eV and  $\Phi_{B2}(0) = 0.11 \pm 0.01$  eV). It is evident that, while the  $\Phi_{B2}(0)$  is very similar for both substrates, the  $\Phi_{B1}$ , which is related to the Schottky contact between the metal and the AlGaN surface, is definitely lower for sample B and the standard deviation is larger.

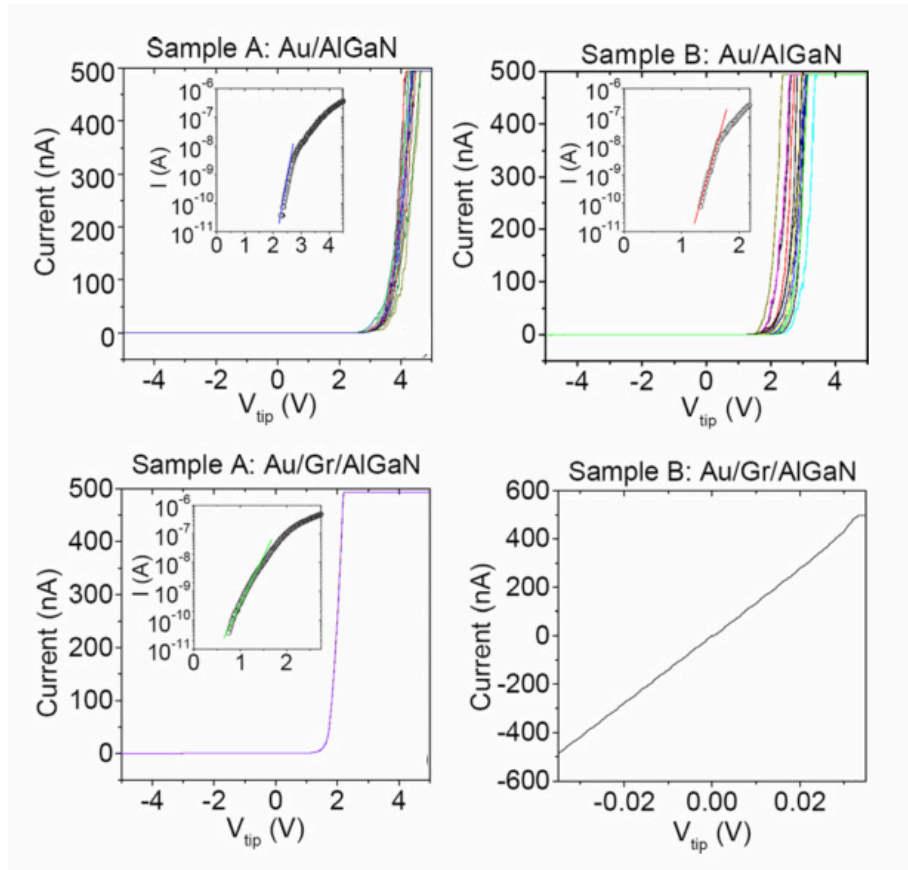


**Figure 4.13:**  $I$ - $V$  characteristics collected on the bare AlGaN surface of samples A (a) and B (b) and on the Gr-coated regions of samples A (c) and B (d). The fitting of representative forward bias  $I$ - $V$  curves (with  $I$  on logarithmic scale) using the thermoionic emission model has been reported in the insets of (a), (b) and (c).

The histograms of the  $\Phi_{BI}$  values obtained for the different Au tip positions on both samples are also reported in Figure 4.14 where lower  $\Phi_{BI}$  values and higher spreads between values (red columns) are evident for sample B compared with  $\Phi_{BI}$  of sample A (blue columns).  $\Phi_{BI}$  values calculated above in the case of Gr on sample A are also reported showing a lower average value and a much narrower distribution.

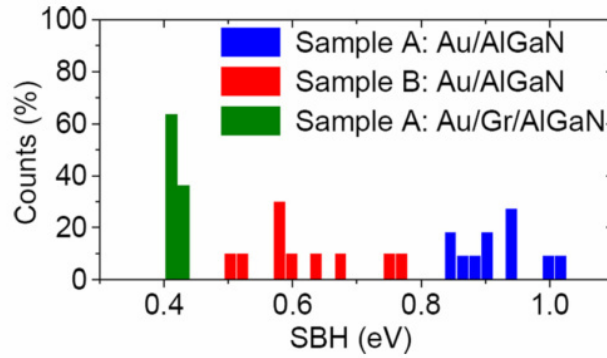


**Figure 4.14:** Histograms of the SBH values obtained from the  $I$ - $V$  characteristics at different tip positions on bare AlGaN (samples A and B) and Gr-coated AlGaN (sample A).

The lower  $\Phi_{BI}$  for sample B can be ascribed to the presence of the V-shaped depressions in the AlGaN barrier layer, described in the previous chapter and acting as preferential current paths from the metal tip to the 2DEG. This was also confirmed collecting simultaneously the morphologies and the corresponding current maps on the AlGaN surface. As reported in Figure 4.15, the depressions visible on the AFM morphology of sample B (Figure 4.15 (a)) perfectly corresponds with an increase of local conduction on the current map (Figure 4.1 (b)).

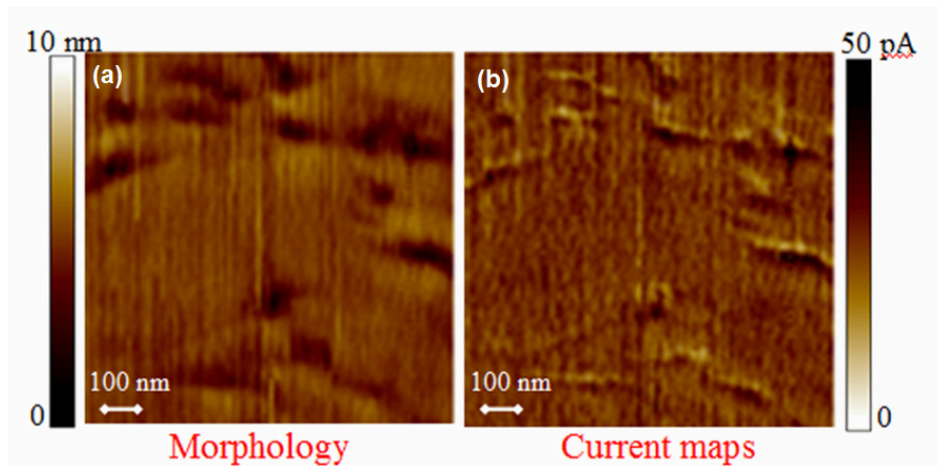


**Figure 4.15:** (a) AFM Morphology and (b) correspondent current map collected for the a highly defective AlGaIn surface of sample B.

The  $I$ - $V$  characteristics measured at different surface positions of the Gr-coated sample B (Figure 4.13 (d)) are reported beside the analogue set of measures collected on Gr on sample A (Figure 4.13 (c)). Recalling that the already discussed case of Gr on sample A shows a rectifying behavior, an interestingly different result is observed in the case of Gr on sample B. In fact, the  $I$ - $V$  characteristics reveal in this case an ohmic behavior. Again, a very limited spread between the different  $I$ - $V$  curves is found, confirming also in this case an excellent lateral homogeneity induced by the presence of Gr.

The ohmic behavior of the Gr contacts to AlGaIn with a high density of V-defects (sample B) can be explained considering the combination of several effects.

In the first approximation:

the local reduction of the AlGaIn thickness in correspondence with the V-shaped defects, as schematically proposed in Figure 4.16 (a) (energy band diagram drawn with by dashed lines)

the value of the Gr/AlGaIn  $\Phi_{Bl}$  lower than for the bare AlGaIn (energy band diagram in Figure 4.16 (b))

are expected to locally increase the direct or Fowler-Nordheim tunnelling rates through the AlGaIn barrier layer, giving rise to many low resistance conduction paths between Gr and the AlGaIn/GaN 2DEG.

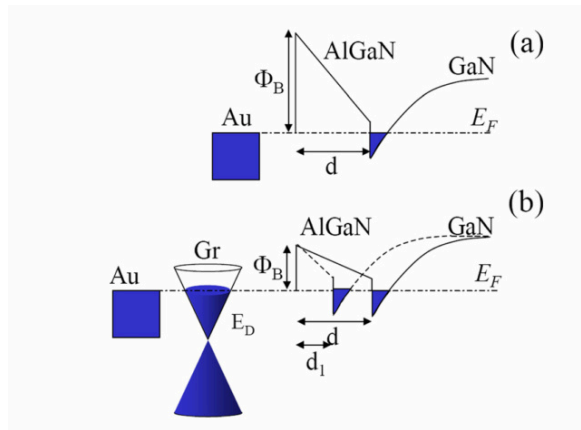


**Figure 4.16:** Schematic band-diagrams for Au contacts (a) on planar AlGaN and Au/Gr contacts (b) on planar AlGaN (solid lines) and on a V-defect (dashed lines), where the AlGaN thickness is locally reduced.

In addition, the averaging effect induced by Gr electrode (demonstrated by the narrow spread between curves collected in different positions of the surface) can be supposed to connect in series several of these vertical conductive paths. It can be assumed since the V-shaped defects separation is similar or even lower (see Figure 3.13 (b)) than the typical Gr electron mean free path which is of the order of  $\sim 0.1 \mu\text{m}$  if supported by a substrate [110]. This would also explain the highly homogeneous Gr ohmic contact even in the presence of a high density of V-defects in the AlGaN.

## 4.2 Lateral and vertical electrical characterization of epitaxial graphene on SiC

### 4.2.1 Lateral current transport

The characterization of lateral current transport in EG grown on SiC has been carried out both at macroscopic scale, using properly fabricated test patterns, and at micro and nanoscale, using scanning probe microscopy techniques.

The EG sheet resistance ( $R_{sh}$ ) was first evaluated using TLM test patterns. Few (from 2 to 3) layers Gr samples grown at 1600°C were used for this experiment. Each TLM test pattern consisted of a set of Ni/Au ohmic contacts at different spacing (from 20 to 100  $\mu\text{m}$  width) on a laterally isolated rectangular EG strip defined by optical lithography and O<sub>2</sub> plasma etching. TLM structures with two different orientations were fabricated, i.e. parallel or perpendicular to the substrate steps as graphically illustrated in Figure 4.17 (a) and (b) and in the correspondent optical image in Figure 4.17 (c).

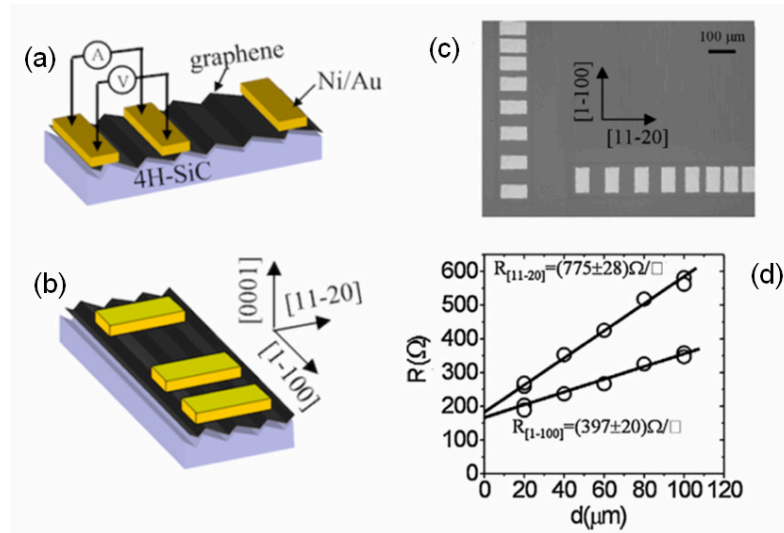


**Figure 4.17:** Schematic representations of TLM test patterns oriented in the direction (a) parallel ([1-100]) and (b) orthogonal [11-20] to the substrate steps. (c) Optical image of the TLM devices. Measured resistance  $R$  vs. the pad distance (d) in the two directions. The calculated sheet resistances from the fit of experimental data are also reported.

These two different configurations allowed evaluating the effects of SiC substrate on the Gr transport properties. The measured resistance  $R$  between pairs of adjacent pads as a function of the distance between pads is reported in Figure 4.17 (d) for the two TLM orientations. The sheet resistances in the two directions were evaluated as the slopes of the two sets of experimental data. In the [11-20] direction a value of  $R_{sh[11-20]} = 775 \pm 28 \text{ } \Omega/\text{sq}$  was found, i.e. almost a factor of 2 higher than the sheet resistance  $R_{sh[1-100]} = 397 \pm 20 \text{ } \Omega/\text{sq}$  in the [1-100] direction. These data clearly demonstrate a macroscopic anisotropy of the lateral current transport in EG.

This anisotropy was reflected in the electrical characteristics of EG-based FETs. Top gated FETs with the channel length parallel or perpendicular to the substrate steps were fabricated on the same EG samples used for TLM structures. After lateral insulation of individual device structures by EG selective etching with  $\text{O}_2$  plasma, source and drain contacts were obtained by lift-off of a Ni/Au bilayer. A  $\sim 40 \text{ nm}$  thick  $\text{Si}_3\text{N}_4$  gate dielectric was deposited by Plasma-Enhanced Chemical Vapor Deposition (PECVD) and, subsequently, selectively etched by  $\text{CHF}_3$  plasma to open the source and drain contact regions. Finally, top gate contacts were obtained by Pt/Au lift-off. A schematic cross-section of the used FET structure is shown in Figure 4.18 (a).

The channel devices were properly built with gate length  $L_G$  from 5 to 20  $\mu\text{m}$  and channel width  $W = 100 \text{ } \mu\text{m}$ , to maximize the contribution of the channel resistance with respect to the contact resistance on the source-drain current. The channel conductance  $g_D = [dI_d/dV_d]_{V_g}$  of EG-based FETs with the channel length in the direction parallel ([1-100]) or perpendicular ([11-20]) to substrate steps was evaluated. For both channel orientations, the channel conductance vs. the top-gate bias ( $g_D - V_{tg}$ ) characteristics (Figure 4.18 (b)) exhibit an ambipolar behavior, with the minimum conductivity (neutrality point) shifted to negative gate bias ( $V_{NP} \approx -10 \text{ V}$ ), consistently with an average n-type doping of EG. The carrier density ( $n$ ) as a function of the gate bias (upper scale in Figure 4.18 (b)) was calculated as  $n = \epsilon_0 \epsilon (V_{tg} - V_{NP}) / (qt)$ , where  $\epsilon_0$  and  $\epsilon \approx 7$  are the vacuum and  $\text{Si}_3\text{N}_4$  relative dielectric constants, respectively,  $q$  is the electron charge and  $t \approx 40 \text{ nm}$  the  $\text{Si}_3\text{N}_4$  film thickness. Interestingly, a significantly higher channel conductance is measured in the [1-100] direction with respect to the [11-20] direction. As an example, at  $V_{tg} \approx 7$ ,  $g_{D[1-100]} \approx 2.3 \text{ mS}$ , i.e.  $\sim 77\%$  higher than  $g_{D[11-20]} \approx 1.3 \text{ mS}$ . The effective channel mobility  $\mu$  in the electron branch was also evaluated as  $\mu = g_d / (qn)$  and is depicted in Figure 4.18 (c). The mobility values for the two

orientation are very similar ( $\sim 2900 \text{ cm}^2\text{V}^{-1}\text{s}^{-1}$ ) at  $V_{tg}$  approaching the neutrality point, whereas  $\mu_{[11-20]} \approx 830 \text{ cm}^2\text{V}^{-1}\text{s}^{-1}$  and  $\mu_{[1-100]} \approx 1470 \text{ cm}^2\text{V}^{-1}\text{s}^{-1}$  were obtained at  $V_{tg} = 0 \text{ V}$ .

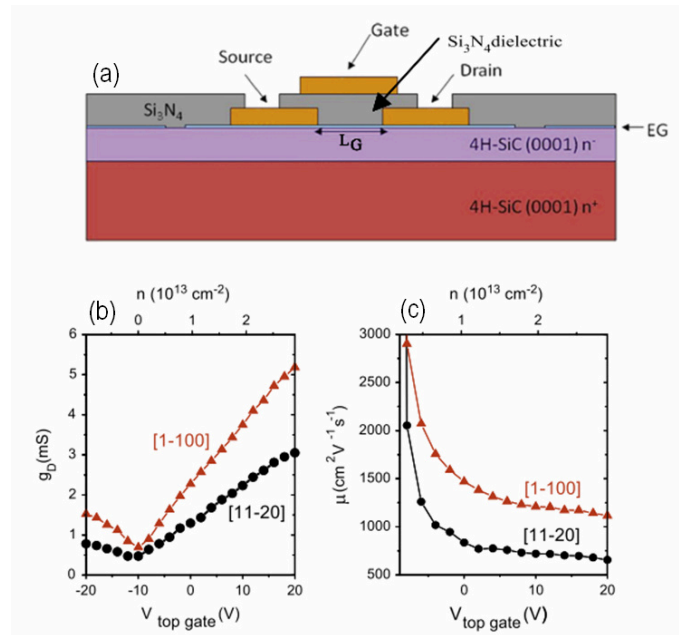


**Figure 4.18:** Cross-section schematics of a top-gated EG field effect transistor with channel length  $L_G = 10 \mu\text{m}$  and channel width  $W = 100 \mu\text{m}$  (a). Channel conductance vs. top-gate bias and carrier density for FETs with the channel length along the [11-20] direction, i.e. orthogonal to the SiC steps, and the [1-100] direction, i.e. parallel to the SiC Steps (b). Calculated mobility  $\mu$  in the electron branch for FETs with the channel length along [11-20] and [1-100] directions (c).

Beside this macroscopic analysis, a microscopic investigation was also performed using CAFM to get a direct comparison between topography and electrical properties with nanoscale lateral resolution [111]. Pt/Ir coated highly-doped Si tips (tip apex curvature radius  $r_{tip} \approx 20 \text{ nm}$ ) were used as probes. Measurements were carried out at room temperature. Local conductance maps were obtained measuring the current flowing laterally in EG between the nanometric tip and the macroscopic ohmic contact of a TLM pad. During the scan, a  $\sim 10 \text{ mV}$  bias was applied to the macroscopic contact and a current amplifier connected to the tip measured the current. Figure 4.19 (a) and (b) report the morphology and the corresponding

current map collected on EG over a  $1\ \mu\text{m} \times 1\ \mu\text{m}$  area. The morphology and current line profiles in Figure 4.19 (c) and (d) clearly indicate a significant decrease from  $\sim 1\ \mu\text{A}$  to  $\sim 0.4\ \mu\text{A}$ , i.e., by more than a factor of 2, in the local current measured on the (11-2n) facets compared to the values measured on the (0001) basal plane terraces.

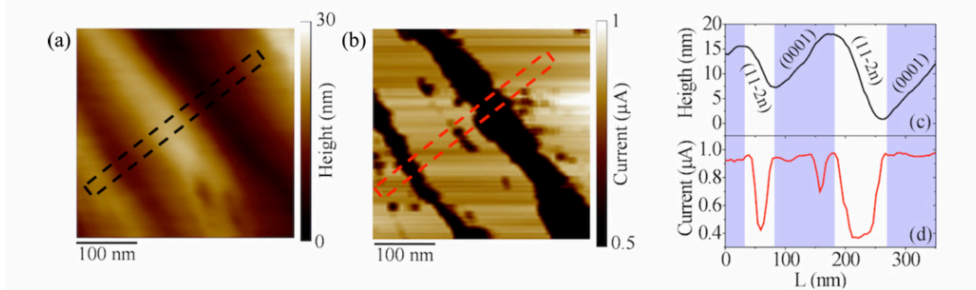


**Figure 4.19:** Surface morphology (a) and the corresponding current map (b) measured by CAFM on the as-grown EG/4H-SiC(0001) sample. Line-profiles of the height (c) and of the current (d) along the indicated directions in the maps.

In order to get deeper analyses of the resistance contributions leading to the observed local reduction of current on (11-2n) facets than on the basal plane, CAFM measurements have been performed very close to the macroscopic contact [28]. Figure 4.20 (a) reports the 3D plot of the surface morphology measured by AFM in a Gr region partially covered by a 200 nm-thick Ni/Au pad belonging to a TLM structure (oriented parallel to the substrate steps). A representative surface morphology and the corresponding resistance map in a  $100\ \text{nm} \times 100\ \text{nm}$  square (indicated by the circle of Figure 4.20 (a)) are reported in Figure 4.20 (b) and (c), respectively. The scanned region includes both (0001) and (11-2n) faces, as shown in the line profile reported as insert of Figure 4.20 (b). A region where the Ni/Au contact partially covers EG is also present in the topmost part of the images. Very low resistance values (dark blue contrast in Figure 4.20 (c)) are measured when the tip is scanned directly on that contact area, whereas a sudden increase of the local resistance can be observed moving from the contact into EG. Interestingly significantly different resistance values are measured on the (11-2n) and (0001) faces. This is clearly shown in Figure 4.20 (d), reporting a line-scan of the resistance values extracted from Figure 4.20 (c) along the dashed horizontal arrow. The local resistance  $R$  measured onto EG includes two different



contributions, i.e. the tip/Gr contact resistance ( $R_{Ctip}$ ) and the local EG sheet resistance  $R_{EG}$ . Being  $R_{Ctip}$  due to the current tunnelling through the Schottky barrier between the tip and EG, it is strongly dependent on the tip/Gr separation and can be minimized by properly setting the contact force between the tip and EG [212].

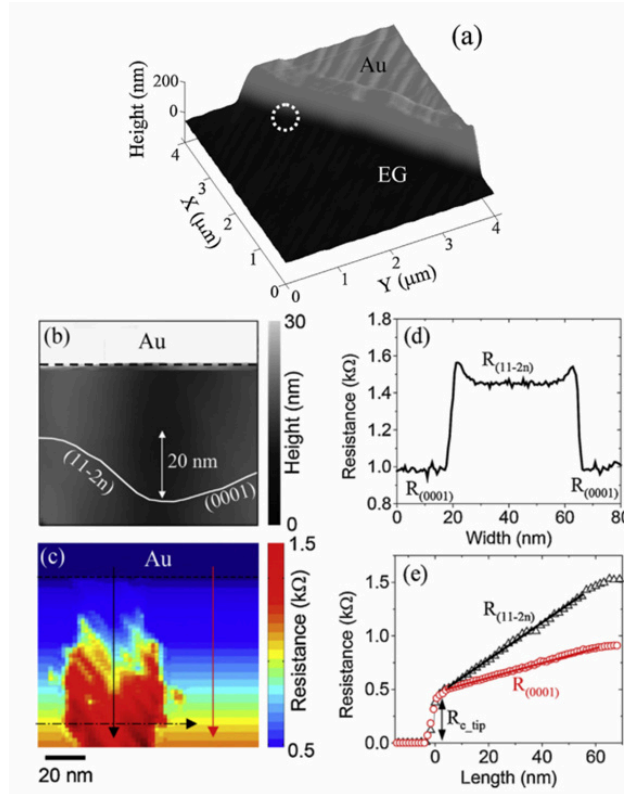


**Figure 4.20:** 3D projection of the surface morphology measured in a region nearby a 200 nm-thick Ni/Au contact onto EG(a). High resolution morphology (b) and resistance map (c) obtained by CAFM in the 100 nm × 100 nm region indicated in (a) by the circle. Line-scan taken in the direction perpendicular to the steps (d), indicated by the horizontal arrow in (c). Line-scans taken in the direction parallel to the steps along (11-2n) and (0001) faces (e), as indicated by the vertical black and red arrows in (c).

Hence, the preliminary operation before a CAFM measurement was setting the contact force, in order to have reproducible contact resistances from scan to scan. The following approach allows disentangling the  $R_{Ctip}$  and  $R_{EG}$  contributions.

Figure 4.20 (e) reports two representative line-scans showing the resistance variation along the two faces in the directions indicated by the black and red vertical arrows in Figure 4.20 (c).

The sharp resistance increase at the border between metal coated and bare EG can be associated to  $R_{Ctip}$ . Noteworthy, comparable  $R_{Ctip}$  values are obtained on (0001) and (11-2n) faces. Moving further inside uncoated EG, the resistance increases with increasing the distance  $d$  from the contact, but with a higher slope within the (11-2n) facet than on the (0001) basal plane. For small values of  $d$ , a linear dependence of the resistance  $R$  on  $d$  was found. This linear trend is consistent with one dimensional (1D) current path between the tip and the macroscopic contact, i.e. it can be assumed that current flows along a rectangular strip of length  $d$  and width  $w \approx 2r_{tip}$ . Applying the linear TLM theory also to this nanoscale current transport, the measured resistance between the tip and the macroscopic contact can be expressed as  $R = R_{Ctip} + R_{EG} d/w$ . By linear fitting of the data, local sheet resistance values  $R_{EG} \approx 290 \Omega/sq$  and  $R_{EG} \approx 680 \Omega/sq$  have been estimated inside the (0001) terrace and (11-2n) facet respectively. For distances  $d$  higher than  $\sim 60$  nm, the  $R$  vs.  $d$  linear trend tends to saturate, indicating that 1D approximation is not any more valid, but a two dimensional (2D) current transport, with a logarithmic dependence of  $R$  on  $d$ , has to be considered [213]. Nevertheless, even far from the macroscopic contact, the differences in the locally measured resistance can be ascribed to different values of  $R_{EG}$ . In Figure 4.21, the histograms of the  $R_{EG}$  values obtained on 20 different terraces and facets within the sample are reported.

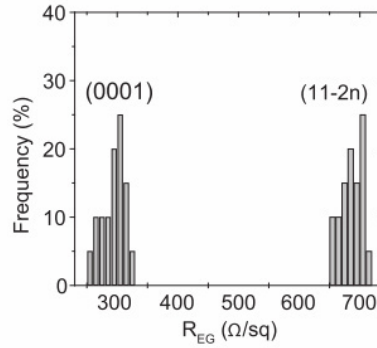


**Figure 4.21:** Histograms of the  $R_{EG}$  values, obtained on 20 different terraces and facets within the EG sample.

The average value and the standard deviation for the two distributions were extracted by Gaussian fitting of the histograms, obtaining  $R_{EG} = (300 \pm 18) \Omega/\text{sq}$  on the terraces and  $R_{EG} = (688 \pm 24) \Omega/\text{sq}$  on facets.

These local variations of the EG resistance are clearly reflected in the macroscopically measured current transport anisotropy using TLM and FET devices. In fact, using a simplified model, the sheet resistance  $R_{sh[11-20]}$  measured by TLM can be described as the series combination of the (0001) terraces resistances of the (11-2n) facets resistances, whereas the sheet resistance  $R_{sh[1-100]}$  in the direction parallel to the steps can be expressed as the parallel combination. Clearly, this purely classical model provides only a qualitative explanation of the difference in the macroscopic resistance values measured by TLM, since it is not able to account for all the effects involved in the anisotropic current transport in EG, including quantum effects related to the interference of electrons wave functions at the boundaries between the (0001) and (11-2n) faces. A more refined modeling of these effects deserves further studies.

Similarly to what already said for the TLM, the macroscopic channel conductance of EG-based FETs measured in the direction perpendicular to the substrate steps can be expressed as the series combination of the local conductance of (0001) terraces and (11-2n) facets, whereas the channel conductance in the direction parallel to the steps can be expressed as the parallel combination. As a matter of fact, the channel conductance resulting from the series combination is lower than the one resulting from the parallel combination.

The electrical characterization of the TLM and FET devices provided macroscopic (average) information on electronic transport in few layers EG, while the CAFM measurements allowed highlighting a different conductivity of EG on terraces and facets.

Other authors, using different measurement techniques, have reported similar anisotropic transport effects. As an example, Yakes et al. [214] evaluated the EG resistance as a function of the steps orientation using a micro-four-point-probe system integrated within a Scanning Electron Microscope, allowing a precise alignment of the probes with respect to the steps. In particular, the measured resistance values with the four probes aligned parallel and perpendicular to the steps was  $660 \Omega$  and  $940 \Omega$ , respectively. Schumann et al. [215] recently performed magneto-transport measurements on EG residing on stepped SiC surfaces, reporting values of  $\sim 3 \text{ k}\Omega$  and  $\sim 5 \text{ k}\Omega$ , respectively, for the longitudinal

resistance  $\rho_{xx}$  (at zero magnetic field) measured on Hall bars patterned in the directions parallel and perpendicular to the steps. Clearly, the absolute resistance values reported in the different literature works depend on the Gr growth conditions as well as on the measuring technique. Noteworthy, a significant difference in the resistance values along the two directions is consistently reported in all these works.

As illustrated in the previous chapter, EG obtained by graphitization of off-axis 4H-SiC (0001) exhibits different structural properties on terraces and facets. In fact, the first carbon layer directly in contact with the substrate shows a change of the chemical configuration as a function of the underlying SiC orientation. This first carbon layer (the “buffer layer”) exhibits a partial  $sp^3$ -hybridization (due to a covalent interaction with SiC) on the (0001) oriented terraces. Conversely, on the (11-2n) oriented facets a complete  $sp^2$ -hybridization and a v. d. W. interaction with the underlying SiC is observed, which makes the same carbon layer a QFEG layer. These different structural properties of epitaxial Gr on terraces and facets can explain the locally different resistance values measured on steps and facets.

In fact, since the average n-type doping of EG on the Si face is ascribed to the presence of the interfacial buffer layer, a local delamination of this layer from (11-2n) facets would imply  $E_F$  very close to  $E_D$  for EG on those regions. This would explain, in part, the higher resistance locally measured on facets with respect to terraces.

In addition to the effect on the local carrier density in EG, the buffer layer’s delamination from facets can have an effect also on “local” Gr transport properties, i.e. on electron mean free path. To this aim, the spatial distribution of electron mean free path in EG was locally probed by scanning-probe-based capacitance measurements [29]. Capacitance was probed using the SCM sensor. Pt coated Si tips with  $\sim 10$  nm contact radius were displaced on an array of positions on bare EG, and local capacitance measured at each position was converted into mean free path according to the procedure illustrated in Ref. [111]. Measurements were performed in a bare EG region of  $\sim 1 \mu\text{m}^2$  size. On that area the tip is displaced on a regular array of  $10 \times 10$  positions spaced by  $\sim 100$  nm and for each position the local electron mean free path ( $l_{loc}$ ) was measured. Clearly this array includes both terraces and facets regions. In Figure 4.17, the histogram of the probed  $l_{loc}$  values is reported. A distribution ranging from  $\sim 10$  nm to  $\sim 120$  nm can be observed, with two main peaks (at  $\sim 30$  nm and  $\sim 100$  nm), that are associated to the mean free path

values on (0001) terraces and (11-2n) facets, respectively. This latter measurement is a direct evidence of a significant improvement ( $\sim 3\times$ ) of transport properties in buffer layer-free EG on facets, probably due to a strong reduction of Coulomb scattering of Gr electrons.

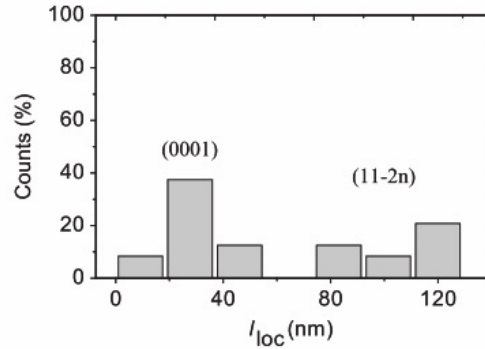


**Figure 4.22:** Histogram of the local mean free path distribution in EG grown on 8° off axis 4H-SiC (0001) by annealing at 1600 C.

Such an increase of Gr electron mean free paths on SiC facets is consistent with recent literature reports showing the evidence of ballistic transport (i.e. large mean free paths) in Gr nanoribbons a selectively grown on SiC facets [216,217].

While the origin of these peculiar effects is currently the object of debate [218,219,213,220,195], there is a common consensus on the different electrical properties of EG on the basal plane and on facets.

An anisotropy of lateral current transport with respect to the steps orientation has been observed, to some extent, also in the case QFEG obtained after hydrogen intercalation at the interface with SiC [221]. The origin of this effect, in this case is different from the as-grown EG, since the buffer layer is expected to be uniformly delaminated from the substrate due to hydrogen intercalation. Among the possible sources of this phenomenon, one of the explanations can be the different local doping of Gr induced by substrate polarization effects from the polar (0001) face (p-type doping) and the non-polar (11-2n) facets (no-doping).

Such effects are particularly relevant in the vertical current transport through QFEG/SiC (0001) Schottky contacts, as shown in the next section.

#### 4.2.2 Vertical current transport through EG/SiC interface

As discussed in the previous chapter, QFEG on two different set of SiC samples, off-axis and an on-axis substrate, were prepared by graphitization and subsequent hydrogen intercalation of the buffer layer.

Before proceeding with the description of the nanoscale current transport characterization by CAFM, it should be point out that, to date, there is a disagreement between the SBH values extracted from  $I$ - $V$  measurements (0.9 - 1 eV) on large contacts and those obtained from  $C$ - $V$  analyses and by XPS (~1.5 eV) [23]. Such a discrepancy can be explained assuming a laterally inhomogeneous Schottky contact, consisting of nanometric size regions with low SBH embedded in the macroscopic contact area with higher SBH. These inhomogeneities act as preferential conduction paths through the Schottky interface and can account for the reduced effective SBH value in forward bias ( $I$ - $V$  characterizations), whereas they are expected not to affect the SBH evaluated from reverse bias  $C$ - $V$  analysis. In this sense CAFM is the ideal tool to characterize the variation of the SBH over the surface by local current-voltage measurements [222]. Preliminary CAFM experiments carried out on QFBLG contacts on off-angled SiC substrates are already reported revealing that these preferential conduction paths correspond to SiC step edges [223].

In the following, the impact of these preferential paths on the reduction of the SBH is better clarified. To this aim, a series of contacts of various sizes (ranging from 200 down to 1  $\mu\text{m}$ ), on two set of substrates with different miscut angles (see Figure 3.24 and the realization method described in the previous chapter), were exploited, in order to change the average size of SiC terraces and the density of step edges comprised in the contact area.

In particular, four groups of samples were fabricated: two groups of Au coated Gr circular contacts and two groups of metal-free Gr circular contacts, both on the on-axis (Figure 3.24 (b,d)) and the on off-axis (Figure 3.24 (a,b)) 4H-SiC substrates.

Au coated Si tips connected to the CAFM current measuring module were used to collect the  $I$ - $V$  characteristics on the Au capped Schottky contacts with different sizes, and to perform nanoscale resolution current mapping [222,223] within the uncapped QFBLG-SiC contacts.

The representative forward bias  $I$ - $V$  characteristics measured on Au-capped QFBLG contacts to on-axis SiC is reported in Figure 4.23 with different diameters,

i.e.  $10\ \mu\text{m}$  (Figure 4.23 (a)) and  $1\ \mu\text{m}$  (Figure 4.23 (b)). As shown in the AFM images in the inserts, several SiC terraces are included in the contact area in the case of the  $10\ \mu\text{m}$  contacts (Figure 4.23 (a)), whereas  $1\ \mu\text{m}$  contacts are mostly fully residing inside SiC terraces (Figure 4.23 (b), red curve) while a fraction of them intercept a step (Figure 4.23 (b), blue curve). The SBH values were extracted from the linear region of the  $\log(I)$ - $V$  curves using the thermoionic emission model. While similar SBH values ( $\sim 1\ \text{eV}$ ) were obtained from the  $I$ - $V$  characteristics measured on the two representative  $10\ \mu\text{m}$  contacts, higher and significantly different SBH values are obtained for the two representative  $1\ \mu\text{m}$  contacts, i.e.  $\sim 1.55\ \text{eV}$  for the contact inside the terrace and  $\sim 1.4\ \text{eV}$  for the contact on the step. These latter measurements revealed the critical role of steps in reducing the  $I$ - $V$  measured effective SBH and suggest a different electrical behavior of the QFBLG interface on terraces and on steps.

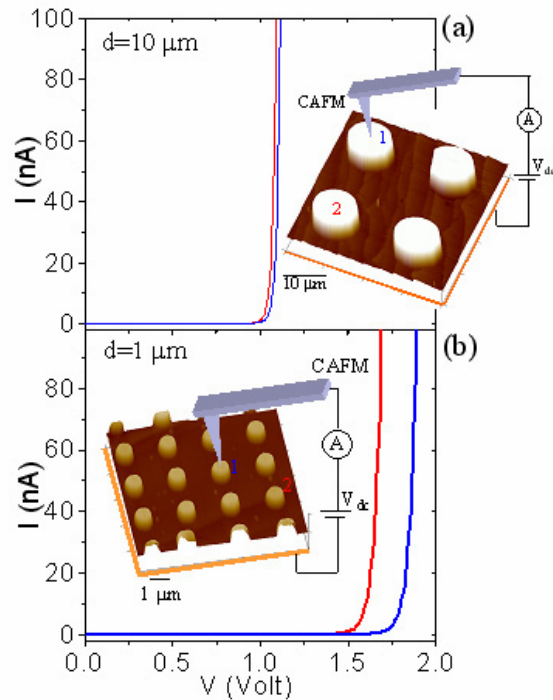


**Figure 4.23:** Representative  $I$ - $V$  characteristics measured on Au capped QFBLG contacts to SiC with  $10\ \mu\text{m}$  (a) and  $1\ \mu\text{m}$  diameter (b). AFM morphologies of the contacts are shown in the inserts.

The dependence of the measured SBH on the contacts diameter is reported in Figure 4.24 for QFBLG contacts fabricated on on-axis SiC (Figure 4.24 (a)) and 3.5° off-axis SiC (Figure 4.24 (b)). The error bars result from the statistics on numerous contacts for each contact diameter. The larger standard deviation obtained for very large (100-200  $\mu\text{m}$  diameter) diodes results from a strong contact-to-contact variation due to SiC defects in the contact area. Clearly, a gradual increase of the SBH is observed for contact diameters below  $\sim 5 \mu\text{m}$  in the large terraces sample and for contact sizes below  $\sim 2 \mu\text{m}$  in the small terraces one. In both cases, the SBH is found to increase up to a value approaching the “ideal” one, measured by C-V and XPS analysis for very small contacts. This trend has been fitted with sigmoid curves, which serve as a guide for eyes.

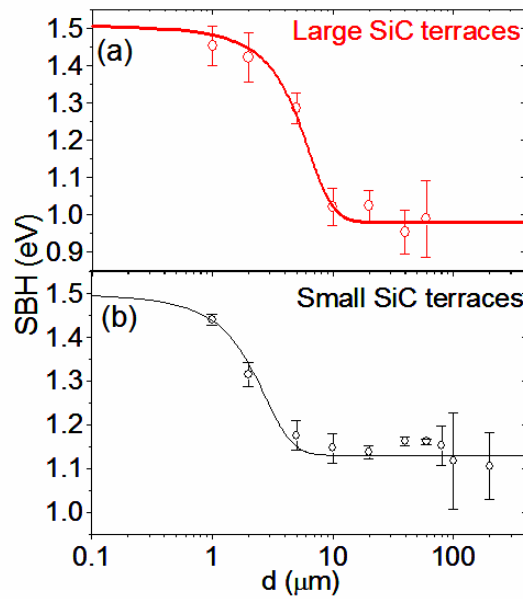


**Figure 4.24:** Dependence of the measured SBH on the contacts diameter for QFBLG contacts fabricated on SiC substrates with large (a) and small terraces (b).

AFM morphologies and the correspondent current maps on the uncapped QFBLG contacts are reported both on on-axis SiC (Figure 4.25 (a, b)) and 3.5° off-axis SiC ((Figure 4.25 (c,d)). Current maps reveal for both samples a higher current flowing through the QFBLG-SiC interface on (11-20) oriented step edges and on (11-2n)



facets than on terraces. This indicates that edges and facets provide low SBH paths, which are responsible for the reduced average Schottky barrier on large contacts. Recently, several literatures works revealed different electrical and structural properties of as-grown Gr residing on the SiC basal plane (0001) and on the step edges or facets, oriented in the (11-20) or (11-2n) directions. In particular, it has been demonstrated a local delamination of the C buffer layer from step edges, with a consequent reduced doping with respect to the  $n^+$ -doping of Gr on the SiC basal plane [195]. Similar local electrical characterization is not available in the case of hydrogen-intercalated QFEG. Macroscopic analyses (XPS, ARPES) indicate an average p-type doping of QFEG, explained as a result of piezoelectric polarization from the (0001) polar SiC surface [152]. On the other hand, lowly doping or even intrinsic Gr is expected on the (11-20) non-polar faces [224]. Using a Shottky-Mott model to describe the QFEG/SiC interface, the lower SBH on the step edges with respect planar (0001) surface can be qualitatively accounted by a locally reduced doping of QFBLG residing on step edges.

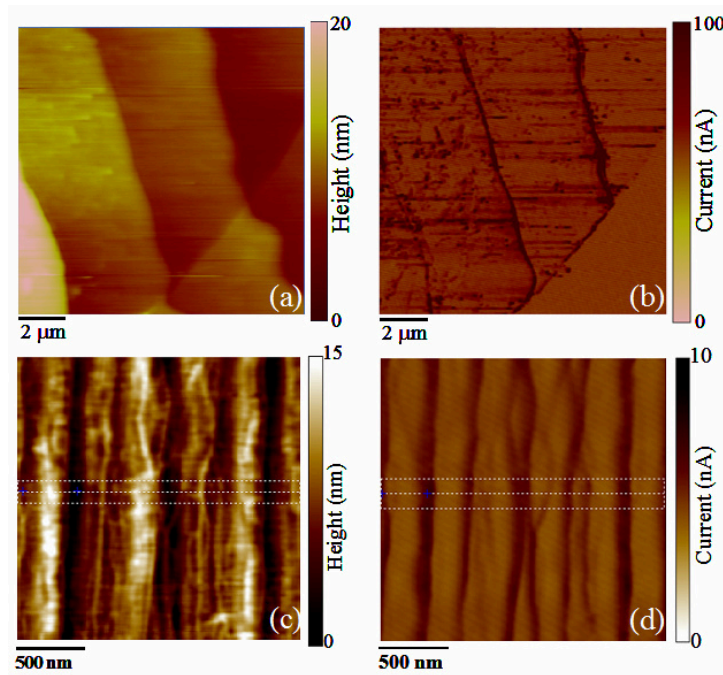


**Figure 4.25:** CAFM morphology (a,c) and current map (b,d) on uncapped QFBLG-SiC contacts to on on-axis SiC (upper images) and 3.5° off-axis SiC (lower images).

The ideality factor ( $n$ ) extracted together with the SBH from the linear region of the  $\log(I)-V$  is reported in Figure 4.26 (a) for the different contacts diameter.

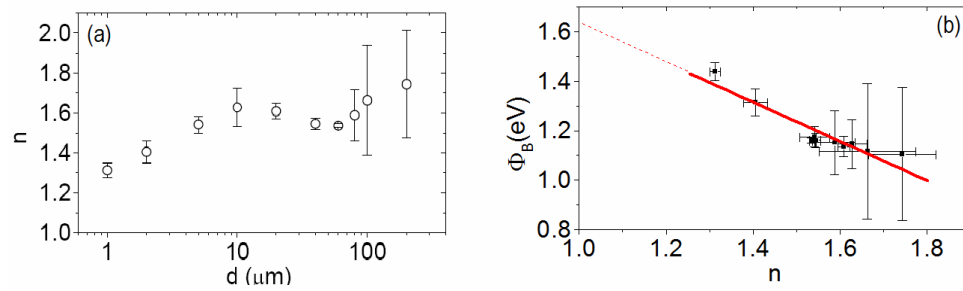


**Figure 4.26:** (a) Dependence of the ideality factor on the contacts diameter for QFBLG contacts fabricated on SiC substrates with small terraces. (b) plot of the ideality factor vs. the correspondent SBH. The red line is the linear fit which indicates that when  $n$  tends to the unity the SBH approximate the value  $\sim 1.6$  eV.

Ideality factor values larger than unity are typically observed in the case of inhomogeneous Schottky barriers. Furthermore, a linear correlation between the SBH and the  $n$  is typically observed in these systems with an increasing barrier height corresponding to a decreasing value of  $n$  [153]. Interestingly, such a correlation is found also in the case of QFEG on SiC where the increase of the SBH value for smaller contacts is accompanied to an increase of the value of  $n$  as illustrated in Figure 4.26 (b). In particular, a linear fit of the SBH vs.  $n$  data is reported and the extrapolation of the SBH for  $n = 1$  is  $\sim 1.6$  eV, very close to the measured value by  $C-V$  characteristics ( $\sim 1.5$  eV).

### 4.3 Perspective vertical devices based on Gr/WBS heterostructures

The basic understanding of the electrical properties of Gr/WBS heterostructures reached during this thesis represents a starting point for the design and the fabrication of electronic device prototypes based on this kind of system. This work will be the continuation of this Ph.D. activity.

Basing on the results of the electrical characterizations presented in this chapter, it is possible to make an evaluation of the performance improvements expected using the QFEG/SiC or Gr/AlGaIn/GaN heterostructures in some of the vertical device structures introduced in Chapter 2.

The following structures will be considered:

- (i) a *Barristor* [9] based on the QFEG/SiC Schottky barrier;
- (ii) a HET [11] based on the Gr/AlGaIn/GaN heterostructure, where Gr is the base and the AlGaIn/GaN 2DEG the emitter.

The calculated DC electrical characteristics of these devices are compared with those of the counterparts based on more conventional materials: Si and SiO<sub>2</sub>.

#### 4.3.1 Barristor based on the QFEG/SiC Schottky barrier

A schematic representation of a QFEG/SiC vertical *Barristor* cross section is reported in Figure 4.27.

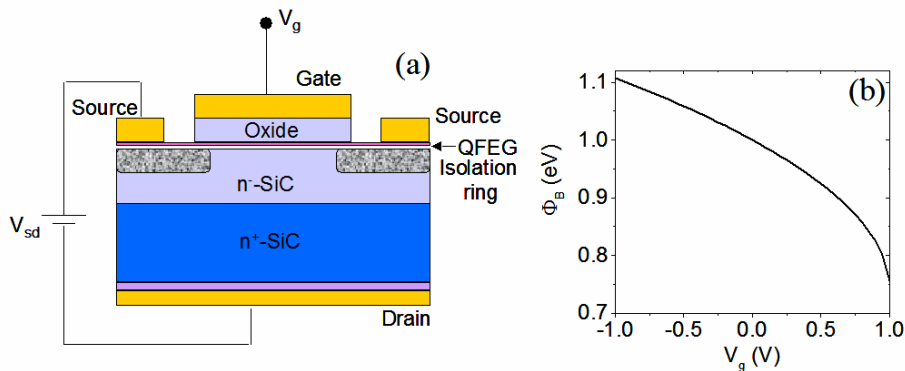


**Figure 4.27:** (a) schematic cross section of a QFEG/SiC vertical Barristor and (b) expected behavior of  $\Phi_B$  vs.  $V_g$ .

The QFEG Schottky contact is supposed to be formed on a n-type doped 4H-SiC epitaxial layer ( $N = 10^{16} \text{ cm}^{-3}$ ) with thickness  $t_{epi} = 2 \mu\text{m}$ . This SiC epilayer is grown on a highly doped SiC substrate ( $N = 10^{19} \text{ cm}^{-3}$ ). The Schottky contact area ( $A \approx 3.14 \times 10^{-4} \text{ cm}^2$ ) is laterally insulated by an insulating ring (that can be obtained by Al or B implantation in SiC). The source contact on QFEG is on the ring area, while the drain is on the highly doped substrate. A thin gate insulator ( $\text{Al}_2\text{O}_3$ , with relative dielectric permittivity  $\epsilon_r \approx 9$ , and thickness  $t_{ox} = 10 \text{ nm}$ ) on QFEG is used to modulate Gr workfunction by the gate bias ( $V_g$ ) applied to a top gate electrode. The dependence of the SBH  $\Phi_B$  on  $V_g$  can be expressed as:

$$\Phi_B(V_g) = \Phi_{B0} + \hbar v_F \left[ \sqrt{\pi \left( \frac{\epsilon_0 \epsilon_r V_g}{q t_{ox}} \right) + n_0} - \sqrt{\pi n_0} \right] \quad (4.23)$$

where  $\Phi_{B0}$  is the SBH and  $n_0$  is Gr carrier density at  $V_g = 0$ . For QFEG on SiC (0001), the experimental values of  $\Phi_{B0}$  and  $n_0$  are  $\Phi_{B0} \approx 1 \text{ eV}$  and  $n_0 \approx -5 \times 10^{12} \text{ cm}^{-2}$  where the negative sign is for p-type doping. The behavior of  $\Phi_B$  vs.  $V_g$  is reported in Figure 4.1 (b).

The effect of the gate bias on the source-drain current voltage characteristics ( $I_{sd} - V_{sd}$ ) in the case of forward biased Schottky junction ( $V_{sd} > 0$ ), can be derived using Equation (4.23) in combination with the thermionic emission expression of the current:

$$I_{sd} = AA^* T^2 \exp \left[ -\frac{\Phi_B(V_g)}{k_B T} \right] \exp \left[ \frac{V_{sd} - I_{sd} R_s}{n k_B T} \right] \quad (4.24)$$

Here  $A^* = 146 \text{ A cm}^{-2} \text{ K}^{-2}$  is the theoretical Richardson's constant for 4H-SiC and  $n$  is the ideality factor of the QFEG/SiC Schottky junction. The experimental value of  $n \approx 1.6$  has been considered in this case.

Assuming that the series resistance  $R_s$  is mainly due to current drift in the SiC epitaxial layer, it can be expressed as:

$$R_s = \frac{t_{epi}}{q N \mu A} \quad (4.25)$$

where  $\mu \approx 700 \text{ cm}^2 \text{ V}^{-1} \text{ s}^{-1}$  is the 4H-SiC mobility for a dopant concentration  $N \approx 10^{16} \text{ cm}^{-3}$ .

A plot of the calculated forward bias  $I_{ds} - V_{ds}$  characteristics for different values of  $V_g$  is reported in Figure 4.28 (a). Furthermore, the  $I_{ds} - V_g$  transcharacteristics for different  $V_{sd}$  voltages are reported in Figure 4.28 (b), clearly showing a current modulation by a factor  $\sim 10^6$  for  $V_{sd}$  bias from 0 to 0.8 V. For larger  $V_{sd}$  values, the current modulation range is reduced due to the effect of the series resistance.

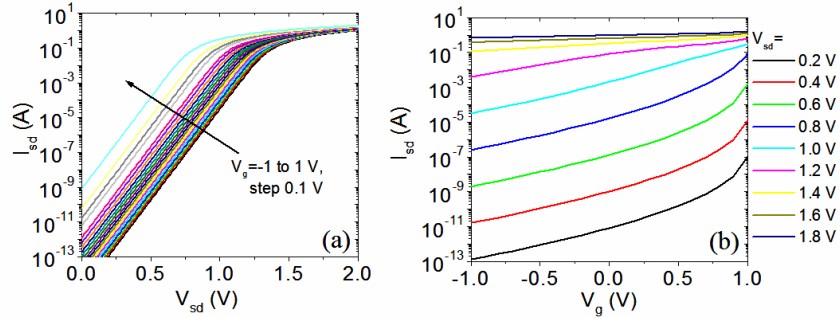


**Figure 4.28:** (a) forward bias  $I_{ds} - V_{ds}$  characteristics for different values of  $V_g$  and (b)  $I_{ds} - V_g$  transcharacteristics for different  $V_{sd}$  voltages calculated for a *barristor* based on the QFEG/SiC Schottky barrier.

A schematic representation of a *Barristor* device in Si, with the same geometry of the previously considered SiC one, is reported in Figure 4.29 (a).

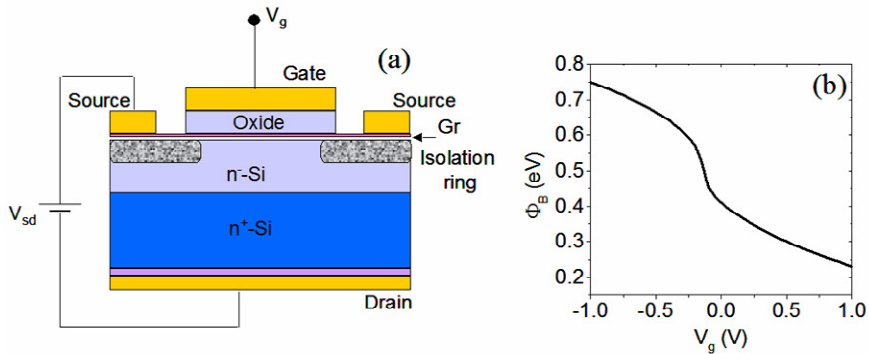


**Figure 4.29:** (a) schematic cross section of a Gr/Si vertical Barristor, considering an ideal Gs/Si interface obtainable by hydrogen passivation of the Si surface. (b) Expected behavior of  $\Phi_B$  vs.  $V_g$  for this device.

In this case, the Si surface is supposed to be passivated by a hydrogen treatment and Gr subsequently transferred on it, in order to achieve a nearly ideal Gr/Si interface, as discussed in Ref. [9]. The dependence of  $\Phi_B$  on the gate bias  $V_g$  is reported in Figure 4.29 (b). At  $V_g = 0$  the Gr/Si SBH is  $\Phi_B \approx 0.4$  eV and Gr is lowly n-type doped with  $n_0 \approx 7 \times 10^{11} \text{ cm}^{-2}$ .

The calculated forward bias  $I_{ds} - V_{ds}$  characteristics for different values of  $V_g$  are shown in Figure 4.30 (a), while the  $I_{ds} - V_g$  transcharacteristics for different  $V_{sd}$  voltages are reported in Figure 4.30 (b).

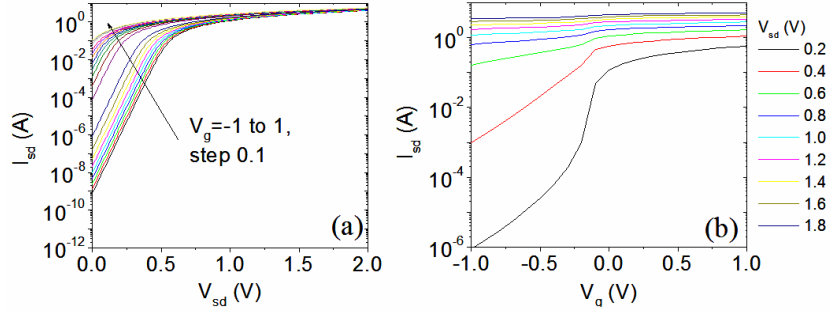


**Figure 4.30:** (a) forward bias  $I_{ds} - V_{ds}$  characteristics for different values of  $V_g$  and (b)  $I_{ds} - V_g$  transcharacteristics for different  $V_{sd}$  voltages calculated for a *Barristor* based on the Gr/Si Schottky barrier.

Clearly, the comparison of the electrical characteristics in Figure 4.28 and Figure 4.30 highlights the advantages of the QFEG/SiC (0001) Schottky contact over the Gr/Si one for the implementation of the *Barristor* device concept. Due to lower Schottky barrier, the Gr/Si based device exhibits significantly higher current levels in the off-state. Furthermore, the current modulation range in the  $I_{sd} - V_g$  transcharacteristics is reduced due to the enhanced weight of the series resistance. In addition to the better performances for the forward biased Schottky contact, the QFEG/SiC (0001) device is also expected to exhibit much higher breakdown voltage, due to the  $\sim 12$  times higher critical electric field of SiC than Si.

### 4.3.2 Graphene base HET based on the Gr/AlGaN/GaN heterostructure

In Chapter 2, the structure of a HET fabricated on a Si substrate and based on the vertical stack of Metal/ $\text{Al}_2\text{O}_3$ /Gr/ $\text{SiO}_2$ /Si (with Si working as the emitter, Gr as the base and the Metal as the collector electrode) has been illustrated [10,11]. This device, recently reported in the literature, actually demonstrates the functionality of a Gr-base HET. However, its main limitations are represented by the low collector current density and by the low common-base current gain  $\alpha$  ( $\sim 10^{-4} - 10^{-2}$ ) [11]. These limitations are mainly due to the use of  $\text{SiO}_2$  as the emitter-base barrier and to the tunneling mechanism ruling current injection through this barrier.

In this context, replacing Gr/ $\text{SiO}_2$ /Si with a Gr/AlGaN/GaN heterostructures has been recently proposed as a possible solution to increase both the collector current density and the current gain [225]. In this new HET scheme the thin AlGaN layer would work as the emitter-base barrier, the 2DEG at AlGaN/GaN interface as the emitter and Gr as the base. Differently than in the case of Gr/ $\text{SiO}_2$ /Si, current injection to the Gr base is ruled in this case by thermoionic emission. Furthermore, the high carrier density and mobility of the AlGaN/GaN 2DEG are also beneficial, favoring current injection and reducing the emitter access region series resistance. Clearly, the Gr/AlGaN/GaN heterostructure represent the main building block of this HET scheme. The accurate description of the vertical transport properties at this interface allows making some evaluation on the electrical characteristics of this kind of device.

Schematic representations of the cross-section and of the top-view of a Metal/ $\text{Al}_2\text{O}_3$ /Gr/AlGaN/GaN HET are reported in Figure 4.31 (a) and (b), respectively.

A device active area  $A \approx 3.14 \times 10^{-4} \text{ cm}^2$ , corresponding to the collector area (with radius  $R = 100 \text{ }\mu\text{m}$ ), is considered for calculations. A 25 nm thick  $\text{Al}_{0.25}\text{Ga}_{0.75}\text{N}$  barrier layer was considered as the emitter-base barrier and a 10 nm thick  $\text{Al}_2\text{O}_3$  layer as the base-collector barrier.

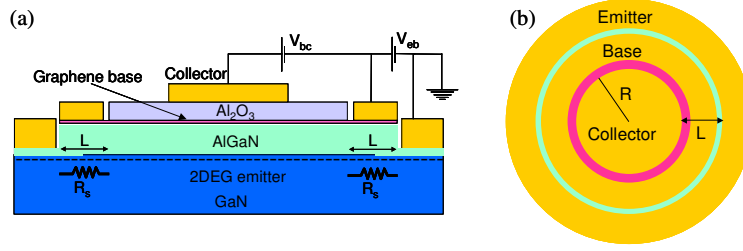


**Figure 4.31:** Schematic representations of the cross-section (a) and of the top-view (b) of a Metal/ $\text{Al}_2\text{O}_3$ /Gr/ $\text{AlGaIn}$ /GaN HET where the  $\text{AlGaIn}$  layer works as the emitter-base barrier, the 2DEG at  $\text{AlGaIn}/\text{GaN}$  interface as the emitter and Gr as the base.

In Figure 4.32 the energy band diagrams for this system have been represented for three different bias conditions.

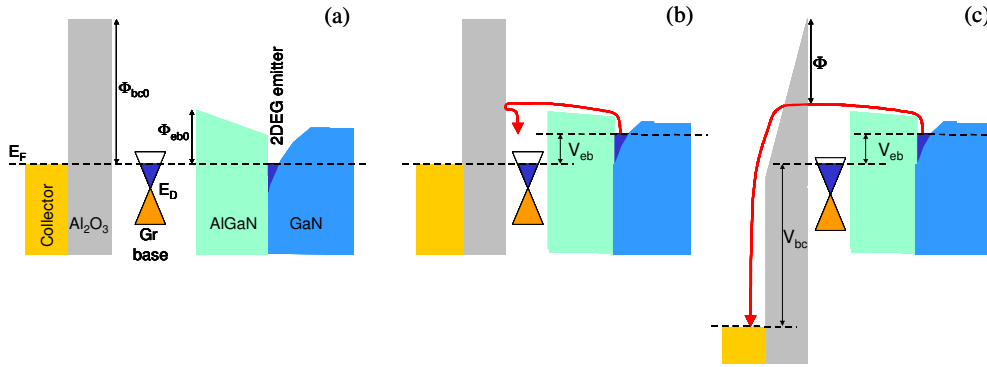


**Figure 4.32:** energy band diagram of the Metal/ $\text{Al}_2\text{O}_3$ /Gr/ $\text{AlGaIn}$ /GaN HET: for  $V_{eb} = 0$  and  $V_{bc} = 0$  (a), for  $V_{eb} > 0$  and  $V_{bc} = 0$  and finally for  $V_{eb} > 0$  and  $V_{bc} > \Phi_{bc0} - \Phi_{eb0}$ , when an  $I_c$  is observed for Fowler-Nordheim tunneling across an affective barrier  $\Phi \approx \Phi_{bc0} - V_{eb}$  (c).

For  $V_{eb} = 0$  and  $V_{bc} = 0$  (Figure 4.32 (a)), the Fermi levels of the  $\text{AlGaIn}/\text{GaN}$  2DEG, Gr and Metal are aligned. For simplicity, we have assumed that the difference between the metal and Gr workfunctions is  $W_M - W_{gr0} = 0$ . The barrier height for electrons injection from the emitter to the base is the Gr/ $\text{AlGaIn}$  Schottky barrier height ( $\Phi_{eb0} = 0.41$  eV). The base-collector barrier height  $\Phi_{bc0}$  is given by the energy difference between the Gr Fermi level  $E_{Fgr}$  and  $\text{Al}_2\text{O}_3$  conduction band



edge  $E_{cox}$ . Considering the high n-type doping of Gr on AlGaN ( $n_{gr0} = 1.3 \times 10^{13} \text{ cm}^{-2}$ ), it can be expressed as:

$$\Phi_{bc0} = (E_{cox} - E_D) - \hbar v_F \sqrt{\pi n_{gr0}} \approx 2.9 eV \quad (4.26)$$

with  $E_{cox} - E_D = 3.3 \text{ eV}$  the energy difference between the  $\text{Al}_2\text{O}_3$  conduction band edge and Gr Dirac point. In these conditions, no current is injected from the emitter to the base.

For  $V_{eb} > 0$  and  $V_{bc} = 0$  (Figure 4.32 (b)), the Gr/AlGaN Schottky contact is forward biased and a current  $I_b$  is injected from the emitter to the Gr base by thermoionic emission. However, only a negligible fraction of these electrons can tunnel through the base-collector barrier, so that all the current is measured on the base terminal.

The thermoionic emission base current can be expressed as:

$$I_b = AA^* T^2 \exp\left[-\frac{\Phi_{eb0}}{k_B T}\right] \exp\left[\frac{V_{eb} - I_b R_s}{nk_B T}\right] \quad (4.27)$$

where  $A^* = 1.6 \text{ A cm}^{-2} \text{ K}^{-2}$  is the experimental value of the effective Richardson's constant,  $T$  is the temperature,  $k_B$  is the Boltzman's constant,  $n = 5.44$  the ideality factor of the Gr/AlGaN Schottky barrier and  $R_s$  is the series resistance contribution due to the current flow in the AlGaN/GaN 2DEG from the emitter contact to the active region. This contribution, which limits current injection to the base at higher  $V_{eb}$ , has been estimated as  $R_s = L/(qn_s \mu R) \approx 20 \Omega$  for the considered device geometry ( $R = 100 \mu\text{m}$ ,  $L = 10 \mu\text{m}$ ) and 2DEG carrier density  $n_s = 5 \times 10^{12} \text{ cm}^{-2}$  and mobility  $\mu = 1000 \text{ cm}^2 \text{ V}^{-1} \text{ s}^{-1}$ .

A plot of the current injected in the base as a function of  $V_{eb}$  bias is reported in Figure 4.33 (a).

For  $V_{eb} > 0$  and  $0 < V_{bc} < \Phi_{bc0} - \Phi_{eb0}$ , electrons have to tunnel through the 10 nm  $\text{Al}_2\text{O}_3$  thickness, resulting in a low collector current.

For  $V_{eb} > 0$  and  $V_{bc} > \Phi_{bc0} - \Phi_{eb0}$  (see Figure 4.31 (c)), a Fowler-Nordheim tunneling across a triangular barrier occurs, with a collector current  $I_c$  that can be expressed as:

$$I_c = I_b P(E_{ox}, \Phi) = I_b \exp\left[-\frac{4\sqrt{2qm_{ox}} \Phi^{3/2}}{3\hbar E_{ox}}\right] \quad (4.28)$$

where  $P(E_{ox}, \Phi)$  represents the tunneling probability, which depends on the electric field  $E_{ox}$  across the oxide and on the effective barrier  $\Phi$  seen by the electrons, with  $m_{ox}$  the effective tunnelling mass of electrons in  $\text{Al}_2\text{O}_3$  ( $\sim 0,4 m_e$ ). In particular,  $E_{ox}$  can be expressed as:

$$E_{ox} = \frac{V_{bc} + \hbar v_F \sqrt{\pi \left( n_{gr0} + \frac{\epsilon_0 \epsilon_{ox} V_{bc}}{q t_{ox}} \right)}}{t_{ox}} \quad (4.29)$$

Moreover, as illustrated in Figure 4.32 (c), if the electrons injected in the base do not lose their kinetic energy (hot electrons), they see an effective barrier for tunneling

$$\Phi = \Phi_{bc0} - V_{eb} - \hbar v_F \left[ \sqrt{\pi \left( n_{gr0} + \frac{\epsilon_0 \epsilon_{ox} V_{bc}}{q t_{ox}} \right)} - \sqrt{\pi n_{gr0}} \right] \quad (4.30)$$

The calculated collector current  $I_c$  as a function of  $V_{eb}$  for different values of  $V_{bc}$  are reported in Figure 4.33 (b) and (c), showing a strong dependence of the  $I_c$ - $V_{eb}$  characteristics from the  $V_{bc}$  bias, differently than in the case of the Metal/ $\text{Al}_2\text{O}_3$ /Gr/ $\text{SiO}_2$ /Si device discussed in Chapter 2. Furthermore, the maximum collector current density estimated for this Metal/ $\text{Al}_2\text{O}_3$ /Gr/AlGaIn/GaN device is  $\sim 30 \text{ A/cm}^2$ , i.e.  $\sim 10^8$  times higher than those reported for the  $\text{SiO}_2$ /Si based device (in the order of  $\sim 100 \text{ nA/cm}^2$ ).

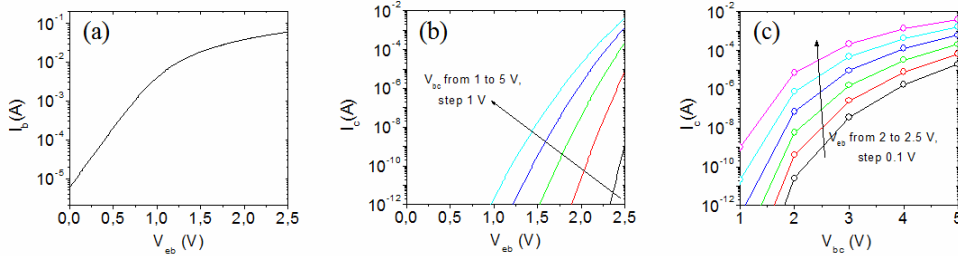


**Figure 4.33:** estimated plot of the  $I_b$  injected in the base as a function of  $V_{eb}$  (a). The calculated  $I_c$  plotted as a function of  $V_{eb}$  for various values of  $V_{bc}$  (b) and vice versa as a function of  $V_{bc}$  for various values of  $V_{eb}$  (c). A strong dependence of the  $I_c$  from the  $V_{bc}$  bias is clearly visible.

In Figure 4.34, is reported a comparison between the emitter current  $I_e = V_{eb}/R_s$ , the current injected in the base  $I_b$  and the collector current  $I_c$  (for  $V_{bc} = 5$  V) as a function of  $V_{eb}$ . The ratio  $I_c/I_e$  represents the current gain, which is in the order of 10% for  $V_{eb} = 2.5$  V. This is much larger than the current gain for the SiO<sub>2</sub>/Si based HET reported in the literature (ranging from 0.01% to 1%).

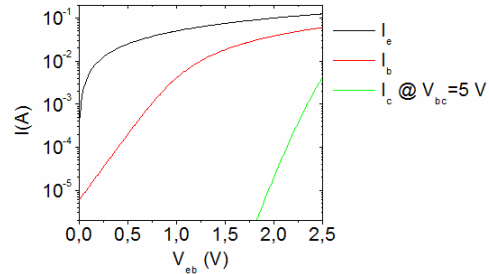


**Figure 4.34:** comparison between the emitter current ( $I_e$ ), the current injected in the base ( $I_b$ ) and the collector current ( $I_c$ ) plotted vs. the  $V_{be}$  for a fixed value of  $V_{bc}$ .

*This*

*Page*

*Intentionally*

*Left*

*Blank*

## Summary

Due to its excellent physical properties, Gr is a material with wide application potentialities. Its possible use in the electronics and optoelectronics fields is currently limited to low power RF transistors, interconnects, transparent conductive electrodes, photodetectors... The zero bandgap in Gr band structure hinders its use as channel material in MOSFETs devices for logic or switching applications, which typically require a ratio between the on-state and off-state currents ( $I_{on}/I_{off}$ ) of several orders of magnitude and a very low  $I_{off}$  to minimize power dissipation. Novel device concepts based on vertical Gr heterostructures with semiconductors or insulators have been recently considered, which potentially allow achieving the desired high  $I_{on}/I_{off}$  ratios for switching applications.

This thesis work gave a contribution in this research field, through the fabrication, and structural and electrical characterization of high quality Gr heterostructures with WBSs (SiC and AlGa<sub>x</sub>N/GaN heterojunctions).

Gr integration with SiC and GaN deserves particular interest, due to the strategic role of these WBS in high power and high frequency electronics. This can result in the demonstration of novel electronic device concepts or in the introduction of new functionalities in existing SiC and GaN devices.

In order to develop Gr vertical junctions with SiC and Al<sub>x</sub>Ga<sub>1-x</sub>N/GaN heterostructures, two main issues have been addressed in this thesis work:

- (i) The fabrication of high quality Gr contacts on large area on both substrates, by the controlled graphitization of SiC surface and the delamination of CVD grown Gr from copper and its transfer to the AlGa<sub>x</sub>N surface, respectively
- (ii) The electrical characterization of “in plane” and “vertical” transport properties through these Gr/semiconductor interfaces, employing advanced nanoscale-resolved characterization techniques (conductive atomic force microscopy and scanning capacitance spectroscopy), in order to correlate the local structural and electrical properties.

Chapter 1 reported an overview of the Gr physical properties and of the main Gr production methods. Chapter 2 introduced the physics of the Gr/semiconductor junctions and an overview of the most recent device concepts that exploit vertical heterostructures with Gr, such as the Schottky diode with a gate-modulated barrier, the hot electron transistor with a Gr base or the field effect modulated tunnel devices.

Chapters 3 and 4 discussed the experimental activity and the results on the Gr heterostructures fabrication methods and on the electrical characterizations respectively. In particular, Chapter 3 illustrated the experimental activity on the fabrication of Gr heterostructures with both  $\text{Al}_x\text{Ga}_{1-x}\text{N}/\text{GaN}$  and 4H-SiC. Due to the difficulty to grow high quality Gr directly on AlGaN surface, the most viable approach to obtain a single layer of Gr on a large area is transferring CVD grown Gr from Cu to the target substrate. The optimization of this process is of crucial importance to preserve the Gr structural and morphological quality.

A highly controllable and reproducible transfer process was developed exploiting some innovative solutions with respect to the conventionally used Gr transfer. In particular, an electrolytic delamination procedure was adopted to separate Gr from Cu by the mechanical action of hydrogen nano-bubbles developed at the Gr/Cu interface. The delamination kinetic was investigated in details and a microscopic model of the delamination process was proposed. The key role played by Gr wrinkles acting as nucleation sites for  $\text{H}_2$  bubbles at the cathode perimeter was demonstrated and the  $\text{H}_2$  supersaturation generated at the electrode for different electrolyte concentrations was estimated. This model allowed to quantitatively explain the inverse dependence of the delamination duration with the electrolyte concentration.

In addition, a fully automatic thermo-compressive transfer printing was developed to stamp the delaminated Gr from the Cu foil to the target substrate. This method allowed obtaining Gr membranes with high and reproducible quality on several kinds of substrates (Si,  $\text{SiO}_2$ , SiC, GaN, plastics) by a proper control of the temperature and pressure ramps as a function of the time. In particular, this procedure was adopted to transfer Gr with identical high quality on AlGaN/GaN substrates with different AlGaN layer microstructure.

Gr heterostructures with 4H-SiC (0001) were obtained by controlled graphitization during high temperature annealing processes in inert gas (Ar) at atmospheric pressure. The effect of the annealing temperature and of wafer miscut angle on the number of Gr layers was investigated. Atomic resolution structural and electrical

analyses elucidated the different properties of Gr/SiC interface on the (0001) terraces and on (11-2n) facets of SiC. The first C layer at the interface with the substrate (buffer layer) results to be partially bonded over the (0001) terraces, whereas it is locally delaminated from (11-2n) facets (QFEG). A hydrogen treatment at high temperature was also exploited to completely convert this buffer layer into QFEG over the entire SiC surface with important implications on the electrical behavior.

Chapter 4 was dedicated to the detailed description of the electrical characterization of the Gr heterostructures with 4H-SiC and  $\text{Al}_x\text{Ga}_{1-x}\text{N}/\text{GaN}$ .

The “in plane” electrical properties of Gr residing on these substrates was investigated by properly fabricated test devices (TLM, FET) extracting characteristic Gr electrical properties such as the sheet resistance. The test device arrays were defined with various orientations in order to clarify the anisotropy on the lateral current transport eventually induced in Gr by the underlying substrate.

The vertical current transport through the Gr/semiconductor interfaces was also extensively investigated. In particular, the nature of the junction and the lateral uniformity of the contact were investigated by advanced nanoscale electrical measurements such as Conductive AFM and Scanning Capacitance Microscopy.

The vertical current transport through Gr contacts onto AlGaN/GaN heterostructures with a highly homogeneous AlGaN layer, has been investigated at nanoscale, demonstrating a low SBH ( $\Phi_B \sim 0.4$  eV) and an excellent lateral uniformity. This low barrier height value was related to the high n-type doping ( $\sim 1.3 \times 10^{13} \text{ cm}^{-2}$ ) of Gr in contact with AlGaN, due to the charge transfer from the donor-like surface states at the AlGaN surface. Furthermore, a very efficient modulation of the AlGaN/GaN 2DEG by modulation of the Fermi level ( $E_F - E_D$ ) in the Gr electrode was demonstrated. The vertical current transport of Gr was also investigated onto AlGaN/GaN heterostructures with a high density of microstructures in the AlGaN layer. An ohmic behavior was observed with the defects-rich AlGaN layer. This result is very interesting, since the ohmic behavior has been readily achieved using as-transferred Gr contacts without any thermal treatment, whereas ohmic contacts on GaN and AlGaN are typically obtained by Ti/Al-based metal stacks and require high thermal budgets (from 500 to 800°C), that can impact the AlGaN/GaN heterostructure quality. These results have been explained in terms of the peculiar properties of Gr (high conformability with the substrate, high electron mean free path) and of the low Schottky barrier between Gr and AlGaN.

In the case of Gr on 4H-SiC (0001), a peculiar anisotropy of the lateral current transport was observed both in the sheet resistance measured by differently oriented TLM test device ( $R_{sh[11-20]} = 775 \pm 28 \Omega/\text{sq}$  in the [11-20] direction and  $R_{sh[1-100]} = 397 \pm 20 \Omega/\text{sq}$  in the [1-100] direction) and in the electrical characteristics measured by FETs. This specific behavior was related to the peculiar morphology of SiC substrate, which exhibits parallel steps originating from the wafer miscut angle. Nanoscale resolution conductivity mapping in Gr by CAFM revealed lower doping level of Gr residing on the (11-2n) facets of SiC with respect to the (0001) terraces, which allowed to explain the observed macroscopic anisotropy in the lateral current transport. A similar anisotropy is known even after the hydrogen intercalation that converts the buffer layer in a QFEG. In this case, considering the uniform delamination from the substrate, different explanations have to be searched, such as the polar nature of the (0001) face (n-type doping) and the non-polar (11-2n) facets (no-doping).

The vertical current transport through the Gr/SiC heterostructure after the hydrogen intercalation was characterized as well. It is well known that the hydrogen intercalation is able to convert an ohmic behavior of the vertical heterojunction with the as grown epitaxial Gr on SiC (0001) in a rectifying contact. Moreover, it is worth noticed that a certain discrepancy between the SBH measured in forward bias (0.9 – 1 eV measured by  $I$ - $V$  analyses) and in reverse bias (~1.5 eV measured by C- $V$  analyses) is denoted for the vertical current transport through the hydrogen intercalated Gr/SiC heterostructure. This is a typical indication of laterally inhomogeneous Schottky contacts, consisting of nanometer size regions with low SBH embedded in macroscopic contact areas with higher SBH.

In order to elucidate the origin of this discrepancy, the vertical current transport was measured by nanoscale resolution  $I$ - $V$  characterizations CAFM on differently sized metal contacts (from 100  $\mu\text{m}$  to 1  $\mu\text{m}$ ) and on substrates with different miscut angles. It was observed that the more the contact size approximated the terrace width dimension the higher was the observed SBH, until values that resemble these observed measuring in reverse bias. In this sense, the gap of the SBH measured with different macroscopic approaches is almost explained considering the lowly doped facets under the metal contact.

As a way of conclusion, and based on the knowledge acquired about the heterostructures composed by Gr with 4H-SiC and AlGa $\text{N}$ /Ga $\text{N}$ , some device hypothesis was proposed.



It was calculated the expected performance in a *Barristor* device (which is a Schottky diode with a gate modulated barrier) substituting epitaxial Gr Schottky contact to the Gr contact on Si. Lower current dissipation in the off-state and a higher breakdown voltage is expected. With regard to Gr on AlGa<sub>N</sub>/Ga<sub>N</sub> heterostructures it was hypothesized the possibility to exploit Gr as the base of a HET where the AlGa<sub>N</sub> layer would work as emitter-base barrier and the 2DEG at the heterointerface between AlGa<sub>N</sub> and Ga<sub>N</sub> as emitter.

*This*

*Page*

*Intentionally*

*Left*

*Blank*

# Bibliography

---

- [1] A. K. Geim and K. S. Novoselov, *Nat. Mater.* **6**, 183 (2007)
- [2] K. S. Novoselov, A. K. Geim, S. V. Morozov, D. Jiang, M. I. Katsnelson, I. V. Grigorieva, S. V. Dubonos, and A. A. Firsov, *Nature* **438**, 197 (2005)
- [3] A. K. Geim and I. V. Grigorieva, *Nature* **499**, 419 (2013)
- [4] K. I. Bolotin, K. J. Sikes, Z. Jiang, M. Klima, G. Fudenberg, J. Hone, P. Kim and H. L. Stormer, *Solid State Commun.* **146**, 351 (2008)
- [5] F. Bonaccorso, Z. Sun, T. Hasan and A. C. Ferrari, *Nature Photonics* **4**, 611 (2010)
- [6] R. R. Nair, P. Blake, A. N. Grigorenko, K. S. Novoselov, T. J. Booth, T. Stauber, N. M. R. Peres and A. K. Geim, *Science* **320**, 1308 (2008)
- [7] A. Balandin, S. Ghosh, W. Bao, I. Calizo, D. Teweldebrahn, F. Miao C. N. and Lau, *Nano Lett.* **8**, 902 (2008)
- [8] C. Lee, X. Wei, J. W. Kysar and J. Hone, *Science* **321**, 385 (2008)
- [9] H. Yang, J. Heo, S. Park, H. J. Song, D. H. Seo, K. E. Byun, P. Kim, I. Yoo, H. J. Chung, K. Kim, *Science* **336**, 1140 (2012)
- [10] S. Vaziri, G. Lupina, C. Henkel, A. D. Smith, M. Östling, J. Dabrowski, G. Lippert, W. Mehr and M. C. Lemme, *Nano Lett.* **13**, 1435 (2013)
- [11] C. Zeng, E. B. Song, M. Wang, S. Lee, C. M. Torres, J. Tang, B. H. Weiller and K. L. Wang, *Nano Lett.* **13**, 2370 (2013)
- [12] L. Britnell, R. V. Gorbachev, R. Jalil, B. D. Belle, F. Schedin, A. Mishchenko, T. Georgiou, M. I. Katsnelson, L. Eaves, S. V. Morozov, N. M. R. Peres, J. Leist, A. K. Geim, K. S. Novoselov and L. A. Ponomarenko, *Science* **335**, 947 (2012)
- [13] M. Shur, S. Rumyanstev, M. Levinshtein, *SiC Materials and Devices*, *World Scientific, Singapore* (2006)
- [14] M. Asif Khan, J. M. Van Hove, J. N. Kuznia and D. T. Olson, *Appl. Phys. Lett.* **58**, 2408 (1991)
- [15] O. Ambacher, J. Smart, J. R. Shealy, N. G. Weimann, K. Chu, M. Murphy, W. J. Schaff, L. F. Eastman, R. Dimitrov, L. Wittmer, M. Stutzmann, W. Rieger, and J. Hilsenbeck, *J. Appl. Phys.* **85**, 3222 (1999)
- [16] H. Morkoc, *Wide Band Gap Electronic Devices*, *World Scientific, Singapore* (2003)
- [17] S. Nakamura, M. Senoh, and T. Mukai, *Jpn. J. Appl. Phys.* **30**, L1708 (1991)

- 
- [18] C. Berger, Z. Song, X. Li, X. Wu, N. Brown, C. Naud, D. Mayou, T. Li, J. Hass, A. N. Marchenkov, E. H. Conrad, P. N. First and W. A. de Heer, *Science* **312**, 1191 (2006)
- [19] K. V. Emtsev, A. Bostwick, K. Horn, J. Jobst, G. L. Kellogg, L. Ley, J.L. McChesney, T. Ohta, S. A. Reshanov, J. Rohrl, E. Rotenberg, A. K. Schmid, D. Waldmann, H. B. Weber and T. Seyller, *Nature Mater.* **8**, 203 (2009)
- [20] C. Virojanadara, M. Syvajarvi, R. Yakimova, L.I. Johansson, A.A. Zakharov and T. Balasubramanian, *Phys. Rev. B* **78**, 245403 (2008)
- [21] Y.-M. Lin, C. Dimitrakopoulos, K.A. Jenkins, D.B. Farmer, H.-Y. Chiu, A. Grill, Ph. Avouris, *Science* **327**, 662 (2010)
- [22] C. Riedl, C. Coletti, T. Iwasaki, A. A. Zakharov and U. Starke, *Phys. Rev. Lett.* **103**, 246804 (2009)
- [23] S. Hertel, D. Waldmann, J. Jobst, A. Albert, M. Albrecht, S. Reshanov, A. Schöner, M. Krieger and H. B. Weber, *Nature Communications* **3**, 957 (2012)
- [24] F. Varchon, R. Feng, J. Hass, X. Li, B. Ngoc Nguyen, C. Naud, P. Mallet, J.-Y. Veuillein, C. Berger, E. H. Conrad and L. Magaud, *Phys. Rev. Lett.* **99**, 126805 (2007)
- [25] S. Chandramohan, J. H. Kang, B. D. Ryu, J. H. Yang, S. Kim, H. Kim, J. B. Park, T. Y. Kim, B. Jin Cho, E.-K. Suh, and C.-H. Hong, *ACS Appl. Mater. Interfaces* **5**, 958 (2013)
- [26] Z. Yan, G. Liu, J. M. Khan, and A. A. Balandin, *Nat. Commun.* **3**, 827, (2012)
- [27] G. Fisichella, S. Di Franco, F. Roccaforte, S. Ravesi and F. Giannazzo, *Appl. Phys. Lett.* **104**, 233105 (2014)
- [28] F. Giannazzo, I. Deretzis, G. Nicotra, G. Fisichella, C. Spinella, F. Roccaforte and A. La Magna, *Appl. Surf. Sci.* **291**, 53 (2014)
- [29] F. Giannazzo, I. Deretzis, G. Nicotra, G. Fisichella, Q.M. Ramasse, C. Spinella, F. Roccaforte and A. La Magna, *J. Cryst. Growth* **393**, 150 (2014)
- [30] G. Fisichella, G. Greco, F. Roccaforte and F. Giannazzo, *Nanoscale* **6**, 8671 (2014)
- [31] G. Fisichella, G. Greco, F. Roccaforte and F. Giannazzo, *Appl. Phys. Lett.* **105**, 063117 (2014)
- [32] F. Giannazzo, S. Hertel, A. Albert, G. Fisichella, A. La Magna, F. Roccaforte, M. Krieger, H. B. Weber, *Materials Science Forum* (2014) in press.
- [33] S. Iijima, *Nature* **354**, 56 (1991)
- [34] H. W. Kroto, J. R. Heath, S. C. O'Brien, R. F. Curl and R. E. Smalley, *Nature* **318**, 162 (1985)
- [35] E. Ozawa, H. W. Kroto, P. W. Fowler and E. Wassermann, *Phil. Trans. R. Soc. Lond. A* **343**, 1 (1993)
- [36] L. Pauling, The Nature of Chemical Bonds, *Cornell UP*, 429 (1972)
- [37] P. R. Wallace, *Phys. Rev.* **71**, 622 (1947)
- [38] S. Reich, J. Maultzsch, C. Thomsen, and P. Ordejón, *Phys. Rev. B* **66**, 035412 (2002)
- [39] C. Bena and S. A. Kivelson, *Phys. Rev. B* **72**, 125432 (2005)
- [40] Y. Zhang, Y.-W. Tan, H. L. Stormer, and P. Kim, *Nature* **438**, 201 (2005)

- 
- [41] V. P. Gusynin and S. G. Sharapov, *Phys Rev. Lett.* **95**, 146801 (2005)
- [42] A. H. Castro Neto, F. Guinea, N. M. R. Peres K. S. Novoselov and A. K. Geim, *Rev. Mod. Phys.*, **81**, 109 (2009)
- [43] C. R. Dean, A. F. Young, I. Meric, C. Lee, L. Wang, S. Sorgenfrei, K. Watanabe, T. Taniguchi, P. Kim, K. L. Shepard and J. Hone, *Nat. Nanotechnol.* **5**, 722 (2010)
- [44] A. S. Mayorov, R. V. Gorbachev, S. Morozov, L. Britnell, R. Jalil, L. Ponomarenko, P. Blake, K. S. Novoselov, K. Watanabe, T. Taniguchi and A. K. Geim, *Nano Lett.* **11**, 2396 (2011)
- [45] L. Wang, I. Meric, P. Y. Huang, Q. Gao, Y. Gao, H. Tran, T. Taniguchi, K. Watanabe, L. M. Campos, D. A. Muller, J. Guo, P. Kim, J. Hone, K. L. Shepard and C. R. Dean, *Science* **342**, 614 (2013)
- [46] T. Stauber, N. M. R. Peres and F. Guinea, *Phys. Rev. B* **76**, 205423 (2007)
- [47] E. H. Hwang, S. Adam and S. DasSarma, *Phys. Rev. Lett.* **98**, 186806 (2007)
- [48] J. H. Chen, C. Jang, S. Xiao, M. Ishigami and M. S. Fuhrer, *Nat. Nanotechnol.* **3**, 206 (2008)
- [49] T. Ando, *J. Phys. Soc. Jpn.* **75**, 074716 (2006)
- [50] N. M. R. Peres, F. Guinea and A. H. Castro Neto, *Phys. Rev. B*, **73**, 125411(2006)
- [51] T. O. Wehling, S. Yuan, A. I. Lichtenstein, A. K. Geim and M. I. Katsnelson, *Phys. Rev. Lett.* **105** (2010) 056802.
- [52] S. Bae, H. Kim, Y. Lee, X. Xu, J.-S. Park, Y. Zheng, J. Balakrishnan, T. Lei, H. Ri Kim, Y. I. Song, Y.-J. Kim, K. S. Kim, B. Ozyilmaz, J.-H. Ahn, B.H. Hong and S. Iijima, *Nat. Nanotechnol.* **5**, 574 (2010)
- [53] A. B. Kuzmenko, E. van Heumen, F. Carbone, D. van der Marel, *Phys. Rev. Lett.* **100**, 117401 (2008)
- [54] C. Casiraghi, A. Hartschuh, E. Lidorikis, H. Qian, H. Harutyunyan, T. Gokus, K. S. Novoselov and A. C. Ferrari, *Nano Lett.* **7**, 2711 (2007)
- [55] K. S. Novoselov, A. K. Geim, S. V. Morozov, D. Jiang, Y. Zhang, S. V. Dubonos, I. V. Grigorieva, A. A. Firsov, *Science* **306**, 666 (2004)
- [56] G. Jo, M. Choe, C. Y. Cho, J. H. Kim, W. Park, S. Lee, W. K. Hong, T. W. Kim, S. J. Park, B. H. Hong, Y. H. Kahng, T. Lee, *Nanotechnology* **21**, 175201 (2010)
- [57] X. Huang, Zeng, Z. Fan, Z. Liu, J. Zhang, H. *Adv. Mater.* **24**, 5979 (2012)
- [58] T. H. Han, Y. Lee, M. R. Choi, S. H. Woo, S. H. Bae, B. H. Hong, J. H. Ahn and T. W. Lee, *Nat. Photon.* **6**, 105 (2012)
- [59] S. Chen, A. L. Moore, W. Cai, J. W. Suk, J. An, C. Mishra, C. Amos, C. W. Magnuson, J. Kang, L. Shi, R. S. Ruoff, *ACS Nano* **5**, 321 (2010)
- [60] A. A. Balandin, *Nat. Mater.* **10**, 569 (2011)
- [61] S. Chen, Q. Wu, C. Mishra, J. Kang, H. Zhang, K. Cho, W. Cai, A. A. Balandin, R.S. Ruoff, *Nat. Mater.* **11**, 203 (2012)
- [62] C. Y. Ho, R. W. Powell, P. E. Liley, *J. Phys. Chem.* **1**, 279 (1972)
- [63]. T. Tohei, A. Kuwabara, F. Oba, I. Tanaka, *Phys. Rev. B* **73**, 064304 (2006)

- 
- [64] G. D. Sanders, A. R. T. Nugraha, K. Sato, J.-H. Kim, J. Kono, R. Saito and C. J. Stanton, *J. Phys. Condens. Matter* **25**, 144201 (2013)
- [65] E. Pop, V. Varshney and A.K. Roy, *MRS bulletin* **37**, 1273 (2012)
- [66] B. Qiu and X. Ruan, *Appl. Phys. Lett.* **100**, 193101 (2012)
- [67] B. I. Yakobson, C. J. Brabec and J. Bernholc, *Phys. Rev. Lett.* **76**, 2511 (1996)
- [68] F. Liu, P. M. Ming and J. Li, *Phys. Rev. B* **76**, 064120 (2007)
- [69] R. Khare, S. L. Mielke, J. T. Paci, S. Zhang, R. Ballarini, G. C. Schatz and T. Belytschko, *Phys. Rev. B* **75**, 075412 (2007)
- [70] A. A. Griffith, *Philos. Trans. R. Soc. London Ser. A* **221**, 163 (1921)
- [71] X. Du, I. Skachko, A. Barker and E. Y. Aandrei, *Nat. Nanotechnol.* **3**, 491 (2008)
- [72] I. W. Frank, D. M. Tanenbaum, A. M. Van Der Zande and P. L. McEuen, *J. Vac. Sci. Technol. B* **25**, 2558 (2007)
- [73] T. J. Booth, P. Blake, R. R. Nair, D. Jiang, E. W. Hill, U. Bangert, A. Bleloch, M. Gass, K. S. Novoselov, M. I. Katsnelson and A. K. Geim, *Nano Lett.*, **8**, 2442 (2008)
- [74] M. Cai, D. Thorpe, D. H. Adamson and H. C. Schniepp, *J. Mater. Chem.* **22**, 24992 (2012)
- [75] C. Gomez-Navarro, M. Burghard and K. Kern, *Nano Lett.* **8**, 2045 (2008)
- [76] Y. Hernandez, V. Nicolosi, M. Lotya, F. M. Blighe, Z. Y. Sun, S. De, I. T. McGovern, B. Holland, M. Byrne, Y. K. Gun'ko, J. J. Boland, P. Niraj, G. Duesberg, S. Krishnamurthy, R. Goodhue, J. Hutchison, V. Scardaci, A. C. Ferrari and J. N. Coleman, *Nat. Nanotechnol.* **3**, 563 (2008)
- [77] M. Lotya, Y. Hernandez, P. J. King, R. J. Smith, V. Nicolosi, L. S. Karlsson, F. M. Blighe, S. De, Z. Wang and I. T. McGovern, *J. Am. Chem. Soc.* **131**, 3611 (2009)
- [78] X. Q. Wang, P. F. Fulvio, G. A. Baker, G. M. Veith, R. R. Unocic, S. M. Mahurin, M. F. Chi and S. Dai, *Chem. Commun.* **46**, 4487 (2010)
- [79] H. C. Schniepp, J. L. Li, M. J. McAllister, H. Sai, M. Herrera-Alonso, D. H. Adamson, R. K. Prud'homme, R. Car, D. A. Saville and I. A. Aksay, *J. Phys. Chem. B* **110**, 8535 (2006)
- [80] J. A. Zheng, C. A. Di, Y. Q. Liu, H. T. Liu, Y. L. Guo, C. Y. Du, T. Wu, G. Yu and D. B. Zhu, *Chem. Commun.* **46**, 5728 (2010)
- [81] B. C. Banerjee, T. J. Hirt and P. L. Walker, *Nature* **192**, 450 (1961)
- [82] A. E. Karu and M. J. Beer, *J. Appl. Phys.* **37**, 2179 (1966)
- [83] S. D. Robertson, *Nature* **221**, 1044 (1969)
- [84] C. Mattevi, H. Kim and M. A. Chhowalla, *J. Mater. Chem.* **21**, 3324 (2011)
- [85] M. Eizenberg and J. M. Blakely, *Surf. Sci.* **82**, 228 (1979)
- [86] Q. Yu, L. A. Jauregui, W. Wu, R. Colby, J. Tian, Z. Su, H. Cao, Z. Liu, D. Pandey, D. Wei, T. F. Chung, P. Peng, N. P. Guisinger, E. A. Stach, J. Bao, S.-S. Pei and Y. P. Chen, *Nature Mater.* **10**, 443 (2011)
- [87] P. Y. Huang, C. S. Ruiz-Vargas, A. M. Zande, W. S. Whitney, S. Garg, J. S. Alden, C. J. Hustedt, Y. Zhu, J. Park, P. L. McEuen and D. A. N. Muller, *Nature* **469**, 389 (2011)

- 
- [88] K. Kim, Z. Lee, W. Regan, C. Kisielowski, M. F. Crommie and A. Zettl, *ACS Nano* **5**, 2142 (2011)
- [89] A. W. Tsen, L. Brown, M. P. Levendorf, F. Ghahari, P. Y. Huang, R. W. Havener, C. S. Ruiz-Vargas, D. A. Muller, P. Kim, J. Park, *Science* **336**, 1143 (2012)
- [90] Y. Wei, J. Wu, H. Yin, X. Shi, R. Yang and M. Dresselhaus, *Nat. Mater.* **11**, 759 (2012)
- [91] X. Li, W. Cai, J. An, S. Kim, J. Nah, D. Yang, R. Piner, A. Velamakanni, I. Jung, E. Tutuc, S. K. Banerjee, L. Colombo and R. S. Ruoff, *Science* **324**, 1312 (2009).
- [92] Y. Hao, M. S. Bharathi, L. Wang, Y. Liu, H. Chen, S. Nie, X. Wang, H. Chou, C. Tan, B. Fallahazad, H. Ramanarayan, C. W. Magnuson, E. Tutuc, B. I. Yakobson, K. F. McCarty, Y.-W. Zhang, P. Kim, J. Hone, L. Colombo, R. S. Ruoff, *Science*, **342**, 720 (2013)
- [93] L. Gao, W. Ren, H. Xu, L. Jin, Z. Wang, T. Ma, L.-P. Ma, Z. Zhang, Q. Fu, L.-M. Peng, X. Bao and H.-M. Cheng, *Nat. Commun.* **3**, 699 (2012)
- [94] J. Lee, E. Lee, W. Joo, Y. Jang and B. Kim, *Science* **80**, 286 (2014)
- [95] D. V. Badami, *Carbon* **3**, 53 (1965)
- [96] A. J. van Bommel, J. E. Crombeen and A. X. van Tooren, *Surf. Sci.* **48**, 463 (1975)
- [97] C. Berger, Z. Song, T. Li, X. Li, Y. Asmerom, Y. Ogbazghi, R. Feng, Z. Dai, A. N. Marchenkov, E. H. Conrad, P. N. First and W. de Heer, *J. Phys. Chem.* **108**, 19912 (2004)
- [98] E. Rollingsa, G.-H. Gweona, S. Y. Zhoua, B.S. Munb, J. L. McChesneyc, B. S. Hussainb, A. V. Fedorovc, P. N. Firstd, W. A. de Heerd and A. Lanzara, *J. Phys. Chem. Solids* **67**, 2172 (2006)
- [99] T. Ohta, A. Bostwick, T. Seyller, K. Horn and E. Rotenberg, *Science* **313**, 951 (2006)
- [100] Th. Seyller, K.V. Emtsev, F. Speck, K.-Y. Gao and L. Ley, *Appl. Phys. Lett.* **88**, 242103 (2006)
- [101] C. Riedl, U. Starke, J. Bernhardt, M. Franke and K. Heinz, *Phys. Rev. B* **76**, 245406 (2007)
- [102] W. A. de Heer, C. Berger, X. Wu, P. N. First, E. H. Conrad, X. Li, T. Li, M. Sprinkle, J. Hass, M. L. Sadowski, M. Potemski and G. Martinez, *Solid State Commun.* **143**, 92 (2007)
- [103] I. Forbeaux, J.-M. Themlin and J.-M. Debever, *Phys. Rev. B* **58**, 16396, (1998)
- [104] J. Hass, F. Varchon, J. E. Millan-Otoya, M. Sprinkle, N. Sharma, W. A. de Heer, C. Berger, P. N. First, L. Magaud and E. H. Conrad, *Phys. Rev. Lett.* **100**, 125504 (2008)
- [105] M. L. Sadowski, G. Martinez, M. Potemski, C. Berger and W. A. de Heer, *Phys. Rev. Lett.* **97**, 266405 (2006)
- [106] K. V. Emtsev, F. Speck, Th. Seyller and L. Ley, *Phys. Rev. B* **77**, 155303 (2008)
- [107] F. Speck, J. Jobst, F. Fromm, M. Ostler, D. Waldmann, M. Hundhausen, H. Weber and T. Seyller, *Appl. Phys. Lett.* **99**, 122106 (2011)
- [108] J. Jobst, D. Waldmann, F. Speck, R. Hirner, D. K. Maude, Th. Seyller and H. B. Weber, *Phys. Rev. B* **81**, 195434 (2010)
- [109] Z. H. Ni, L. A. Ponomarenko, R. R. Nair, R. Yang, S. Anissimova, I. V. Grigorieva, F. Schedin, P. Blake, Z. X. Shen, E. H. Hill, K. S. Novoselov and A. K. Geim, *Nano Lett.* **10**, 3868 (2010)

- 
- [110] F. Giannazzo, S. Sonde, R. Lo Nigro, E. Rimini and V. Raineri, *Nano Lett.* **11**, 4612 (2011)
- [111] S. Sonde, F. Giannazzo, V. Raineri, R. Yakimova, J.-R. Huntzinger, A. Tiberj, J. Camassel, *Phys. Rev. B: Condens. Matter* **80**, 241406R (2009)
- [112] M. Ostler, I. Deretzis, S. Mammadov, F. Giannazzo, G. Nicotra, C. Spinella, Th. Seyller and A. La Magna, *Phys. Rev. B* **88**, 085408 (2013)
- [113] J. Kang, D. Shin, S. Bae and B. H. Hong, *Nanoscale* **4**, 5527 (2012)
- [114] K. S. Kim, Y. Zhao, H. Jang, S. Y. Lee, J. M. Kim, K. S. Kim, J.-H. Ahn, P. Kim, J.-Y. Choi and B. H. Hong, *Nature* **457**, 706 (2009).
- [115] X. Li, Y. W. Zhu, W. W. Cai, M. Borysiak, B. Y. Han, D. Chen, R. D. Piner, L. Colombo and R. S. Ruoff, *Nano Lett.* **9**, 4359 (2009)
- [116] S. J. Kang, B. Kim, K. S. Kim, Y. Zhao, Z. Chen, G. H. Lee, J. Hone, P. Kim and C. Nuckolls, *Adv. Mater.* **23**, 3531 (2011)
- [117] A. Reina, X. Jia, J. Ho, D. Nezich, H. Son, V. Bulovic, M. Dresselhaus and J. Kong, *Nano Lett.* **9**, 30 (2009)
- [118] J. W. Suk, A. Kitt, C. W. Magnuson, Y. Hao, S. Ahmed, J. An, A. K. Swan, B. B. Goldberg and R. S. Ruoff, *ACS Nano* **5**, 6916 (2011)
- [119] Z. Cheng, Q. Zhou, C. Wang, Q. Li, C. Wang and Y. Fang, *Nano Lett.* **11**, 767 (2011)
- [120] J. Kedzierski, P. L. Hsu, A. Reina, J. Kong, P. Healey, P. Wyatt and C. Keast, *IEEE Electron Device Lett.* **30**, 745 (2009)
- [121] J. Kang, S. Hwang, J. H. Kim, M. H. Kim, S. J. Seo, B. H. Hong, M. K. Kim and J.-B. Choi, *ACS Nano* **6**, 5360 (2012)
- [122] S. K. Hong, S. M. Song, O. Sul and B. J. Cho, *J. Electrochem. Soc.* **159**, K107 (2012)
- [123] Y. Lin, C. Lu, C. Yeh, C. Jin, K. Suenaga and P. Chiu, *Nano Lett.* **12**, 414 (2012)
- [124] E. H. Lock, M. Baraket, M. Laskoski, S. P. Mulvaney, W. K. Lee, P. E. Sheehan, D. R. Hines, J. T. Robinson, J. Tosado, M. S. Fuhrer, S. C. Hernandez and S. G. Walton, *Nano Lett.* **12**, 102 (2012)
- [125] T. Yoon, W. C. Shin, T. Y. Kim, J. H. Mun, T. Kim and B. J. Cho, *Nano Lett.* **12**, 1448 (2012)
- [126] P. Gupta, P. D. Dongare, S. Grover, S. Dubey, H. Mangain, A. Bhattacharya and M. M. Deshmukh, *Sci. Rep.* **4**, 3882 (2014)
- [127] Y. Wang, Y. Zheng, X. Xu, E. Dubuisson, Q. Bao, J. Lu and K. P. Loh, *ACS Nano* **5**, 9927 (2011)
- [128] C. J. L. de la Rosa, J. Sun, N. Lindvall, M. T. Cole, Y. Nam, M. Loeffler, E. Olsson, K. B. K. Teo and A. Yurgens, *Appl. Phys. Lett.* **102**, 022101 (2013)
- [129] D. Zhuang and J. H. Edgar, *Mater. Sci. Eng. R.* **48**, 1 (2005)
- [130] S. Unarunotai, Y. Murata, C. E. Chialvo, H. S. Kim, S. MacLaren, N. Mason, I. Petrov and J. A. Rogers, *Appl. Phys. Lett.* **95**, 202101 (2009)
- [131] S. Unarunotai, J. C. Koepke, C. L. Tsai, F. Du, C. E. Chialvo, Y. Murata, R. Haasch, I. Petrov, N. Mason, M. Shim, J. Lyding and J. A. Rogers, *ACS Nano* **4**, 5591 (2010)



- 
- [132] D. Caldwell, T. J. Anderson, J. C. Culbertson, G. G. Jernigan, K. D. Hobart, F. J. Kub, M. J. Tadjer, J. L. Tedesco, J. K. Hite and M. A. Mastro, *ACS Nano* **4**, 1108 (2010)
- [133] J. Kim, H. Park, J. B. Hannon, S.-W. Bedell, K. Fogel, D. K. Sadana and C. Dimitrakopoulos, *Science* **342**, 833 (2013)
- [134] M. Y. Han, B. Ozyilmaz, Y. Zhang and P. Kim, *Phys. Rev. Lett.* **98**, 206805 (2007).
- [135] D. C. Elias, R. R. Nair, T. M. G. Mohiuddin, S. V. Morozov, P. Blake, M. P. Halsall, A. C. Ferrari, D. W. Boukhvalov, M. I. Katsnelson, A. K. Geim and K. S. Novoselov, *Science* **323** 610 (2009).
- [136] J. T. Robinson, J. S. Burgess, C. E. Junkermeier, S. C. Badescu, T. L. Reinecke, F. K. Perkins, M. K. Zalalutdniov, Jeffrey W. Baldwin, J. C. Culbertson, P. E. Sheehan and E. S. Snow, *Nano Letters* **10**, 3001 (2010)
- [137] Y. Zhang, T. T. Tang, C. Girit, Z. Hao, M. C. Martin, A. Zettl, M. F. Crommie, Y. R. Shen, F. Wang, *Nat. Lett.* **459**, 820 (2009)
- [138] Z. H. Ni, T. Yu, Y. H. Lu, Y. Y. Wang, Y. P. Feng and Z. X. Shen, *ACS Nano* **2**, 2301 (2008).
- [139] L. Yu, Y.-H. Lee, X. Ling, E. J. G. Santos, Y. C. Shin, Y. Lin, M. Dubey, E. Kaxiras, J. Kong, H. Wang, T. Palacios, *Nano Lett.* **14**, 3055 (2014)
- [140] T. Georgiou, R. Jalil, B. D. Belle, L. Britnell, R. V. Gorbachev, S. V. Morozov, Y.-J. Kim, A. Gholinia, S. J. Haigh, O. Makarovskiy, L. Eaves, L. A. Ponomarenko, A. K. Geim, K. S. Novoselov and A. Mishchenko, *Nat. Nanotechnol.* **8**, 100 (2013)
- [141] J. Ristein, W. Zhang, F. Speck, M. Ostler, L. Ley and T. Seyller, *J. Phys. D* **43**, 345303 (2010)
- [142] A. Bostwick, T. Ohta, T. Seyller, K. Horn and E. Rotenberg, *Nature Phys.* **3**, 36 (2007)
- [143] T. Ohta, A. Bostwick, J.L. McChesney, T. Seyller, K. Hom and E. Rotenbarg, *Phys. Rev. Lett.* **98**, 206802 (2007)
- [144] G. Giovannetti, P. A. Khomyakov, G. Brocks, V. M. Karpan, J. van den Brink, and P. J. Kelly, *Phys. Rev. Lett.* **101**, 026803 (2008)
- [145] M. Sze and K. K. Ng, *Physics of Semiconductor Devices* 3rd ed. *Wiley Interscience* (2007)
- [146] H. Zhong, K. Xu, Z. Liu, G. Xu, L. Shi, Y. Fan, J. Wang, G. Ren and H. Yang, *J. Appl. Phys.* **115**, 013701 (2014)
- [147] H. Zhong, Z. Liu, G. Xu, Y. Fan, J. Wang, X. Zhang, L. Liu, K. Xu and H. Yang, *Appl. Phys. Lett.* **100**, 122108 (2012)
- [148] H. Seyller, K.V. Emtsev, K. Gao, F. Speck, L. Ley, A. Tadich, L. Broekman, J. D. Riley, R. C. G. Leckey, O. Rader, A. Varykhalov and A. M. Shikin, *Surf. Sci.* **600**, 3906 (2006)
- [149] J. Crofton, L. M. Porter and J. Williams, *Phys. Status Solidi B* **202**, 581 (1997)
- [150] W. Lu, W. C. Mitchel, G. R. Landis, T. R. Crenshaw and W. E. Collins, *J. Appl. Phys.* **G**, 5379 (2003)
- [151] W. Lu, W. C. Mitchel, C. Thornton, G. R. Landis and W. E. Collins, *J. Electron. Mater.* **32**, 426 (2003)
- [152] J. Ristein, S. Mammadov and Th. Seyller, *Phys. Rev. Lett.* **108**, 246104 (2012)

- 
- [153] R.T. Tung, *Phys. Rev. B: Condens. Matter* **45**, 13509 (1992).
- [154] C. Chen, M. Aykol, C. Chang, A. F. J. Levi and S. B. Cronin, *Nano Lett.* **11**, 1863 (2011)
- [155] X. M. Li, H. Zhu, K. Wang, A. Cao, J. Wei, C. Li, Y. Jia, Z. Li, X. Li and D. Wu, *Adv. Mater.* **22**, 2743 (2010)
- [156] X. Miao, S. Tongay, M. K. Petterson, K. Berke, A. G. Rinzler, B. R. Appleton, A. F. Hebard, *Nano Lett.* **12**, 2745 (2012)
- [157] X. An, F. Liu, Y. J. Jung and S. Ka, *Nano Lett.* **13**, 909 (2013)
- [158] F. J. Himpsel, G. Hollinger, R. A. Pollak, *Phys. Rev. B* **28**, 7014 (1983)
- [159] S. M. Sze, *Physics of Semiconductor Devices*, Wiley, New York (1981)
- [160] S. Tongay, T. Schumann and A. F. Hebard, *Appl. Phys. Lett.* **95**, 222103 (2009)
- [161] S. Tongay, M. Lemaitre, X. Miao, B. Gila, B. Appleton and A. F. Hebard, *Phys. Rev. X* **2**, 011002 (2012)
- [162] W. Jie, F. Zheng and J. Hao, *Appl. Phys. Lett.* **103**, 233111 (2013)
- [163] C. X. Guo, G. H. Guai, and C. M. Li, *Adv. Energy Mater.* **1**, 448 (2011)
- [164] S. Chandramohan, J. Kang, H. Y. S. Katharria, N. Han, Y. Beak, S. K. B. Ko, J. B. Park, H. K. Kim, E. K. Suh and C. H. Hong, *Appl. Phys. Lett.* **100**, 023502 (2012)
- [165] C. A. Mead, *J. Appl. Phys.* **32**, 646 (1961).
- [166] A. Principi, M. Carrega, R. Asgari, V. Pellegrini and M. Polini, *Phys. Rev. B* **86**, 085421 (2012)
- [167] U. K. Mishra, P. Parikh and Y.-F. Wu, *Proc. IEEE* **90**, 1022 (2002)
- [168] P. S. Park, K. M. Reddy, D. N. Nath, Z. Yang, N. P. Pature and S. Rajan, *Appl. Phys. Lett.* **102**, 153501 (2013)
- [169] U. K. Mishra, P. Parikh, and Y. Wu, in *IEEE Proc.* **90**, pp. 1022 (2002).
- [170] W. Zhu, T. Low, V. Perebeinos, A. A. Bol, Y. Zhu, H. Yan, J. Tersoff and P. Avouris, *Nano Lett.* **12**, 3431 (2012)
- [171] C. Neagu, H. Jansen, H. Gardeniers and M. Elwenspoek, *Mechatronics* **10**, 571 (2000)
- [172] L. Heyderman, H. Schiff, C. David, J. Gobrecht, and T. Schweizer, *Microelectron. Eng.* **54**, 229 (2000)
- [173] A. Ghatak and R. B. Dupaix, *Int. J. Struct. Changes Sol.* **2**, 53 (2010).
- [174] S. F. Jones, G. M. Evans and K. P. Galvin, *Adv. Colloid Interface Sci.* **80**, 27 (1999)
- [175] S. F. Jones, K. P. Galvin, G. M. Evans and G. J. Jameson, *Chem. Engineering Sci.* **53**, 169 (1998)
- [176] A. J. Bard, G. Inzelt, F. Scholz, *Electrochemical Dictionary* 2nd edition, Springer (2012)
- [177] X. H. Wu, C. R. Elsass, A. Abare, M. Mack, S. Keller, P. M. Petroff, S. P. DenBaars, J. S. Speck and S. J. Rosner, *Appl. Phys. Lett.* **72**, 692 (1999)
- [178] B. Pecz, Z. Makkai, M. A. di Forte-Poisson, F. Huet and R. E. Dunin-Borkowski, *Appl. Phys. Lett.* **78**, 1529 (2001)
- [179] Z. Bougrioua, I. Moerman, L. Nistor, B. Van Daele, E. Monroy, T. Palacios, F. Calle and M. Leroux, *Phys. Status Solidi A* **195**, 93 (2003)

- 
- [180] H. Sasaki, S. Kato, T. Matsuda, Y. Sato, M. Iwami and S. Yoshida, *Jpn. J. Appl. Phys.* **45**, 2531 (2006)
- [181] S. Roensch, V. Sizov, T. Yagi, S. Murad, L. Groh, S. Lutgen, M. Krieger and H. B. Weber, *Material Sci. Forum* **502**, 740 (2013)
- [182] A. Caoa, J. A. Teetsov, F. Shahedipour-Sandvik and S. D. Arthur, *J. Cryst. Growth* **264**, 172 (2004)
- [183] J. E. Northrup, L. T. Romano and J. Neugebauer, *Appl. Phys. Lett.* **74**, 2319 (1999)
- [184] K. Cheng, M. Leys, S. Degroote, H. Bender, P. Favia, G. Borghs and M. Germain, *J. Cryst. Growth* **353**, 88 (2012)
- [185] A. Das, S. Pisana, B. Chakraborty, S. Piscanec, S. K. Saha, U. V. Waghmare, K. S. Novoselov, H. R. Krishnamurthy, A. K. Geim, A. C. Ferrari and A. K. Sood *Nat. Nanotechnol.* **3**, 210(2008)
- [186] G. Fisichella, S Di Franco, P. Fiorenza, R. Lo Nigro, F. Roccaforte, C. Tudisco, G. G. Condorelli, N. Piluso, N. Spartà, S. Lo Verso, C. Accardi, C. Tringali, S. Ravesi, F. Giannazzo, *Beilstein J. Nanotechnol.* **4**, 234 (2013)
- [187] C. R. Eddy and D. K. Gaskill, *Science* **324**, 1398 (2009)
- [188] G. Prakash, M. A. Capano, M. L. Bolen, D. Zemlyanov and R. G. Reifenger, *Carbon* **48**, 2383 (2010)
- [189] G. F. Sun, J. F. Jia, Q. K. Xue and L. Li, *Nanotechnology* **20**, 355701 (2009)
- [190] J. Röhrli, M. Hundhausen, K. V. Emtsev, T. Seyller, R. Graupner and L. Ley, *Appl Phys Lett.* **92**, 201918 (2008)
- [191] A. C. Ferrari, J. C. Meyer, V. Scardaci, C. Casiraghi, M. Lazzeri, F. Mauri, S. Piscanec, D. Jiang, K. S. Novoselov, S. Roth and A. K. Geim, *Phys. Rev. Lett.* **97**, 187401 (2006)
- [192] C. Vecchio, S. Sonde, C. Bongiorno, M. Rambach, R. Yakimova, V. Raineri and F. Giannazzo, *Nanoscale Res. Lett.* **6**, 269 (2011)
- [193] O. L. Krivanek, G. J. Corbin, N. Dellby, B. F. Elston, R. J. Keyse, M. F. Murfitt, C. S. Own, Z. S. Szilagy and J. W. Woodruff, *Ultramicroscopy* **108**, 179 (2008)
- [194] O. L. Krivanek, M. F. Chisholm, V. Nicolosi, T.J. Pennycook, G.J. Corbin, N. Dellby, M.F. Murfitt, C.S. Own, Z.S. Szilagy, M.P. Oxley, and S. T. Pantelides and S. J. Pennycook, *Nature* **464**, 571 (2010)
- [195] G. Nicotra, Q. M. Ramasse, I. Deretzis, A. La Magna, C. Spinella and F. Giannazzo, *ACS Nano* **7**, 3045 (2013)
- [196] D. K. Schroder, Semiconductor Material and Device Characterization, 3rd ed. *John Wiley and Sons: Hoboken, New York* (2006).
- [197] F. Giannazzo, V. Raineri and E. Rimini, Transport properties of graphene with nanoscale lateral resolution, in Scanning Probe Microscopy in Nanoscience and Nanotechnology, ed. B. Bhushan, *Springer-Verlag, Berlin, Heidelberg* (2011)
- [198] F. Iucolano, F. Roccaforte, F. Giannazzo and V. Raineri, *J. Appl. Phys.* **102**, 113701 (2007)

- [199] Y. Lv, Z. Lin, T. D. Corrigan, J. Zhao, Z. Cao, L. Meng, C. Luan, Z. Wang and H. Chen, *J. Appl. Phys.* **109**, 074512 (2011)
- [200] C. H. Chen, S. M. Baier, D. K. Arch and M. S. Shur, *IEEE Trans. Electron Devices* **35**, 570 (1988)
- [201] W. Schottky, *Z. Phys.* **113**, 367 (1939)
- [202] N. F. Mott, *Proc. Cambridge Philos. Soc.* **34**, 568 (1938)
- [203] J. Bardeen, *Phys. Rev.* **71**, 717 (1947)
- [204] S. M. Song, J. K. Park, O. J. Sul and B. J. Cho, *Nano Lett.* **12**, 3887 (2012)
- [205] F. Giannazzo, S. Sonde, V. Raineri, G. Patanè, G. Compagnini, F. Aliotta, R. Ponterio and E. Rimini, *Phys. Status Solidi* **7**, 1251 (2010)
- [206] L. Tapasztò, G. Dobrik, P. Nemes-Incze, G. Vertesy, Ph. Lambin and L. P. Birò, *Phys. Rev. B* **78**, 233407 (2008)
- [207] P. S. Park, D. N. Nath and S. Rajan, *IEEE Electron Device Lett.* **33**, 991 (2012)
- [208] S. Luryi, *Appl. Phys. Lett.* **52**, 501 (1988)
- [209] J. Xia, F. Chen, J. Li and N. Tao, *Nat. Nanotechnol.* **4**, 505 (2009)
- [210] F. Giannazzo, S. Sonde, V. Raineri and E. Rimini, *Nano Lett.* **9**, 23 (2009)
- [211] O. Ambacher, B. Foutz, J. Smart, J. R. Shealy, N. G. Weimann, K. Chu, M. Murphy, A. J. Sierakowski, W. J. Schaff, L. F. Eastman, R. Dimitrov, A. Mitchell and M. Stutzmann, *J. Appl. Phys.* **87**, 334 (2000)
- [212] M. Nagase, H. Hibino, H. Kageshima and H. Yamaguchi, *Nanotechnology* **20**, 445704 (2009)
- [213] F. Giannazzo, I. Deretzis, A. La Magna, F. Roccaforte, R. Yakimova, *Phys. Rev. B* **86**, 235422 (2012)
- [214] M. K. Yakes, D. Gunlycke, J. L. Tedesco, P. M. Campbell, R. L. Myers-Ward, C. R. Eddy Jr., D. K. Gaskill, P. E. Sheehan and A. R. Laracuente, *Nano Lett.* **10**, 1559 (2010)
- [215] T. Schumann, K.-J. Friedland, M. H. Oliveira Jr., A. Tahraoui, J. M. J. Lopes, H. Riechert, *Phys. Rev. B* **85**, 235402 (2012)
- [216] J. Hicks, A. Tejada, A. Taleb-Ibrahimi, M. S. Nevius, F. Wang, K. Shepperd, J. Palmer, F. Bertran, P. Le Fèvre, J. Kunc, W. A. de Heer, C. Berger, E. H. Conrad, *Nature Phys.* **9**, 49 (2013)
- [217] J. Baringhaus, M. Ruan, F. Edler, A. Tejada, M. Sicot, A.T.-Ibrahimi, A.-P. Li, Z. Jiang, E. H. Conrad, C. Berger, C. Tegenkamp and W. A. de Heer, *Nature* **506**, 34 (2014)
- [218] S.-H. Ji, J. B. Hannon, R. M. Tromp, V. Perebeinos, J. Tersoff, F. M. Ross, *Nature Mater.* **11**, 114 (2012)
- [219] T. Low, V. Perebeinos, J. Tersoff, Ph. Avouris, *Phys. Rev. Lett.* **108**, 096601 (2012)
- [220] F. Giannazzo, I. Deretzis, A. La Magna, S. Di Franco, N. Piluso, P. Fiorenza, F. Roccaforte, P. Schmid, W. Lerch and R. Yakimova, *Mater. Sci. Forum* **740–742**, 113 (2013)
- [221] E. Pallecchi, F. Lafont, V. Cavaliere, F. Schopfer, D. Mailly, W. Poirier and A. Ouerghi, *Sci. Rep.* **4**:4558, 1 (2014)

- 
- [222] F. Giannazzo, F. Roccaforte, F. Iucolano, V. Raineri, F. Ruffino and M. G. Grimaldi, *J. Vac. Sci. Technol. B* **27**, 789 (2009)
- [223] F. Giannazzo, S. Hertel, A. Albert, A. La Magna, F. Roccaforte, M. Krieger and H. B. Weber, *Mat. Sci. Forum* **778-780**, 1142 (2014)
- [224] M. Ostler, I. Deretzi, S. Mammadov, F. Giannazzo, G. Nicotra, C. Spinella, Th. Seyller and A. La Magna, *Phys. Rev. B* **88**, 085408 (2013)
- [225] A. Zubair, O. Saadat, Y. Song, J. Kong, M. Dresselhaus and T. Palacios, *APS March Meeting 2014*, **59**, 1.

*This*

*Page*

*Intentionally*

*Left*

*Blank*

# Curriculum Vitae

Name	Gabriele Fisichella
Date of Birth	1987, January, 5
Nationality	Italian
E-mail	gabrielefisichella@outlook.com

## *Education*

2014, September	International School of Physics and Technology of Matter, Otranto
2012, January	Professional Chemist License, Italian Chemists Professional Order
2011, July	Master Degree in Organic and Bioorganic Chemistry (evaluation: 110/110 cum laude), Department of Chemistry - University of Catania  Thesis title: <i>"Design of New Antibacterial Compounds Against Multidrug-Resistant Pathogens"</i>
2009, April	Bachelor Degree in Chemistry (evaluation: 110/110), Department of Chemistry - University of Catania  Thesis title: <i>"Gadolinium Doped Cerium Oxide and Platinum Film Layers Deposition on Silicon to Develop Solid Oxide Fuel Cells"</i>
2005, June	High School License with address in Mathematics and Physics (evaluation: 100/100)

## ***Publications***

- 2014 G. Fisichella, G. Greco, S. Ravesi, F. Roccaforte, F. Giannazzo, "Current transport in graphene/AlGaIn/GaN heterostructures", proceeding IEEE-NMDC, submitted
- 2014 A. Piazza, S. Agnello, I. Deretzis, A. La Magna, M. Scuderi, G. Nicotra, C. Spinella, G. Fisichella, F. Roccaforte, M. Cannas, F. M. Gelardi, R. Yakimova, F. Giannazzo, "Micro-Raman characterization of graphene grown on SiC (000-1)", proceeding IEEE-NMDC, submitted
- 2014 G. Fisichella, G. Greco, F. Roccaforte and F. Giannazzo, "Electrical properties of graphene contacts to AlGaIn/GaN heterostructures", Materials Science Forum, in press
- 2014 F. Giannazzo, S. Hertel, A. Albert, G. Fisichella, A. La Magna, F. Roccaforte, M. Krieger, H. B. Weber, "Electrical properties of hydrogen intercalated epitaxial graphene/SiC interface investigated by nanoscale current mapping", Materials Science Forum, in press
- 2014, October G. Fisichella, G. Greco, S. Di Franco, F. Roccaforte, S. Ravesi and F. Giannazzo, "Nanoscale electrical characterization of graphene contacts to AlGaIn/GaN heterostructures", Physica Status Solidi C 11, 1551–1555
- 2014, August G. Fisichella, G. Greco, F. Roccaforte and F. Giannazzo, "Microscopic mechanisms of graphene electrolytic delamination from metal substrates", Applied Physics Letters 105, 063117(5)
- 2014, June G. Fisichella, S. Di Franco, F. Roccaforte, S. Ravesi, and F. Giannazzo, "Microscopic mechanisms of graphene electrolytic delamination from metal substrates", Applied Physics Letters 104, 233105(5)
- 2014, May G. Fisichella, G. Greco, F. Roccaforte, F. Giannazzo, "Current transport in graphene/AlGaIn/GaN vertical heterostructures probed at nanoscale", Nanoscale 6, 8671-8680
- 2014, May F. Giannazzo, I. Deretzis, G. Nicotra, G. Fisichella, Q.M. Ramasse, C. Spinella, F. Roccaforte and A. La Magna, "High resolution study of structural and electronic properties of epitaxial graphene grown on off-axis 4H-SiC (0001)", Journal of Crystal Growth 393, 150-155



- 2014, February F. Giannazzo, I. Deretzis, G. Nicotra, G. Fisichella, C. Spinella, F. Roccaforte and A. La Magna, "*Electronic properties of epitaxial graphene residing on SiC facets probed by conductive atomic force microscopy*", Applied Surface Science 291, 53-57
- 2013, September R. Lo Nigro, P. Fiorenza, M. R. Catalano, G. Fisichella, F. Roccaforte, G. Malandrino, "*Binary and complex oxide thin films for microelectronic applications: An insight into their growth and advanced nanoscopic investigation*", Surface & Coatings Technology 230, 152-162
- 2013, September P. Fiorenza, G. Greco, G. Fisichella, F. Roccaforte, G. Malandrino, R. Lo Nigro, "*High permittivity cerium oxide thin films on AlGaIn/GaN heterostructures*", Applied Physics Letters 103, 112905-112909
- 2013, June F. Giannazzo, G. Fisichella, R. Lo Nigro, P. Fiorenza, S. Di Franco, A. Marino, N. Piluso, E. Rimini, F. Roccaforte, "*Scanning probe microscopy investigation of the mechanisms limiting electronic transport in substrate-supported graphene*", Physica Status Solidi C 10, 1188-1192
- 2013, April G. Fisichella, S. Di Franco, P. Fiorenza, R. Lo Nigro, F. Roccaforte, C. Tudisco, G. G. Condorelli, N. Piluso, N. Spartà, S. Lo Verso, C. Accardi, C. Tringali, S. Ravasi, F. Giannazzo, "*Micro- and nanoscale electrical characterization of large-area graphene transferred to functional substrates*", Beilstein journal of nanotechnology 4, 234-242
- 2013, January R. Lo Nigro, G. Greco, L. Swanson, G. Fisichella, Patrick Fiorenza, F. Giannazzo, S. Di Franco, C. Bongiorno, A. Marino, G. Malandrino, F. Roccaforte, "*Potentialities of Nickel Oxide as Dielectric for GaN and SiC Devices*", Materials Science Forum 740-742, 777-780

## ***Conferences***

- 2014, October Oral Presentation, IEEE-NMDC 201 – Aci Castello (IT)  
Presentation title: "Current transport in graphene/AlGaIn/GaN heterostructures"
- 2014, May Oral Presentation, EMRS 2014 spring meeting – Lille (FR)  
Presentation title: "Nanoscale electrical characterization of graphene contacts to AlGaIn/GaN heterostructures"

- 2014, May                      Poster Section, Graphene 2014 – Toulouse (FR)  
  
Poster title: *“Large-area graphene from catalytic metals to arbitrary substrates by electrochemical delamination and transfer printing”*
- 2012, September              Oral Presentation, EMRS 2012 fall meeting – Warsaw (PL)  
  
Presentation title: *“Micro and Nanoscale Electrical Characterization of Large Area Graphene Transferred to Functional Substrates”*
- 2011, October                 Poster Section, XXIV National Congress, Italian Chemical Society – Lecce (IT)  
  
Poster title: *“Design of New Antibacterial Compounds Against Multiresistant Pathogens”*

### ***Awards***

- 2014, May                      Graduate Student Award, EMRS 2014 Spring Meeting – Lille (FR),  
European Materials Research Society